Technische Universität München
TUM School of Engineering and Design

Model Order Reduction of Non-linear Magnetodynamic Systems

Application to Active Magnetic Bearings

Johannes Q. Maierhofer

Vollständiger Abdruck der von der TUM School of Engineering and Design der Technischen Universität München zur Erlangung eines

Doktors der Ingenieurwissenschaften (Dr.-Ing.)

genehmigten Dissertation.

Vorsitz: Prof. Dr.-Ing. Michael W. Gee

Prüfende der Dissertation:

1. Prof. dr.ir. Daniel J. Rixen
2. Prof. dr.ir. Christophe Geuzaine
3. Prof. Dr. Stéphane Clénet

Die Dissertation wurde am 29.05.2024 bei der Technischen Universität München eingereicht und durch die TUM School of Engineering and Design am 15.10.2024 angenommen.

Foreword

Every writing process should have its target audience. A thesis like this needs to span a broad audience. There are beginners in the topic that need to understand the basics and want to be taken by the hand at some point to not lose the global overview. On the other side, there are professionals that have dealt with one or the other topic in deep detail for a long time. They need to quickly find the one detail they are looking for. The third party is the examination committee, which has to decide on the scientific quality of the work.

For that reason, the first part is more in the style of a lecture script to introduce the magnetodynamic systems and their computation with finite elements. The part does not claim completeness in every possible way but serves a self-contained presentation of what is needed later. This first part could be completely skipped by the advanced reader. The second part, where the model order reduction methods are developed, starts methodological and turns into a detailed discussion of the results. The third part has more of the flavor of a report of one exemplary experimental study that utilizes the basics of the beforehand developed methods.

As a special ingredient, each part comes with a short historical section that should give the interested reader an insight into where methods are coming from and who the persons were that made major contributions.

Abstract

Simulating mechatronic systems accurately and efficiently is challenging due to their complexity and high computational costs. Considering not only the usability and flexibility of simulations with intensive resource utilization but also in the light of increasing sustainability concerns, it becomes clear that more efficient simulation strategies are needed. This need has precipitated the exploration and development of model order reduction techniques, particularly for non-linear systems.

In this thesis, we conduct an in-depth study of non-linear magnetodynamic-mechanical systems from the perspective of model order reduction. The theoretical framework for magnetodynamic systems is initially provided, deriving the field quantities and global quantities such as the mechanical force from the fundamental Maxwell's equations, the most general description of electrodynamic systems. Assuming a low-frequency domain and leveraging the finite element method for computations, the open-source software NGSolve, combined with Python, is chosen to perform the computations. The validity of the proposed framework is subsequently confirmed through various well-known benchmark systems provided by the Compumag Society.

Following this, the concept of model order reduction and hyperreduction is explored, initially in an abstract manner, before being adapted explicitly to magnetodynamic systems. Two distinct hyperreduction methods, namely Discrete Empirical Interpolation Method (DEIM) and Energy Conserving Sampling and Weighting (ECSW), are presented and evaluated against simple academic systems and the established benchmark systems. Additionally, we propose new ideas to exploit the ECSW method in two important aspects. Due to the fact that only part of the domain is non-linear (due to saturation), the implementation of ECSW can be significantly improved. Further, in applications where forces need to be derived from the electromagnetic simulation, the ECSW idea can be exploited to reduce the computational cost of the post-processing step significantly.

Finally, a practical use case of an active magnetic bearing is presented, showcasing the application of a reduced-order model in a monitoring scenario. The outcomes of this application are then replicated via an experimental setup and discussed in detail.

Overall, this work not only illustrates the potential of model order reduction in enhancing the usability and efficiency of large-scale simulations of complex mechatronic systems but also emphasizes the challenges and opportunities in this emerging field.

Zusammenfassung

Die akkurate und effiziente Simulation von mechatronischen Systemen stellt aufgrund ihrer Komplexität und der hohen damit verbundenen Rechenkosten eine Herausforderung dar. Nicht nur im Hinblick auf die Nutzbarkeit und Flexibilität der Simulationen mit intensiver Ressourcennutzung, sondern auch vor dem Hintergrund zunehmender Bewusstheit hinsichtlich der Nachhaltigkeit wird deutlich, dass effizientere Simulationsstrategien erforderlich sind. Diese Notwendigkeit treibt die Erforschung und Entwicklung von Techniken zur Modellordnungsreduktion, insbesondere für nichtlineare Systeme, voran.

In dieser Arbeit werden nichtlineare magnetodynamisch-mechanische Systeme aus der Perspektive der Modellordnungsreduktion untersucht. Zunächst wird der theoretische Rahmen für magnetodynamische Systeme geschaffen, indem neben den Feldgrößen auch die globalen Größen wie die mechanische Kraft aus den grundlegenden Maxwell-Gleichungen, der allgemeinsten Beschreibung elektrodynamischer Systeme, abgeleitet werden. Unter der Annahme eines niederfrequenten Bereichs und der Nutzung der Finite-Elemente-Methode für die Berechnungen wird die Open-Source-Software NGSolve in Kombination mit Python für die Durchführung der Berechnungen gewählt. Die Gültigkeit des vorgeschlagenen Frameworks wird anschließend durch verschiedene bekannte Benchmark-Systeme bestätigt, die von der Compumag-Gesellschaft bereitgestellt werden.

Anschließend wird das Konzept der Modellordnungsreduktion und Hyperreduktion untersucht, zunächst auf abstrakte Weise, bevor es speziell an magnetodynamische Systeme angepasst wird. Zwei verschiedene Hyperreduktionsmethoden, nämlich die Discrete Empirical Interpolation Method (DEIM) und die Energy Conserving Sampling and Weighting (ECSW), werden vorgestellt und anhand von einfachen akademischen Systemen und den etablierten Benchmark-Systemen bewertet. Zusätzlich werden neue Ideen vorgeschlagen, um die ECSW Methode bezüglich zweier Aspekte zu erweitern. Aufgrund der Tatsache, dass nur ein Teil der Domäne nichtlinear ist (aufgrund der Sättigung), ist eine erheblich verbesserte Implementierung der ECSW Methode möglich. Darüber hinaus kann bei Anwendungen, bei denen Kräfte aus der elektromagnetischen Simulation abgeleitet werden, die ECSW-Idee genutzt werden, um die Berechnungskosten des Postprocessings deutlich zu senken.

In den letzten Abschnitten schließlich erfolgt eine praktische Implementierung eines aktiven Magnetlagers präsentiert, die die Anwendung eines Modells reduzierter Ordnung in einem Überwachungsszenario demonstriert. Die Ergebnisse dieser Anwendung werden dann anhand eines Versuchsaufbaus repliziert und im Detail diskutiert.

Insgesamt veranschaulicht diese Arbeit nicht nur das Potenzial der Modellordnungsreduktion bei der Verbesserung der Nutzbarkeit und Effizienz von groß angelegten Simulationen komplexer mechatronischer Systeme, sondern unterstreicht auch die Herausforderungen und Möglichkeiten in diesem aufstrebenden Bereich.

Acknowledgement

Die vorliegende Arbeit entstand während meiner Tätigkeit als wissenschaftlicher Mitarbeiter am Lehrstuhl für Angewandte Mechanik der Technischen Universität München.

Mein erster Dank gilt meinem Doktorvater Prof. dr.ir. Daniel Rixen für die mir gegebene Möglichkeit und das in mich gesetzte Vertrauen. Die stets wohlwollende fachliche sowie menschliche Begleitung und Unterstützung wusste ich immer zu schätzen. Die großen Freiräume im Bereich der Forschung ermöglichten es mir ein Thema zu finden, das mich bis heute begeistert und fesselt.

Nicht nur fachlich durfte ich in meiner Zeit am Lehrstuhl ein sehr breites Spektrum erleben, auch persönlich durfte ich ganz wunderbare Menschen kennen lernen. Besonders hervorzuheben sind die KollegInnen, die schnell zu engen Freunden wurden. Aus Konferenzbesuchen wurden spannende Studienreisen, aus kleinen Kaffeepausen inspirierende Philosophiestunden. Ich kann wirklich aus Überzeugung sagen, dass meine Zeit am Lehrstuhl zur bisher besten Zeit meines Lebens wurde. Ich möchte keinen einzigen Tag missen.

Bedanken möchte ich mich an dieser Stelle auch noch speziell bei meinen FreundInnen aus der Musik. Ihr habt mich immer wieder geerdet, abgelenkt und auf die anderen Freuden des Lebens gebracht. Dabei habt ihr aber nie vergessen mich für diese Arbeit zu motivieren und wart immer verständnisvoll wenn die Priorität wieder einmal dieser Arbeit galt.

Ganz besonders herzlich danke ich meiner gesamten Familie, insbesondere meinen Eltern Felicitas und Max. Ohne Euere Förderung, Unterstützung und ohne Eueren Glauben an mich und meine Arbeit wäre dies niemals möglich gewesen.

Munich, October 01, 2023 *Johannes Maierhofer*

Educational Contributions

The first part of the thesis represents a self-contained summary of the physical theory of magnetodynamic systems, including the finite element method. To the author's knowledge, one cannot find a short yet overarching compilation of the state-of-the-art simulation techniques for magnetodynamic systems in that degree of detail as given here.

- Formulation of the magnetodynamic equations from Maxwell's equations in a vector potential
- Description of a non-linear material behavior
- Derivation of global quantities (e.g. forces) using the local Jacobian method
- Discretization using finite element method, considering edge elements
- Solution of a time series, using Backward-Euler and Newton-Raphson

Scientific Contributions

Full Field Model Order Reduction

The thesis's methodological part concerns the full field model order reduction of magnetodynamic FEM problems. These systems examined have a few specific properties, and it is unclear how they interfere with hyperreduction methods.

- Explanation of DEIM and ECSW in the context of magnetodynamic FEM Systems
- Application of the ECSW method on magnetodynamic systems for the first time
- Extensive comparison of DEIM and ECSW results
- Simulation study on international benchmark examples

Force-Based Model Order Reduction

An extension of the ECSW method for electro-mechanical systems with the computation of the force is introduced.

- Adaption of the ECSW method to force computation
- Simulation study on international benchmark examples

Experimental Analysis

Finally, an experimental dynamic analysis of an active magnetic bearing is conducted.

- Test rig construction and simulation setup
- Static measurements for parameter calibration
- Multi-physical simulation (force and temperature) and comparison with measurements

Publications

[1] Maierhofer, J., Wagner, C., Thümmel, T., and Rixen, D. “Progress in Calibrating Active Magnetic Bearings with Numerical and Experimental Approaches”. In: *Mechanisms and Machine Science*. Springer International Publishing, Aug. 2018, pp. 249–261. DOI: 10.1007/978-3-319-99272-3_18.

[2] Maierhofer, J. and Rixen, D. J. “Model order reduction using hyperreduction methods (DEIM, ECSW) for magnetodynamic FEM problems”. In: *Finite Elements in Analysis and Design* 209 (Oct. 2022), p. 103793. DOI: 10.1016/j.finel.2022.103793.

[3] Maierhofer, J., Dietz, C., Zobel, O. M., and Rixen, D. J. “Multiphysical Simulation, Model Order Reduction (ECSW) and Experimental Validation of an Active Magnetic Bearing”. In: *Actuators* 11.6 (June 2022), p. 169. DOI: 10.3390/act11060169.

[4] Maierhofer, J. and Rixen, D. J. “Strategies for Finding Training Snapshots for the Hyperreduction Method ECSW in Magnetodynamic Systems”. In: *PAMM* 22.1 (Mar. 2023). DOI: 10.1002/pamm.202200106.

[5] Maierhofer, J. and Rixen, D. J. “Computing Forces by ECSW-Hyperreduction in Nonlinear Magnetodynamic FEM Problems”. In: *IEEE Transactions on Magnetics* 60.1 (Jan. 2024), pp. 1–13. ISSN: 1941-0069. DOI: 10.1109/tmag.2023.3332210.

Contents

Frequently Used Symbols

Abbreviations

AMB	Active Magnetic Bearing
DEIM	Discrete Empirical Interpolation Method
dof	Degree of Freedom
ECSW	Energy Conserving (Mesh) Sampling and Weighting
EMCP	Electro Magnetic Computing Problem
FEA	Finite Element Analysis
FEM	Finite Element Method
FESS	Flywheel Energy Storage System
FOM	Full-Order Model
HFM	High-Fidelity Model
MOR	Model Order Reduction
MST	Maxwell Stress Tensor
PDE	Partial Differential Equation
POD	Proper Orthogonal Decomposition
POM	Proper Orthogonal Modes
PWM	Pulse Width Modulation
RE	Relative Error
rhs	right-hand-side
ROM	Reduced-Order Model
sNNLS	spare Non-Negative Least Square
SVD	Singular Value Decomposition
TEAM	Testing of Electromagnetic Analysis Methods

Mathematical Symbols

$\int_\Gamma \mathrm{d}\Gamma$	Surface integral (line integral in 2D)
$\int_\Omega \mathrm{d}\Omega$	Volume integral (area integral in 2D)
∇	Nabla operator
$\oint_\Gamma \mathrm{d}\Gamma$	Closed surface integral (closed line integral in 2D)
$\boldsymbol{n}$	Unit normal vector
$\boldsymbol{t}$	Unit tangential vector

Constants

		Value
μ_0	Natural permeability	$4\pi \times 10^{-7}\,\mathrm{V\,s\,A^{-1}\,m}$
ε_0	Natural permittivity	$8.855 \times 10^{-12}\,\mathrm{A\,s\,V^{-1}\,m^{-1}}$
c_0	Speed of light	$2.997 \times 10^{8}\,\mathrm{m\,s^{-1}}$

Electromagnetics

		Unit
μ	Magnetic permeability	$\mathrm{V\,s\,A^{-1}\,m}$
ν	Magnetic reluctivity	$\mathrm{A\,m\,V^{-1}\,s}$
Φ	Electric scalar potential	V
Ψ	Magnetic Scalar Potential	A
ρ	Charge density	$\mathrm{C\,m^{-3}}$
σ	Electrical conductivity (isotropic)	Ω^{-1}
$\boldsymbol{A}$	Magnetic vector potential	$\mathrm{V\,s\,m^{-1}}$
ε	Electric permittivity	$\mathrm{A\,s\,V^{-1}\,m^{-1}}$
$\boldsymbol{B}$	Magnetic flux density	$\mathrm{T = V\,s\,m^{-2}}$
$\boldsymbol{D}$	Electric flux density	$\mathrm{C\,m^{-2}}$
$\boldsymbol{E}$	Electric field	$\mathrm{V\,m^{-1}}$
$\boldsymbol{F}_m$	Mechanical force	N
$\boldsymbol{H}$	Magnetic field	$\mathrm{A\,m^{-1}}$
$\boldsymbol{j}$	Current density	$\mathrm{A\,m^{-2}}$
$\boldsymbol{T}$	Current Vector Potential	$\mathrm{A\,m^{-1}}$
W'_m	Magnetic co-energy	J
W_m	Magnetic energy	J

Finite Element Method

$\mathcal{J}$	Jacobian
$\boldsymbol{f}$	Discretized load
$\boldsymbol{g}(\boldsymbol{u})$	Discretized internal currents
$\boldsymbol{M}$	Discretized mass matrix
$\boldsymbol{u}$	Discretized vector potential

Model Order Reduction

σ	Singular value
τ	Tolerance of sNNLS
$\boldsymbol{q}$	Non-linear reduced generalized coordinates
$\boldsymbol{V}$	Reduced basis

Notations

Continuous Fields

For continuous field quantities, non-bold symbols denote scalar fields and bold characters vector fields. A (scalar) potential function for each position (x,y,z) in the domain is written as

$$\Psi(x,y,z).$$

The (vectorial) magnetic flux density in Cartesian coordinates is written as

$$\boldsymbol{B}(x,y,z) = \begin{pmatrix} B_x(x,y,z) \\ B_y(x,y,z) \\ B_z(x,y,z) \end{pmatrix} = \boldsymbol{B}(\boldsymbol{x}) = \boldsymbol{B}.$$

However, the dependency of the space coordinates is omitted to maintain readability. In contrast to the upper case symbols, lower case symbols often denote field densities. Examples are the energy or force density (w,f) that must be integrated over the volume.

Discrete Vectors

Unlike a field, a vector does not assign a value to every point in space, but rather it is a single entity with its magnitude and direction. Vectors are often used to represent entities in space (like field quantities) but at countable sets of points. We will use bold characters to denote vectors and matrices. In general (exceptions are necessary here and there), lowercase non-bold symbols represent scalars, lowercase bold symbols represent uni-column matrices whereas uppercase ones denote multi-column matrices. For instance,

$$a = \begin{bmatrix} a_1 \end{bmatrix} \qquad \boldsymbol{a} = \begin{bmatrix} a_1 \\ a_2 \\ \vdots \end{bmatrix} \qquad \boldsymbol{A} = \begin{bmatrix} a_{11} & a_{12} & a_{13} & \cdots \\ a_{21} & a_{22} & \cdots & \\ a_{31} & \vdots & \ddots & \\ \vdots & & & \end{bmatrix}.$$

Tensors

A tensor represents a physical property at a particular point in space. A tensor field is a tensor-valued function of position in space. Tensors of rank two are marked with a double underline. For example for the permeability tensor:

$$\boldsymbol{B} = \underline{\underline{\mu}}\boldsymbol{H}$$

Complex Values

Complex values are noted with a single underline. The same holds for complex-valued vectors:

$$\underline{u} = a + \mathrm{i}b \qquad \underline{\boldsymbol{u}} = \begin{bmatrix} a_1 + \mathrm{i}b_1 \\ a_2 + \mathrm{i}b_2 \\ \vdots \end{bmatrix}$$

Differential Operators

A small recap is given here for the differential operators that will be used in the following. The *Nabla* symbol ∇ denotes the differentiation matrix operator, in some regions also called *del* operator:

$$\boldsymbol{\nabla} = \begin{pmatrix} \frac{\partial}{\partial x} \\ \frac{\partial}{\partial y} \\ \frac{\partial}{\partial z} \end{pmatrix}$$

Scalar Fields $u(x,y,z)$ The gradient of a scalar field results in a vector field that indicates the direction and magnitude of the steepest increase of the scalar field at each point in space.

$$\boldsymbol{\nabla} u = \operatorname{grad}(u)$$

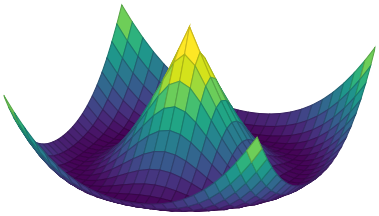

Scalar field

Vector Fields $\boldsymbol{u}(x,y,z)$ The rotation of a vector field results in another vector field that indicates the direction and magnitude of the local circulation of the original vector field at each point in space. The divergence of a vector field results in a scalar field that indicates the rate at which the vector field is spreading out or converging at each point in space.

$$\boldsymbol{\nabla} \times \boldsymbol{u} = \operatorname{curl}(\boldsymbol{u})$$
$$\boldsymbol{\nabla} \cdot \boldsymbol{u} = \operatorname{div}(\boldsymbol{u})$$

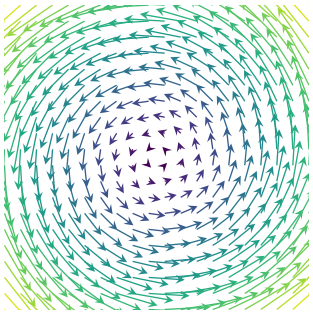

Vector field

Chapter 1

General Introduction

Mechatronic systems are complex engineering systems that integrate multiple disciplines, including mechanical, electrical, and control engineering. Increasing complexity in mechatronic systems leads to a growing need for more advanced simulation methodologies. Despite rapid advancements in computational power, these large-scale simulations continue to pose significant challenges due to the extensive demand for computational resources, including processing power and memory footprint. Model Order Reduction (MOR) is a promising technique to address this challenge by reducing the size and complexity of mathematical models while preserving their essential dynamic behavior.

The main objective of this thesis is to demonstrate the advantages of MOR for simulating mechatronic systems where magnetic forces play a crucial role. By developing and applying MOR techniques to a range of mechatronic systems, this thesis aims to show that MOR can significantly reduce the simulation time and computational cost while maintaining the accuracy of the simulation results. The findings of this thesis can provide valuable insights for researchers and practitioners in the field of mechatronics and help improve the design and development of mechatronic systems.

1.1 Motivation

The motivation for this thesis has two facets: On the one hand, the development of mechatronic systems should be accelerated to build less resource-intensive devices by optimal design. This requires simulation-based optimization processes, and the speed of these simulations is crucial. The faster a single simulation, the more time is available for finding the optimal solution. Rather than increasing computational resources, MOR can be used to reduce computational costs and improve simulation efficiency.

On the other hand, to ensure the reliable and safe operation (i.e. being free from harm, danger, risk, or injury) of already manufactured systems for as long as possible, smart monitoring systems are needed. These systems can observe the state of a machine using low edge-computing power and report its health status to the user. Additionally, the security of operation becomes a more crucial consideration. Security refers to the state of being protected from threats, risks, or potential harm that may arise from deliberate actions, such as criminal activities, unauthorized access, or malicious intent. Therefore, companies often do not want to have a full model for every device to protect critical information and, last but not least, to protect their intellectual property. The use of MOR is proposed as part of the solution to both challenges.

In this thesis, electromagnetic systems are specifically considered as a subgroup of mechatronics. This group has a high potential for incorporating newly developed techniques quickly, as they are already equipped with sensors and microcontrollers.

1.2 Objective

The simulation of non-linear magnetodynamic systems in vector potential formulation is a challenging task that requires significant computational resources. MOR and, in particular, hyperreduction, an existing approach from the field of structural dynamics, have shown promising results in reducing the computational complexity of MOR for such systems in the context of the finite element method. Therefore, the following research questions arise:

How can hyperreduction, an existing approach from the field of structural dynamics, be adapted and effectively implemented in the context of the finite element method to apply model order reduction to magnetodynamic systems in vector potential formulation while maintaining the accuracy of the simulation results?

How can hyperreduction be specialized and effectively applied to compute the mechanical forces generated by magnetodynamic systems while maintaining the simulation results' accuracy and considering the non-linearities and coupling between the electromagnetic and mechanical subsystems?

1.3 Outline of the Thesis

The thesis is structured in three parts. Each part is self-contained, including its references, and can be read individually without losing context. Part I and II are purely methodologically oriented. Part III shows a demo application on an experimental setup.

Part I

First, the fundamental physics and how it can be modeled and computed using the finite element method are explained. These are all state-of-the-art techniques. An attempt is made to give a complete, but not too deep, account as an overview. With the references provided, the reader is able to get a deeper insight into mathematical details on his own at any point. Using generic numerical examples, reference calculations are set up to depict the further needed phenomena in the static and dynamic case of magnetodynamic systems.

Part II

The second part first gives an introduction to model order reduction techniques. From there, different known approaches are adapted and tested with the academic example. New methods as an extension to the known methods are developed in the following and discussed after a comparison.

Part III

Part III shows the application side with the example of an active magnetic bearing. This part can also be read as a stand-alone part. The principle of active magnetic bearings is shown, and the exact exemplar of the here used bearing is described. This part has an extended scope as it describes the overall mechatronic system. The focus of the part is the simulation of the magnetic bearing with the basics from part I, the application of the developed methods from part II, and finally, the calibration with a special purpose-built test rig.

Part I

Fundamentals

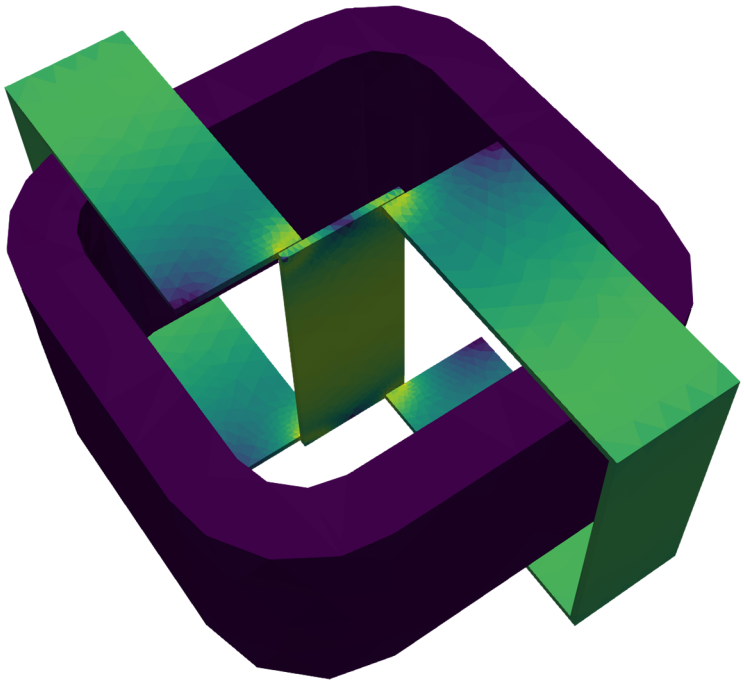

Chapter 2

Short History of Magnetic Field Calculations

2.1 Physical Description

The effect of electromagnetic forces was discovered around 1800 by different people. H.C. ØRSTED (*1777-†1851) was in 1820 the first who investigated the effect in more detail [9]. Allegedly, he noticed during a lecture that current-carrying wires can influence a compass needle [1]. Later, with his name, the unit (oe) was developed for the strength of the magnetic field. For the centennial celebration of this discovery, PUPIN compares 1920 the development of mechanics that happened in the 17th century with that of electrodynamics in the 19th century. "What Copernicus, Kepler, Galileo, and Newton achieved for our knowledge of the matter in motion, that was achieved by Oersted, Ampère, Faraday and Maxwell for our knowledge of electricity in motion. Oersted is the Copernicus, Ampère is the Kepler, Faraday is the Galileo, and Maxwell is the Newton of the science of electrodynamics, the science of electricity in motion.", [52]. Just as NEWTON formulated the laws of motion on the shoulders of his predecessors, JAMES CLERK MAXWELL (*1831-†1879) managed to aggregate all the known phenomena of electromagnetism in his famous paper *A Dynamical Theory of the Electromagnetic Field* in 1865. The complete findings were published in a book series *A treatise on electricity and magnetism* with two volumes [44, 45].

The next big step to our modern application of Maxwell's equation is attributed to OLIVER HEAVISIDE (*1850-†1925). BUCKLEY gives 1950 a tribute at [14] to HEAVISIDE. UNZ summarizes 1963 HEAVISIDE's contributions: "Heaviside developed the vector analysis and started to use it exclusively for Maxwell's equations in 1882. [...] Heaviside expounded Maxwell's theory in detail and in very clear, systematic terms, much in the same form as since has become classical.", [74].

A good reference to study the field of electromagnetism is the textbook *Introduction to Electrodynamics* by DAVID J. GRIFFITHS [28].

2.2 Finite Element Method

Structural Mechanics FEM Theoretical pre-work for the Finite Element Method (FEM) can be seen to be done by J.S. RAYLEIGH (*1842-†1919), B.G. GALERKIN (*1871-†1945) and W. RITZ (*1878-†1909). RITZ's article [56] proposed a new method for solving boundary value problems by transforming them into variation problems. The method involved assumes a trial function that satisfies the essential boundary conditions and finds the parameters that minimize the energy of the system. This method can be seen as the predecessor of FEM. While the Rayleigh-Ritz method (an improvement of the original Ritz method) is aimed at solving an approximated eigenproblem, the Galerkin method finds an approximation solution of a partial differential equation in a finite subspace by projection. FEM is therefore interpreted

as a specific Ritz-Galerkin method. The terminus *Finite Element Method* was first seen in 1960 in the paper *The finite element method in plane stress analysis* by R.W. CLOUGH from Berkeley University, [18]. It relies on the work of M.J. TURNER [73] during the Boeing Summer Faculty Program 1952-1953. Obviously, the origins of the computer-based calculation method lie in the field of aerospace engineering, whose pioneers had the opportunity to use one of the first computers, e.g., the IBM 701. The task was to calculate the stiffness of a wing structure assembled of various one- and two-dimensional elements representing the spar, ribs, and skin. Through the work of E.L. WILSON, the field of civil engineering was entered, where FEM was first applied to the stress analysis of a concrete dam with a crack. From then on, the method spread to various disciplines and was developed further into many different formulations. CLOUGH himself documented a review of the development in his publication *Original formulation of the finite element method*, [17]. Only a few years later than the original published reference code, many commercial finite element analysis software packages were developed and launched, namely NASTRAN (initiated by NASA), ANSYS, LS-DYNA, and ABAQUS another 10 years later, [41]. The strong development, of course, went along with the increasingly available computational power of the computer era.

Electrodynamic FEM Since the early days of FEM, the method has been generalized for modeling physical systems in many engineering disciplines, including fluid dynamics, thermal analysis, and electromagnetism. One of the first papers making extensive use of the reasonably new method was "Finite Element Solution of Saturable Magnetic Field Problems" by P. SILVESTER [65] in 1970. They discuss static, non-linear, two-dimensional magnetic fields with the assumption that the magnetic vector potential is only a scalar field. Following the variational principle, they find the FEM using linear, triangular elements. The resulting equation system was solved using a Newton-Raphson scheme. They achieved remarkable results despite their limited computational power.

C. TROWBRIDGE reviews the development of magnetic field calculation by computers for the first time in 1972, [71]. His conclusion at that time was that two-dimensional, static models could be analyzed by numerous computer codes. In his second review of the field of electromagnetic computing in 1988, [68], he states FEM is the most successful numerical method for two- and three-dimensional magnetic field computations. The following increasingly available computational power allowed more advanced pre- and postprocessing. Regarding eddy current calculations, no consensus was obvious at that time.

In 1976, the first *Compumag* conference was held, continuing in a series of conferences up to today. The two main topics deal with the computation of static fields and time-varying fields, primarily using FEM. TROWBRIDGE reviews the development of the Compumag Conference from the early days up to the late 1990s, [70]. The contributions are published in the *IEEE Transactions on Magnetics*. Two important developments during that time shall be named here as they form the basis of this thesis: The introduction of three-dimensional solutions using finite elements for static and time-dependent problems (non-linear) with the understanding of the gauge problem as well as the innovation of the Edge (Whitney) elements as basis functions for FEM.

Further names who played an important role in that development process up to today's capabilities are J.L. COULOMB and G. MEUNIER. Their first co-author publication can be found in 1979, [3]. Together they have published a few articles; one is about how to compute the magnetic force via the principle of virtual work in the FEM context, [20]. In the field of eddy current computation with FEM, O. BIRO and K. PREIS have contributed a lot. A famous paper is their work *On the use of the magnetic vector potential in the finite-element analysis of three-dimensional eddy currents*, [5]. A. BOSSAVIT explains the use of edge elements in various publications, among others in [10]. In the same field A. KAMEARI investigates until

today, where he is co-author of a paper introducing a new type of second-order edge-element type for magnetodynamic systems, [2]. Also, he recently started to investigate model order reduction using the Cauer Ladder Network Method, [43].

Three books are named here that give a good entry point into the numerical simulation of electrodynamic systems: [34], [46], [29].

Chapter 3

Theory of Maxwell's Equations

The fundamental equations to describe the physics of electromagnetism are the *Maxwell's Equations*. Here, they are shown in the vectorial notation, as O. HEAVISIDE formulated them 1882. The chapter is constructed in a deductive way. The equations in full generality are stated first, and, via different restrictions, they are simplified to the set of equations that is further used. In the first section, the equations are stated and explained. The second section contains some definitions of linguistic terms, followed by a section that gives thoughts on well-known phenomena of electromagnetism and a quantification which conditions must be fulfilled to observe each effect. This leads to the assumptions that are made for the use in this thesis.

3.1 Basic Equations in Differential Form

Written in differential form, the first two laws arise from *Faraday's law* eq. (3.1) and *Ampere's law* eq. (3.2) in which MAXWELL included the *displacement current density* $\frac{\partial \boldsymbol{D}}{\partial t}$. This term is needed to hold the conservation of charges [32] and allows electromagnetic waves to travel through empty space. To fully govern the system, the two divergence equations eq. (3.3) and eq. (3.4) are necessary. One could also say that a vector field is fully described by the definition of its curl and divergence. The structure of the divergence equations allows a statement about the nature of the two fields: The electric field can have sources and sinks defined by charges, expressed by the charge density ρ. The magnetic field does neither have sources nor sinks.

$$\nabla \times \boldsymbol{E} = -\frac{\partial \boldsymbol{B}}{\partial t} \qquad \text{Faraday's law} \tag{3.1}$$

$$\nabla \times \boldsymbol{H} = \boldsymbol{j} + \frac{\partial \boldsymbol{D}}{\partial t} \qquad \text{Ampere's law} \tag{3.2}$$

$$\nabla \cdot \boldsymbol{D} = \rho \tag{3.3}$$

$$\nabla \cdot \boldsymbol{B} = 0 \tag{3.4}$$

where:

$\boldsymbol{E}$:	Electric field
$\boldsymbol{D}$:	Electric flux density, aka magnetic induction
$\boldsymbol{H}$:	Magnetic field
$\boldsymbol{B}$:	Magnetic flux density, aka electric induction
$\boldsymbol{j}$:	Current density
ρ:	Charge density

The four equations are not fully symmetric. This is due to the common sense that *magnetic monopoles* do not exist [1] in contrast to electric charges that may be present as monopoles. The electric field is a vortex-free source field, while the magnetic field is a source-free vortex field. Due to the curl operator, magnetic and electric fields are always orthogonal to each other.

In the scheme fig. 3.1, Maxwell's equations are visualized. The first cutout shows the current density $\boldsymbol{j}$ applied to an infinite conductor around which a circular magnetic field is induced due to *Ampere's law*. The second cutout visualizes the interplay between a changing magnetic flux density and the electric field. The bottom two pictograms represent the properties of a pure vortex field where the field lines never cross in an arbitrary control volume. On the contrary, all field lines of a source field coincide in one point, which here represents the charges of the control volume.

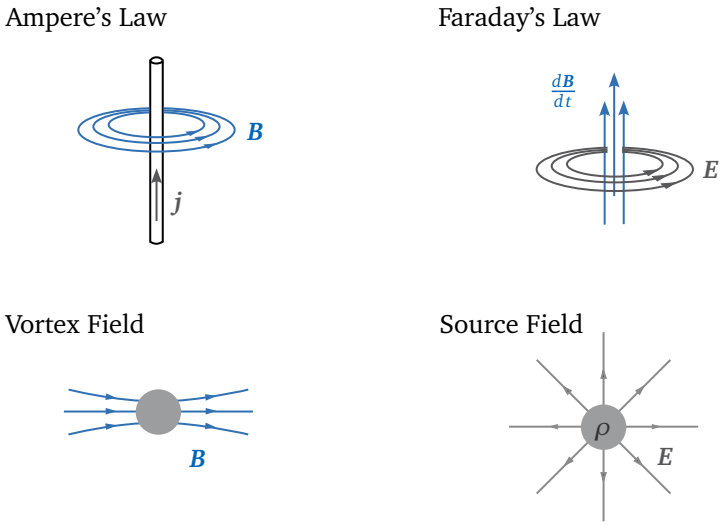

Figure 3.1: Maxwell's equations visualized, [51].

Remark

Caution: In newer literature, the magnetic flux is also often just called the magnetic field. It is important to not mix them up. The magnetic flux density is the only physical field that can be measured. The magnetic field is an artificial construct to express the magnetic influence of electrical currents and magnetized materials.

Constitutive Equations For the governing equations of electromagnetism, two additional constitutive equations are necessary. The first is the relation between the electrical field $\boldsymbol{E}$ and the electric flux density $\boldsymbol{D}$ via the *electrical permittivity* $\underline{\varepsilon}$. The second constitutive equation relates the magnetic field $\boldsymbol{H}$ and the magnetic flux density $\boldsymbol{B}$. This factor is named *magnetic permeability* $\underline{\underline{\mu}}$. Both are material-dependent tensors of rank 2, which is denoted with a double underline.

$$\boldsymbol{D} = \underline{\varepsilon}\boldsymbol{E} \qquad \text{in general: } \boldsymbol{D} = \boldsymbol{D}(\boldsymbol{E}) \tag{3.5}$$

$$\boldsymbol{B} = \underline{\underline{\mu}}\boldsymbol{H} \qquad \boldsymbol{B} = \boldsymbol{B}(\boldsymbol{H}) \tag{3.6}$$

Further information and necessary assumptions are described in detail in chapter 4.

[1] A guide to the literature on magnetic monopoles is found at [26]

Moving Charges On top of the already seen set of equations, moving charges, evoked by an electric field, need to be considered. A collective motion of charge carriers results in a macroscopic current. The current density in conducting material is expressed by Ohm's law, which accounts for the conductivity σ (isotropic and constant) of the material:

$$\boldsymbol{j} = \sigma \boldsymbol{E} \tag{3.7}$$

3.2 Definition of Terminology

Depending on the application, different aspects of Maxwell's equations dominate, and certain terms of the equations may be neglected. Different terms have emerged over time for the individual aspects. This section defines the terms as they are used in this work. The classification widely follows [32] and [34].

Electromagnetism is the branch of physics that studies the electromagnetic force, one of the four fundamental forces of nature, and the interplay between electric and magnetic fields, explaining a wide range of phenomena. Mathematically, electromagnetism is fully described by the basic equations of Maxwell, shown in section 3.1. The linked equations are valid for all ranges of frequencies.

Electrodynamics is synonymously used for *electromagnetism*. The word *electrodynamics* was used rather in the time before Maxwell. The term emphasizes the moving charges that cause the effects of electromagnetism. Today it is more common to use *electromagnetism*. A further term was introduced in the mid of the 20th century, *quantum electrodynamics*, that corresponds to the fairly new field of *quantum mechanics*, but this is far beyond the scope of this thesis.

Magnetodynamics assumes low frequencies, so electrodynamics is simplified to a set of equations where no radiation of waves is prescribed, i.e., the displacement currents are neglected. The low-frequency behavior still interconnects a quasi-static magnetic- with a quasi-static electric system via the so-called eddy currents. Additionally, the term magnetodynamics often includes the assumption of a material without hysteresis effects.

Magnetostatics describes a constant motion of charges (i.e. the current is constant). The equations decouple entirely, as a constant magnetic field does not induce any electrical field which would feedback to the motion of the charges.

Electrostatics applies when the charges are at rest (or at least at very low speeds). No magnetic field is expected for that case. Electromagnetic forces are purely generated by the electric field.

Electrokinetic This term does **not** belong directly to the topic of electromagnetism. Electrokinetic phenomena describe effects where surface charges in a non-conducting material are moved due to mechanical forces, or vice-versa forces arise and move a non-conducting material in an electrical field. Effects like electrophoresis and electroosmosis are part of the electrokinetic phenomena.

3.3 Electromagnetic Systems - Dynamic Phenomena

The set of Maxwell's equations represents the complete physics, but as already mentioned in section 3.2, various assumptions can be made to simplify the equations for the case of magnetodynamic systems. This section will elaborate on the importance of the individual dynamic effects and when they can be omitted. The following two effects will be discussed shortly: Wave propagation and eddy currents.

3.3.1 Wave Propagation in Air

A recap of Maxwell's equations without external currents, i.e., $\boldsymbol{j} = 0$, and with assumed linear material, i.e., air $\mu_r = 1, \varepsilon_r = 1$, shows the electrical and magnetic fields' coupling.

$$\nabla \times \boldsymbol{E} = -\mu_0 \frac{\partial \boldsymbol{H}}{\partial t} \tag{3.8}$$

$$\nabla \times \boldsymbol{H} = \varepsilon_0 \frac{\partial \boldsymbol{E}}{\partial t} \tag{3.9}$$

Considering only one Cartesian direction, the equation becomes a classic wave equation. The wave field $u(x,t)$ is a placeholder for any Cartesian component of the $\boldsymbol{E}$ or $\boldsymbol{H}$ field.

$$\varepsilon_0 \mu_0 \frac{\partial^2 u}{\partial t^2} - \frac{\partial^2 u}{\partial x^2} = 0 \tag{3.10}$$

A schematic wave propagating in the z-direction is visualized in fig. 3.2.

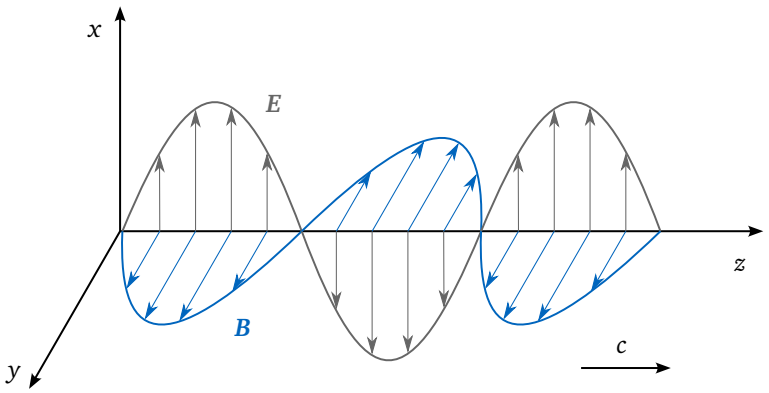

Figure 3.2: Electromagnetic wave - coupled by the terms $\frac{\partial E}{\partial t}$ and $\frac{\partial B}{\partial t}$.

From D'Alambert's solution of the homogeneous wave equation eq. (3.10), the velocity of propagation of the wave results in:

$$c = \frac{1}{\sqrt{\varepsilon \mu}} \quad \text{i.e. in vacuum: } c_0 = \frac{1}{\sqrt{\varepsilon_0 \mu_0}} = 2.997 \times 10^8 \,\mathrm{m\,s^{-1}} \tag{3.11}$$

From this, the wavelength λ can be calculated as a function of the frequency $f = \frac{\omega}{2\pi}$:

$$\lambda = \frac{2\pi c_0}{\omega} = \frac{c_0}{f} \tag{3.12}$$

Indicator Values A dimensionless indicator g_1 is introduced, which compares the characteristic length ℓ_c of the system under consideration and the wavelength λ [57].

$$g_1 = \left(\frac{\lambda}{\ell_c}\right) \tag{3.13}$$

- For $g_1 \gg 1$ the system is either electric or magnetic.
- For $g_1 \approx 1$ the system is electromagnetic.
- For $g_1 \ll 1$, geometrical optics has to be used.

Assuming classic mechatronic devices (electrical motors, solenoids, sensors), the above given values for the speed of light and the following wavelength for low-frequencies, the indicator is clearly $g_1 \gg 1$, leading to a purely electric or magnetic problem. In our case, we are interested in the magnetic domain.

Radiation Power To estimate the importance of the energy radiation via electromagnetic wave propagation in air, the radiation power eq. (3.14) is considered, assuming the electromagnetic system is an antenna [32].

$$P_{\text{radiation}} \propto I_0^2 \left(\frac{\ell}{\lambda}\right)^2 \tag{3.14}$$

Assume a current in the order of $I_0 \approx 10\,\text{A}$, oscillating in a conductor of length $\ell \approx 1\,\text{m}$, at a frequency of $f \approx 1\,\text{kHz}$, and a $\lambda \approx 300 \times 10^3\,\text{m}$ for the speed of light, the radiation power is in the order of $P_{\text{radiation}} \approx 1\,\text{nW}$. So, the radiation power is non-significant and can therefore be neglected.

3.3.2 Eddy Currents

The effect of eddy currents is observed only for conducting materials that are penetrated by electromagnetic waves. The effect describes currents in the material caused by the electrical field that drives charges according to the given conductivity. These eddy currents themselves induce a magnetic field, the change of which in its turn induce a new electrical field. As the current in the material does not flow without loss, the energy of the penetrating wave is dissipated, and the electromagnetic wave decays. In sum, the effect of eddy currents is a second kind of coupling between the Maxwell equations,

$$\nabla \times \boldsymbol{H} = \boldsymbol{j}_{\text{source}} + \boldsymbol{j}_{\text{eddy}} + \frac{\partial \boldsymbol{D}}{\partial t} \tag{3.15}$$

$$\nabla \times \boldsymbol{E} = -\frac{\partial \boldsymbol{B}}{\partial t} \tag{3.16}$$

$$\boldsymbol{j}_{\text{eddy}} = \sigma \boldsymbol{E} \tag{3.17}$$

with σ being the isotropic conductivity.

An artificial indicator value g_2 compares the electrical conductivity σ with the electrical displacement under the frequency f to estimate the importance of the two:

$$g_2 = \frac{\sigma}{2\pi f \varepsilon} \tag{3.18}$$

- For $g_2 \gg 1$ the approach is magnetodynamic.

- For $g_2 \approx 1$ the approach is electrodynamic.
- For $g_2 \ll 1$ the approach is electrostatic.

The characteristic factor g_2 can also be interpreted as the ratio of conduction current density $\boldsymbol{j}$ to displacement current density $\frac{\partial \boldsymbol{D}}{\partial t}$ [37]:

$$\boldsymbol{j} \leftrightarrow \frac{\partial \boldsymbol{D}}{\partial t} \tag{3.19}$$

$$\sigma \boldsymbol{E} \leftrightarrow \varepsilon \frac{\partial \boldsymbol{E}}{\partial t} \tag{3.20}$$

$$\sigma \leftrightarrow \varepsilon 2\pi f \tag{3.21}$$

Since the electrical conductivity in the air is infinitesimally low, the indicator becomes $g_2 \ll 1$ for the air domain. Therefore, the problem is electrostatic in the air that surrounds individual components of mechatronic devices. For systems where also magnetodynamic parts play a role, the electrostatic effects become unimportant as they are magnitudes smaller. Assuming again magnetic actuator systems, components of iron and copper are crucial for the operation. In these domains g_2 is getting very big ($g_2 \gg 1$) because of the high conductivity of the materials in the range of $\sigma = 10^6\,\mathrm{S\,m^{-1}}$ to $10^7\,\mathrm{S\,m^{-1}}$. Thus, the displacement current density compared to the conduction current density is to be neglected up to very high frequencies (GHz), so that the quasi-stationary approach is permissible [37]. This case is called magnetodynamic, and the magnetic flux density $\boldsymbol{D}$ is neglected for the entire system.

The structure of the eddy currents under the magnetodynamic assumption is seen by applying the magnetodynamic equation (3.22) on the iron domain, under the requirement that no external power source, $\boldsymbol{j}_{\mathrm{source}} = 0$, is connected to that domain.

$$\nabla \times \boldsymbol{H} = \underbrace{\boldsymbol{j}_{\mathrm{source}}}_{=0} + \underbrace{\sigma \boldsymbol{E}}_{=\boldsymbol{j}_{\mathrm{eddy}}} \tag{3.22}$$

With the general identity $\nabla \cdot (\nabla \times \boldsymbol{H}) = 0$, it follows that $\nabla \cdot (\sigma \boldsymbol{E}) = \nabla \cdot \boldsymbol{j}_{\mathrm{eddy}} = 0$. The electron flow generated by the electric field is therefore solenoidal, i.e., $\boldsymbol{j}_{\mathrm{eddy}}$ is an eddy current. Thus, in the iron domain, eddy currents occur, which dissipate energy from the electromagnetic field.

3.3.3 Skin Effect - Wave Propagation in Conducting Material

The so-called *skin effect* is characterized by the phenomena of current flowing only near the boundaries of well-conducting materials [58]. For highly conducting materials, the coupling by the displacement currents $\frac{\partial \boldsymbol{D}}{\partial t}$ is neglected. The only coupling arises from the eddy current effect.

The source current is defined to be $\boldsymbol{j}_{\mathrm{source}} = 0$. Furthermore, a complex permittivity is introduced to account for the eddy currents, governed by σ and the frequency ω.

$$\varepsilon_c = \varepsilon + \mathrm{i}\frac{\sigma}{\omega} \tag{3.23}$$

Similar to the wave equation eq. (3.10) obtained from eq. (3.8) and eq. (3.9), the wave equation for the electrical field, considering the eddy currents, now becomes:

$$\nabla^2 \boldsymbol{E} - \gamma^2 \boldsymbol{E} = 0 \tag{3.24}$$

with $\gamma = \sqrt{\mathrm{i}\omega\mu(\sigma + \mathrm{i}\omega\varepsilon)} = \alpha + \mathrm{i}\beta$. The identity for the square root of the imaginary number is:

$$\sqrt{\mathrm{i}} = (1+\mathrm{i})\frac{1}{\sqrt{2}}$$

For good conductors, the permittivity can be neglected ($\sigma \gg \omega\varepsilon$):

$$\gamma = \sqrt{\mathrm{i}\omega\mu\sigma} = (1+\mathrm{i})\sqrt{\frac{\omega\mu\sigma}{2}} \tag{3.25}$$

$$\alpha = \sqrt{\frac{\omega\mu\sigma}{2}} = \sqrt{\pi f\mu\sigma} \tag{3.26}$$

The solution of the wave equation is now written with two exponential-functions

$$E = E_0 e^{-\alpha z} e^{-\mathrm{i}\beta z}. \tag{3.27}$$

The depth, to which the field penetrates the material is called penetration depth δ and is defined as:

$$\delta = \frac{1}{\alpha} = \frac{1}{\sqrt{\pi f\sigma\mu}}. \tag{3.28}$$

The depth of penetration thereby indicates the length after which the electromagnetic field has decayed by a factor of $\frac{1}{e} \approx 37\,\%$. The values resulting for the iron domain are indicated in table 3.1. It can be seen that the skin effect increases with increasing frequency. For dynamic electromechanical systems, this has the most significant influence.

Table 3.1: $\delta(f)$ for iron ($\sigma = 10^7\,\mathrm{S\,m^{-1}}$ and $\mu = 2000 \cdot \mu_0$).

f	$\delta(f)$
1 Hz	3.57 mm
1 kHz	0.11 mm
100 kHz	0.01 mm

3.4 Quasi-stationary Electromagnetism - Magnetodynamic Systems

For this thesis, only dynamic effects in the lower frequency range are relevant. That means, considering eq. (3.12), that the wavelength λ is much bigger than the dimensions of the devices investigated. So, the influence of the changing electrical field on the magnetic field is neglected in the following, i.e., ($\frac{\partial \boldsymbol{D}}{\partial t} = 0$). Additionally, it is assumed that in the whole domain Ω no free charges are present ($\rho = 0$). A non-hysteresis material law leads to the so-called quasi-stationary Maxwell equations, which consider the effect of eddy currents.

$$\boldsymbol{\nabla} \times \boldsymbol{E} = -\frac{\partial \boldsymbol{B}}{\partial t} \tag{3.29}$$

$$\boldsymbol{\nabla} \times \boldsymbol{H} = \boldsymbol{j} \tag{3.30}$$

$$\boldsymbol{\nabla} \cdot \boldsymbol{D} = 0 \tag{3.31}$$

$$\boldsymbol{\nabla} \cdot \boldsymbol{B} = 0 \tag{3.32}$$

These partial differential equations of order 1 in space and time are valid in a Lipschitz Domain $\Omega \subset \mathbb{R}^2$ or $\Omega \subset \mathbb{R}^3$. In fig. 3.3, the domains are visualized. As the magnetic field

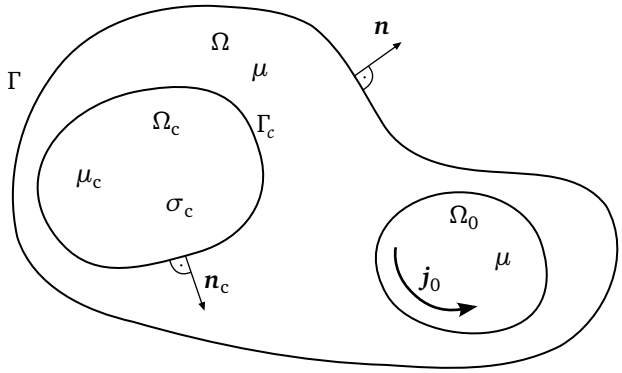

Figure 3.3: Domains of the eddy current equation, where Ω is the enclosing air domain, Ω_c is conductive, and Ω_0 carries the applied current density $\boldsymbol{j}_0$.

would propagate to infinity, the domain Ω has to be large enough to represent the field well. The boundary Γ is conditioned such that all field lines have to be tangential to Γ.

Eddy currents can only occur in the electrical conductive domain $\Omega_c \in \Omega$.

$$\sigma(\boldsymbol{x}) = \begin{cases} \sigma_c & \forall \boldsymbol{x} \in \Omega_c \\ 0 & \forall \boldsymbol{x} \in \Omega \setminus \Omega_c \end{cases} \tag{3.33}$$

Because of eq. (3.33) and Ohm's law, no eddy currents are generated in the domains around Ω_c. Additionally, no eddy current can flow into the non-conducting domain, so eq. (3.34) has to hold [36].

$$\boldsymbol{n}_c \cdot \boldsymbol{j}_c = 0 \quad \text{on } \Gamma_c \tag{3.34}$$

The excitation is applied in the domain Ω_0 and is assumed to be controlled such that the source current density is fully known. Therefore, the eddy currents do not influence this domain. In conclusion, the controlled domain must not be overlapping with the free conductive domain: $\Omega_0 \cap \Omega_c = \emptyset$.

Chapter 4

Magnetic Material Properties

The response of a material to external stimulation is described by the constitutive law. In the electromagnetic context, constitutive laws relate the electric flux density $\boldsymbol{D}$ and the magnetic field intensity $\boldsymbol{H}$ to the electric field $\boldsymbol{E}$ and the magnetic flux density $\boldsymbol{B}$, respectively. These relationships are expressed as mathematical equations [34].

$$\boldsymbol{D} = \underline{\varepsilon}\boldsymbol{E} \tag{4.1}$$

$$\boldsymbol{B} = \underline{\underline{\mu}}\boldsymbol{H} \tag{4.2}$$

In general, the material properties are tensors of rank 2 and describe a linear relationship between two sets of vectors, such as the magnetic field and magnetic flux density in a material. For this thesis, we assume isotropic material properties, i.e., the material behaves similarly in every direction. This implies that the input and output vectors are always considered to be co-linear, i.e., they do not change their orientation due to the material.

The following sections deal with the three, for this thesis important material properties, and the here used way to consider them in the equations. The permittivity and conductivity are only briefly mentioned as they are considered in their most simple nature. The permeability is explained in more detail.

4.1 Dielectric Permittivity

The relation of the electric flux density $\boldsymbol{D}$ and the electric field $\boldsymbol{E}$ is called permittivity ε. For this thesis, the electric field's constitutive equation is considered linear and not dependent on frequency. The permittivity is typically split into two parts, whereas ε_0 is known as a natural constant. The relative permittivity ε_r forms the material-specific constant.

$$\varepsilon = \varepsilon_0 \varepsilon_r \qquad \varepsilon_0 = 8.854 \times 10^{-12} \, \frac{\mathrm{A\,s}}{\mathrm{V\,m}} \tag{4.3}$$

Material Values The relative permittivity for air is approximated as $\varepsilon_r = 1$. Plastic materials typically have higher permittivities, and special piezo-electric materials can even reach values in the order of 1000 [34]. For conductive materials, it is not meaningful to rate the relative permittivity as an electric field leads to moving electrons (i.e. a current) that is oriented such to balance the electric field. The conductivity of these materials is, therefore, the more important property given.

4.2 Electrical Conductivity

For non-isolating materials, the conductivity σ, in combination with Ohm's law, describes the resulting current density $\boldsymbol{j}$ arising from an electrical field. The conductivity is relatively strongly dependent on the material's temperature T.

$$\boldsymbol{j} = \sigma(T)\boldsymbol{E} \tag{4.4}$$

The temperature coefficient can be positive or negative, which results in two material categories: A negative temperature coefficient lowers the material's electric resistance, i.e., raises the electrical conductivity. A positive temperature coefficient, on the other hand, raises the material's resistance (lowers the conductivity). This is the case for iron compounds as used in electric machines. The lower conductivity leads to lower currents for the same electrical field, which leads to lower heat production, the system is stable. The effect is modeled and experimentally shown in part III. For part I and part II, the conductivity is assumed to be constant as no thermal model is considered.

Material Values Typical material values for σ are in the range of order $10^6\,\mathrm{S\,m^{-1}}$ to $10^7\,\mathrm{S\,m^{-1}}$. The conductivity for copper is $5.8\times10^7\,\mathrm{S\,m^{-1}}$. For steel, it is around $5\times10^6\,\mathrm{S\,m^{-1}}$ with a wide variety of different alloy types.

4.3 Magnetic Permeability

Permeability, denoted by μ, is the term used to describe the relationship between the magnetic field intensity $\boldsymbol{H}$ and the magnetic flux density $\boldsymbol{B}$. This material property is the only non-linear one assumed throughout this thesis. After a short physical description, a few materials are shown, and one non-linear permeability model, used in this work, is presented.

4.3.1 Physical Description

Similar to the permittivity, the *permeability* relates the magnetic field $\boldsymbol{H}$ and the magnetic flux $\boldsymbol{B}$ and is, therefore, a kind of *magnetic conductivity*. It is very complex to characterize ferromagnetic materials in all details as all the microscopic effects need to be gathered into a macroscopic law. The ferromagnetism is a quantum mechanical property that stems from the intrinsic spin and orbital angular momentum of the electrons within the material. The direction of this spin, along with how the electrons are distributed in various energy levels and orbital configurations, ultimately dictates the overall magnetic behavior of the material.

The majority of practical applications use phenomenological macroscopic models, such as the Jiles-Atherton or Preisach models, to describe the behavior of ferromagnetic materials. These models, while not able to fully capture all microscopic effects, can give a good approximation of macroscopic behavior under certain conditions.

Besides the isotropy assumption throughout this thesis, the permeability is also assumed to be frequency independent, and no hysteresis is considered. Both are effects that can play major roles in mechatronic devices but are neglected here for the sake of focusing on the development of solution methods.

The permeability is denoted in an analogous way to the permittivity using the relative permeability μ_r and the permeability for vacuum μ_0, which is also called the permeability of free space and is called a natural constant:

$$\mu = \mu_r \mu_0 \qquad \mu_0 = 4\pi \times 10^{-7} \frac{\mathrm{Vs}}{\mathrm{Am}} \tag{4.5}$$

The inverse of the permeability is called the *reluctivity* ν, which can be seen as a *magnetic resistivity* [32, 34]:

$$\nu = \frac{1}{\mu} \tag{4.6}$$

Categorization of Materials Materials are categorized into three types regarding their relative permeability.

μ_r	< 1	Diamagnetic
μ_r	> 1	Paramagnetic
μ_r	$\gg 1$	Ferromagnetic

Dia- and paramagnetic materials are more or less linear, while ferromagnetic substances are highly non-linear. To illustrate the given categories, a few comments are made [39]:

Diamagnetic materials have a μ_r (slightly) smaller than air, which indicates they are pushed out of the magnetic field. This means, for example, that they are repelled by permanent magnets. Materials like water and some metals (lead, bismuth) are diamagnetic. Using that effect, researchers made levitating a living frog in a very strong magnetic field possible.

Paramagnetic materials show the exact opposite behavior of diamagnetic properties. These materials have a slightly higher μ_r than air and are therefore pulled into the magnetic field. For example, all alkaline metals are paramagnetic.

Ferromagnetic materials distinguish themselves from paramagnetic materials through their ability to exhibit spontaneous magnetization. As a result, after switching off the external magnetic field, a residual magnetization remains for the ferromagnetic materials. Due to this, different alloys are used as permanent magnets. Iron is the most commonly known ferromagnetic material.

4.3.2 Ferromagnetic Material Models

In general, the magnetic behavior of ferromagnetic materials is very complex and a detailed material science description would go far beyond the scope of this thesis. Different models were developed to predict the various effects [46]. Several different alloys of steel are available that serve special characteristics for different purposes. Here, only the relevant concepts and assumptions are explained. At the center are the so-called hysteresis curves under the influence of a magnetic field as seen in the schematic fig. 4.1.

Bringing a non-magnetized material of ferromagnetic properties into an external magnetic field (curve ①), regions of the preferred magnetization direction start growing. These regions are also known as magnetic domains, found in 1906 by the French physicist P.E. WEISS (*1865-†1940). This first magnetization process is reversible, and the magnetic flux density increase is moderate (phase I). With increasing field intensity, irreversible processes

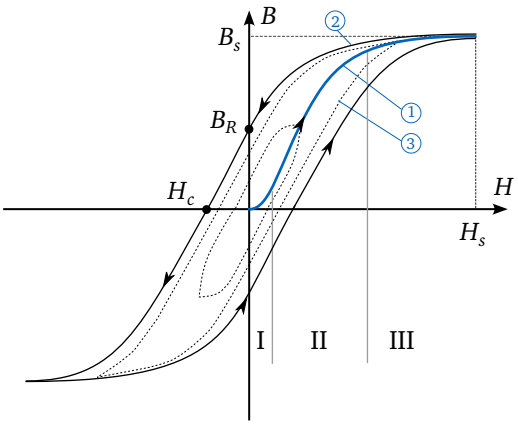

Figure 4.1: Schematic non-linear material behavior with hysteresis.

start, i.e., the regions' magnetization directions flip to match the external field direction. This leads to a steep ascend in the flux density (phase II). For phase III, all magnetic regions are oriented and a further increase of the driving field has the same effect as in vacuum, which means that the permeability saturates towards a relative permeability of $\mu_r \to 1$. Reaching this point is called saturation H_s and B_s. A following relaxation of the external field (following curve ②) cannot reverse the irreversible changes in the material. Therefore, a remanent magnetic induction B_R remains. Applying a negative external field until no remanent magnetic induction is left is called the coercitive magnetic field H_c. For smaller amplitudes, smaller hysteresis loops are driven through, as shown in ③. Note that it is only possible to go through each curve counterclockwise. Passing one hysteresis cycle also means that magnetic energy is transformed into heat due to the losses of the irreversible material processes. The energy loss density is the area between the forward and backward curves [34]. For materials with low coercitive forces (so-called soft magnetic materials) it is sufficient to only consider the new magnetization curve ① in fig. 4.1. Therefore, the hysteresis effect is neglected, and the simulation becomes drastically easier as each simulation step becomes independent of the previous states. Note that each curve in the BH-diagram must be monotonic for physical reasons.

Additionally, the material behavior of ferromagnetic materials is influenced by temperature. These changes are generally rather small, but at temperatures above the Curie temperature, the material reacts like paramagnetic material. Mechatronic systems, as considered in this thesis, operate in a temperature range far below the critical Curie temperature, which is why the temperature influence on permeability is not considered further for this work [16].

Definitions of the Permeability By definition, the *permeability* is the quotient from magnetic flux density B and the magnetic field H.

$$\mu = \frac{B}{H} \tag{4.7}$$

Approximating the permeability by tangents on the BH-curve for each point leads to the definition of the *differential permeability* μ_d written as the differential of B with respect to H.

$$\mu_d = \frac{\mathrm{d}B}{\mathrm{d}H} \tag{4.8}$$

The relation between the BH-cure and the differential permeability is depicted in fig. 4.2. The advantage of the differential permeability becomes visible when the magnetic system is

solved using an iterative solver, see chapter 8. To find the next step, the Jacobian needs to be calculated, which is exactly the differential permeability.

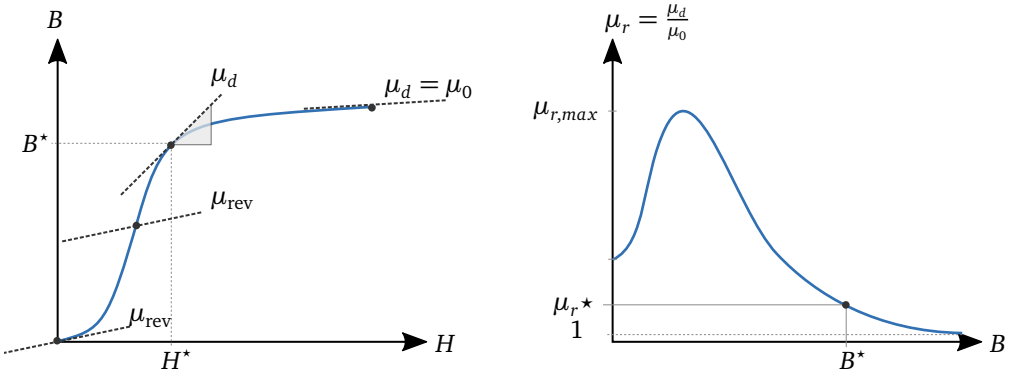

Figure 4.2: Left: Differential permeability curve for non-linear material, visualizing the different definitions of permeability. Right: Relative, differential permeability plotted over magnetic flux density.

An often overseen issue arises due to the physical principle of the orientation of the magnetic domains that flip after a certain point of excitation. Starting from a point $H^\star$ and applying only a small ΔH does **not** induce an irreversible flip of any magnetic domain. Instead, the same **smaller** slope as for the new magnetization curve at $H = 0$ occurs. If the excitation amplitude ΔH remains bounded to small values, the magnetization of the material is completely reversible. But this means that the effective permeability, also called *reversible permeability* μ_{rev}, is smaller than $\mu_d(H^\star)$ [34, 46, 77].

$$\mu_{\text{rev}} = \left.\frac{\mathrm{d}B}{\mathrm{d}H}\right|_{H=H^\star} \quad \forall \quad \Delta H \ll 1 \tag{4.9}$$

Remark

This effect of the reversible permeability is necessary to demagnetize material once magnetized. A sinusoidal excitation with decreasing amplitude is applied to the specimen. Due to the reversible permeability, the remanent induction can be driven down in a spiral-formed hysteresis trajectory towards zero. In measurement equipment, this method is used to demagnetize current sensing tools.

In the course of this thesis, the reversible permeability does not play a role. The applied field amplitudes are assumed to be bigger than the purely reversible effects. Additionally, it is very complicated to gather the necessary material data for each point. This is only possible by specialized measurement campaigns. Also, the implementation is not clear. As both do not contribute to the objective of the thesis, it is mentioned here but neglected further on.

Experimental Characterization In practice, the non-linear material model is determined via an experimental setup for every type of material, refer to fig. 4.3. A ring of the desired material is wound with two wire coils. The first coil is used as the primary side, and a sinusoidal current is imposed. The second coil is seen as a secondary coil, and the received voltage is measured. The exact procedure is standardized in ASTM standard[1].

[1]ASTM A596/A596M21: Standard Test Method for Direct-Current Magnetic Properties of Materials Using the Point by Point (Ballistic) Method and Ring Specimens

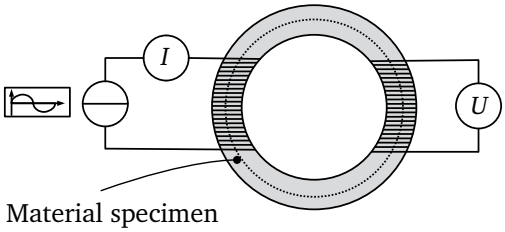

Figure 4.3: Experiment to measure the permeability of a material test sample.

Material Values Air unveils a relative permeability of around $\mu_r = 1$. Copper has a constant permeability of $\mu_r = 1$. It is called magnetically invisible as it behaves like air. Low-alloy steel behaves very similarly to pure iron. The permeabilities for higher alloy steels can vary much, which allows to design materials for different purposes in terms of their magnetic properties. Three examples are given in the following, namely pure iron, recent electric steel in production, and two material samples taken from international benchmark setups.

Iron The BH-measurement points for pure iron were taken from the material database of the software femm [21]. In contrast to the alloyed steels, no reversible permeability is seen from the measurement points. Phase I of the magnetization process is not present or very small. This is also seen from the permeability plot in fig. 4.4, which starts at its maximum value and does not increase any further.

Electrical Steel M270-35A This material is an example of non-grain oriented electrical steels that are specified in the DIN EN 10106[2]. The naming convention is as follows: A starting **M** is followed by the value of the remagnetization loss at a specific operation point. This value is an indicator of the magnetic softness of the material. The smaller the loss factor, the softer the material. After a hyphen, the thickness of the metal sheet is given in tenths of a millimeter. A following **A** indicates the final-annealed condition. The international material number for the *M270-35A* is 1.0801. The magnetic properties can then be read from the datasheet of the manufacturer. A table with H and corresponding B points is given in the data sheet [66] and can then be linearly interpolated. This material, for example, is produced by *Thyssenkrupp* under the market name *powercore*. This thesis's active magnetic bearing in part III is built with this material.

TEAM13,20 Material The name of this material relates to official simulation benchmark examples that were introduced to test magnetic simulation software. The systems were also built and measured. The exact material test specimen BH-measurement data are provided to implement them into our own software framework. More information is given in chapter 11.

Generic Material A generic material model is proposed that is specially designed for easy implementation. Also, the effect of reversible permeability is not modeled, as it is not considered in the simulation anyway. The expression for the permeability of the material as a function of the magnetic flux is formulated as

$$\mu_r(B) = \frac{c_1}{c_2 + c_3 \cdot \left(\frac{B}{\mathrm{T}}\right)^8} + 1 \quad c_1 = 3500 \quad c_2 = c_3 = 0.4 \tag{4.10}$$

where the magnetic flux density is given in Tesla (T).

[2]EN 10106: Cold rolled non-oriented electrical steel strip and sheet delivered in the fully processed state; German version EN 10106:2015

Material Plots A comparison of different material models is shown in fig. 4.4. Whereas the BH-curve seems relatively similar for all materials, the permeability plot shows big deviations. It is recommended to consider the differential (relative) permeability $\mu_{r,d}$ to assess and compare material properties at the maximum (differential) permeability.

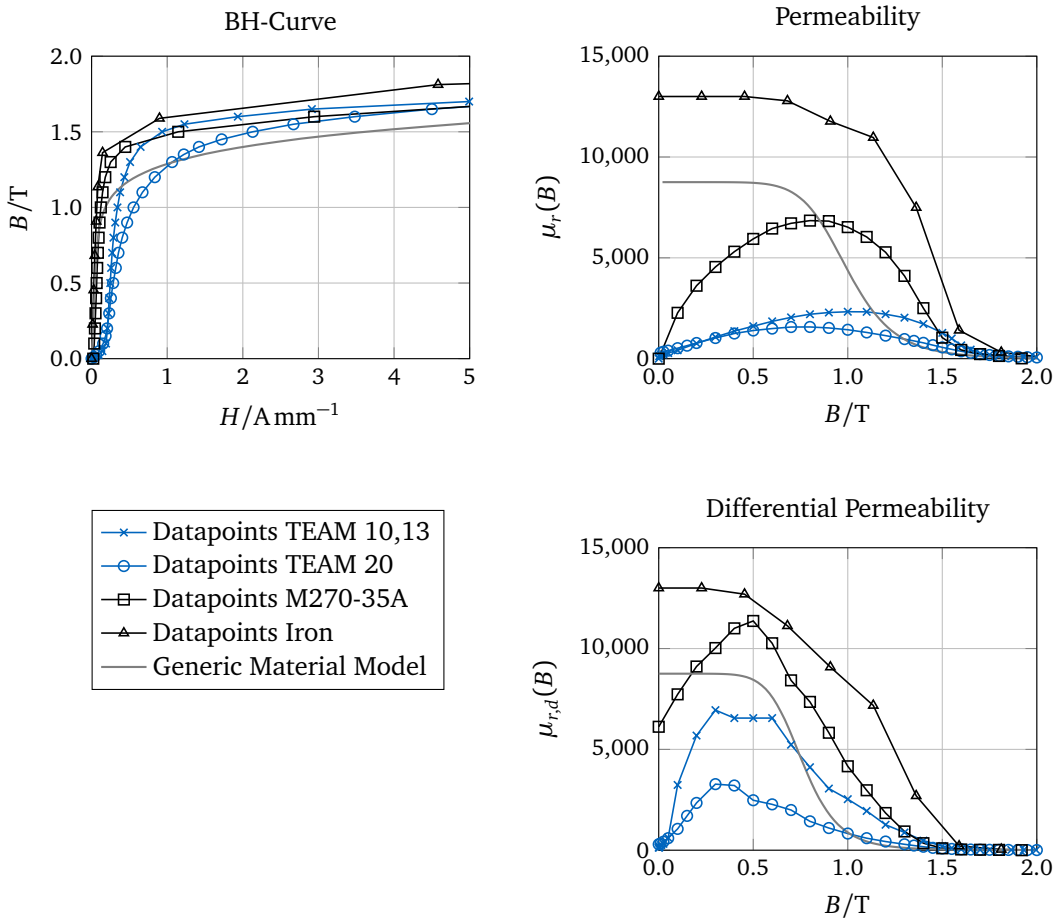

Figure 4.4: Comparison of different material descriptions.

4.3.3 Permanent Magnets

Materials that have the ability to permanently generate and retain a magnetic field are called *permanent magnets*. In modern mechatronic devices, permanent magnets play an important role. They are used in big electric motors as well as in tiny headphones. The most widely used type of rare-earth magnet is the so-called Neodymium Magnet (also known as NdFeB = Neodymium Iron Boron). During the manufacturing process, a fine powder of the ingots is sintered to the desired shapes. Then the special ferromagnetic material is magnetized. In general, the permanent magnets behave like ferromagnetic steel shown in fig. 4.1 but are delivered to the customer in a pre-magnetized state. Additionally, the area in the hysteresis loop is very large, which is often referred to as magnetic hard. The two important characteristic material properties of permanent magnets are:

Remanence, B_R The remanence measures the strength of the magnetic flux density when no outer field is applied to the system.

Coercitivity, H_c The coercitivity is the magnetic field that is necessary to cancel the magnetic flux coming from the permanent magnet.

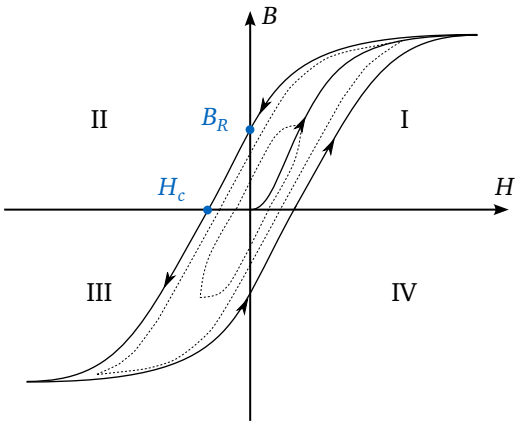

Figure 4.5: Schematic non-linear material behavior with hysteresis.

The magnet, once magnetized, operates in the second quadrant of fig. 4.5. This quadrant is often referred to as the demagnetization curve. In approximation, the permanent magnets are modeled by their major cycle, i.e., only the upper branch of the hysteresis curve. For that, the magnetic field during operation must stay in the range where the magnetization effect is reversible. The slope μ of such magnets is approximated in most cases as constant μ for materials such as NdFeB. To incorporate permanent magnets into Maxwell's equations, eq. (3.6) transforms to:

$$B = B_R + \mu(H)H \tag{4.11}$$

Chapter 5

Formulation of Magnetodynamic Systems

This section gives a glimpse into the various options for defining a formulation that solves Maxwell's equations. BOSSAVIT wrote a book *Computational electromagnetism* [12] where he explains the need for a formulation for magnetodynamic systems. BIRO reviews different possible formulations in combination with edge elements in his paper [8]. MEUNIER collected much of the prime literature, which was investigated mainly by the researchers named in the short history of magnetic field calculations chapter 2 [46].

The first question that arises at this point is: Why are different formulations necessary or even possible to solve Maxwell's equations? The answer is twofold. First, due to the symmetry of Maxwell's equations, two complementary formulations lie on the hand, a magnetic formulation and an electric formulation. Second, Maxwell's equations, as written, assume the differentiability of the fields. For example, the B-field is not continuous due to the general structure of electrodynamic systems, which combines domains of different permeability and conductivity in one system. These jumps in material lead to discontinuous solutions, which can not be represented without modifications in the finite element method for the primary unknown, refer chapter 7, section 7.2.3. To overcome this issue, a step towards potentials as working variables is taken.

5.1 Duality of Maxwell's Equations

As in mechanics, the unknowns force and displacement form a dual pair against each other. The same is true in electrodynamics for the electric field $\boldsymbol{E}$ and the magnetic field $\boldsymbol{H}$. Solving electrodynamic problems, this duality leads to *electric formulations* and *magnetic formulations* where either the electric field or the magnetic field are solved in a strong sense. The respective counterpart is then computed with the help of the constitutive laws, which satisfies their continuity conditions and the second governing equation only in a weak sense. Therefore one needs to decide which field is the desired one and choose the formulation accordingly. To achieve the best solution in conducting and non-conducting domains, the best approach would be to use two dual formulations and select the best solution for each domain [46].

For this thesis, the magnetic flux is the important and desired field quantity, as the mechanical force relies on the magnetic flux density. Additionally, the effect of eddy currents is important for the systems under consideration. For that, the electric formulation is chosen.

The following sections give an introduction into both formulations using potential functions and give a direction when to use which formulation.

5.2 Potential Functions

In vector calculus, a vector potential is a vector field whose curl is a given vector field. This is analogous to a scalar potential, i.e., a scalar field whose gradient is a given vector field.

Looking at the original publications of Maxwell [44], one can see that Maxwell already developed his equations during his research using the concept of (vector) potential functions. According to [76] the idea came from THOMSON. Both already knew that the vector potential is not uniquely described by the equations. Heaviside later introduced the vector calculation and with that he canceled out the vector potential. This reveals the more understandable set of equations that we know nowadays. Interestingly, many textbooks introduce the vector potential as something 'nonphysical' to make the equations calculable, so the story is turned around. In 2014, YANG published an article [76] where he researched the fine details of the origins and the development of Maxwell's equations and their way into our days.

To calculate magnetic flux fields for a general case, the concept of vector potential is widely used [46]. This chapter shows the application of the (vector) potentials and the gauging (i.e. the condition) to make the vector potential unique.

Remark

The combination of an electric scalar potential and a magnetic vector potential to the so-called *Electromagnetic Four-Potential* and the closed mathematics of *four-vectors* is omitted here as it is not used in the further course. The interested reader is referred to [38].

5.2.1 Magnetic Formulation

The magnetic formulation aims to directly find the magnetic field $\boldsymbol{H}$. The intuitive way to find the magnetic field leads to the use of $\boldsymbol{H}$ as the unknown variable. Looking at the governing equation

$$\nabla \times \boldsymbol{H} = \boldsymbol{j} \tag{5.1}$$

shows that the field in non current-carrying domains ($\nabla \times \boldsymbol{H} = 0$) could be named a *reaction field*. That means, the only way a magnetic field can occur inside such a domain can be that it is applied via the boundary conditions. According to BOSSAVIT in [11], this approach leads to a well-posed system for the magnetic field, but does not unambiguously determine the electric field. However, to compute eddy currents, the electric field is needed. For the primary unknown being the magnetic field, the electric field needs to be computed as a post-processing step. This leads to the issue that the electric field is not determined in a unique way by the magnetic field calculated only by Ampere's law [11, 46]. It is though possible to overcome this issues using an additional scalar potential, but a more elegant solution is the use of an electric formulation as seen later.

The same equations and problematic rise by the formulation in vector potential notation, which is the same as before but in the terminology of potentials.

Current Vector Potential The current vector potential $\boldsymbol{T}$, also known as the electric vector potential, is defined under the premise of $\nabla \cdot \boldsymbol{j} = 0$ as:

$$\boldsymbol{j} = \nabla \times \boldsymbol{T} \tag{5.2}$$

The current vector potential is, in general, not sufficient to govern the equations for non-conductive domains. It needs the following magnetic scalar potential for the non-conducting, current-free domains.

Magnetic Scalar Potential The magnetic scalar potential, denoted as Ψ, is directly defined on the magnetic field $\boldsymbol{H}$ when there are no free currents in the system. This is, for example, the case for systems containing only permanent magnets. The magnetic field follows from the gradient of the magnetic scalar potential by definition:

$$\boldsymbol{H} = -\boldsymbol{\nabla}\Psi \tag{5.3}$$

Replacing the magnetic field with its potential in Ampere's law, yields:

$$\boldsymbol{\nabla} \times \boldsymbol{\nabla}\Psi = 0 \iff \boldsymbol{\nabla} \times \boldsymbol{H} = 0 \qquad \forall \boldsymbol{j} = 0 \wedge \frac{\partial \boldsymbol{D}}{\partial t} = 0 \tag{5.4}$$

As source for the magnetic field the divergence of $\boldsymbol{M}$ (sometimes called *bound magnetic charge*) is calculated to find the corresponding Ψ:

$$\Delta\Psi = \boldsymbol{\nabla} \cdot \boldsymbol{M} \tag{5.5}$$

5.2.2 Electric Formulation

In contrast to the magnetic formulation, the electric formulation has the objective of finding the electric field $\boldsymbol{E}$ by the definition of a potential function.

Magnetic Vector Potential It sounds unintuitive to find the electric field $\boldsymbol{E}$ using the so-called magnetic vector potential. But seeing Faraday's law without derivation as $\boldsymbol{E} = \frac{\partial \boldsymbol{A}}{\partial t}$, the objective is to find a vector field $\boldsymbol{A}$ to finally represent $\boldsymbol{E}$. Historically, the magnetic vector potential formulation seemed to be invented around 1985 and A. BOSSAVIT tried the method first in [11]. Z. REN did not use the term magnetic vector potential in [54] but derived a variational formulation for the electric field under the use of a vector potential $\boldsymbol{e}$ which later became known as the magnetic vector potential $\boldsymbol{A}$.

In general, any vector field $\boldsymbol{a}$, which is at least two times continuously differentiable, satisfies:

$$\boldsymbol{\nabla} \cdot (\boldsymbol{\nabla} \times \boldsymbol{a}) = 0 \tag{5.6}$$

The vector potential for the magnetic flux density field $\boldsymbol{B}$ is now defined such that the curl of the unknown field $\boldsymbol{A}$ represents the given field $\boldsymbol{B}$. As the magnetic flux is a solenoidal vector field, i.e., $\boldsymbol{\nabla} \cdot (\boldsymbol{B}) = 0$ (see Maxwell's Equation, eq. (3.4)) it is always true to write:

$$\boldsymbol{B} = \boldsymbol{\nabla} \times \boldsymbol{A} \tag{5.7}$$

The vector $\boldsymbol{A}$ is called the *magnetic vector potential*. If one knows $\boldsymbol{A}$, one can directly calculate $\boldsymbol{B}$. The other way around is not true. The question of uniqueness of $\boldsymbol{A}$ is discussed in the next section 5.5.

The magnetic vector potential is generally sufficient to describe the time-dependent Maxwell's equations without restrictions. A closer look in the further course unveils the difficulties of the magnetic vector potential formulation, see section 5.3.

Electric Scalar Potential It is also possible to compute the electric field using a scalar potential formulation. Unfortunately this formulation is very restricted as shown in the following.

Any arbitrary scalar field V holds:

$$\boldsymbol{\nabla} \times \boldsymbol{\nabla} V = \mathbf{0} \tag{5.8}$$

The electric scalar potential Φ is searched such that the gradient of the unknown scalar field gives the vector field $\boldsymbol{E}$.

$$\boldsymbol{E} = -\boldsymbol{\nabla}\Phi \tag{5.9}$$

In counter analogy, the electric field is only a curl-free vector function for static magnetic fields, i.e., $\frac{\partial \boldsymbol{B}}{\partial t} = 0$, the electric scalar potential is not sufficient to solve general electric and magnetic fields. For static conditions, the electric field can be found

$$\boldsymbol{\nabla} \times \boldsymbol{\nabla}\Phi = \mathbf{0} \iff \boldsymbol{\nabla} \times \boldsymbol{E} = \mathbf{0} \qquad \forall\, \rho = 0 \quad \wedge \quad \frac{\partial \boldsymbol{B}}{\partial t} = \mathbf{0} \tag{5.10}$$

5.3 Modified Vector Potential

The major conclusion from the previously shown basic potentials states that the magnetic vector potential is the only potential that applies to time-dependent magnetic fields due to its definition of the divergence-free condition of the magnetic flux density. The *modified* vector potential additionally makes use of the null space of the curl-curl operator. A gradient of an arbitrary scalar potential V is added to the vector potential, which is now declared as *modified*. Some authors mark the modified vector potential with a star, i.e., $\boldsymbol{A}^{\star}$.

For magnetodynamic problems, i.e., with relative low-frequency content, the influence of the changing electrical field ($\frac{\partial \boldsymbol{E}}{\partial t}$) on the magnetic field is neglected in the following (refer to section 3.4). Additionally, it is assumed that no free charges ($\rho = 0$) are present in the whole domain Ω. Assuming that the material does not exhibit any hysteresis, the so-called quasi-stationary Maxwell equations are obtained, which include the effect of eddy currents. A more sophisticated derivation can be found in [34]:

$$\boldsymbol{\nabla} \times \boldsymbol{E} = -\frac{\partial \boldsymbol{B}}{\partial t} \tag{5.11}$$

$$\boldsymbol{\nabla} \times \boldsymbol{H} = \boldsymbol{j} \tag{5.12}$$

The formulation of the problem in terms of the modified vector potential formulation to solve the quasi-stationary magnetodynamic equations is generally well-known, although it can be presented in different manners. A short version is presented here. Substituting the vector potential ($\boldsymbol{\nabla} \times \boldsymbol{A} = \boldsymbol{B}$) in Faraday's eq. (5.11) and Ampere's law eq. (5.12) leads to the curl-curl formulation for $\boldsymbol{A}$ (see eq. (5.14)).

$$\boldsymbol{\nabla} \times \boldsymbol{E} = -\boldsymbol{\nabla} \times \frac{\partial \boldsymbol{A}}{\partial t} \tag{5.13}$$

$$\boldsymbol{\nabla} \times \left(\frac{1}{\mu(B)} \boldsymbol{\nabla} \times \boldsymbol{A} \right) = \boldsymbol{j} \tag{5.14}$$

The gradient of any arbitrary scalar field V can be added to the vector potential $\boldsymbol{A}$ without changing the magnetic field density $\boldsymbol{B}$. Also, a gradient field grad V can be added to the $\boldsymbol{E}$-field since it would not modify equation eq. (5.13). Therefore, also considering Ohm's law, $\boldsymbol{j} = \sigma \boldsymbol{E}$ can be used to write the equation expressing the eddy current in terms of $\boldsymbol{A}$ and V:

$$\boldsymbol{j}_{\text{eddy}} = \sigma \boldsymbol{E} = -\sigma \frac{\partial \boldsymbol{A}}{\partial t} + \sigma \boldsymbol{\nabla} V \tag{5.15}$$

Splitting the current into its individual sources ($\boldsymbol{j}_0$ indicates the applied current density), eq. (5.14) can now be written as the governing equation in terms of the vector and the scalar potential:

$$\boldsymbol{\nabla} \times \left(\frac{1}{\mu(|\boldsymbol{\nabla} \times \boldsymbol{A}|)} \boldsymbol{\nabla} \times \boldsymbol{A} \right) = \boldsymbol{j}_0 - \sigma \frac{\partial \boldsymbol{A}}{\partial t} + \sigma \boldsymbol{\nabla} V \tag{5.16}$$

To find a valid scalar field V, an additional (naturally given) condition for eq. (5.16) is evaluated: The divergence of the right-hand-side (rhs) of eq. (5.16) has to be zero as $\boldsymbol{H}$ in eq. (5.12) can only generate a solenoidal vector field. Additionally, the Coulomb gauging $\text{div}(A) = 0$ is chosen to be applied, refer to section 5.5. With that, the divergence of the first two terms of the rhs of eq. (5.16) are zero by default, and for the special case of spatially constant conductivity σ, the third term has to satisfy $\sigma \,\text{div}(\text{grad}\, V) = 0$. One valid solution for that is $V = 0$, which comes in handy, as the degrees of freedom for V vanish completely [5].

Finally, by solving eq. (5.17) for the magnetic vector potential, the magnetic and electric field intensities, as well as flux densities, can be obtained, thus eliminating the need to directly solve Maxwell's equations for the magnetic and electric field intensities.

$$\boldsymbol{\nabla} \times \left(\frac{1}{\mu(|\boldsymbol{\nabla} \times \boldsymbol{A}|)} \boldsymbol{\nabla} \times \boldsymbol{A} \right) = \boldsymbol{j}_0 - \sigma \frac{\partial \boldsymbol{A}}{\partial t} \tag{5.17}$$

With $\sigma = 0$ in $\Omega \setminus \Omega_c$, the formulation is identical to the magnetostatic formulation. As the vector potential $\boldsymbol{A}$ is non-unique for the areas of $\sigma = 0$, a regularization term is introduced for the system as shown in section 5.5.

5.4 Alternative Formulations

Apart from the detailed formulation shown in terms of the modified vector potential, other formulations which combine the different potentials for the different domains (conducting / non-conducting) were developed. For the sake of completeness, they are listed here in short but are not further used in the course of this thesis. A special class of formulations are the so-called *Hybrid Formulations* that combine electric and magnetic formulations to find the best results for the different domains.

The notation for the different formulations is defined as follows: The domain can be treated as one entity or can be divided into subdomains 1 and 2, where the first domain, by definition, is the non-conducting part of the domain, the second the conducting domain. For each domain entity, a potential or combination of potentials is formulated. The potentials are named by their variable, as shown in the previous sections. Example: The notation $\boldsymbol{A}^\star$ says that the full domain is governed by the modified vector potential. The notation $\boldsymbol{A}$,$\boldsymbol{A}$-Φ means that in the Ω_1 the potential $\boldsymbol{A}$ is used and in Ω_2 the potential $\boldsymbol{A}$ and the potential Φ as combination.

Basically all combinations are feasible, besides the exclusive use of Φ in a non-conducting region and dual the exclusive use of $\boldsymbol{T}$ in a conducting region. Unfortunately, different authors denote the two above-shown scalar potentials with very different names. This leads to a cumbersome comparison of formulations.

$A^\star$ Formulation is exactly the modified vector potential formulation as already seen. Its major limitation is the assumption that the conductivity σ needs to be spatially constant. The second drawback is the non-uniqueness in non-conducting domains. According to [8], a poor numerical stability is reported. It is not mentioned whether this is due to the named singularity or anything beyond. The advantage of this formulation is its simplicity and the sparse, symmetric equations in a finite element context.

A-Φ Formulation leads to the unknowns magnetic vector potential ($\boldsymbol{A}$) and the electric scalar potential (Φ). The electrodynamic equation is written in full generality as a combination of the vector and the scalar potential:

$$\boldsymbol{E}(t) = -\boldsymbol{\nabla}\Phi - \frac{\partial \boldsymbol{A}}{\partial t} \tag{5.18}$$

Therefore the electric and magnetic fields can then be computed as derivatives of these potentials. Due to the structure of the weak form, the set of equations is finally non-symmetric. A detailed derivation can be found in literature, [46].

T-Ψ Formulation is the dual formulation to the A-Ψ formulation.

$$\boldsymbol{H}(t) = \boldsymbol{T} - \boldsymbol{\nabla}\Psi \tag{5.19}$$

where $\boldsymbol{T}$ needs to represent the exciting current $\boldsymbol{j}_0$ and the eddy currents. It is shown to have advantages for problems that rely on a precise skin effect [6, 30].

A-Ψ Formulation is a so-called hybrid formulation as it makes use of the modified vector potential $\boldsymbol{A}$ in combination with the magnetic scalar potential Ψ.

5.5 Gauging - Uniqueness of Potentials

Gauge fixing (also called choosing a gauge) denotes a mathematical procedure for dealing with redundant degrees of freedom in field variables. Originally, the word *gauge* describes a distance measurement. Related to the electromagnetic fields, the electric field $\boldsymbol{E}$ and the magnetic flux density $\boldsymbol{B}$ are measurable, while the before seen potentials are not. It is the difference between potentials that is measureable, which inspired former researchers to use the terminology of *gauge-fixing* [50]. For electromagnetism, a certain change of the potentials could lead to the same measurements of the fields. To demonstrate the issue, the vector potential ($\boldsymbol{\nabla}\times\boldsymbol{A} = \boldsymbol{B}$) is inserted in Ampere's law eq. (3.2) that leads to the curl-curl formulation for $\boldsymbol{A}$ (see eq. (5.20)).

$$\boldsymbol{\nabla} \times \frac{1}{\mu(B)} \boldsymbol{\nabla} \times \boldsymbol{A} = \boldsymbol{j} \tag{5.20}$$

It can be shown that the curl-curl formulation eq. (5.20) does not specify the divergence of the magnetic vector potential $\boldsymbol{A}$. As result of this, the gradient of any scalar field Φ can be added to the vector potential. That means that every $\boldsymbol{A} + \operatorname{grad}\Phi$ is also a solution of eq. (5.20). On the one hand that shows that the curl-curl operator has a non-trivial null space. Therefore, also the load $\boldsymbol{j}$ cannot have any arbitrary shape. It has to be orthogonal to the null-space. On the other hand, this non-trivial null space will become a benefit for the later introduced *modified vector potential*, which makes use of this freedom. To find a unique solution for $\boldsymbol{A}$ and overcome the singular system, several solutions have been known since the beginning of the simulation of magnetic systems. The individual methods depend highly on the used discretization method and especially on the finite element space used. The methods are commonly called *gauging methods* or *gauge fixing methods* as they ensure a unique vector potential.

Coulomb Gauging The Coulomb gauging is known in various fields of physics, and its gauge fixing condition is setting the divergence of the field to zero:

$$\nabla \cdot \boldsymbol{A} = 0 \tag{5.21}$$

In electromagnetism, it is commonly used for static systems and is supposed to fix the issue of the non defined divergence of the vector potential $\boldsymbol{A}$ directly. The shown approach to include the Coulomb Gauge is based on the assumption that $\nabla \cdot \boldsymbol{j} = 0$ and will fail if this cannot be assured. More information can be found in [38]. Utilizing the relation between the differential operators (only valid for Cartesian coordinates)

$$\nabla \times \nabla \times \boldsymbol{A} = \nabla(\underbrace{\nabla \cdot \boldsymbol{A}}_{=0}) - \Delta \boldsymbol{A}, \tag{5.22}$$

the curl-curl equation can be rewritten. Applying the Coulomb Gauging, the final partial differential equation for the vector potential of magnetostatic problems is:

$$\Delta \boldsymbol{A} = -\mu \boldsymbol{j} \tag{5.23}$$

This kind of equation is known as the *Poisson-Equation*. It is a second-order elliptic partial differential equation, which can be solved using the finite element approach. Any Dirichlet condition on $\boldsymbol{A}$ fixes the solution to a unique one. The intuitive and direct approach comes with a significant disadvantage that becomes evident while implementing the finite element method with edge elements. As explained in the following chapters, these elements are essential or highly beneficial, particularly in 3D scenarios. However, the finite element space linked with them is unable to determine divergence (see chapter 7,section 7.1.1), thereby preventing the application of Coulomb gauging.

Perturbation Gauging The before-seen Coulomb Gauging div($\boldsymbol{A}$) cannot be applied directly for spaces where the divergence is not defined (as in the $\boldsymbol{H}^{\text{curl}}$-space). Instead, a perturbation term of order $\mathcal{O}\kappa$ is added to the equation that ensures a solvable system that is not singular.

$$\nabla \times \frac{1}{\mu} \nabla \times \boldsymbol{A} + \kappa \boldsymbol{A} = \boldsymbol{j} \tag{5.24}$$

The effect can be understood for a very large κ that overshadows the influence of the curl-curl relationship and leads to:

$$\kappa \boldsymbol{A} = \boldsymbol{j} \tag{5.25}$$

For $\boldsymbol{j}$ being a solenoidal current ($\nabla \cdot \boldsymbol{j} = 0$) as assumed in the requirements, $\boldsymbol{A}$ satisfies automatically $\nabla \cdot \boldsymbol{A} = 0$. In consequence, κ has to be chosen such that, on the one hand, an acceptable condition number is achieved for the discretized system. On the other hand, the perturbed solution must not have a large discrepancy relative to the true solution. A more mathematical derivation of the regularization term can be found in [63].

Generalized Coulomb Gauging Further methods for gauging can be found in [40], for example the generalized Coulomb Gauging. The method seems to be related with the so-called Auto Gauging, which is described in [55]. There, the system becomes automatically unique by the operating principle of iterative solvers. As a third method, which could be sorted to the generalized Coulomb Gauging methods, the load can be strictly filtered to be exactly orthogonal to the null space of the curl operator [55]. In all cases, the system's solution becomes unique.

Lorentz Gauging For the case of dynamic electromagnetism systems, the so-called *Lorentz Gauging* can be applied. The Lorentz gauge converges to the Coulomb gauge for constant fields.

$$\nabla \cdot \boldsymbol{A} + \frac{1}{c^2} \frac{\partial \Phi}{\partial t} = 0 \tag{5.26}$$

This gauging is suitable for mixed formulations with a vector potential $\boldsymbol{A}$ for the magnetic field and a scalar potential Φ. In this work, no mixed formulation approaches are used.

Tree, Co-tree Gauging A very different approach of gauging the curl-curl formulation relies on the it's solution via the finite element method where the domains are discretized in elements and, therefore, form a mesh.

Assume the nodes and edges of the mesh build a network. The number of nodes is denoted as n, the number of edges as e. A subgraph of the network can be chosen to be a tree. The tree must not have any circuits and, therefore, $n-1$ branches that correspond to the edges of the mesh. The choice of tree is not unique. The branches that are not included in the chosen tree build a subgraph, the so-called co-tree. This subgraph, seen as finite element space, has $e-n-1$ degrees of freedom. Together they represent all edges of the mesh [35]. The circulation values of the tree's edges are then arbitrarily fixed to zero [42]. The tree-cotree technique has one drawback: Finding the best tree graph for fast convergence of the solution costs high effort [40].

Chapter 6

Global Quantities

Up to this point, the physics and the associated mathematics for calculating the magnetic field distribution were in the foreground. The view is now widened from the microscopic level to a more macroscopic one. This section shows the definition and computation of global quantities, namely the magnetic energy, the power loss, and the total force on rigid bodies in the system.

6.1 Magnetic Energy

The *magnetic energy* W_{mag} describes the energy that is stored in the magnetic flux field. The magnetic energy for a non-linear (isotropic) material is [28]:

$$W_{\mathrm{mag}} = \int_{\Omega} \int_{0}^{B} H(\tilde{B}) \, \mathrm{d}\tilde{B} \, \mathrm{d}\Omega \tag{6.1}$$

To write the definition as in eq. (6.1), it is necessary to assume an isotropic material. In that case, $\boldsymbol{B}$ and $\boldsymbol{H}$ have the same direction, which allows us to write eq. (6.1) in terms of scalar amplitudes in the volume integral. A major drawback is seen here for the term $H(\tilde{B})$ as it is the inverse function of the common material description in the form of $B(\tilde{H})$. For $H \gg 0$ and a strongly saturating material, the inverse becomes ill-posed. To overcome that issue, the so-called *co-energy* is calculated. The co-energy is, therefore, an artificial construct in energy units and is later useful for calculating magnetic forces. It is mostly denoted with an apostrophe:

$$W'_{\mathrm{mag}} = \int_{\Omega} \int_{0}^{H} B(\tilde{H}) \, \mathrm{d}\tilde{H} \, \mathrm{d}\Omega \tag{6.2}$$

For a linear constitutive law $B = \mu H$, energy and co-energy are equal, and no distinction needs to be made. For a non-linear behavior, this is not true anymore. Physically stored in the magnetic system is only the energy W_{mag}. For the further course, the subscript is shortened to keep the notation slender, $W_m = W_{\mathrm{mag}}$ and $W'_m = W'_{\mathrm{mag}}$.

The relation between energy and co-energy is visualized in fig. 6.1. The sum of both is denoted as the $\square$ energy, $W_{\square}$. From fig. 6.1 one can see that:

$$W_{\square} = W_{\mathrm{mag}} + W'_{\mathrm{mag}} \tag{6.3}$$

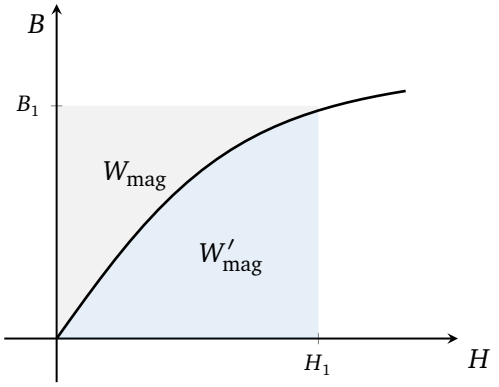

Figure 6.1: Energy W_{mag} and co-energy W'_{mag} for a non-linear material.

Another way to express the □ energy is in terms of the work done by the current density $\boldsymbol{j}$ in association with the vector potential $\boldsymbol{A}$. The index 1 indicates the terminal value. Note that the following vector identity holds without restrictions: $(\boldsymbol{\nabla}\times\boldsymbol{H})\cdot\boldsymbol{A}-\boldsymbol{H}\cdot(\boldsymbol{\nabla}\times\boldsymbol{A})=\boldsymbol{\nabla}\cdot(\boldsymbol{H}\times\boldsymbol{A})$. One can thus write:

$$\begin{aligned} W_{\square} &= \int_{\Omega} \boldsymbol{H}_1\cdot\boldsymbol{B}_1\,\mathrm{d}\Omega \\ &= \int_{\Omega} \boldsymbol{H}_1\cdot(\boldsymbol{\nabla}\times\boldsymbol{A}_1)\,\mathrm{d}\Omega \\ &= \int_{\Omega} (\boldsymbol{\nabla}\times\boldsymbol{H}_1)\cdot\boldsymbol{A}_1\,\mathrm{d}\Omega - \int_{\Omega} \boldsymbol{\nabla}\cdot(\boldsymbol{H}_1\times\boldsymbol{A}_1)\,\mathrm{d}\Omega \end{aligned} \tag{6.4}$$

Using Ampere's law, the first integral is written in terms of the current density $\boldsymbol{j}$. The second integral is rewritten using the Gauss theorem from a volume integral into a surface integral.

$$W_{\square} = \int_{\Omega} \boldsymbol{j}_1\cdot\boldsymbol{A}_1\,\mathrm{d}\Omega - \oint_{\Gamma} \boldsymbol{n}\cdot(\boldsymbol{H}_1\times\boldsymbol{A}_1)\,\mathrm{d}\Gamma \tag{6.5}$$

The surface Γ an be chosen arbitrarily for eq. (6.5) as long as all currents $\boldsymbol{j}$ are inside. Widening the boundary, both $\boldsymbol{H}$ and $\boldsymbol{A}$ decay and the contribution becomes smaller. Increasing the integration domain Ω to infinity, the surface integral vanishes and all contributions are summed up in the volume integral, finally yielding:

$$W_{\square} = \int_{\Omega_\infty} \boldsymbol{j}_1\cdot\boldsymbol{A}_1\,\mathrm{d}\Omega \tag{6.6}$$

6.2 Power Loss

Magnetodynamic systems under the influence of eddy currents are non-conservative systems. Electric power loss in a conductive material is due to the phenomenon known as Joule heating (or resistive heating). The induced eddy currents in the conducting domain are dissipated to heat.

The eddy current density $\boldsymbol{j}_{\text{eddy}}$ is driven by the electric field, which provokes a flow of electrons within a conductor with the conductivity σ. As the electric field is induced by a

changing magnetic flux density, the expression eq. (6.7) is written in terms of the change of $\boldsymbol{A}$, the magnetic vector potential.

$$\boldsymbol{j}_{\text{eddy}} = -\sigma \frac{\partial \boldsymbol{A}}{\partial t} \tag{6.7}$$

The power loss eq. (6.8) is computed as the volumetric integral over the domain of the power loss density, which comes from the electric potential integrated over the flow.

$$P_{\text{loss}} = \int_{\Omega} \boldsymbol{j}_{\text{eddy}} \cdot \boldsymbol{E} \, \mathrm{d}\Omega \tag{6.8}$$

$$P_{\text{loss}} = \int_{\Omega} \frac{\boldsymbol{j}_{\text{eddy}} \cdot \boldsymbol{j}_{\text{eddy}}}{\sigma} \, \mathrm{d}\Omega \tag{6.9}$$

Since the conductivity is responsible for both, the generation and dissipation of eddy currents, it is difficult to grasp its influence on the power loss. A higher conductivity (see eq. (6.7)) leads to a more pronounced eddy current (which is closer to the skin due to the skin-effect, see section 3.3.3) but, on the other hand, lowers the power loss, see eq. (6.8).

6.3 Electromagnetic Force

The electromagnetic force is one of the four fundamental forces of nature, with the other three being gravity, the strong nuclear force, and the weak nuclear force. The theory that describes the electromagnetic force is known as quantum electrodynamics but is not touched on here.

The forces in electrodynamic systems manifest in very different phenomena depending on the system's structure and scale. The primary widely used ones are the reluctance and Lorentz forces. Conversely, the magnetostrictive force sees little practical usage.

6.3.1 Physical Description

The next paragraphs describe the phenomenological forces and their usage. Finally, the thesis will focus on the reluctance forces, although the methods are valid for all electrodynamic forces.

Reluctance Forces Reluctance forces arise from nature's will to bring systems to the state of the lowest potential energy possible. Therefore the forces are directed such that air gaps in electromagnetic systems tend to close. They occur at the transition between different materials, respectively, different permeabilities leading to a term grad(μ). From this follows, the force is always orthogonal to the surface. The most common cases are air gaps between iron core materials. Examples of the use of reluctance forces are reluctance motors (mainly stepper motors), magnetic bearings, and solenoids.

Lorentz Force The view on the Lorentz forces is completely different. These forces are the most direct manifestation of the fundamental electromagnetic force. They arise from a moving charge in a given magnetic field. The resulting direction of the force is orthogonal to the moving charges and to the surrounding magnetic field. The best-known examples of an application of the Lorentz forces are electrical machines.

Magnetostrictive Force The phenomenon of *magnetostrictive force* describes the effect of a deformation of a ferromagnetic material in relation to its magnetic field. The effect is more precisely called the *Joule-Magnetostriction*. A second effect, volumetric magnetostriction, is a changing permeability due to changes in the material's density. The converse effect is the piezoelectric effect due to the existence of an electric field. Both effects are a macroscopic manifestation of the fundamental electromagnetic force. Exemplary applications of magnetostriction are ultrasonic transducers (e.g. for sonars), mostly made from nickel alloys as they have a pronounced magnetostrictive behavior [15, 22]. For this thesis, the effect is not further relevant.

Permanent Magnet Forces The force between permanent magnets is also a manifestation of the electromagnetic force. Permanent magnets generate a magnetic field due to the alignment of the magnetic moments of the atoms in the material. This alignment is usually achieved during the magnet's creation process when an external magnetic field is applied to a ferromagnetic material.

Remark

Forces between permanent magnets can be modeled by substitution currents that are constructed such that they represent the permanent magnet. Therefore, no extra treatment is needed in the theory of forces.

To calculate forces on rigid bodies in electromagnetic systems, there are two main methods, namely the virtual work approach and the Maxwell stress tensor. It can be shown that both are identical in continuous systems but have some practical differences in the finite element framework. In the following course, the derivation of the force is shown via the virtual work idea. A final section will shortly mention the equivalence with the Maxwell stress tensor and give an idea of the issue regarding the necessary surface integral for discretized systems.

6.3.2 Force Calculation - Virtual Work

The following section focuses on the computation of reluctance forces. To explain the force calculation, a system needs to be defined that contains at least a current-carrying domain (the coil) and a domain where the force is applied. We call that the target domain. To create a force, the target domain must provide a permeability different from air. Additionally, a core domain to influence the magnetic field is added (but is not mandatory). Figure 16.1 visualizes the general system setup considered for the next explanations.

The physically intuitive approach to calculating the global force on a target body is based on the conservation of energy. Changing the position of the target body changes the stored magnetic energy. The variation of the target's position is denoted with the parameter $\delta \boldsymbol{s}$. The principle of virtual work states: Assuming no losses from one position to the other, the change in energy can be identified as a force times the distance along the force vector. From the system's point of view, the magnetic force $\boldsymbol{F}_m$ is the rate of change of the energy function related to the displacement.

$$\boldsymbol{F}_m = -\frac{\mathrm{d}W_m}{\mathrm{d}\boldsymbol{s}} \tag{6.10}$$

To calculate the forces, two different thought experiments can be conducted, which lead to different results for non-linear material, but are equivalent for linear material. First, the magnetic flux density field $\boldsymbol{B}$ is held constant for a configurational variation (i.e. the abstract term for a positional variation of the target). Second, the current density $\boldsymbol{j}$ and therefore $\boldsymbol{H}$ is held constant and again a configurational variation is applied.

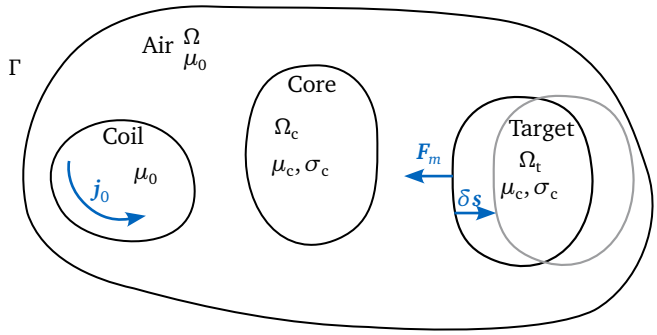

Figure 6.2: Domains for the force F_m calculation on the target domain Ω_t, where Ω is the enclosing air domain, Ω_c represents the core, Ω_0 carries the applied current density $\boldsymbol{j}_0$.

Constant B-field

Keeping the $\boldsymbol{B}$-field constant during a configuration update, i.e., applying a virtual displacement to the target body, leads to a change in the internal current density $\boldsymbol{j}$. There is no source connected to the coil, which means that no energy can cross the system's boundary. This way of computing the force by the partial derivative of the magnetic energy is, for example, used in passive systems with permanent magnets. The derivations are written for the specific forces $\boldsymbol{f}_m$, the force density (considered here to avoid dealing with integral relations).

$$\boldsymbol{f}_m = -\frac{\mathrm{d}w_m}{\mathrm{d}\boldsymbol{s}} = -\frac{\partial w_m}{\partial \boldsymbol{s}} - \frac{\partial w_m}{\partial \boldsymbol{A}} \underbrace{\frac{\partial \boldsymbol{A}}{\partial \boldsymbol{s}}}_{=0} \tag{6.11}$$

The following two notations are used interchangeably, with the gradient index indicating the parameter with respect to which the derivative is taken.

$$\boldsymbol{f}_m = -\frac{\partial w_m}{\partial \boldsymbol{s}} = -\boldsymbol{\nabla}_{\boldsymbol{s}} w_m \tag{6.12}$$

The partial derivative indicates that the change of energy due to the change of position is computed, while the magnetic flux density or alternative, the vector potential $\boldsymbol{A}$ is fixed.

Constant Current

For most mechatronic applications, it is the case that the current density $\boldsymbol{j}$ is controlled and therefore fixed. During a displacement of the movable target, energy will flow in/out of the system, e.g., via the coils to maintain a constant current density.

$$\begin{aligned} \boldsymbol{f}_m &= -\frac{\mathrm{d}w_m}{\mathrm{d}\boldsymbol{s}} + \frac{\mathrm{d}\boldsymbol{j}^T\boldsymbol{A}}{\mathrm{d}\boldsymbol{s}} \\ &= -\frac{\mathrm{d}w_\square}{\mathrm{d}\boldsymbol{s}} + \frac{\mathrm{d}\boldsymbol{j}^T\boldsymbol{A}}{\mathrm{d}\boldsymbol{s}} + \frac{\mathrm{d}w'_m}{\mathrm{d}\boldsymbol{s}} \end{aligned} \tag{6.13}$$

Using the equality for $w_\square = \boldsymbol{j}^T\boldsymbol{A}$, as shown in eq. (6.6), to substitute in eq. (6.13) writes

$$\boldsymbol{f}_m = -\frac{\mathrm{d}\boldsymbol{j}^T\boldsymbol{A}}{\mathrm{d}\boldsymbol{s}} + \frac{\mathrm{d}\boldsymbol{j}^T\boldsymbol{A}}{\mathrm{d}\boldsymbol{s}} + \frac{\mathrm{d}w'_m}{\mathrm{d}\boldsymbol{s}}. \tag{6.14}$$

Finally, the partial derivative of the co-energy gives the mechanical force for constant currents:

$$\boldsymbol{f}_m = \frac{\partial w'_m}{\partial \boldsymbol{s}} = \boldsymbol{\nabla}_{\boldsymbol{s}} w'_m \tag{6.15}$$

Again, the partial derivative indicates that the change of energy due to the change of position is computed while the magnetic flux density or, alternatively, the vector potential $\boldsymbol{A}$ is fixed.

6.3.3 Finite Differences

The easiest way to apply the idea of virtual work is to approximate the gradient eq. (6.10) by solving the magnetic field for two neighboring positions of the target and writing in terms of energy:

$$F_m \approx \frac{W_1 - W_0}{\delta s} \tag{6.16}$$

The size of the variation δs has to be determined for every case. Generally, it can be said that a bigger δs introduces more error due to the non-linearity in the result. A δs being too small introduces inaccuracies due to machine precision in the computation.

The next section introduces a method to shift the approximation of the derivative to the Jacobian, i.e., a purely geometrical description of the virtual deformation. As will be seen, the Jacobian is a linear function, so the finite difference is no approximation of the partial derivative. This allows a robust force calculation by definition.

Remark

The following Jacobian derivative method needs a relatively deep intrusion in the finite element code. A non-intrusive (i.e. no change in the FEM framework code) way of exploiting at least the idea of the virtual work approach is the following: Perform the integration of the energy (or co-energy) for the given field solution, distort the mesh by a finite distance but keep the mesh's topology. Then again, integrate the energy. As the code needs to recalculate the Jacobian matrices from unit elements to the actual deformed elements, the derivative of the Jacobian as demanded in eq. (6.34) is calculated in a finite difference sense.

6.3.4 Jacobian Derivative Method

The first publication developing the *Jacobian derivative method* to compute magnetic forces using the virtual work principle, was proposed by COULOMB in [20]. He derived the method in the framework of finite elements. The core idea relies on the definition of the Jacobian matrix $\mathcal{J}$ as a coordinate transformation between two configurations that change due to a virtual deformation of the domain. The derivation in this section is one abstraction layer above the finite element method, to show that the method is generally applicable.

The setup in fig. 6.3 shows the minimal requirements for the method to be derived in a general representation. The considered system contains two domains: An outer domain with linear material and an inner domain with arbitrary material behavior, $\Omega = \Omega_{\text{outer}} \cup \Omega_{\text{inner}}$. The outer domain must fully enclose the inner domain. The force on the inner domain is desired as a global quantity under the assumption that the inner domain is fully rigid. The virtual deformation degenerates to a virtual displacement of the inner domain in the direction $\boldsymbol{\delta}$. Therefore two configurations of the whole system can be defined: The original configuration is denoted as Ω, and the deformed configuration as $\Omega^\star$.

Scalar- or vector fields in the undeformed configuration are expressed in terms of the coordinates (x, y, z), whereas for the new, deformed configuration $\star$, in terms of (ξ, η, ζ).

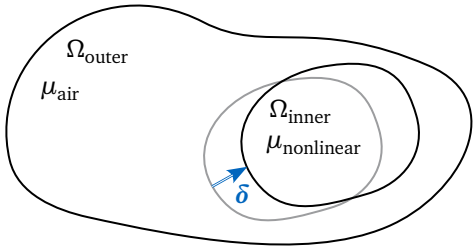

Figure 6.3: Configurational change where the inner domain Ω_{inner} is shifted by $\delta \boldsymbol{s}$.

The new coordinates are defined by a shift with the displacement field $\boldsymbol{s} = \begin{pmatrix} s_x & s_y & s_z \end{pmatrix}^T$ written in vector notation in the vector $\boldsymbol{x}$ and $\boldsymbol{\xi}$:

$$\boldsymbol{\xi} = \boldsymbol{x} + \boldsymbol{s} = \begin{cases} \xi = x + s_x \\ \eta = y + s_y \\ \zeta = z + s_z \end{cases} \tag{6.17}$$

The Jacobian $\mathcal{J}$ describes the coordinate transformation from the deformed configuration $\Omega^\star$ to the undeformed Ω. This definition follows the definition of the finite element transformation into isoparametric elements, which are written in the so-called local coordinate system (ξ, η, ζ).

$$\mathcal{J} = \frac{\partial(x, y, z)}{\partial(\xi, \eta, \zeta)}, \qquad \det(\mathcal{J}) = |\mathcal{J}| = \frac{\mathrm{d}\Omega}{\mathrm{d}\Omega^\star} \tag{6.18}$$

The transformation of the vector field representation from one configuration to the other is done with the Jacobian matrix. A star is put in the upper left index to express the vector in the deformed configuration. For an arbitrary vector field $\boldsymbol{u}(\boldsymbol{x})$ this means ${}^\star\boldsymbol{u}(\boldsymbol{\xi})$. Following the notations commonly used for rotational matrices, the left subscript of $\mathcal{J}$ shows the configuration the system is transformed into. The right subscript indicates the configuration, the field is coming from. As the definition of the Jacobian is fixed in eq. (6.18), the subscripts are dropped as they are not necessary. The transformation using the Jacobian is therefore written for an arbitrary vector $\boldsymbol{u}$

$$\boldsymbol{u} = {}_{\Omega}\mathcal{J}_{\Omega^\star}\, {}^\star\boldsymbol{u} = \mathcal{J}\, {}^\star\boldsymbol{u} \tag{6.19}$$

$${}^\star\boldsymbol{u} = {}_{\Omega^\star}\mathcal{J}_{\Omega}\boldsymbol{u} = \mathcal{J}^{-1}\boldsymbol{u} \tag{6.20}$$

For the shown setup, two consequences arise: Firstly, for the initial configuration, $\boldsymbol{s} = 0$ and so $\boldsymbol{x} = \boldsymbol{\xi}$ and therefore $\mathcal{J} = \boldsymbol{I}$ and $\det(\mathcal{J}) = 1$. And secondly, due to the rigidity of the inner domain ($\Omega_{\text{inner}} = \Omega^\star_{\text{inner}}$), a displacement $\boldsymbol{\delta}$ only generates a change of the Jacobian in the outer domain ($\Omega_{\text{outer}} \neq \Omega^\star_{\text{outer}}$).

From the definition of $\mathcal{J}$, it follows that the change of the transformation and the following back-transformation due to the virtual displacement $\boldsymbol{\delta}$ must be zero.

$$\frac{\partial(\mathcal{J}^{-1}\mathcal{J})}{\partial \boldsymbol{\delta}} = \frac{\partial \boldsymbol{I}}{\partial \boldsymbol{\delta}} = 0 \tag{6.21}$$

Applying the chain rule gives a relation between the change of the Jacobian and the inverse of the Jacobian:

$$\frac{\partial \mathcal{J}^{-1}}{\partial \boldsymbol{\delta}}\mathcal{J} + \mathcal{J}^{-1}\frac{\partial \mathcal{J}}{\partial \boldsymbol{\delta}} = 0 \qquad \rightarrow \qquad \frac{\partial \mathcal{J}^{-1}}{\partial \boldsymbol{\delta}} = -\mathcal{J}^{-1}\frac{\partial \mathcal{J}}{\partial \boldsymbol{\delta}}\mathcal{J}^{-1} \tag{6.22}$$

Force Computation The global force as a finite difference in terms of the magnetic energy W_m for the two configurations is written:

$$\boldsymbol{F}_m^T \boldsymbol{\delta} = W_m^\star - W_m \tag{6.23}$$

Working out a partial differential formulation shows that the force can be derived from either the original configuration or the new configuration:

$$\boldsymbol{F}_m \underset{|\boldsymbol{\delta}|\to 0}{=} \frac{W_m^\star - W_m}{\boldsymbol{\delta}} = \frac{W_m + \frac{\partial W_m^\star}{\partial \boldsymbol{\delta}}\boldsymbol{\delta} - W_m}{\boldsymbol{\delta}} = \frac{\partial W_m^\star}{\partial \boldsymbol{\delta}} \tag{6.24}$$

$$= \frac{W_m^\star - \left(-\frac{\partial W_m}{\partial \boldsymbol{\delta}}\boldsymbol{\delta} + W_m^\star\right)}{\boldsymbol{\delta}} = \frac{\partial W_m}{\partial \boldsymbol{\delta}} \tag{6.25}$$

Considering the magnetic energy in the outer domain (linear material),

$$W_m = \frac{1}{2\mu}\int_{\Omega_{\text{outer}}} \boldsymbol{B}^T\boldsymbol{B}\ \mathrm{d}\Omega_{\text{outer}} \tag{6.26}$$

$$W_m^\star = \frac{1}{2\mu}\int_{\Omega^\star_{\text{outer}}} {}^\star\boldsymbol{B}^T\,{}^\star\boldsymbol{B}\ \mathrm{d}\Omega^\star_{\text{outer}} \tag{6.27}$$

a change in configuration brings a change in the (outer) integration domain and a change in $\boldsymbol{B}$ arises, as $\boldsymbol{B} = \boldsymbol{\nabla}\times\boldsymbol{A}$. The rotation operator, as a spatial derivative operator, is also dependent on the domain. As the permeability μ is constant and does not depend on the domain, it can be drawn out of the integral. The subscript *outer* will now be omitted for the sake of simplicity.

The ordinary nabla operator holds the derivative with respect to the coordinates (x, y, z), which is omitted normally $\boldsymbol{\nabla}_{\boldsymbol{x}} = \boldsymbol{\nabla}$. For the perturbed configuration $\star$, the nabla writes as $\boldsymbol{\nabla}_{\boldsymbol{\xi}}$. Performing the curl operation in the $\star$ domain leads to:

$$\boldsymbol{B} = \boldsymbol{\nabla}_{\boldsymbol{x}}\times\boldsymbol{A} \tag{6.28}$$

$$\boldsymbol{B} = \mathcal{J}\boldsymbol{\nabla}_{\boldsymbol{\xi}}\times{}^\star\boldsymbol{A} = \mathcal{J}\,{}^\star\boldsymbol{B} \tag{6.29}$$

Recalling the thought experiment with constant $\boldsymbol{B}$-field in section 6.3.2, the vector potential $\boldsymbol{A}$ is constant for the two configurations, i.e., $\boldsymbol{A} = {}^\star\boldsymbol{A}$. The derivative $\frac{\partial \boldsymbol{B}}{\partial \boldsymbol{s}}$ follows:

$$\begin{aligned}\frac{\partial \boldsymbol{B}}{\partial \boldsymbol{\delta}} &= \frac{\partial \boldsymbol{\nabla}}{\partial \boldsymbol{\delta}}\times\boldsymbol{A} + \boldsymbol{\nabla}\times\underbrace{\frac{\partial \boldsymbol{A}}{\partial \boldsymbol{\delta}}}_{=0,\boldsymbol{A}={}^\star\boldsymbol{A}}\\ &= \frac{\partial \mathcal{J}\boldsymbol{\nabla}_{\boldsymbol{\xi}}}{\partial \boldsymbol{\delta}}\times\boldsymbol{A}\\ &= \frac{\partial \mathcal{J}}{\partial \boldsymbol{\delta}}\,{}^\star(\boldsymbol{\nabla}\times\boldsymbol{A})\\ &= \frac{\partial \mathcal{J}}{\partial \boldsymbol{\delta}}\,{}^\star\boldsymbol{B} = \frac{\partial \mathcal{J}}{\partial \boldsymbol{\delta}}\,\mathcal{J}^{-1}\boldsymbol{B}\end{aligned} \tag{6.30}$$

With an analog thought process, the integration can be expressed in the star configuration ($\mathrm{d}\Omega = |\mathcal{J}|\,\mathrm{d}\Omega^\star$) where the variation $\boldsymbol{\delta}$ only affects the Jacobian. To match the equations configuration, we find $\mathrm{d}\Omega^\star$ using $|\mathcal{J}|^{-1}$. Finally, the following identity can be used wherever needed to avoid the derivation of $\mathrm{d}\Omega$ [34].

$$\frac{\partial\,\mathrm{d}\Omega}{\partial \boldsymbol{\delta}} = \frac{\partial|\mathcal{J}|}{\partial \boldsymbol{\delta}}\,\mathrm{d}\Omega^\star \tag{6.31}$$

$$\frac{\partial\,\mathrm{d}\Omega}{\partial \boldsymbol{\delta}} = \frac{\partial|\mathcal{J}|}{\partial \boldsymbol{\delta}}|\mathcal{J}|^{-1}\,\mathrm{d}\Omega \tag{6.32}$$

Using this relations to avoid the derivation of $\boldsymbol{B}$ and instead derive the Jacobian, the derivation of the energy W_m or $W_m^\star$ leads to the same result after the coordinate transformation. Both variants can be implemented into finite element codes. More common is the implementation of the integration on the original configuration. Starting from the original configuration, the chain rule is applied to the magnetic energy, including the change of the integration domain, expressed with the term $\frac{\partial\,\mathrm{d}\Omega}{\partial\boldsymbol{\delta}}$, the change of energy writes:

$$\begin{aligned}\frac{\partial W_m}{\partial\boldsymbol{\delta}} &= \frac{1}{2\mu}\int_\Omega \frac{\partial \boldsymbol{B}^T}{\partial\boldsymbol{\delta}}\boldsymbol{B}\,\mathrm{d}\Omega + \frac{1}{2\mu}\int_\Omega \boldsymbol{B}^T\frac{\partial\boldsymbol{B}}{\partial\boldsymbol{\delta}}\,\mathrm{d}\Omega + \frac{1}{2\mu}\int_\Omega \boldsymbol{B}^T\boldsymbol{B}\frac{\partial\,\mathrm{d}\Omega}{\partial\boldsymbol{\delta}}\\ &= \frac{1}{\mu}\int_\Omega \boldsymbol{B}^T\frac{\partial\boldsymbol{B}}{\partial\boldsymbol{\delta}}\,\mathrm{d}\Omega + \frac{1}{2\mu}\int_\Omega \boldsymbol{B}^T\boldsymbol{B}\frac{\partial\,\mathrm{d}\Omega}{\partial\boldsymbol{\delta}}\\ &= -\frac{1}{\mu}\int_\Omega \boldsymbol{B}^T\frac{\partial\mathcal{J}}{\partial\boldsymbol{\delta}}\mathcal{J}^{-1}\boldsymbol{B}\,\mathrm{d}\Omega + \frac{1}{2\mu}\int_\Omega \boldsymbol{B}^T\boldsymbol{B}\frac{\partial|\mathcal{J}|}{\partial\boldsymbol{\delta}}|\mathcal{J}|^{-1}\,\mathrm{d}\Omega\end{aligned} \tag{6.33}$$

The derivation of the second configuration, i.e. all vectors are written in the $\star$ configuration, is not shown here as a simple switch of definitions leads to the exact same formulas just from the other point of view. Finally, the force formula for the magnetic flux vector written in the original configuration becomes:

$$\boldsymbol{F}_m = -\frac{1}{\mu}\int_\Omega \boldsymbol{B}^T\frac{\partial\mathcal{J}}{\partial\boldsymbol{\delta}}\mathcal{J}^{-1}\boldsymbol{B}\,\mathrm{d}\Omega + \frac{1}{2\mu}\int_\Omega \boldsymbol{B}^T\boldsymbol{B}\frac{\partial|\mathcal{J}|}{\partial\boldsymbol{\delta}}|\mathcal{J}|^{-1}\,\mathrm{d}\Omega \tag{6.34}$$

Note that the post-processing step of the force computation itself is **not** dependent on the material of the target body, as long as is assumed to behave rigidly, because the Jacobian of the inner domain is then zero. Only the outer domain needs to be integrated for the energy. For nearly all applications, the outer domain will be air and therefore a linear behavior is justified.

Remark

Generalization to arbitrary Systems For systems, where the material in the outer domain is not linear, the seen procedure needs to be conducted using the general energy (or co-energy) integral. The derivation becomes more cumbersome as the integral limits also can be dependent on the configuration change. Finally, the following formula for the force in the case of the constant $\boldsymbol{B}$-field, i.e. no current source connected to the system, results for all vectors written in the original configuration:

$$\boldsymbol{F}_m = \int_\Omega \Big[\underbrace{-\boldsymbol{B}^T\frac{\partial\mathcal{J}}{\partial\boldsymbol{\delta}}\mathcal{J}^{-1}\boldsymbol{H}}_{\text{Change due to curl operator}} + \underbrace{\int_0^B H(\tilde{B})\,\mathrm{d}\tilde{B}\frac{\partial|\mathcal{J}|}{\partial\boldsymbol{\delta}}|\mathcal{J}|^{-1}}_{\text{Change due to geometry}}\Big]\mathrm{d}\Omega\Big|_{\boldsymbol{B}=\text{const}} \tag{6.35}$$

For the second thought experiment, i.e. the source current is constant, the force is derived via the co-energy, leading to:

$$\boldsymbol{F}_m = \int_\Omega \Big[\underbrace{-\boldsymbol{B}^T\frac{\partial\mathcal{J}}{\partial\boldsymbol{\delta}}\mathcal{J}^{-1}\boldsymbol{H}}_{\text{Change due to curl operator}} + \underbrace{\int_0^H B(\tilde{H})\,\mathrm{d}\tilde{H}\frac{\partial|\mathcal{J}|}{\partial\boldsymbol{\delta}}|\mathcal{J}|^{-1}}_{\text{Change due to geometry}}\Big]\mathrm{d}\Omega\Big|_{j=\text{const}} \tag{6.36}$$

Jacobian Derivation via Finite Differences For now, the derivative of the Jacobian was given. Computing the derivative of the Jacobian is a purely geometrical task. The drawback of this method is the need for a deep implementation in the finite element code to get the derivative of the Jacobian with respect to the variation $\boldsymbol{\delta}$. Fortunately, the Jacobian is a linear function of the coordinates, which allows the computation via a finite difference scheme without approximation. The following paragraphs sketch why this is so. Calculating the Jacobian via a finite difference by changing the domain, i.e., the coordinates of all evaluation points are shifted by a displacement vector field $\boldsymbol{s}(\boldsymbol{x}, \boldsymbol{\delta})$ built from the virtual displacement $\boldsymbol{\delta}$ and the location $\boldsymbol{x}$. Assuming a linear distribution of the shift $\boldsymbol{\delta}$, the displacement field follows as a linear interpolation between the fixed outer boundaries and the displaced boundary of the inner part.

The coordinate transformation is defined as:

$$\xi = \boldsymbol{x} + \frac{\partial \boldsymbol{s}}{\partial \boldsymbol{x}}\boldsymbol{x} = \boldsymbol{x}(\boldsymbol{I} + \frac{\partial \boldsymbol{s}}{\partial \boldsymbol{x}}) \tag{6.37}$$

From there, the inverse of the Jacobian (again only for one dimension) can be seen:

$$\mathcal{J}^{-1} = \frac{\partial \xi}{\partial x} = 1 + \frac{\partial s(\delta)}{\partial x} \tag{6.38}$$

Working out the Jacobian as the inverse:

$$\begin{aligned} \mathcal{J}\mathcal{J}^{-1} &= 1 \\ \mathcal{J}(1 + \frac{\partial s(\delta)}{\partial x}) &= 1 \\ \mathcal{J} + \frac{\partial x}{\partial \xi}\frac{\partial s}{\partial x} &= 1 \\ \mathcal{J} &= 1 - \frac{\partial s}{\partial \xi} \end{aligned}$$

An assumption is needed at this point. It is assumed for small δ that:

$$\frac{\partial s}{\partial x} \approx \frac{\partial s}{\partial \xi} = \text{const} \tag{6.39}$$

From there, the derivation of the Jacobian with $\boldsymbol{\delta}$ is approached.

$$\begin{aligned} \frac{\partial}{\partial \delta \boldsymbol{s}}\mathcal{J} &= -\frac{\partial}{\partial \boldsymbol{\delta}}\left(\frac{\partial \boldsymbol{s}(\boldsymbol{x}, \delta s)}{\partial \xi}\right) \\ &= \frac{\partial}{\partial \boldsymbol{\delta}}\boldsymbol{f}(\delta \boldsymbol{s}) \qquad \text{with: } f(\boldsymbol{\delta}) \text{ being } 1^{\text{st}} \text{ order in } \boldsymbol{\delta} \\ &= \text{const} \end{aligned} \tag{6.40}$$

The conclusion from eq. (6.40) can be drawn that a finite difference scheme on $\frac{\partial \mathcal{J}}{\partial \delta s}$ is no approximation.

In a finite difference scheme, it is necessary to shift only in one direction at once (e.g. x-direction), which leads to the x-component of the full $\frac{\partial \mathcal{J}}{\partial \boldsymbol{s}}$, which in eq. (6.34) leads to the x-component of the force $\boldsymbol{F}$, ergo F_x. This needs to be done for each direction of the force, but for most of the practical applications, only one direction of force is of interest.

6.3.5 Maxwell Stress Tensor

For the sake of completeness, this subsection gives a short path from the virtual work principle, as seen before, to the formulation of the so-called Maxwell Stress Tensor (MST). The MST tries to mimic the behavior of the Cauchy stress tensor in continuum mechanics to apply the same way of thinking and techniques. To find the stress tensor, the force derivation is started from the force per volume $\boldsymbol{f}$ rewritten in terms of the co-energy:

$$\begin{aligned} \boldsymbol{f} &= -\boldsymbol{\nabla} w \\ &= -\boldsymbol{\nabla} w_{\square} + \boldsymbol{\nabla} w' \end{aligned} \tag{6.41}$$

Now, the square energy density is written in a generic way, resulting in a second-order tensor $\underline{\underline{\boldsymbol{w}}}_{\square}$, as the outer product of the computed $\boldsymbol{H}$ and $\boldsymbol{B}$. The scalar $w_{\square}$ is found back with the trace operator (Tr) which sums the diagonal elements of a tensor:

$$\underline{\underline{\boldsymbol{w}}}_{\square} = \boldsymbol{H}\boldsymbol{B}^T \tag{6.42}$$

$$w_{\square} = \mathrm{Tr}(\boldsymbol{H}\boldsymbol{B}^T) = \boldsymbol{H}^T\boldsymbol{B} \tag{6.43}$$

Following, the gradient of the square energy is available in two different variants

$$\boldsymbol{\nabla}(\boldsymbol{H}^T\boldsymbol{B}) = \boldsymbol{\nabla}\,\mathrm{Tr}(\boldsymbol{H}\boldsymbol{B}^T) \tag{6.44}$$

Using the properties of linear operations, the trace operator can commute with the derivation operator:

$$\boldsymbol{\nabla}\,\mathrm{Tr}(\boldsymbol{H}\boldsymbol{B}^T) = \mathrm{Tr}(\boldsymbol{\nabla}(\boldsymbol{H}\boldsymbol{B}^T)) \tag{6.45}$$

Interpreting the outer product as a linear map for any position $\boldsymbol{x}$ to a vector $\boldsymbol{V}(\boldsymbol{x}) = (\boldsymbol{H}\boldsymbol{B}^T)\boldsymbol{x}$, its derivative can be seen as its Jacobian $\boldsymbol{J}(\boldsymbol{x}) = \boldsymbol{\nabla}\boldsymbol{V}$. This yields the trace operation of the Jacobian $\boldsymbol{J}$ which is equal to the divergence of its defining vector field function $\boldsymbol{V}$.

$$\mathrm{Tr}(\boldsymbol{J}) = \boldsymbol{\nabla}\cdot\boldsymbol{V} \tag{6.46}$$

Finally, the gradient of the trace (Tr) of the outer product is now written as the divergence of the tensor [1]. A deep insight in the relation between the trace operator and the divergence is given in [64].

$$\boldsymbol{\nabla}\,\mathrm{Tr}(\boldsymbol{H}\boldsymbol{B}^T) = \boldsymbol{\nabla}\cdot(\boldsymbol{H}\boldsymbol{B}^T) \tag{6.47}$$

Replacing the square energy in the force equation, it can now be written in nabla notation as follows:

$$\boldsymbol{f} = -\boldsymbol{\nabla}\cdot(\boldsymbol{H}\boldsymbol{B}^T) + \boldsymbol{\nabla}\int_0^H B(\tilde{H})\,\mathrm{d}\tilde{H} \tag{6.48}$$

To unify the notation, the second term is multiplied with the identity tensor $\boldsymbol{I}$ and therefore the gradient turns into the divergence. This yields the general non-linear form:

$$\boldsymbol{f} = -\boldsymbol{\nabla}\cdot\underbrace{\left(\boldsymbol{H}\boldsymbol{B}^T - \int_0^H B(\tilde{H})\,\mathrm{d}\tilde{H}\,\boldsymbol{I}\right)}_{\underline{\underline{\boldsymbol{T}}}} \tag{6.49}$$

[1] To show the equivalence by evaluation of components, note, that $\boldsymbol{\nabla}\cdot\boldsymbol{V} = \frac{\partial V_{ik}}{\partial x_i}\boldsymbol{e}_k$ under the consideration of Einstein's summation.

For linear material, the magnetic co-energy turns into half of the square energy, which offers a classical notation of the MST:

$$\underline{\underline{\boldsymbol{T}}} = \boldsymbol{H}\boldsymbol{B}^T - \boldsymbol{I}\frac{\boldsymbol{B}^T\boldsymbol{H}}{2} \tag{6.50}$$

In componential notation and with the relation of $B = \mu_0 H$ for air domains with a relative permeability $\mu_r = 1$, the Maxwell stress tensor $\boldsymbol{T}$ becomes the most known expression where δ_{ij} is the Kronecker's delta which is zero, except for $i = j$ where it becomes one:

$$\boldsymbol{T}_{ij} = \frac{B_i B_j}{\mu_0} - \frac{1}{2}\left(\frac{B^2}{\mu_0}\right)\delta_{ij} \tag{6.51}$$

Note that the MST is extendable also to incorporate the electrostatic stresses in a similar way composed from E and D. See [28] for a different way to show the equivalence.

Using the divergence theorem, the volumetric force density can be transformed to a surface integral:

$$\boldsymbol{F} = \int_\Omega \boldsymbol{\nabla} \cdot \underline{\underline{\boldsymbol{T}}}\, \mathrm{d}\Omega = \int_\Gamma \underline{\underline{\boldsymbol{T}}} \cdot \boldsymbol{n}\, \mathrm{d}\Gamma \tag{6.52}$$

Issue of MST in Combination with FEM As already seen, the mathematical description of the forces is identical for the virtual work approach and the Maxwell Stress Tensor (MST) approach. However, in the application with the approximation by finite elements, an important difference exists. The core of the problem will be briefly outlined here.

The following steps are necessary to compute the global force on a rigid body:

- Choose an arbitrary surface Γ which includes only the free rigid body that is of interest
- Integrate the force on the surface Γ

The integration over a surface around the object is an approximation that only holds when the magnetic flux density gradient inside the object is very small, for example, for a ferromagnetic body surrounded by air. The result of the surface integral is not independent of the surface anymore. It depends on where the surface cuts the finite elements, of what types the finite elements are, and how coarse they are meshed.

Already in the first Compumag Conference 1976, a paper [53] and the transcribed discussion show the possibility of using the MST approach to calculate forces on rigid bodies in the magnetic field. The main point in the discussion is the surface integration that gives different values for different paths through the elements and is dependent on the element size or the approximation of the magnetic flux field, respectively.

In [19] COULOMB strengthened that by approximating the continuous field with finite elements, the results of the surface integral of the MST depend on the type of finite element crossed by the surface and the path inside the element. He advises using the stronger, but harder-to-implement virtual work principle and shows an implementation of the finite element method using the local Jacobian derivatives [31].

6.3.6 Justifications

This subsection gives a few final thoughts on the mechanical forces from magnetodynamic systems. Looking into textbooks searching the mechanical force mostly yields the following formulation for the force density:

$$\boldsymbol{f}_m = \boldsymbol{j} \times \boldsymbol{B} - \boldsymbol{\nabla}\mu\frac{|\boldsymbol{H}|^2}{2} \tag{6.53}$$

This formula is composed of two parts. The first unveils the Lorentz forces, where moving charges (current density $\boldsymbol{j}$) in a magnetic field lead to a force in the orthogonal direction. The second part represents the reluctance forces. Therefore it is assumed that μ is a function of the material point but is not dependent on the magnitude of the magnetic flux (density). This coincides with the previously given physical interpretation of reluctance forces which occur at permeability changes. Magnetostrictive forces are neglected, as they were in all the previous considerations. Analogously the electrostatic forces between charges.

A way to find the shown force formula eq. (6.53) starts from the same basic idea

$$\boldsymbol{f} = -\boldsymbol{\nabla}_{\boldsymbol{s}} w_{\mathrm{mag}} \tag{6.54}$$

and without reason, replacing the energy with the co-energy

$$\boldsymbol{f} = -\boldsymbol{\nabla}_{\boldsymbol{s}} w_{\square} + \boldsymbol{\nabla}_{\boldsymbol{s}} w'_{\mathrm{mag}} \tag{6.55}$$

Substituting the already known relation for $w_{\square}$ as being the product of vector potential $\boldsymbol{A}$ and current density $\boldsymbol{j}$ yields:

$$\boldsymbol{f} = -\boldsymbol{\nabla}(\boldsymbol{A}\cdot\boldsymbol{j}) + \boldsymbol{\nabla}\int_0^H B(\tilde{H})\,\mathrm{d}\tilde{H} \tag{6.56}$$

With the following vector identity and the assumption that $\operatorname{div}\boldsymbol{j} = 0$,

$$\boldsymbol{j} \times \underbrace{\nabla \times \boldsymbol{A}}_{\boldsymbol{B}} = \boldsymbol{\nabla}(\boldsymbol{j}\cdot\boldsymbol{A}) - \underbrace{\boldsymbol{A}(\nabla\cdot\boldsymbol{j})}_{\operatorname{div}\boldsymbol{j}=0} \tag{6.57}$$

the force is written as

$$\boldsymbol{f} = -\boldsymbol{j} \times \boldsymbol{B} + \boldsymbol{\nabla}\int_0^H B(\tilde{H})\,\mathrm{d}\tilde{H} \tag{6.58}$$

which is exactly what is read in the textbooks for linear materials, i.e. $B = \mu H$, see eq. (6.53).

In conclusion, the calculation of the mechanical forces arising from a magnetic field is a more complex topic than it might seem at first glance. Especially as effects in the integration process in a FEM framework play an important role. In 2011, BOSSAVIT summarizes the answer to the question on the forces exerted by the magnetic field from a more global point of view where he also encounters the aspects of magnetostriction [13].

Chapter 7

FEM for Electromagnetism

As already seen in the brief outline of the history of the finite element method (see section 2.2), FEM became the most important calculation method for electromagnetic systems. The basic steps from a continuous physical system description to the final discretized algebraic system of equations are depicted in fig. 7.1. This chapter will be divided into the two main actions required in the scheme, namely, the generation of the variational formulation and the subsequent discretization.

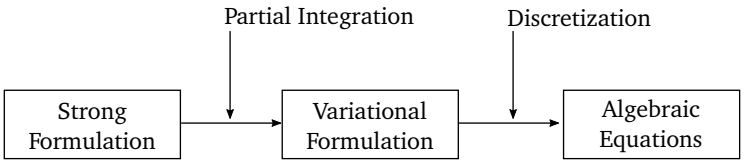

Figure 7.1: The two main steps in the FEM process [34].

The strong formulations for magnetostatic and magnetodynamic systems are known from the previous chapters. The first step is conducted by writing the so-called weak form of the problem, which is a reformulation of the original partial differential equation in terms of an integral equation. The weak form is obtained by multiplying the original equation by a test function and integrating it over the domain of interest.

Once the weak form is obtained, it is discretized by breaking down the domain into smaller elements and approximating the solution within each element using a set of basis functions. These basis functions are usually chosen to be piecewise polynomials, and their coefficients are obtained by solving a set of algebraic equations derived from the weak form at each degree of freedom of the element.

7.1 Weak Form Formulation

The variational formulation is a mathematical technique used in the finite element method to derive the weak form of the governing partial differential equation of a physical system. It involves multiplying the differential equation by so-called *test functions* and integrating over the domain of interest, including its boundary. The *weak form* of a partial differential equation is called *weak* because it imposes less stringent conditions on the functions and their derivatives that satisfy it compared to the original *strong form* of the PDE. The weak form requires the solution to satisfy the equation only in an integral (average) sense.

By applying the principle of virtual work, which states that the sum of work done by all internal and external forces in the direction of compatible motions is zero, we can obtain an

equivalent expression for the weak form of the governing equation. The procedure is shown for the formulation of the magnetodynamic equation in terms of the modified vector potential $\boldsymbol{A}$. This so-called *strong formulation* is an initial-boundary value problem.

$$\sigma \frac{\partial \boldsymbol{A}}{\partial t} + \boldsymbol{\nabla} \times \left(\frac{1}{\mu(|\boldsymbol{\nabla} \times \boldsymbol{A}|)} \boldsymbol{\nabla} \times \boldsymbol{A} \right) = \boldsymbol{j}_0 \tag{7.1}$$

7.1.1 Function Spaces

Although an introduction to function spaces would go far beyond the scope of this chapter, a few comments on function spaces need to be made here as electrodynamic systems demand some special properties that can only be understood after at least defining the terms. Function spaces are sets of mathematical functions that satisfy certain properties or conditions. The choice of function space depends on the problem at hand and the nature of the functions involved.

The L_2 space, also known as the space of square-integrable functions, is a function space that consists of all functions whose square is integrable over a given domain. This space is commonly used in the study of partial differential equations, where it provides a natural setting for defining weak solutions.

The H^1 space, also known as the Sobolev space, consists of all functions with square-integrable derivatives up to a certain order. In other words: The H^1 space contains all functions of L_2, which have a generalized derivative which is also element of L_2. Functions in the H^1 spaces are often used in the study of scalar-valued partial differential equations involving physical quantities like temperature or pressure.

The H^{curl} space is a function space that consists of vector-valued functions whose curl is square integrable over a given domain, ergo are element of L_2. With that definition, the curl of functions, element of H^{curl}, is well defined. In contrast, the divergence is not well defined and can, therefore, not be computed. This was already mentioned in chapter 5 and chapter 6. As the H^{curl} space requires functions whose curl is square-integrable, the space may include functions with discontinuities or singularities. In consequence, this leads to the need for edge elements for FEM computations, as seen later in this chapter, because the H^{curl} space requires only a tangential continuity on the boundaries of domains. The H^{curl} space is commonly used in the study of electromagnetism and fluid dynamics, where it provides a natural setting for describing the behavior of vector fields that represent physical quantities such as magnetic fields and vorticity.

A third function space, the H^{div} space, needs to be mentioned here as it completes the series and is used in the context of electric fields. It is the counterpart to the H^{curl} space for magnetic fields. Functions in the H^{div} space have square-integrable divergence, emphasizing the conservation of quantities like mass or charge. Because of its definition, the space allows functions with certain types of discontinuities. Again, the later-explained edge elements are a good choice.

Finally, we want to state the definition of the function spaces [63]:

$$\begin{aligned} H^{\text{grad}} = H^1 &= \{w \in L_2 : \boldsymbol{\nabla} w \in [L_2]^3\} \\ \boldsymbol{H}^{\text{curl}} &= \{\boldsymbol{u} \in [L_2]^3 : \boldsymbol{\nabla} \times \boldsymbol{u} \in [L_2]^3\} \\ \boldsymbol{H}^{\text{div}} &= \{\boldsymbol{q} \in [L_2]^3 : \boldsymbol{\nabla} \cdot \boldsymbol{q} \in [L_2]\} \end{aligned}$$

The shown spaces form a sequence whose meaning is explained by the *de Rham* theorem, which states that (on simply connected domains) the range of an operator of this sequence

is exactly the kernel of the next operator. This fact will cause an additional effort in the formulation of magnetostatic equations as mentioned in section 5.5.

$$H^{\text{grad}} \overset{\text{grad}}{\rightarrow} H^{\text{curl}} \overset{\text{curl}}{\rightarrow} H^{\text{div}} \overset{\text{div}}{\rightarrow} L_2$$

The arrows in the de Rham complex show how the derivative operator acts on different spaces. It is also common to write the de Rham complex in terms of the nabla operator as a generalized differential operator:

$$H^{\text{grad}} \overset{\boldsymbol{\nabla}}{\rightarrow} H^{\text{curl}} \overset{\boldsymbol{\nabla}\times}{\rightarrow} H^{\text{div}} \overset{\boldsymbol{\nabla}\cdot}{\rightarrow} L_2$$

7.1.2 Variational Formulation

Transforming eq. (7.1) into the weak form can be carried out in two ways which are very related but differ in terms of the required implementation.

Variational Principle The variational formulation starts with the concept of a functional, which is a mathematical function that takes a set of functions as input and produces a real number as output. In physics, a functional is often associated with an energy, which characterizes the physical system under consideration. But in general, the functional can be anything. The goal of the variational formulation is to find the function that minimizes the functional, subject to certain constraints. Therefore, the partial differential equation is multiplied by a so-called *test function* $\boldsymbol{\nu} \in V$ and integrated over the domain Ω.

The resulting demands on the solution are now called weak as the test functions take care of constraints, e.g., the essential boundary conditions. It is therefore easier to find solution functions. Note that the process of deriving a weak formulation is in no terms an approximation as long as the test space is big enough to completely contain the future solution space. Later, in the process of discretization, the number of test functions is bound to a finite number, and with that, the solution becomes an approximation.

A second explanation approach goes in the direction of projecting the equation in the subspace V. As the subspace fully contains the solution space, there will be no residual. It is just a switch of basis. With increasing constraints on the subspace, the solution becomes easier to find. When the space is constrained further, the solution must become an approximation but in an optimal sense such that the residual is orthogonal to the space.

Multiplying the vector potential equation eq. (7.1) with proper test functions $\boldsymbol{\nu}$ and integrating over the domain results in the following weak formulation: Find $\boldsymbol{A}$ such that

$$\sigma \frac{\partial}{\partial t} \int_\Omega \boldsymbol{\nu} \cdot \boldsymbol{A} \, \mathrm{d}\Omega + \int_\Omega \boldsymbol{\nu} \cdot \boldsymbol{\nabla} \times \left(\frac{1}{\mu(|\boldsymbol{\nabla} \times \boldsymbol{A}|)} \boldsymbol{\nabla} \times \boldsymbol{A} \right) \mathrm{d}\Omega - \int_\Omega \boldsymbol{\nu} \cdot \boldsymbol{j}_0 \, \mathrm{d}\Omega = 0 \qquad \forall \boldsymbol{\nu} \in \boldsymbol{H}^{\text{curl}} \quad (7.2)$$

Integration by parts using Green's Integral allows to simplify the curl-curl operator by introducing a boundary integral over the domain's interface Γ and leads to:

$$\sigma \frac{\partial}{\partial t} \int_\Omega \boldsymbol{\nu} \cdot \boldsymbol{A} \, \mathrm{d}\Omega + \int_\Omega (\boldsymbol{\nabla} \times \boldsymbol{\nu}) \cdot \left(\frac{1}{\mu(|\boldsymbol{\nabla} \times \boldsymbol{A}|)} \boldsymbol{\nabla} \times \boldsymbol{A} \right) \mathrm{d}\Omega - \oint_\Gamma \boldsymbol{\nu} \times \left(\frac{1}{\mu(|\boldsymbol{\nabla} \times \boldsymbol{A}|)} (\boldsymbol{\nabla} \times \boldsymbol{A}) \right) \cdot \boldsymbol{n} \, \mathrm{d}\Gamma = \int_\Omega \boldsymbol{\nu} \cdot \boldsymbol{j}_0 \, \mathrm{d}\Omega \qquad \forall \boldsymbol{\nu} \in \boldsymbol{H}^{\text{curl}} \quad (7.3)$$

Additionally to incorporating the natural boundary conditions (see section 7.1.3), the volume integral becomes symmetric. As already seen in detail in chapter 4, the non-linearity arises in the permeability $\mu(B)$. To make use of eq. (7.3), an analytical function for μ in relation of B is needed to further process the weak form and finally solve it.

Principle of Minimum of Total Potential Energy Another way to obtain the same equation is the variation of a functional which represents a physical quantity, here an energy expression. Presuming an internal and external potential energy, its variation leads to the weak formulation. The method can be interpreted as a special variant of the principle of virtual work for conservative external loads. From a practical point of view, the $\mu(B)$ is obtained from material measurements of the BH correlation, which leads to no straightforward analytical expression for the permeability, but the integration of the energy is obvious. The same concept is used for hyperelastic materials, where an energy density function is defined, which is used to calculate the stress.

The total potential energy Π is split into two parts, namely the inner potential U and the external energy V. The variation of the total potential energy vanishes for a system being at its steady state.

$$\Pi = U + V \tag{7.4}$$

$$\delta\Pi = \delta(U + V) = 0 \tag{7.5}$$

In terms of magnetic quantities, the inner potential is the magnetic energy density $w(B)$, computed from the current magnetic flux density state $\boldsymbol{B}$, and the external energy, driven by the current density $\boldsymbol{j}$. The eddy currents are non-conservative (as the damping in structural mechanics) and can not intuitively go into the potentials. Therefore they are neglected and added later as non-conservative currents. Replacing U and V as explained yields for the static system:

$$\delta\Pi = \delta\left(\int_\Omega w(\boldsymbol{B})\,\mathrm{d}\Omega - \int_{\Omega_c} \boldsymbol{j}\cdot\boldsymbol{A}\,\mathrm{d}\Omega_c\right) = 0 \tag{7.6}$$

The variation of the potential Π with $\boldsymbol{A}$ results in the intuitive balance of currents (or, more precisely, of current densities)

$$\boldsymbol{\nabla}_A w(\boldsymbol{\nabla}\times\boldsymbol{A}) - \boldsymbol{j} = \boldsymbol{0}, \tag{7.7}$$

where the gradient of the energy density with respect to the vector potential gives the non-linear internal current density $\boldsymbol{g}(\boldsymbol{A})$. In contrast to the previously retrieved weak form, applying the variational principle to eq. (7.7) leads to an equivalent system to solve, but in terms of a function for the internal energy:

$$\int_\Omega \boldsymbol{v}\cdot\boldsymbol{\nabla}_A w(\boldsymbol{\nabla}\times\boldsymbol{A})\,\mathrm{d}\Omega - \int_\Omega \boldsymbol{v}\cdot\boldsymbol{j}\,\mathrm{d}\Omega = 0 \tag{7.8}$$

The partial integration step is not useful to be applied at that point.

To see the equality of the two weak forms, one can show that the internal current density $\boldsymbol{g}$ is equivalent to the variation of the magnetic energy. Writing the well-known magnetic energy density w in terms of the magnetic flux density B under the assumption of an isotropic material:

$$w(\boldsymbol{B}) = \int_0^{B_x} H_x(\tilde{B}_x)\,\mathrm{d}\tilde{B}_x + \int_0^{B_y} H_y(\tilde{B}_y)\,\mathrm{d}\tilde{B}_y + \int_0^{B_z} H_z(\tilde{B}_z)\,\mathrm{d}\tilde{B}_z \quad \leftrightarrows \quad \boldsymbol{H} = \frac{\partial w}{\partial \boldsymbol{B}} \tag{7.9}$$

The internal current density $\boldsymbol{g}$ is defined as the variation of the energy density with respect to the vector potential $\boldsymbol{A}$.[1]

$$\begin{aligned}
\boldsymbol{g}(\boldsymbol{A}) &= \boldsymbol{\nabla}_A w(\boldsymbol{\nabla}\times\boldsymbol{A}) \\
&= \frac{\partial \boldsymbol{B}}{\partial \boldsymbol{A}} \cdot \boldsymbol{\nabla}_B w(\boldsymbol{B}) \\
&= \frac{\partial (\boldsymbol{\nabla}\times\boldsymbol{A})}{\partial \boldsymbol{A}} \cdot \boldsymbol{\nabla}_B w(\boldsymbol{B}) \\
&= \frac{\partial (\boldsymbol{\nabla}\times\boldsymbol{A})}{\partial \boldsymbol{A}} \cdot \boldsymbol{H} \\
&= \boldsymbol{\nabla}\times\boldsymbol{H} \\
&= \boldsymbol{\nabla}\times\left(\frac{1}{\mu(|\boldsymbol{B}|)}\boldsymbol{B}\right) \\
&= \boldsymbol{\nabla}\times\left(\frac{1}{\mu(|\boldsymbol{\nabla}\times\boldsymbol{A}|)}\boldsymbol{\nabla}\times\boldsymbol{A}\right)
\end{aligned} \tag{7.10}$$

Remark

Abstract Notation The weak form can always be rewritten in a way that follows the abstract notation of bilinear and linear form, which is helpful for finite element codes like NGSolve, FEniCS, etc. Find $\boldsymbol{u}$ such that

$$a(\boldsymbol{u},\boldsymbol{v}) = f(\boldsymbol{v}) \qquad \forall \quad \boldsymbol{v}\in H$$

where $a(\boldsymbol{u},\boldsymbol{v})$ is a so-called *bilinear form* that contains all terms connecting trial- and test-function. $f(\boldsymbol{v})$ is a *linear form* with terms that are independent of the trial function. The discretization to a finite number of degrees of freedom will (for linear systems) result in a matrix form for the bilinear form and a vector form for the linear form. For non-linear relations, the bilinear form can be transformed into a tangential linearized form for a given point $\boldsymbol{u}$.

7.1.3 Boundary Conditions

For a given domain Ω, the vector $\boldsymbol{n}$ is defined as the outside normal vector to the boundary surface Γ. The boundary surface consists in general of two disjunct parts Γ_H and Γ_B, $\Gamma = \Gamma_H \cup \Gamma_B$. To solve eq. (7.3) in Ω, two types of boundary conditions need to be imposed, namely the *natural-* and the *essential conditions*. The conditions on the boundaries are typically written physically interpreted for $\boldsymbol{H}$ and $\boldsymbol{B}$. A difficulty is the translation into the unknown primary variable, the (modified) vector potential, denoted as $\boldsymbol{A}$, and its corresponding test functions $\boldsymbol{v}$.

Natural Boundary The natural (seldom called flux boundary condition), also known as the Neumann boundary condition is usually set via the boundary integral $\oint_{\Gamma_H} \sim \mathrm{d}\Gamma_H$ arising from the integration by parts step. The name *natural* boundary stems from the idea that neglecting the boundary integral in eq. (7.3) implies $\oint_{\Gamma_H} \sim \mathrm{d}\Gamma_H = 0$ which is setting a zero Neumann condition. The natural boundary condition eq. (7.11) does not restrict the trial-

[1] To see the equivalence $\frac{\partial(\boldsymbol{\nabla}\times\boldsymbol{A})}{\partial \boldsymbol{A}} \cdot \boldsymbol{H} = \boldsymbol{\nabla}\times\boldsymbol{H}$, write the operations for the components x, y, z.

and test function space. This means that any arbitrary test function $\boldsymbol{v}$ from the test space is still admissible. Finding solutions such that the boundary integral becomes zero, leads to a $\boldsymbol{H}$-field that is orthogonal to the interface, i.e. parallel to the normal vector $\boldsymbol{n}$, see eq. (7.13). In various publications, this boundary is denoted with the index H at the boundary, e.g. Γ_H. For an isotropic permeability, one can directly say $\boldsymbol{B} \times \boldsymbol{n} = \boldsymbol{0}$, eq. (7.14). For the case of the Coulomb gauge ($\boldsymbol{\nabla} \cdot \boldsymbol{A} = 0$ in Ω), the $\boldsymbol{A}$-field is orthogonal to the surface's normal $\boldsymbol{n}$ [7], as expressed in eq. (7.15).

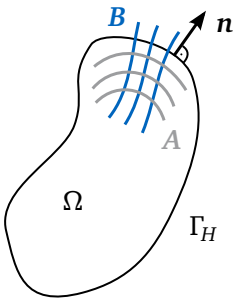

$$\oint_{\Gamma_H} \left(\boldsymbol{v} \times \underbrace{\frac{1}{\mu}(\boldsymbol{\nabla} \times \boldsymbol{A})}_{\boldsymbol{H}} \right) \cdot \boldsymbol{n} \, \mathrm{d}\Gamma_H \stackrel{!}{=} 0 \tag{7.11}$$

$$\oint_{\Gamma_H} \boldsymbol{v} \cdot (\boldsymbol{H} \times \boldsymbol{n}) \, \mathrm{d}\Gamma_H \stackrel{!}{=} 0 \tag{7.12}$$

$$\boldsymbol{H} \times \boldsymbol{n} = \boldsymbol{0} \tag{7.13}$$

$$\boldsymbol{B} \times \boldsymbol{n} = \boldsymbol{0} \tag{7.14}$$

$$\text{for Coulomb gauge} \quad \boldsymbol{A} \cdot \boldsymbol{n} = 0 \tag{7.15}$$

This boundary condition is applied whenever two domains of one system are connected to each other. This can be a ferromagnetic domain embedded in an air domain. Or this could be the individual finite elements connected.

Essential Boundary The essential boundary conditions describe Dirichlet conditions on the $\boldsymbol{B}$ field. They are therefore indicated with B on the boundary, Γ_B. To assign that condition, typically the trial functions are restricted such that they satisfy the Dirichlet boundary conditions. Assuming the same space for trial- and test functions, also $\boldsymbol{v}$ must be restricted. It is assumed that the magnetic field $\boldsymbol{H}$ is tangential to the boundary surface for a Ω that is sufficiently large, refer eqs. (7.16) and (7.17). Finding the restrictions of the trial- and test space at the boundary such that the $\boldsymbol{B}$-field is tangential to the boundary Γ_B leads to $\boldsymbol{v}_{\text{tangent}}(\Gamma_B) \stackrel{!}{=} 0$. With this, the boundary integral in eq. (7.3) vanishes. Using $\boldsymbol{B} = \boldsymbol{\nabla} \times \boldsymbol{A}$, the vector identity $(\boldsymbol{\nabla} \times \boldsymbol{A}) \cdot \boldsymbol{n} = -\nabla \cdot (\boldsymbol{n} \times \boldsymbol{A}) + (\boldsymbol{\nabla} \times \boldsymbol{n}) \cdot \boldsymbol{A}$ and the knowledge that $\boldsymbol{\nabla} \times \boldsymbol{n} = 0$[2], the condition on $\boldsymbol{A}$ writes as $\boldsymbol{A} \times \boldsymbol{n} = \boldsymbol{a}$ where $\boldsymbol{a}$ is any function satisfying $\boldsymbol{\nabla} \cdot \boldsymbol{a} = 0$.

$$\boldsymbol{B} \cdot \boldsymbol{n} = 0 \tag{7.16}$$

$$\boldsymbol{H} \cdot \boldsymbol{n} = 0 \tag{7.17}$$

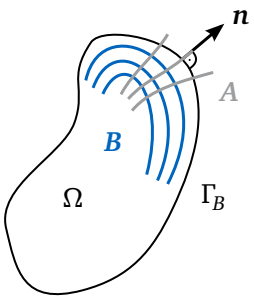

$$\oint_{\Gamma_B} \boldsymbol{v} \cdot \left(\underbrace{\frac{1}{\mu}(\boldsymbol{\nabla} \times \boldsymbol{A})}_{\boldsymbol{H}} \times \boldsymbol{n} \right) \mathrm{d}\Gamma_B = 0 \tag{7.18}$$

$$\oint_{\Gamma_B} \boldsymbol{H} \cdot \underbrace{(\boldsymbol{v} \times \boldsymbol{n})}_{\stackrel{!}{=}0} \, \mathrm{d}\Gamma_B = 0 \tag{7.19}$$

$$\boldsymbol{v}_{\text{tangent}} \stackrel{!}{=} 0 \tag{7.20}$$

$$\boldsymbol{v} \times \boldsymbol{n} = \boldsymbol{0} \tag{7.21}$$

[2]Hint: The surface is described as a function $f(x, y, z) = 0$. The normal is parallel to $\boldsymbol{\nabla} f$. The curl of a gradient is always zero [28].

7.1.4 Degenerated Weak Form for 2D Domains

After deriving the general weak form for the chosen magnetodynamic formulation, this section shows how the equations simplify for the case of two-dimensional investigations. A 2D model can represent a 3D system in two cases, as visualized in fig. 7.2: The 2D cartesian plane represents the cross-section of a prismatic body. In order to neglect fringing effects at the prismatic body's end, we have to assume that the body is considerably longer in the z-direction than in the x-y-direction. In the axisymmetric scenario, the 2D shapes are rotated around the z-axis to construct a three-dimensional volume. This case is not further considered in this work.

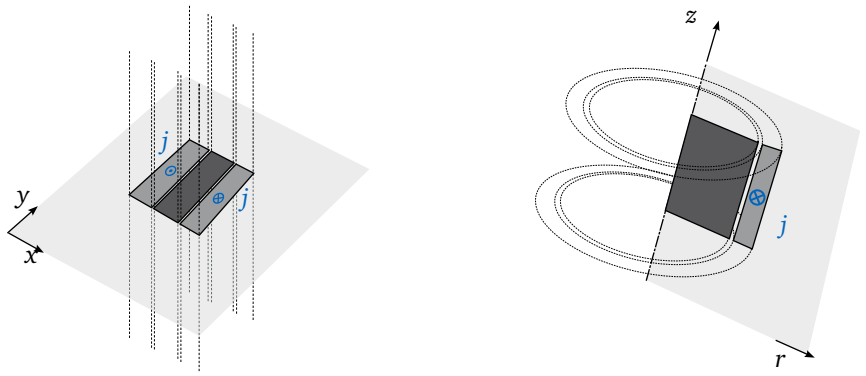

(a) 2D cartesian **(b)** 2D polar

Figure 7.2: Prismatic and revolute interpretation of 2D models. The load $\boldsymbol{j}$ is in both cases perpendicular to the cross section plane.

A further distinction must be made regarding the load case, i.e. the way the external current is applied to the coil. Two results with different properties are derived from the general three-dimensional formulation. The difference is founded in the topology of the external applied current density $\boldsymbol{j}$. Assuming the 2D cartesian case, a 2D system with solenoidal B-field or a 2D system with scalar B-field results accordingly.

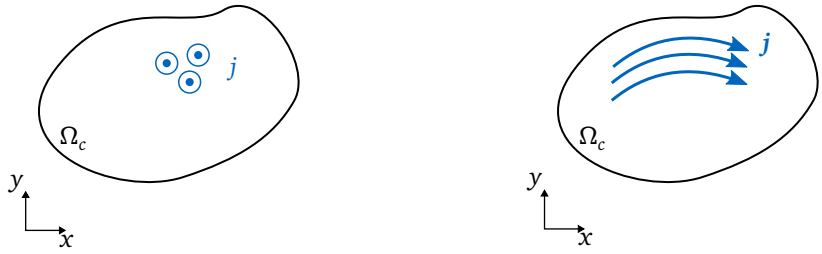

(a) Scalar Load **(b)** Solenoidal Load

Figure 7.3: Scalar- and solenoidal load case in the 2D plane

For the sake of simplicity, the dynamic part is omitted, as it has no influence on the system's topology. Also, the non-linearity of the permeability μ is not written explicitly to keep the notations easy to read. The general weak form, for any appropriate space V for the finite element formulation, can be written as: Find $\boldsymbol{A}$ for every $\boldsymbol{\nu}$ from $\boldsymbol{V}$ such that

$$\int_\Omega \frac{1}{\mu}(\nabla \times \boldsymbol{\nu}) \cdot (\nabla \times \boldsymbol{A}) \, \mathrm{d}\Omega = \int_\Omega \boldsymbol{\nu} \cdot \boldsymbol{j} \, \mathrm{d}\Omega \qquad \forall \boldsymbol{\nu} \in \boldsymbol{V} \tag{7.22}$$

2D - Solenoidal $\boldsymbol{B}$-field The first case assumes a $\boldsymbol{B}$-field completely parallel to the xy-plane and constant in the z direction. As the magnetic flux field is known to be divergence-free, it is called a solenoidal field. To achieve a purely solenoidal $\boldsymbol{B}$-field in a plane, the applied current $\boldsymbol{j}$ is only allowed to be orthogonal to that plane, meaning it can only have a z-component: $\boldsymbol{j} = \begin{pmatrix} 0 & 0 & j \end{pmatrix}^T$. This constraint on the right-hand side of the weak form leads to a simplification of the equation as shown in the following. Inspecting the z-component of the static bilinear form eq. (7.22) shows:

$$\int_\Omega \frac{1}{\mu}(\nabla \times \boldsymbol{\nu}) \cdot (\nabla \times \boldsymbol{A}) \, \mathrm{d}\Omega = \int_\Omega \begin{pmatrix} 0 \\ 0 \\ \nu_z j_z \end{pmatrix} \mathrm{d}\Omega \tag{7.23}$$

$$\int_\Omega \frac{1}{\mu} \begin{pmatrix} 0 \\ 0 \\ \frac{\partial \nu_z}{\partial x}\frac{\partial A_z}{\partial x} + \frac{\partial \nu_z}{\partial y}\frac{\partial A_z}{\partial y} + \frac{\partial \nu_z}{\partial z}\frac{\partial A_z}{\partial z} \end{pmatrix} = \int_\Omega \begin{pmatrix} 0 \\ 0 \\ \nu_z j_z \end{pmatrix} \mathrm{d}\Omega \tag{7.24}$$

By coefficient comparison, the expression can be transformed in a gradient notation on the z-component of the vector potential:

$$\nabla \nu_z \cdot \nabla A_z = \frac{\partial \nu_z}{\partial x}\frac{\partial A_z}{\partial x} + \frac{\partial \nu_z}{\partial y}\frac{\partial A_z}{\partial y} + \frac{\partial \nu_z}{\partial z}\frac{\partial A_z}{\partial z} \tag{7.25}$$

Replacing the curl operator with the previously found gradient operator, a scalar weak form equation for the z-direction of the vector potential is found:

$$\int_\Omega \frac{1}{\mu} \nabla \nu_z \cdot \nabla A_z \, \mathrm{d}\Omega = \int_\Omega \nu_z j_z \, \mathrm{d}\Omega \qquad \forall \nu_z \in H^1 \tag{7.26}$$

To reconstruct the magnetic flux density from the definition of the vector potential, the curl of the scalar field A_z has to be defined by

$$\boldsymbol{B} = \nabla \times A_z = \begin{pmatrix} \frac{\partial A_z}{\partial y} \\ -\frac{\partial A_z}{\partial x} \end{pmatrix}. \tag{7.27}$$

Due to the gradient, a constant offset of A_z is possible. By fixing the essential boundary ($A_{z\Gamma} = 0$), the gauging is sufficiently fulfilled. Concluding, this formulation is the most lightweight formulation of magnetostatic and magnetodynamic systems. Due to the gradient, the finite element space is also simplified to the well-known H^1 space, and with that, the use of nodal elements is also justified.

2D - Scalar B-field A view orthogonal to the previous case results in a scalar B-field, representing the amplitude of the vector $\boldsymbol{B}$, $\boldsymbol{B}$ being always orthogonal to the $x-y$-plane. Such a field arises from currents that are completely in the plane, ergo $\boldsymbol{j} = \begin{pmatrix} j_x & j_y & 0 \end{pmatrix}$. For the known equation

$$\int_\Omega \frac{1}{\mu}(\nabla \times \boldsymbol{A}) \cdot (\nabla \times \boldsymbol{\nu}) \, \mathrm{d}\Omega = \int_\Omega \boldsymbol{\nu} \cdot \boldsymbol{j} \, \mathrm{d}\Omega, \tag{7.28}$$

the resulting vector potential for such a load case will also be purely in-plane

$$\boldsymbol{A} = \begin{pmatrix} A_x \\ A_y \\ 0 \end{pmatrix}, \tag{7.29}$$

and results in a magnetic flux density with only a z-component:

$$\boldsymbol{B} = \boldsymbol{\nabla} \times \boldsymbol{A} = \begin{pmatrix} 0 \\ 0 \\ \frac{\partial A_y}{\partial x} - \frac{\partial A_x}{\partial y} \end{pmatrix} \qquad B_z = \frac{\partial A_y}{\partial x} - \frac{\partial A_x}{\partial y}. \tag{7.30}$$

The vector potential must be gauged to be non-singular. To apply the Coloumb gauge weakly, an additional term can be added:

$$\int_\Omega \frac{1}{\mu}(\boldsymbol{\nabla} \times \boldsymbol{A}) \cdot (\boldsymbol{\nabla} \times \boldsymbol{\nu}) + \kappa \boldsymbol{A} \cdot \boldsymbol{\nu} \, \mathrm{d}\Omega = \int_\Omega \boldsymbol{j} \cdot \boldsymbol{\nu} \, \mathrm{d}\Omega \qquad \forall \boldsymbol{\nu} \in \boldsymbol{H}^{\mathrm{curl}} \tag{7.31}$$

This formulation is basically not different from the full 3D formulation.

7.2 Discretization

Discretization is the process of dividing a continuous domain into a finite number of discrete sub-domains or elements. The discretization process involves approximating the solution within each element using a set of basis functions, typically polynomials, and the unknowns are represented by the coefficients of these basis functions. The weak form of the partial differential equation (PDE) is integrated over each element using the chosen basis functions to obtain a set of element equations. The element equations are then assembled into a global system of equations by combining the equations from each element. This global system of equations represents the entire domain and is used to find the solution.

To finally solve the previously developed variational problems numerically, the continuous equation (infinite-dimensional) is approximated by a finite-dimensional (n) subspace of the original space. It is common to name these functions that approximate the field the *trial functions*. The space containing the trial functions is called the *trial space*. When the trial functions span in the same space as the test functions, the projection is called a *Galerkin* projection. The approximate solution $u(\boldsymbol{x})$ becomes a linear combination of the finite functions $N(\boldsymbol{x})$ (also named FE basis function, shape functions or interpolation functions):

$$u(\boldsymbol{x}) \approx \sum_{k=1}^{n} u_k N_k(\boldsymbol{x}) \tag{7.32}$$

The number n of shape functions depends on the type and order of elements that the system is discretized with.

With the Galerkin projection applied, the following problem states: Find $\boldsymbol{u}_N \subset \boldsymbol{H}^{\mathrm{curl}}$ such that

$$\sigma \frac{\partial}{\partial t} \int_\Omega \boldsymbol{u}_N \cdot \boldsymbol{\nu}_N \, \mathrm{d}\Omega + \int_\Omega \boldsymbol{\nabla} \times \boldsymbol{u}_N \cdot \frac{1}{\mu(\boldsymbol{u}_N)} \boldsymbol{\nabla} \times \boldsymbol{\nu}_N \, \mathrm{d}\Omega = \int \boldsymbol{j}_0 \cdot \boldsymbol{\nu}_N \, \mathrm{d}\Omega \quad \forall \boldsymbol{\nu} \in \boldsymbol{H}^{\mathrm{curl}} \tag{7.33}$$

The index N indicates that the test function, as well as the trial function, are discretized with appropriate shape functions that are only supported in a small part of the domain, the finite element. The test function chosen is used to *test* the PDE by multiplying it and integrating. The Galerkin projection involves choosing the same basis functions for the approximation of the solution and the test function. This results in a system of algebraic equations that can be solved to obtain the coefficients of the solution functions. By evaluating these functions, a solution is found for every position $\boldsymbol{x}$ of the domain. By using the Galerkin projection, we can ensure that the approximation is accurate and that the numerical solution satisfies

certain properties, such as conservation laws and energy bounds. By reducing the element size, the approximated solution converges toward the exact solution, if the true solution is an arbitrary polynomial [34].

For this chapter, 2D triangular elements are presented in H^1 and $\boldsymbol{H}^{\text{curl}}$ space. The extension to 3D with tetrahedral elements in H^1 or $\boldsymbol{H}^{\text{curl}}$ space is not shown here. The interested reader is referred to the literature, e.g., [33, 34].

7.2.1 Mesh

To practically generate the small parts of the domain, the finite elements, a mesh is generated from a given geometry. The term *mesh size* refers to the spatial size of the elements that constitute the mesh. It is often denoted with the length h, which is defined differently for various software packages. Often it is the edge length of an element. The user can set a general upper limit which is, depending on the algorithm, not always strictly adhered to. Also, a grading parameter is often set to limit the growth factor of elements up to the mesh size limits. The local mesh size $h(\boldsymbol{x})$ is bounded by $|\Delta_x h(\boldsymbol{x})| < \frac{1}{\text{grading}}$ [61].

7.2.2 Nodal Elements - H^1 Space

For nodal elements, the coefficients of the shape functions, i.e., the degrees of freedom (dof), typically describe the solution on the vertices of the element. As shape functions, a common choice is the Lagrange polynomials. In that case, the nodal elements are also called *Lagrange elements*. A key property is that for the Sobolev space H^1, the transition conditions between subdomains (for FEM i.e. elements) are continuous in normal- and tangential directions. That means that nodal values at the nodes of adjacent elements are the same, which ensures that the shape functions are continuous across the element boundaries.

An exemplary 1st-order triangle element in 2D is shown in fig. 7.4. The blue nodes represent the dofs of this element. Assembling multiple elements of this type, they share each vertex and their corresponding dof. The interpolation of the solution u of element e at

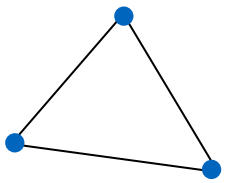

Figure 7.4: 2D triangle, nodal element.

any given point $\boldsymbol{x}$ in the subdomain (i.e. in the element) is a superposition of the individual shape functions N_k weighted by the nodal value u_k.

$$u(\boldsymbol{x}) = \sum_{k=1}^{\text{nodes}} u_k^e N_k(\boldsymbol{x}) \tag{7.34}$$

Per se, the elements represent a scalar field on the mesh. Gathering one scalar field per direction yields systems that can represent vector fields.

7.2.3 Edge Elements - H^{curl} Space

Edge finite elements are a type of finite element that is commonly used in computational electromagnetics and other fields where the vector nature of the solution is important. Unlike traditional finite elements that use scalar functions to approximate the solution, edge finite elements use vector functions that are defined on the edges of the elements.

The use of vector functions on the edges allows for a more accurate approximation of the vector field being solved for. This is particularly important in problems where the solution is highly directional, such as in electromagnetic wave propagation or fluid dynamics.

Whitney Edge Elements are one of the earliest examples of finite edge elements. They were introduced by mathematician H. WHITNEY in 1957 and are based on the use of tangential vector fields defined on the edges of the elements [10, 12].

Nédélec Edge Elements are a more recent development in finite edge elements. They were introduced by mathematician JEAN-CLAUDE NÉDÉLEC in 1980 as mixed elements and are based on the use of curl-conforming vector fields defined on the edges of the elements [49]. BOSSAVIT writes in [10]: "Mixed elements are Whitney forms, rediscovered.". Specifically, the lowest-order elements can be seen as equivalent. In the following, the term *edge element* is used to keep an abstract level.

Edge elements are used to approximate both the electric and magnetic fields in electromagnetic problems and have been shown to provide highly accurate results in a wide range of applications. A visualization of a triangular edge element is given in fig. 7.5. The blue arrows represent the basis vectors. The lengths of these vectors are the dofs of the element.

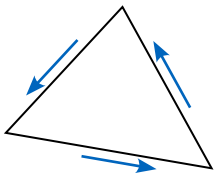

Figure 7.5: Edge element, first order.

Again, the solution $\boldsymbol{u}(\boldsymbol{x})$, now a vector(!), is a superposition of the shape functions $\boldsymbol{N}$, which are also vectorial.

$$\boldsymbol{u}(\boldsymbol{x}) = \sum_{k=1}^{\text{edges}} u_k^e \boldsymbol{N}(\boldsymbol{x})_k \tag{7.35}$$

Modified Vector Potential Using edge elements, the magnetodynamic problem expressed in terms of modified vector potential can be discretized efficiently [35]. The solution space is defined as

$$\boldsymbol{H}_A^{\text{curl}}(\Omega) := \left\{ \boldsymbol{A} \in [L_2(\Omega)]^3 : \boldsymbol{\nabla} \times \boldsymbol{A} \in [L_2(\Omega)]^3 \right\}$$

Due to the constant conductivity assumption in the domain Ω_c and the use of edge elements, the scalar potential V does not have to be solved explicitly. The entire problem is described solely by the modified vector potential.

The formulation leads to a weak form: Find $\boldsymbol{A} \in \boldsymbol{H}_A^{\text{curl}}$, such that

$$\int_\Omega \frac{1}{\mu} (\boldsymbol{\nabla} \times \boldsymbol{A}') \cdot (\boldsymbol{\nabla} \times \boldsymbol{A}) \, \mathrm{d}\Omega + \int_{\Omega_c} \sigma \boldsymbol{A}' \cdot \frac{\partial \boldsymbol{A}}{\partial t} \, \mathrm{d}\Omega_c = \int_{\Omega_0} \boldsymbol{A}' \cdot \boldsymbol{j}_0 \, \mathrm{d}\Omega \tag{7.36}$$

for all $\boldsymbol{A}' \in \boldsymbol{H}^{\mathrm{curl}}_{\boldsymbol{A}'}$. The notation of test- and trail functions as $\boldsymbol{A}$ and $\boldsymbol{A}'$ indicates a Galerkin approximation and is used further on to remind on the meaning of the primary variable being the vector potential.

To ensure the uniqueness of the vector potential $\boldsymbol{A}$ in the area where the conductivity is null, a regularization term κ is introduced.

$$\int_{\Omega \setminus \Omega_c} \frac{1}{\mu} \kappa \boldsymbol{A}' \cdot \boldsymbol{A} \, \mathrm{d}\Omega \tag{7.37}$$

The test function is set to zero on Γ, which is the Dirichlet boundary for $\boldsymbol{A}$. Due to eq. (15.5), this means $\boldsymbol{n} \cdot \boldsymbol{B} = 0$. With that essential boundary, the boundary integral vanishes from the left-hand side of the weak form.

After discretization, eq. (7.36) is written as

$$\boldsymbol{M}_{\boldsymbol{A}} \dot{\boldsymbol{u}}_{\boldsymbol{A}} + \boldsymbol{g}_{\boldsymbol{A}}(\boldsymbol{u}_{\boldsymbol{A}}) = \boldsymbol{f}_{\boldsymbol{A}} \tag{7.38}$$

Hereby $\boldsymbol{M}_{\boldsymbol{A}}$ is the so-called magnetic mass matrix, $\boldsymbol{g}_{\boldsymbol{A}}$ the discretized internal magnetic force, $\boldsymbol{f}_{\boldsymbol{A}}$ the load vector and $\boldsymbol{u}_{\boldsymbol{A}}$ the unknown values of the vector potential. The subscript $\boldsymbol{A}$ will be dropped further on to keep the notation slender.

Chapter 8

Static and Dynamic Solvers

Once the model is discretized using the FEM approach, a set of equations, either linear or nonlinear, must be solved. The chapter is organized in three sections. First, a static system is assumed, which is solved with a Newton-Raphson Algorithm. Second, the solution for a harmonic system is shortly discussed. Finally, the time integration of a dynamic system with an arbitrary load case is explained.

8.1 Static Solution

In steady state, i.e., the static solution for a static current load vector, the internal currents $\boldsymbol{g}$ balance the externally applied currents $\boldsymbol{f}$, see eq. (7.7). Written in discrete form for the FEM discretized problem, where $\boldsymbol{u}$ is the (unknown) magnetic vector potential solution for each dof.

$$\boldsymbol{g}(\boldsymbol{u}) - \boldsymbol{f} \stackrel{!}{=} \boldsymbol{0} \tag{8.1}$$

Computing the vector $\boldsymbol{u}$ yields a classic root-finding problem. One option to accomplish the task is the application of Newton's algorithm.

Newton Raphson Algorithm A commonly used iterative solver algorithm to find the root of an arbitrary function is the Newton Raphson method [75]. As it is nearly impossible to find the solution $\boldsymbol{u}$ in one solution step, the problem is written in a residual form, i.e., the difference of the non-correct solution is assigned to the vector $\boldsymbol{r}$ for each iteration i.

$$\boldsymbol{r}(\boldsymbol{u}_i) = \boldsymbol{g}(\boldsymbol{u}_i) - \boldsymbol{f} \tag{8.2}$$

To find the next iteration, the task is to find a $\boldsymbol{u}$ such that the linearized (!) residuum vanishes.

$$\boldsymbol{r}(\boldsymbol{u}_i) + \left.\frac{\partial \boldsymbol{r}(\boldsymbol{u})}{\partial \boldsymbol{u}}\right|_{\boldsymbol{u}_i} \Delta \boldsymbol{u}_{i+1} = \boldsymbol{0} \tag{8.3}$$

This allows the use of a linear solver to find the update step $\Delta \boldsymbol{u}_{i+1}$.

$$\boldsymbol{u}_{i+1} = \boldsymbol{u}_i + \Delta \boldsymbol{u}_{i+1} \tag{8.4}$$

A new residuum is computed from the newly found vector $\boldsymbol{u}_{i+1}$. The procedure is iterated until the norm of the residuum is smaller than a given tolerance, and the algorithm is converged. The norm used to check the convergence is determined by the user depending on the application. The Newton-Raphson scheme is visualized in fig. 8.1.

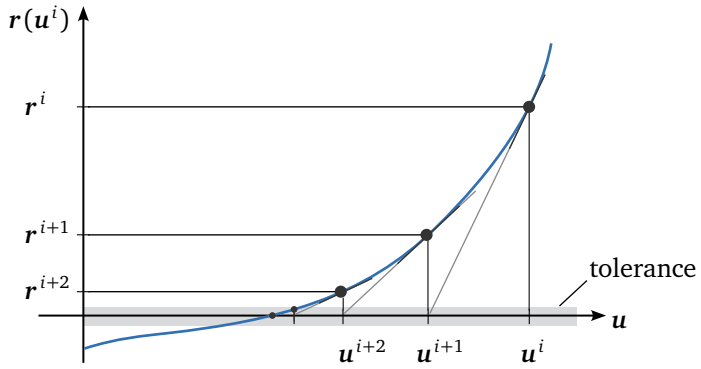

Figure 8.1: Convergence scheme of the Newton-Raphson-algorithm.

Two computationally intensive steps catch the eye, namely the evaluation of the internal currents $\boldsymbol{g}$ and the linearization of the residuum, which roots back to the linearization of the internal current function $\boldsymbol{g}(\boldsymbol{u})$, as the external load is constant by definition.

$$\frac{\partial \boldsymbol{r}}{\partial \boldsymbol{u}} = \frac{\partial \boldsymbol{g}}{\partial \boldsymbol{u}} \tag{8.5}$$

The tangent matrix $\boldsymbol{K}(\boldsymbol{u}^i)$ is defined as

$$\boldsymbol{K}(\boldsymbol{u}_i) = \left.\frac{\partial \boldsymbol{g}}{\partial \boldsymbol{u}}\right|_{\boldsymbol{u}_i} \tag{8.6}$$

In the used framework, this is achieved by linearization of the weak form followed by the discretization of the linearized system. The linear set of equations to solve becomes

$$\boldsymbol{K}(\boldsymbol{u}_i)\Delta\boldsymbol{u}_{i+1} = -\boldsymbol{r}(\boldsymbol{u}_i) \tag{8.7}$$

As a stopping condition, an energy-based criterion is chosen. To normalize the criterion value, a reference energy is used. The stopping criterion can therefore be written as:

$$tol > \left|\frac{\boldsymbol{r}^T\boldsymbol{K}^{-1}\boldsymbol{r}}{\boldsymbol{f}^T\boldsymbol{K}^{-1}\boldsymbol{f}}\right| \approx \left|\frac{\Delta(\boldsymbol{u}_i)^T\boldsymbol{r}(\boldsymbol{u}_i)}{(\boldsymbol{u}_{i+1})^T\boldsymbol{f}}\right| \tag{8.8}$$

Remark

The stopping criterion is an energy-based measure, which is useful for systems with high variability of the stiffness matrix. For electromagnetic systems, this is the case as the stiffness varies up to three orders of magnitude between the air and ferromagnetic domains.

The convergence is quadratic in the vicinity of the solution [75]. Therefore, a predictor (i.e. a good guess of the solution) is needed as an initial solution. For big currents, a load stepping can be beneficial, which means that the load is not applied at once but in small portions, whereas the solution of the previous load step is used as a predictor for the next load step.

Remark

A so-called *line search* function is added additionally. Line search is a method for choosing the step size in each iteration of the Newton-Raphson method. This function basically modifies the update of the solution eq. (8.4) to weight the $\Delta \boldsymbol{u}$ via the condition if the residuum got smaller during the last step.

$$\boldsymbol{u}_{i+1} = \boldsymbol{u}_i + \beta \Delta \boldsymbol{u} \tag{8.9}$$

If the residuum increases, β is set to $\frac{1}{2}$ to prevent the solution from changing too much in the wrong direction.
Also, *damping* could be applied, which also involves a factor $\beta < 1$. The damping factor is set before the iteration process and does not change during the iterations, while the step size in a line search is determined dynamically in each iteration. The term "damping" is often used in the context of solving systems of non-linear equations, where damped steps help to avoid overshooting the solution.
For this thesis, the described line search is implemented but the damping is not applied.

8.2 Harmonic Solution

For a harmonic time solution, the load vector is assumed to synchronously vary around zero with an excitation frequency Ω.

$$\boldsymbol{f}(t) = \hat{\boldsymbol{f}} e^{\mathrm{i}\Omega t} \tag{8.10}$$

Assuming linear material properties for the system, the solution will also follow the excitation frequency, which leads to the complex equation:

$$(\mathrm{i}\omega \boldsymbol{M} + \boldsymbol{K})\hat{\boldsymbol{u}} = \hat{\boldsymbol{f}} \tag{8.11}$$

Due to the fact that the solution vector $\boldsymbol{u}$ is complex, the number of degrees of freedom to solve is doubled. After solving the equation once, the complete time response trajectory for this excitation frequency of the system is available. Repeating this procedure for a series of frequencies leads to a frequency response function. The limitation to a purely linear material is the disadvantage of this method and is therefore not further evolved here. Various derivations and investigations can be found in [5].

8.3 Transient Solution - Time Integration

A time integration scheme is utilized for arbitrary, time-varying load vectors to compute the electromagnetic field progression over time. By construction, the system to solve is a first-order differential equation with a non-linear part that is only dependent on $\boldsymbol{u}$.

$$\boldsymbol{M}\dot{\boldsymbol{u}} + \boldsymbol{g}(\boldsymbol{u}) = \boldsymbol{f}(t) \tag{8.12}$$

The chosen time integration scheme is the *Implicit Euler Method*, also known as the *Backward Euler Method*, which is suitable for time integration of a first-order system primarily because of its stability and accuracy characteristics.

Backward Euler Algorithm The implicit Euler algorithm uses an estimate of the derivative at the next time step rather than the current one, which is the case in the explicit Euler method.

$$\dot{\boldsymbol{u}}_{n+1} \approx \frac{\boldsymbol{u}_{n+1} - \boldsymbol{u}_n}{\Delta t} \tag{8.13}$$

where $\boldsymbol{u}_n$ and $\boldsymbol{u}_{n+1}$ are the solutions at two successive times t_n and t_{n+1}, Δt being the time step $t_{n+1} - t_n$.

This causes a certain level of complexity due to the inherent need for a root-finding algorithm to solve the above equation, making it computationally more intensive than its explicit counterpart. However, this method exhibits a key advantage in the form of A-stability. A numerical method is said to be A-stable if it is stable for all step sizes, Δt, against stiff systems. Stiffness refers to differential equations with solutions that can exhibit rapid variation, often leading to instability when using explicit methods, especially with large step sizes.

The problem eq. (8.12) can thus be solved at t_{n+1} as

$$\boldsymbol{M}\boldsymbol{u}_{n+1} + \Delta t \boldsymbol{g}(\boldsymbol{u}_{n+1}) = \boldsymbol{M}\boldsymbol{u}_n + \Delta t \boldsymbol{f}_{n+1} \tag{8.14}$$

which is a non-linear algebraic problem for $\boldsymbol{u}_{n+1}$.

Newton Raphson Algorithm The non-linear time integration problem eq. (8.14) for a single time step can also be written in the residual form, as already seen in eq. (8.2).

$$\boldsymbol{r}(\boldsymbol{u}_{n+1}) = (\boldsymbol{M}\boldsymbol{u}_n + \Delta t \boldsymbol{f}_{n+1}) - (\boldsymbol{M}\boldsymbol{u}_{n+1} + \Delta t \boldsymbol{g}(\boldsymbol{u}_{n+1})) \stackrel{!}{=} 0 \tag{8.15}$$

Analogous to the static Newton Raphson procedure, the linearized residuum is computed and results in the so-called tangent *stepping* matrix $\boldsymbol{K}(\boldsymbol{u}^i_{n+1})$.

$$\boldsymbol{K}(\boldsymbol{u}^i_{n+1}) = \frac{\mathrm{d}\boldsymbol{r}}{\mathrm{d}\boldsymbol{u}}\Big|_{\boldsymbol{u}^i_{n+1}} = \boldsymbol{M} + \Delta t \left.\frac{\partial \boldsymbol{g}}{\partial \boldsymbol{u}}\right|_{\boldsymbol{u}^i_{n+1}} \tag{8.16}$$

As stopping condition, the same energy-based criterion as for the static system in section 8.1 is chosen.

8.4 Linear Solvers

Different solvers are suitable for the linear problem in the Newton-Raphson iteration (for the static and dynamic cases). In general, two types of linear solvers exist: direct solvers and iterative solvers.

Direct solvers aim to obtain the exact solution of a linear system by applying a sequence of algebraic operations. Examples of direct solvers include LAPACK, which is a collection of linear algebra routines that include solvers for dense and sparse systems of linear equations. UMFPACK is a direct sparse solver that uses an incomplete LU factorization with threshold pivoting, and PARDISO, which is a parallel direct solver that can solve both symmetric and unsymmetric systems of equations.

Iterative solvers, on the other hand, aim to approximate the solution of a linear system by repeatedly improving an initial guess. They work by defining a sequence of iterates that converge to the exact solution. Examples of iterative solvers include the CG and preconditioned CG algorithms. Also, the GMRES, which is an iterative solver that uses the Krylov subspace method.

The choice between direct and iterative solvers depends on the problem at hand. Direct solvers are generally faster for small to medium-sized problems and can handle both dense and sparse matrices. However, they may become computationally expensive for large-scale problems due to their high memory requirements and complexity. Iterative solvers, on the other hand, are more suitable for large-scale problems and can often achieve better performance and memory usage than direct solvers. However, they may require many iterations to converge and are generally slower than direct solvers for small to medium-sized problems.

The mathematical background can be found in [27] and [23].

8.4.1 Direct Solvers

Direct solvers factorize the matrix of the system into a product of simpler matrices, which can be used to solve the system directly. The most common direct solver is Gaussian elimination. Direct solvers are often accurate and robust but can be computationally expensive and memory-intensive for large, dense systems. The following information is excerpts from the packages' websites and the survey of DAVIS [24]. A list of freely available sparse direct solvers is maintained at the Netlib website[1].

PARDISO (Parallel Direct Sparse Solver) is a high-performance, parallel direct solver that can solve both symmetric and unsymmetric systems of equations. It is particularly well-suited for large-scale sparse problems and can exploit parallelism in both shared-memory and distributed-memory architectures. PARDISO also supports various matrix storage formats, including compressed sparse row (CSR) and compressed sparse column (CSC).

LAPACK (Linear Algebra Package) is a collection of Fortran subroutines for solving systems of linear equations, eigenvalue problems, and singular value decomposition. It includes both direct and iterative solvers for dense and sparse matrices, as well as routines for matrix factorization, matrix inversion, and matrix multiplication. LAPACK is widely used in scientific computing and is included in many software packages, including MATLAB and Python's NumPy library.

SuperLU is a high-performance, direct solver for sparse, unsymmetric systems of linear equations. It is based on the LU factorization with partial pivoting and can handle both serial and parallel computation. SuperLU uses a variety of techniques to improve performance, including memory pooling, supernodal factorization, and dynamic pivoting. It is widely used in scientific computing and is included in many software packages, including MATLAB and the PETSc library.

UMFPACK (Unsymmetric Multi Frontal Package) is a high-performance, direct solver for unsymmetric, sparse systems of linear equations. It is based on the multi-frontal method, which is a generalization of the LU factorization that exploits sparsity in the matrix. UMFPACK uses a variety of techniques to improve performance, including threshold pivoting, numerical dropping, and symmetric pruning. It is widely used in scientific computing and is included in many software packages, including MATLAB and the SuiteSparse library.

MUMPS (Multifrontal Massively Parallel Solver) is a high-performance, direct solver for large-scale, sparse systems of linear equations. It is based on the multi-frontal method

[1] www.netlib.org/utk/people/JackDongarra/la-sw.html, last check June-2023

and can exploit parallelism in both shared-memory and distributed-memory architectures. MUMPS uses a variety of techniques to improve performance, including memory pooling, pivoting, and load-balancing. It is widely used in scientific computing and is included in many software packages, including PETSc and the SuiteSparse library.

8.4.2 Iterative Solvers

Iterative solvers use an iterative process to find the solution to the system. These methods start with an initial guess for the solution and then iteratively refine the solution until it converges to a desired level of accuracy. Iterative solvers can be faster and more memory-efficient than direct solvers for large, sparse systems but can be sensitive to the choice of preconditioner and can require many iterations to converge. An in-depth mathematical background for iterative solvers is given in [59]. More practical information and advice are presented in [4].

CG (Conjugate Gradient) is a widely used iterative method for solving symmetric, positive-definite linear systems. CG is relatively simple to implement and is very memory-efficient, requiring only one vector to be stored at a time. However, it can be slow to converge for ill-conditioned systems. Accurate predictions of the convergence cannot be made.

PCG (Preconditioned Conjugate Gradient) is an extension of CG that uses a preconditioner to improve convergence. The PCG can be more effective than CG, but it can be challenging to compute an efficient preconditioner $\boldsymbol{M}$ and requires more memory.

GMRES (Generalized Minimal Residual) is an iterative method that was developed to solve non-symmetric linear systems. GMRES is more effective than applying CG or PCG on the equivalent symmetrized operator (i.e. solving $\boldsymbol{A}^T\boldsymbol{A}\boldsymbol{x} = \boldsymbol{A}^T\boldsymbol{b}$) for non-symmetric systems. If no so-called restarts are used, GMRES stores all previously computed vectors and will converge in n steps. In practice, the GMRES needs to restart to keep the memory consumption controlled and is often combined with a preconditioning method to speed up the convergence.

More advanced methods and extensions are available but are not relevant in the course of this thesis.

8.4.3 Solver Selection

The choice between direct and iterative solvers depends on several factors, such as the matrix structure, sparsity pattern, condition number, and available memory and computational resources. However, as a rule of thumb, direct solvers are typically more efficient for small to medium-sized systems (up to a few thousand equations), while iterative solvers are more efficient for larger systems (tens of thousands or more equations).

The choice of solver for the full-order system is not obvious. In general, the choice of the solver for the Newton scheme will depend on the properties of the Jacobian matrix, which is typically dense or highly structured and can be computationally expensive to factorize or invert. If the Jacobian matrix is small to medium-sized and has a high degree of fill-in or other structures that make iterative methods less efficient, a direct solver may be a more efficient and accurate option. If the Jacobian matrix is large and highly sparse, an iterative solver may be more memory-efficient and faster than a direct solver.

For the reduced-order systems, the choice for a direct solver is relatively clear. The systems are small by construction. Although they are densely populated, their small size determines everything. The later results show that the solution-effort itself isn't relevant compared to the data handling and Newton iteration steps.

Full-Order Systems When the `sparsecholesky` option is chosen for the inverse parameter in NGSolve, the solver used is a sparse direct solver based on the Cholesky factorization with symmetric pivoting. The Cholesky factorization is used to decompose the sparse matrix into a lower-triangular matrix and its transpose, and then the resulting system of equations is solved using forward and backward substitution. Symmetric pivoting is used to improve the numerical stability of the factorization. NGSolve uses the PARDISO solver as the default solver for sparse direct linear algebra computations.

To compare the results, an own Newton implementation is conducted in Python, using the SciPy library. The `scipy.sparse.linalg.spsolve` function in SciPy uses a sparse direct solver based on LU factorization with partial pivoting. This solver is similar to the SuperLU solver, but it is implemented specifically for the sparse matrices in SciPy. The `spsolve` function solves the sparse linear system $\boldsymbol{Ax} = \boldsymbol{b}$ for the unknown vector $\boldsymbol{x}$, where $\boldsymbol{A}$ is a sparse matrix, and $\boldsymbol{b}$ is a dense vector.

Under the hood, `spsolve` uses the UMFPACK solver, which is a high-performance, direct solver for unsymmetric, sparse systems of linear equations. UMFPACK is part of the SuiteSparse package, which is a collection of software libraries for sparse matrix computations. The SuiteSparse package is included in SciPy as a dependency, so `spsolve` uses UMFPACK to solve the linear system.

Reduced-Order System For the reduced-order systems, our own Newton implementation is utilized, but in a dense matrix description. The `scipy.linalg.solve` command in SciPy uses a dense linear algebra solver based on LU factorization with partial pivoting. Under the hood, `scipy.linalg.solve` calls the LAPACK `gesv` routine, which is part of the LAPACK library. This solver is used to solve a system of linear equations of the form $\boldsymbol{Ax} = \boldsymbol{b}$, where $\boldsymbol{A}$ is a square matrix and $\boldsymbol{b}$ is a vector. The `solve` function computes the LU factorization of the matrix $\boldsymbol{A}$ and then uses forward and backward substitution to solve the system for the unknown vector $\boldsymbol{x}$.

Chapter 9

Software Framework

A distinction has to be made between software that has general FEM capabilities and highly specialized software for electromagnetic problems. A further criterion to evaluate software is the possibility to include one's own algorithms and methods or at least receive various raw data in between the sequence steps. Many of the available finite element analysis (FEA) software are scriptable, but the codes are often closed source, so no insight into the exact algorithms is given. Implementing own algorithms or extracting data during a simulation can become a big challenge. Mostly, this demand leads to open-source projects that have many advantages on the one hand but also the drawback of no extensive documentation and no service. The following section will give an (incomplete) overview of major FEM software packages capable of calculating electromagnetic problems. The section is divided into commercially available software and open-source code.

9.1 Commercial

Since the early days of FEA, commercial software started to be available. The main advantage of commercial software is that it is well-tested and often even certified. A small list of the most common software is given in the following.

Nastran (short for NASA Structural Analysis) is an FEA software package used for structural analysis in engineering. Initially developed by NASA in the 1960s as one of the first FEM software, Nastran has since been commercialized and is now used by various industries, including aerospace, automotive, and civil engineering. The code is written mainly in Fortran. Nastran can be used to solve a wide range of problems, including static and dynamic analyses, thermal analyses, and optimization. It includes a large library of pre-built finite element models and supports a variety of element types and material models. Nastran also includes advanced features for modeling complex structures, such as composites and multibody systems, and for handling large-scale problems through parallel processing. Nastran is widely regarded as a reliable and powerful tool for structural analysis and is often used in conjunction with other software packages for design optimization and verification. Nastran is primarily used for structural analysis and does not have built-in capabilities for electrodynamic simulations. However, it is possible to use Nastran in conjunction with other software packages, such as ANSYS or Abaqus, that have specialized modules for electrodynamic simulations. In this way, Nastran can be used to model the mechanical response of a structure to electrodynamic loads, while specialized software is used to calculate the electromagnetic fields and forces.

ANSYS is an engineering simulation software package that allows users to analyze and design products and structures across a wide range of industries, including aerospace, automotive, and electronics. ANSYS provides a comprehensive suite of structural, thermal, fluid dynamics, and electromagnetic simulation tools.

In particular, ANSYS includes specialized modules for electromagnetic simulations, such as ANSYS Maxwell, ANSYS HFSS, and ANSYS Q3D Extractor. These modules allow users to simulate various electromagnetic phenomena, such as electromagnetic fields, interference, and compatibility. ANSYS Maxwell is specifically designed for low-frequency electromagnetic simulations, such as motor and transformer design, whereas on the other hand, ANSYS HFSS is optimized for high-frequency electromagnetic simulations, such as antenna and microwave design. ANSYS Q3D Extractor is a 3D electromagnetic field solver specializing in the simulation of interconnect structures, such as printed circuit boards.

In addition to its electromagnetic simulation capabilities, ANSYS also provides a wide range of tools for geometry creation, meshing, and post-processing of simulation results.

In the course of this thesis, two reference simulations were conducted using Ansys Mechanical and Ansys Maxwell to check the solution of our own code. The results did not bring new facts, so they are skipped here.

Abaqus is a finite element analysis (FEA) software package developed by Dassault Systèmes. It is used for structural, thermal, and multiphysics simulations in a wide range of industries. Abaqus is known for its sophisticated non-linear material descriptions.

While Abaqus does not have built-in capabilities for electromagnetic simulations, it can be used in conjunction with other software packages that specialize in electromagnetics, such as CST Studio Suite. In this way, Abaqus can be used to model the mechanical response of a structure to electromagnetic loads, while specialized software is used to calculate the electromagnetic fields and forces.

Abaqus provides a wide range of tools for geometry creation, meshing, and post-processing of simulation results. It also includes advanced features for modeling complex structures, such as composites and multi-body systems.

A Python interface allows scripting Abaqus in a convenient way. This is useful for developing model order reduction methods. A student thesis was conducted in 2022 to perform the ECSW method for hyperelastic rubber elements. There, the same Python code routines used for this thesis were running as a co-simulation in combination with Abaqus. Abaqus is used to mesh the geometry, assemble the matrices, and hold the material behavior.

COMSOL Multiphysics is a powerful software package for modeling and simulating physical phenomena in a wide range of fields, including electromagnetics, structural mechanics, fluid dynamics, and heat transfer.

In particular, COMSOL provides a comprehensive suite of tools for electromagnetic simulations, allowing users to simulate a wide range of electromagnetic phenomena, such as electromagnetic fields, wave propagation, and microwave circuits. It includes several specialized modules, such as the RF Module, Wave Optics Module, and Plasma Module, which allow users to simulate specific electromagnetic applications.

COMSOL also provides a variety of tools for geometry creation, meshing, and post-processing of simulation results.

9.2 Open-Source

One focus of this work was to use as much open-source software as possible to keep the barrier to the methods studied and the results obtained as low as possible. In the end, it turned out that all results shown in this thesis are computed with open-source software.

femm, an open-source simulation software, is a 2D finite element software with a special focus on magnetics written by D. MEEKER [21]. The software comes with a GUI and different scripting interfaces (e.g., Matlab, Lua 4.0). Femm includes a mesh generator, and the solver uses first-order triangular elements. A *BH*-curve can be provided for the material to solve the non-linear problem. Being only capable of 2D systems is a major restriction. A second downside can be seen, as the program is only compatible to run on Windows.

FEniCSx is a popular open-source software package for solving PDEs using finite element methods. It provides a flexible and efficient interface for defining and solving various types of PDEs, including linear and non-linear problems, time-dependent and steady-state problems, and problems defined on complex geometries. FEniCS includes a high-level Python interface for specifying the PDE problem and a C++ library for solving the resulting equations using finite element methods.

FEniCSx is a fork of FEniCS that aims to extend and improve upon the functionality of the original package. It includes several additional features, such as support for hybridized discontinuous Galerkin methods, high-order geometry representations, and enhanced parallelism. FEniCSx also includes a more user-friendly interface for defining and solving PDE problems, making it easier for users to get started with the package.

AMfe was developed at the Chair of Applied Mechanics (TUM) as a Python finite element software code that focuses on modularity, extensibility, and easy prototyping of new methods for research. The code basis was written by J RUTZMOSER to develop new hyperreduction methods where access to the assembly process was needed. Different hyperreduction methods, inter alia, Energy Conserving Sampling and Weighting (ECSW), were investigated for geometric non-linear structures.

AMfe provides a high-level interface for defining and solving structural mechanics problems, including linear and non-linear static and dynamic analysis, contact and friction problems, and geometrically non-linear analysis. AMfe includes several built-in element types, material models, and solvers, as well as support for parallel processing and visualization of results. Its flexible and modular design allows users to easily extend and customize the package for their specific needs.

As the focus of this framework is clearly set to structural dynamics, the effort was not taken to implement edge-element types for non-linear electromagnetism. Also, no basic preprocessor is included, which means additional effort to generate even simple proof-of-concept models.

NGSolve is an open-source, object-oriented finite element core library, written in C++ with a full Python API, which is inspired by the Python interface to *FEniCS*. Closely connected to NGSolve is the open-source automatic mesh generator *NETGEN*, which was started in 1994 by JOACHIM SCHÖBERL. NETGEN is capable of meshing 2- and 3D geometries provided by a Constructive Solid Geometry (CSG) or standard STL file format. NETGEN contains modules for mesh optimization and hierarchical mesh refinement. Curved elements of arbitrary order are also supported [62]. Both libraries are compiled into all three major operating systems

and are distributed via the conda package manager. This makes the framework very handy for teaching and collaboration in a university environment. The framework supports edge elements by nature. Additionally, the element matrices are derived automatically from the continuous weak formulation, which the user can specify in a symbolic manner. That allows the user to see the finite element process more or less transparent from the continuous physical description to the discretized model [60].

For solving non-linear problems, a Newton scheme is implemented in NGSolve. For each linear solution step, a sparse direct solver based on Cholesky factorization with symmetric pivoting is used. Under the hood, NGSolve uses the PARDISO solver as the default solver for sparse direct linear algebra computations. However, NGSolve also supports other sparse linear solvers, such as UMFPACK and MUMPS, which can be specified by the user.

Selected Framework Both the FEniCS and the NGSolve frameworks fulfill the needs for the work. The decision was made in favor of NGsolve, as it also brings geometry and mesh tools in the same framework. Additionally, it seems more compact and finally better tailored to the needs of this thesis.

Chapter 10

Academical Example

An academic electromagnetic system is introduced that serves as a minimal model to show the explained theory and phenomena. The system is inspired by solenoid valve systems and is already meant to be related to the application of active magnetic bearings shown in part III. The aim is to also apply the investigated model order reduction techniques on that example in part II to be able to keep track of each element manually to have the best insight possible. First, a system description is given, and then results for the magnetostatic solution followed by the transient time simulation are shown.

10.1 Electro Magnetic Computing Problems

For this thesis, we developed our own reference systems to demonstrate our methods. They are called *Electro Magnetic Computing Problems* in short *EMCP*. The shown systems try to mimic real-world magnetic actuators in a minimal way, maintaining the main characteristics such as dimensions, materials, and shape. The first of the developed problems is visualized in fig. 10.1 and will accompany us through the entire chapter as well as the first chapters of part II.

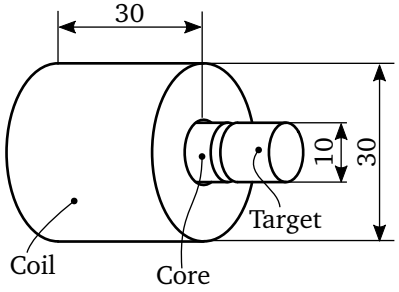

Figure 10.1: Geometry of the *Electro Magnetic Computing Problem 1* (EMCP1), inspired by solenoid actuators. All dimensions are given in mm.

The shown geometry will be used in 3D (named **EMCP1a**) and, further, two different 2D models corresponding to different cross sections will be considered, namely the transversal **EMCP1b** and the sagittal cross-section **EMCP1c**, see fig. 10.2. The system consists of three parts. A cylindrical core of (non-linear) steel is surrounded by a thin layer of air and a concentrical coil. In front of the core, a smaller cylinder (called a target) is placed. One advantage of the system is its axis symmetry or circular symmetry, respectively. That will reduce the complexity later for explaining the model order reduction techniques, as low mode numbers will represent the system's behavior very well.

The shown geometries (3D and the two 2D cuts) are modeled from primitives (i.e. arcs and lines) in Netgen and meshed with triangular elements using a Delaunay algorithm. The

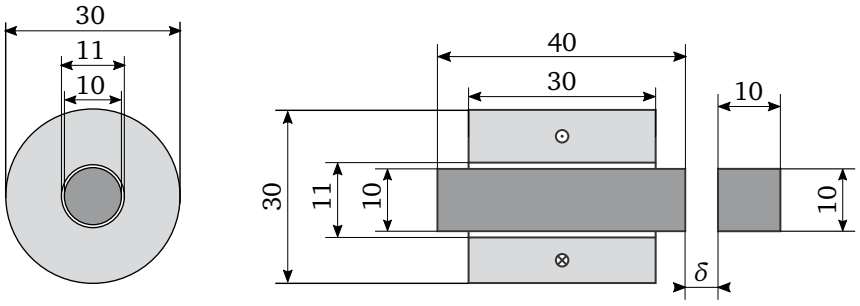

Figure 10.2: Cross sections of the EMPC1. Left: The transversal cut. Right: The sagittal cut.

resulting mesh is colorized in fig. 10.3 for the different materials. Light gray symbolizes air, orange is for the current carrying copper and blue is the (non-linear) core material. The pink part is made of the same material as the core but is the mobile target which the force is calculated for. Obviously, the transversal cut (EMPC1b) is missing the target, and a force calculation is not meaningful. The material used throughout the chapter is pure iron material

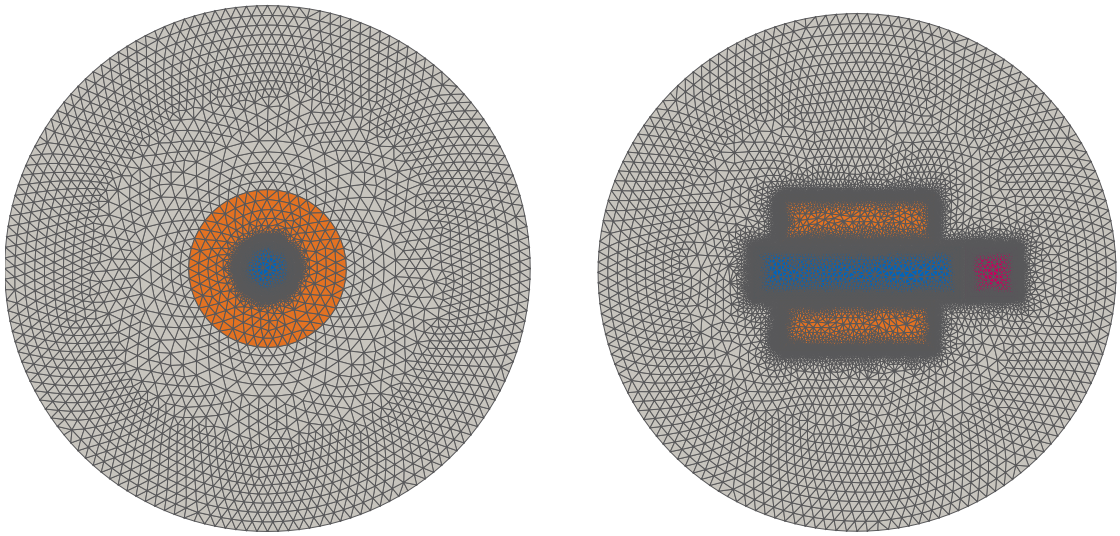

(a) EMCP-1b **(b)** EMCP-1c

Figure 10.3: Standard mesh topography for the EMCP1 example.

as it incorporates the saturation effect without irreversible effects for low magnetic fields. The conductivity is assumed to be constant and the source current in the coil is assumed to be given.

Remark

Note that for the 2D variant of the example, all quantities have to be considered as densities as the integrations are performed over 2D domains, which is of course not possible in the real world. For example, the forces (energies) are forces (energies) per length.

Remark

Using NETGEN to generate a 2D geometry and mesh, the minimal code is listed below. NETGEN defines the mesh size parameter h as the length of an element. This limit is not strictly adhered to. The default grading parameter is 0.3. The meshing algorithm is a Delaunay algorithm.

```
from netgen.geom2d import SplineGeometry

geo = SplineGeometry()
geo.AddRectangle(p1=(-1,-1),
p2=(1,1),
bc="rectangle",
leftdomain=1,
rightdomain=0)
geo.AddCircle(  c=(0,0),
r=0.5,
bc="circle",
leftdomain=2,
rightdomain=1)
geo.SetMaterial (1, "outer")
geo.SetMaterial (2, "inner")

geo.SetDomainMaxH(2, 0.02)
ngmesh = geo.GenerateMesh(maxh=0.1,grading=0.3)
```

Converting the NETGEN-mesh object into a NGSolve mesh:

```
from ngsolve import *
mesh = Mesh(ngmesh)
```

10.2 Magnetostatics

Starting with the magnetic field computation for static loads (i.e. currents), the effect of the regularization term and the saturation of the material can be demonstrated without blurring by dynamic effects.

10.2.1 Stationary Maxwell Equations

For *magnetostatics*, the equations boil down to a minimum set of only three necessary equations. The magnetic flux density and the displacement current density are constant. Therefore, the time derivatives vanish. The equations are now decoupled, and it is sufficient to only solve the magnetic equations:

$$\nabla \times \boldsymbol{H} = \boldsymbol{j} \tag{10.1}$$

$$\nabla \cdot \boldsymbol{B} = 0 \tag{10.2}$$

$$B = \mu(B)H \tag{10.3}$$

As the complete chapter for the academic example is conducted in 2D, the FEM formulation needs to be considered with the corresponding weak forms for 2D domains, which is discussed in detail in section 7.1.4.

10.2.2 Field Solution

For the transversal cross-section, the current density in the coil is of solenoidal structure in the x-y-plane. This leads to the general vector potential formulation, which is also valid in 3D, repeated here with the explicit notation of the use of the curl operator to highlight the difference to the grad-grad formulation. From a 3D perspective, this formulation assumes an infinite prismatic extension of the physics.

Find $\boldsymbol{A} \in \boldsymbol{H}^{\text{curl}}$, such that

$$\int_\Omega \frac{1}{\mu} (\text{curl}\boldsymbol{A}) \cdot (\text{curl}\boldsymbol{A}') + \kappa \boldsymbol{A} \cdot \boldsymbol{A}' \, \mathrm{d}\Omega = \int_\Omega \boldsymbol{j} \cdot \boldsymbol{A}' \, \mathrm{d}\Omega \qquad \forall \quad \boldsymbol{A}' \in \boldsymbol{H}^{\text{curl}}. \tag{10.4}$$

Remark

The function spaces are implemented in the FEM framework NGSolve on all common element shapes (trigs, quads, tets, ...). As a first step, a `finite element space` (fes) is defined on a mesh. Functions are then defined as children of the finite element space. The `GridFunction` (gfu) is the discrete representation of all degrees of freedom of the system.

```
1         fes = HCurl(mesh, order=2)
2         gfu = GridFunction(fes)
```

The function spaces know their canonical derivatives. These operations are efficiently implemented by transformation from the reference element.

The result for a static current density is shown in fig. 10.4b. Without scaling, this structure of the solution is true for every amplitude of the current density. As the B-field is a scalar field (i.e. the z-component of the curl of $\boldsymbol{A}$), it is visualized as a heatmap indicating the value of B. The core is a material with a relative permeability significantly higher than one, which results in the concentration of the magnetic flux density in the core. A discontinuous step of the magnetic flux density towards the coil and air domain (both $\mu_r = 1$) is possible due to the properties of the used edge-elements as described in section 7.2.3. The B-field vanishes towards the outer boundary. This fits with the set Dirichlet boundary condition for the vector potential $\boldsymbol{A}$, which is set to zero on the outer dofs (i.e. edges).

Regularization Term κ As already mentioned in section 5.5, the used magnetodynamic formulation with the modified vector potential is not a unique description of the system. This leads to the need for gauging, which is done here with a regularization term κ. The influence of κ is shown in fig. 10.5. As a local comparison value, the (scalar) B-field in the center of the core is chosen and plotted against the regularization term for different current densities. To also see the global influence, the magnetic energy is plotted in the same manner.

The smallest regularization that enabled all solutions to converge was found at $\kappa = 10^{-8}$. For increased values of κ, the $\boldsymbol{B}$-field as well as the magnetic energy, begin to drop considerably at around $\kappa = 10^{-4}$ depending on the load. A kappa too big led again to convergence problems. Finally, a $\kappa = 10^{-6}$ is chosen for all the following computations. This value shows sufficient stability in the calculation process, and the influence on the results seems negligible.

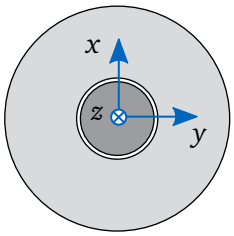

(a) EMCP-1b geometry with frame of reference

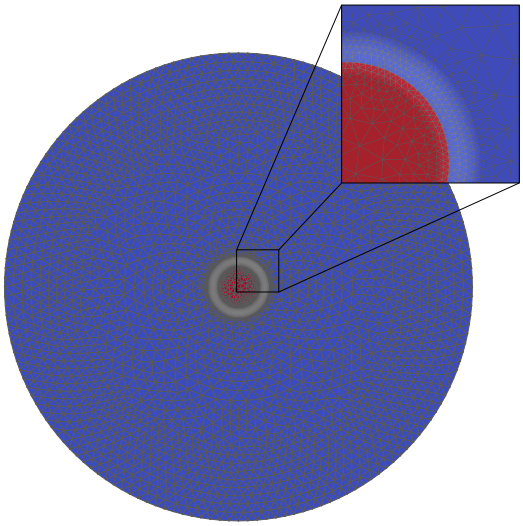

(b) B-field solution as scalar field

Figure 10.4: Static B-field solution for the EMCP-1b example. The field intensity is high (red) in the core and rapidly drops to almost zero (blue) in the non-ferromagnetic domain.

Remark

In NGSolve the steps are represented as follows. Note that the function for ν could be any derivable function:

```
1         from ngsolve import *
2
3         fes = HCurl(mesh, order=3, dirichlet="outer")
4         u,v = fes.TnT() #Trial and Testfunction
5
6         mu0 = 4*pi*1e-7
7         mur = { "steel" : 1000, "air" : 1, "coil" : 1 }
8         nu  = 1.0 / mu0 / mesh.MaterialCF(mur)
9
10        a  = BilinearForm(fes)
11        a += SymbolicBFI (nu*curl(u)*curl(v)+ kappa*u*v)
12
13        f  = LinearForm(fes)
14        f += SymbolicLFI(j*curl(v), definedon=mesh.Materials("coil"))
```

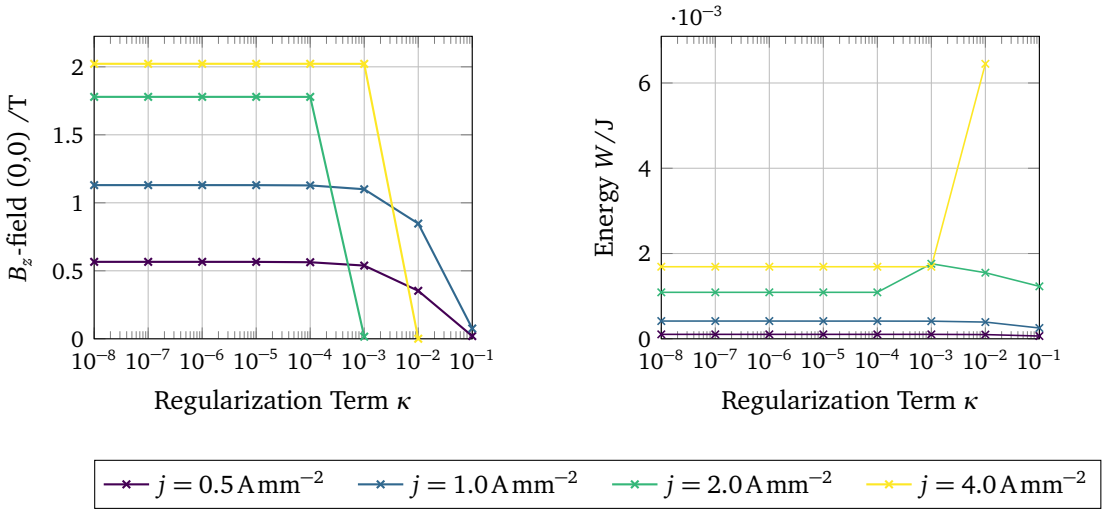

Figure 10.5: Influence of the regularization term to the B-field and the magnetic energy. Too big κ leads to a noticeable deterioration of the field result.

Mesh size The mesh size is mostly defined by the air gap between the core and the coil. The gap is only 0.5 mm wide and so the maximum element edge line is around that length. The general upper element size h for this model is varied between 0.5 mm and 2.0 mm. The grading parameter (see section 7.2.1) is varied from the default 0.3 to 5. In consequence, the numbers of total elements vary between roundabout 5000 to 20 000 elements. The results of the solution are extremely close together which allows the conclusion that the mesh is converged to a refinement that allows to compute accurate results for magnetostatic problems.

10.2.3 Force Calculation

To demonstrate the force calculation, the model of the sagittal cross-section of the EMCP1 (see fig. 10.6) needs to be considered. Although the geometry is axis-symmetric, the physics of the cross-section is assumed to be prismatically extended to infinity. The extension of the equations to compute revolute parts is not handled in this thesis because the following benchmark examples (TEAM10,13,20, chapter 11) and application examples (Active Magnetic Bearings, chapter 19) are either 3d or 2d prismatic. To avoid the need for all global quantities to be written as quantity per depth, the prismatic extension is set to a unity depth of 1 mm. The effect is that the load vector (alias the current density vector) becomes a scalar field (i.e. only the z-direction is not zero, $\boldsymbol{j} = \begin{pmatrix} 0 & 0 & j \end{pmatrix}^T$), leading to a scalar magnetostatic equation. This is solvable in the H^1 Space with well-known node elements. The curl operator

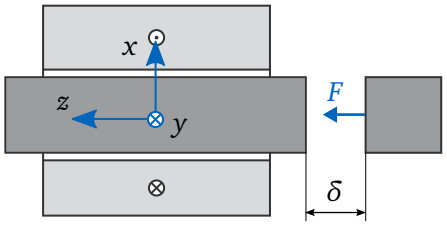

Figure 10.6: EMCP-1c geometry with frame of reference

changes to the gradient operator, which is explicitly written in the equation to highlight the difference to the curl-curl formulation. Find $\boldsymbol{A} \in H^1$, such that

$$\int_\Omega \frac{1}{\mu} (\operatorname{grad} \boldsymbol{A}) \cdot (\operatorname{grad} \boldsymbol{A}') \, \mathrm{d}\Omega = \int_\Omega \boldsymbol{j} \cdot \boldsymbol{A}' \, \mathrm{d}\Omega \qquad \forall \quad \boldsymbol{A}' \in H^1. \tag{10.5}$$

This formulation leads to the nice benefit that there is no regularization term needed. To reconstruct the $\boldsymbol{B}$-field from the z-direction of the vector potential, see section 7.1.4.

Remark

NGSolve provides the Jacobian matrix and implements the inverse and determinant:

```
from ngsolve import *

G = specialcf.JacobianMatrix(3)
G_inv = Inv(G) # --> same as fem.Inv
G_det = Det(G) # --> same as fem.Det
```

To find the change of the Jacobian, a finite difference is applied:

```
gfu_G = GridFunction(MatrixValued(L2(mesh)))
gfu_G.Set(G)
gfu_G_det = GridFunction(L2(mesh))
gfu_G_det.Set(G_det)

vdisplacement = CoefficientFunction((0,0,0.001))
gfu_struc = GridFunction(VectorH1(mesh))
gfu_struc.Set(vdisplacement, definedon=mesh.Materials('target'))
mesh.SetDeformation(gfu_struc)

gfu_G2 = GridFunction(MatrixValued(L2(mesh)))
gfu_G2.Set(G)
gfu_G2_det = GridFunction(L2(mesh))
gfu_G2_det.Set(G_det)

# Find |G|/ds and G/ds by finite differences
G_det_ds = (gfu_G2_det-gfu_G_det)/Norm(vdisplacement)
G_ds = (gfu_G2-gfu_G)/Norm(vdisplacement)
```

The force is finally computed for the undeformed configuration:

```
mesh.UnsetDeformation()
F_vw = Integrate(-nu*B*(G_ds*G_inv*B) + 0.5*nu*B*B*G_det_ds*
    G_det_inv, mesh=mesh, definedon=mesh.Materials('air'))
```

A generic static solution can then be drawn with so-called field lines (see fig. 10.7). The color indicates the value of the B-field at that position. The line follows the vectors of the magnetic flux density at each point. A kink in the lines is seen at the boundary of the ferromagnetic material and the surroundings. One can follow the field lines and find the source-free structure of the magnetic field. At the outer border, the field lines are parallel to the boundary. The magnetic vector potential is set to zero at these outer nodes.

Remark

Note that the continuous current density for real applications should not exceed $j = 10\,\mathrm{A\,mm^{-2}}$ as the thermal loading would increase to a level that is not permanently durable for the material. Due to the inefficient design of the EMCP example, much higher currents are necessary to show effects such as saturation of the core.

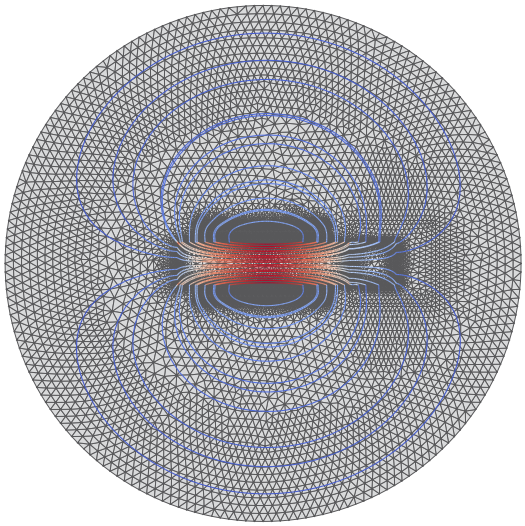

Figure 10.7: Static $\boldsymbol{B}$-field solution EMCP-1c example. The color of the field lines indicates the magnitude of the vector field where red is for high intensities and blue for low intensities.

Characteristic Force Map To characterize a magnetic actuator, it is of interest what force the actor can deliver at which position and which current. To show this in one graph, a 3D graph is drawn with the force plotted against the air gap between the core and the target and the current density in the coil. The air gap is varied from 0.1 mm to 3 mm in equidistant points, whereas the current steps form a geometric series:
$j = \left\{5.0\,\mathrm{A\,mm^{-2}}; 10\,\mathrm{A\,mm^{-2}}; 20\,\mathrm{A\,mm^{-2}}; 40\,\mathrm{A\,mm^{-2}}; 80\,\mathrm{A\,mm^{-2}}\right\}$
The resulting fig. 10.8 reveals two non-linear characteristics: The material saturation in the axis of current and the non-linear relation between position and force.

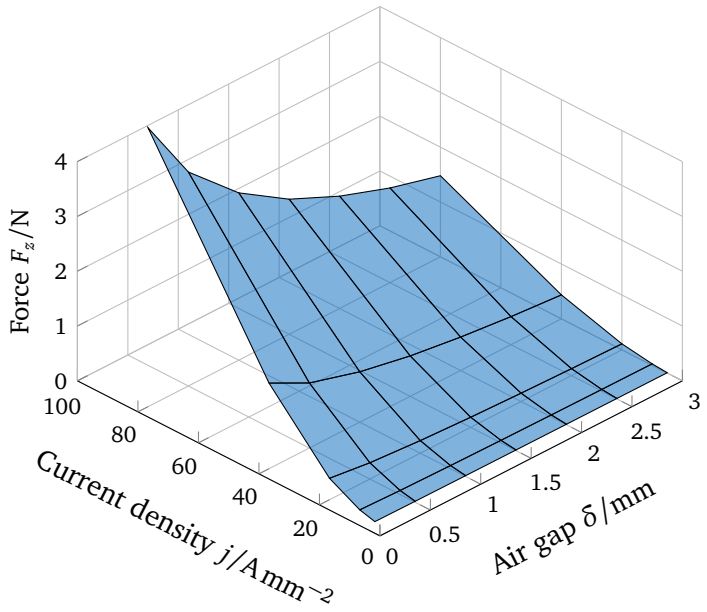

Figure 10.8: Static force in dependency of air gap δ and current density j. Smallest air gap is $\delta = 0.1\,\mathrm{mm}$.

10.3 Transient Solution

To include time-varying effects such as eddy currents, a current source that is mono-harmonic in time is applied. Since the material will enter the saturation region, the solution will not be mono-harmonic but will exhibit higher harmonics. Therefore, every simulation is treated as a *transient* simulation.

Mesh Density In the area of the skin effect, large gradients for the magnetic field and, therefore, strong eddy currents [25] are present. To capture these local effects properly, a fine FE-mesh is required. The element size h in the area of the skin effect should be small enough to fulfill the condition [46]:

$$\frac{\delta}{h} > 1.5 \tag{10.6}$$

Here δ is determined by eq. (10.7).

$$\delta = \frac{1}{\sqrt{\pi f \sigma \mu}} \tag{10.7}$$

If the material properties (μ, σ) and the frequency range (max frequency f) of the simulation are known in advance, eq. (10.6) can be taken into account in the mesh generation. Note that the required mesh fineness does not depend on the characteristic size of the problem. This is the driving reason for electrodynamic problems having many degrees of freedom, even for simple geometries.

Time Step Size Choosing the step size in the backward Euler method is a trade-off between accuracy, stability, and computational cost. Smaller step sizes can yield more accurate solutions but at the expense of higher computational costs, as each step requires solving a nonlinear equation, here using the Newton-Raphson method. Too big time steps lead to diverging in the Newton-Raphson iterations, as the time stepping matrix becomes badly conditioned. This is explained by the ratio between the conductivity, which makes the matrix non-singular and the magnetic stiffness matrix, which is non-unique as seen in section 5.5. As of this, no regularization term is needed in domains with conductivity. The time step size Δt describes the ratio between the two matrices in the stepping matrix. The stepping matrix is repeated here from section 8.3:

$$\boldsymbol{K}(\boldsymbol{u}_{n+1}^{i}) = \boldsymbol{M} + \Delta t \left.\frac{\partial \boldsymbol{g}}{\partial \boldsymbol{u}}\right|_{\boldsymbol{u}_{n+1}^{i}}$$

For the simulation shown here, the time step size was determined empirically to a value of $\Delta t = 0.001\,\mathrm{s}$.

10.3.1 2D Transversal Cross Section Model

The effects that occur due to the non-linear material and the therefore needed transient simulation are shown on that same example geometry fig. 10.9.

The results for a sine excitation of the current at 10 Hz are plotted in fig. 10.10. Four experiments are conducted where the amplitude of the current is doubled for each run. This allows us to comprehend the resulting quantities regarding their linearity. All transient time simulations are started from a state where all quantities are zero for t_0, so the transient response can be observed. Three different results are discussed in detail in the following paragraphs.

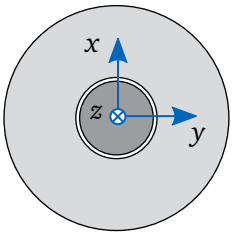

Figure 10.9: EMCP-1b geometry with frame of reference

B-field Time Series A very local way to look at the result is to look at the B-field at one point. Here, the center point of the geometry is chosen. As the load currents are in-plane, the B-field is a scalar field in z-direction. Investigating fig. 10.10, a large time delay is noticeable before the B value starts rising. This comes from the rising eddy currents that prevent the B-field from penetrating further to the center. As the energy of the eddy currents dissipates further and further through the electric resistance in the core, the B-field can penetrate the center. No big differences can be seen between the first and second periods. The transient oscillation for the center point is nearly at once in a steady state.

The second effect that can be drawn from fig. 10.10 is the saturation effect of the core material. The excitation amplitude of $1\,\mathrm{A\,mm^{-2}}$ is chosen such that the material is not saturated. A load of $5\,\mathrm{A\,mm^{-2}}$ leads to material parts where the material is well-saturated. This results in a flattened B-field.

Magnetic Energy In contrast to the local B-field observation, the magnetic energy is a global measure for the system. After a small transient process, the system is in a steady state. The magnetic energy shows double the peaks because, as a quadratic measure, there is no discrimination between the positive and negative direction of the magnetic field. The saturation becomes visible when comparing the higher excitation amplitudes. A doubling of the amplitude does not lead to a doubling of the magnetic energy.

Power Loss A second global characteristic measurement of the system can be evaluated using the time series of the power loss in fig. 10.10. It is obvious that the system is not immediately at a steady state as the time integration started with a zero solution. At very low frequencies, the phase is shifted by $\frac{\pi}{2}$ in relation to the excitation. This can be explained by looking at the equation eq. (3.29), which shows a 90° phase shift. Since power is related to the square of the output, the phase shift is doubled. Assuming a highly predominant sine share, the phase shift is around π as expected from theory. In fig. 10.10 one can see that the power loss peaks alternate with those of the magnetic energy but are slightly shifted to the right for higher amplitudes. The magnetic field generated by the eddy current strengthens, and there is noticeable feedback between the electrical and magnetic fields. This causes an additional phase shift of the eddy current power.

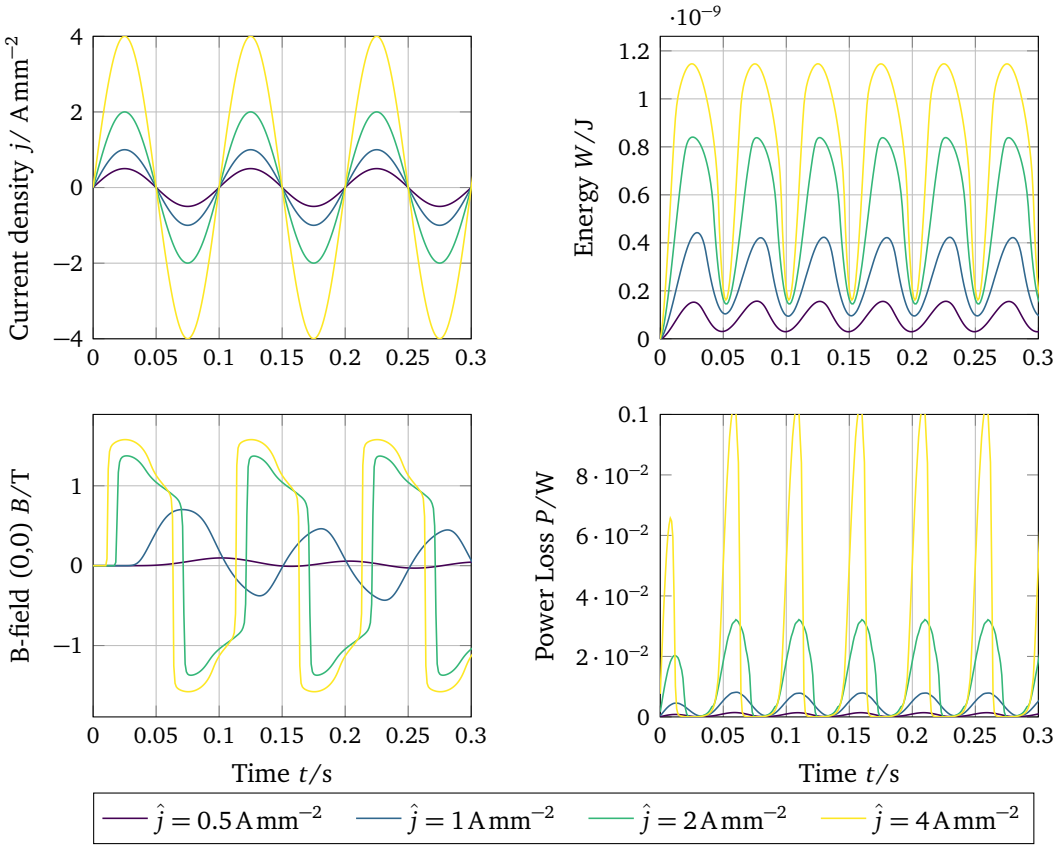

Figure 10.10: Response of the magnetic field to a sinusoidal excitation in the origin of the geometry. The nonlinear effects become pronounced for higher amplitudes of the excitation. A doubling of the excitation does not double either the magnetic energy and even less the magnetic flux density.

10.3.2 2D Sagittal Cross Section Model

Changing the geometry to the sagittal cross-section allows us to compute forces. Due to the eddy currents, the forces become a frequency-dependent quantity.

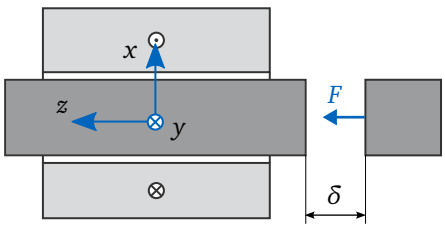

Figure 10.11: EMCP-1c Geometry as an example.

Skin Effect Skin effect describes the phenomenon of alternating current being distributed in such a way that the current density is greatest near the surface of an electrically conductive material, such as a metal, and decreases exponentially with greater depth within the material. This occurs when the material is subjected to an alternating or varying magnetic field. With increasing frequency, the current displacement towards the surface of the body becomes more and more pronounced. As the mesh size is limited, the frequency of the transient simulation is

also limited. The results can be interpreted meaningfully only for the low range of frequency excitation.

Table 10.1: Skin effect depth $\delta(f)$ for iron ($\sigma = 10^7\,\mathrm{S\,m^{-1}}$ and $\mu = 10\,000 \cdot \mu_0$).

f	$\delta(f)$
0.1 Hz	5.0 mm
1 Hz	1.6 mm
10 Hz	0.5 mm
100 Hz	0.2 mm

A meshsize of $h = 0.3\,\mathrm{mm}$ at the core boundary layer allows statements up to $f = 10\,\mathrm{Hz}$. The plot for 50 Hz is colored gray, as this would demand a higher mesh density which would have increased the computational effort a lot. The validity limit of the discretized model in the result can be seen in the drop of eddy currents at a depth of around $d = 2\,\mathrm{mm}$, which should be much closer to the core's surface. As with increasing frequency, the eddy currents have wave-like dynamics going from the outside to the inside of the core. It is difficult to graph the results in a static plot. Therefore, the maximum amplitude of the eddy current over one cycle is plotted in fig. 10.12.

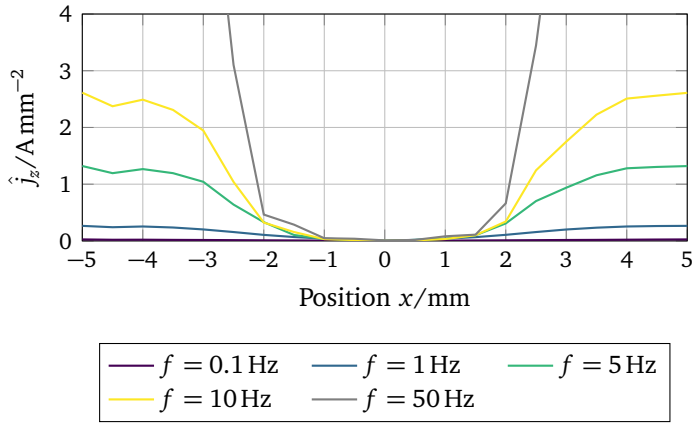

Figure 10.12: The skin effect for different frequencies shows the concentration of the eddy currents towards the core's boundary while the intensity of the eddy current increases.

10.3.3 Full 3D Model

For the consideration of forces, the full 3D model is applied. The integration of the global quantities now leads to real forces, not force per area. The geometry is embedded in a sphere of air with 50 mm radius. The meshing process results in a system with 33 910 elements and 40 159 total dofs. A static solution is demonstrated in fig. 10.13b. The blue color indicates a low magnitude of the $\boldsymbol{B}$-field in the air.

Power Loss With the increase of the frequency, also the power loss due to the thermal dissipation of the eddy currents increases. The relation is difficult to forecast. MEUNIER claims that the power loss increases linearly with the frequency, which could not be found in our simulations. An exemplary power loss versus frequency plot is shown in fig. 10.14. Note the log-log scaling of the plot. For the recognizable increase of the power loss, the main issue

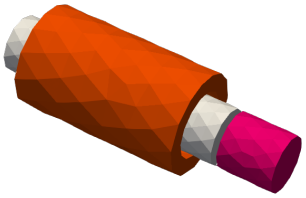

(a) Meshed system.

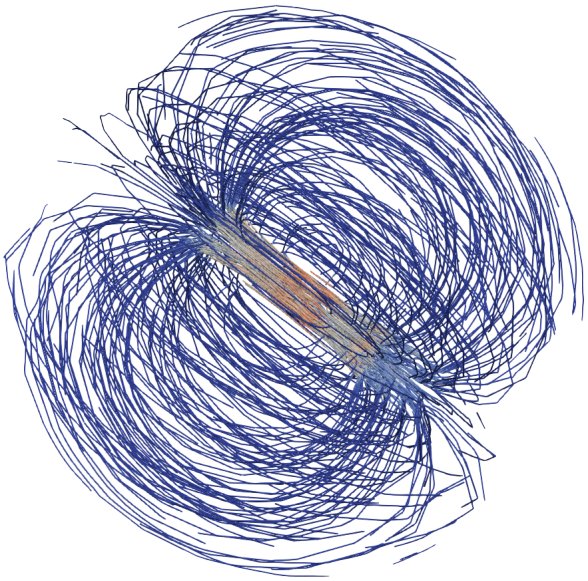

(b) Field lines of the B-field.

Figure 10.13: Static $\boldsymbol{B}$-field solution for the 3D EMCP-1a example. The air elements are invisible, and the elements of the core and target are shaded in a slight gray tone. The color of the field lines indicates the magnitude of the vector field where red is for high intensities and blue for low intensities.

could be the mesh size which is not appropriate for higher frequencies. MEUNIER [46] claims that the eddy current power loss approximates the true value for increasing mesh density asymptotically.

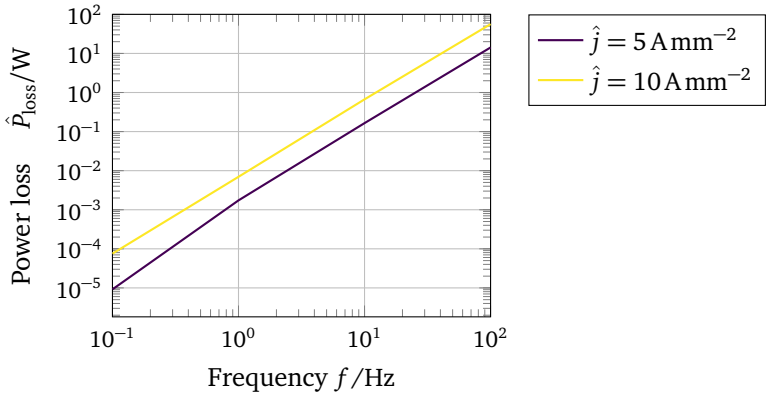

Figure 10.14: Power loss influence of the frequency in a log-log visualization.

Dynamic Force Finally, the dependency of the mechanical force on the excitation frequency is investigated. Due to the eddy currents, the magnetic field is weakened, which leads to a decrease in the mechanical force. Also, a phase shift is expected, as the eddy current dampens the magnetic field reaction and the force is directly connected with the magnetic flux density. For four different frequencies, fig. 10.15 shows the magnetic flux density in the center of the air gap and the following mechanical force. To plot different frequency results into one plot,

the results are plotted over the sinusoidal excitation phase. Note that the results for 1000 Hz must be seen as a rough estimate because of the inappropriate mesh size.

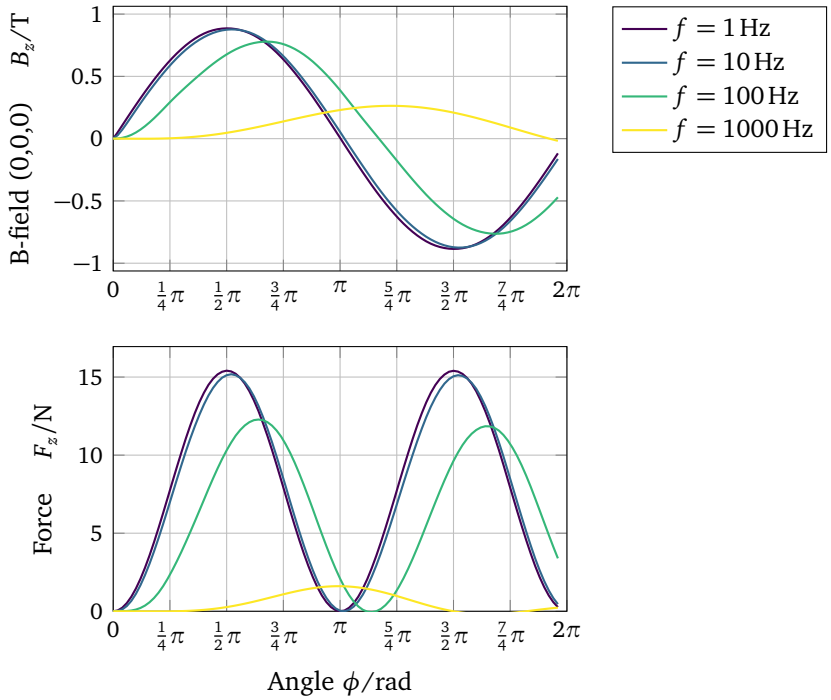

Figure 10.15: Magnetic flux density and mechanical force influenced by the excitation frequency. Higher frequencies lead to higher power losses, which decreases the force amplitude and shifts the phase.

A visualization of the magnitude drop of the force in fig. 10.16 is achieved by taking the quotient of the force's peak value related to the static force.

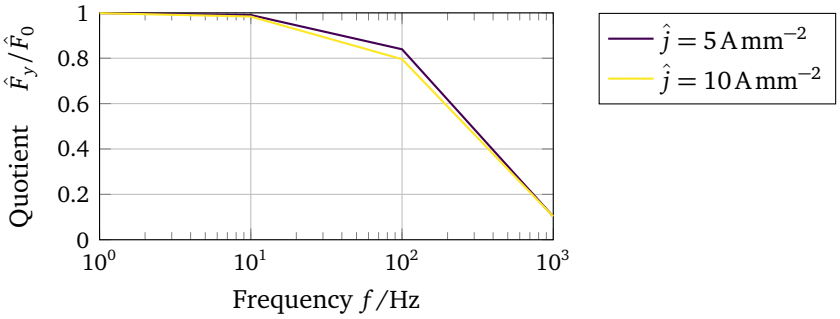

Figure 10.16: Force quotient influence of the frequency.

Chapter 11

Benchmark Example

In 1976 the conference series *Compumag* was born. The main goal is to discuss the broad topic of numerical computation of electromagnetic fields [69]. In 1985 the suggestion for the compilation of different benchmark systems for *Testing of Electromagnetic Analysis Methods* (TEAM) was formulated. Over the years, several workshops were organized with growing interest. The TEAM problems are very specialized and cover mostly one specific computational challenge. In 1990 TURNER states that some of the problems were considered to be solved over time, and others still need attention [72].

To conclude part I, three examples (TEAM10, TEAM13, TEAM20) are presented, which aim to prove the code's implementation of non-linear magnetostatic and -dynamic physics in comparison with the official reference measurements. The detailed information and the original measurement values can be found in [47, 48, 67]. All examples are very related, especially TEAM10 and TEAM13, which share the same material law and geometry.

11.1 Material Parameters

The non-linear BH-curve of the steel is given in a tabular form which is plotted in fig. 11.1. The differential permeability is plotted next to it. For the following investigations, the energy-based formulation is used. Therefore, a basis spline interpolation of the material data points with order two is performed to obtain a continuous function that is integrable in order to find the energy density. The conductivity is given as a constant $\sigma = 7.505 \times 10^6\,\mathrm{S\,m^{-1}}$ neither depending on the magnetic flux density nor the current density.

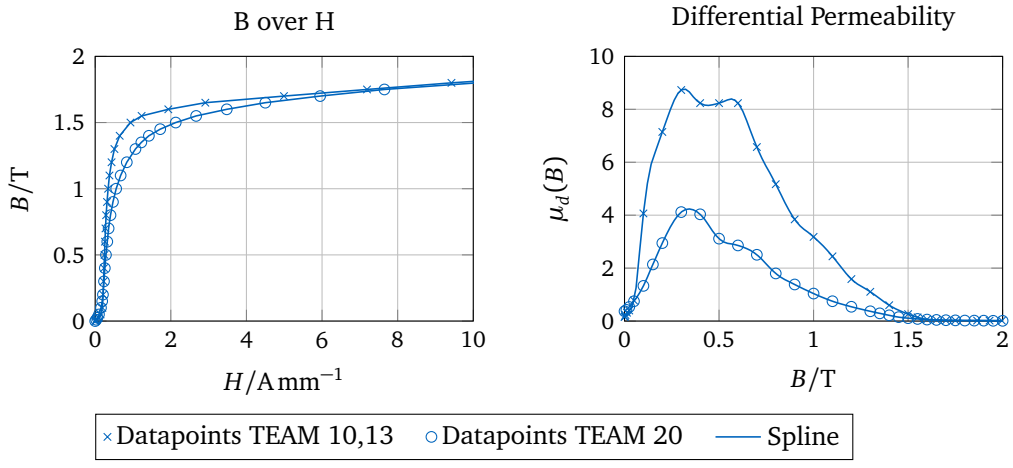

Figure 11.1: Official material parameters compared with their associated spline functions.

11.2 TEAM13 - Non-linear Magnetostatic

The TEAM13 problem features three thin steel plates around a central coil. The coil forms a quadratic shape with rounded corners. In the center of the coil, a thin sheet metal strip is placed. Two C-shaped sheet metal parts of the same material as the center plate embrace the coil and leave a small air gap to the center plate. The two C-braces are not aligned but build a point-symmetric system. Details and dimensions can be seen in fig. 11.2.

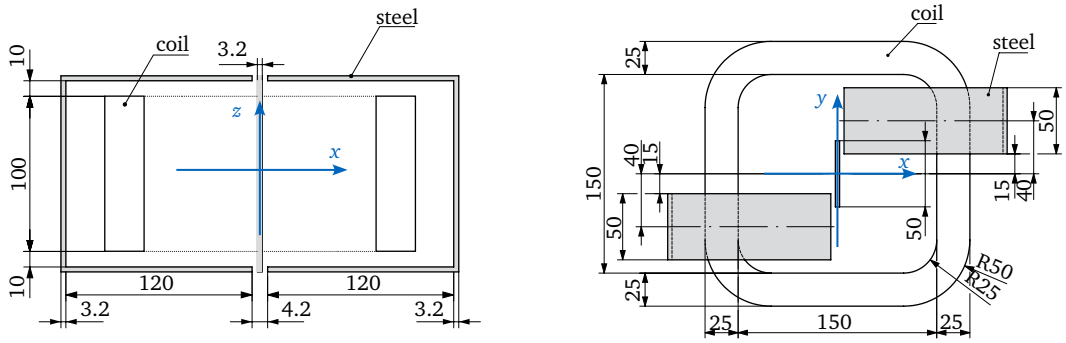

(a) Front view

(b) Plan view

Figure 11.2: TEAM13 technical drawings (not drawn to scale to improve readability).

The TEAM examples are modeled in Netgen using geometric primitives and are then meshed with a Delaunay algorithm. The system is embedded in a cube of air elements. The mesh of the thin plates is visualized in fig. 11.3. Note that the air elements are switched to invisibility to clearly view the system's inside.

To perform a static analysis of the magnetic field, the coil is excited by a set of DC-currents with a resulting applied magnetomotive force of 1000 AT and 3000 AT, respectively. With a cross section of 2500 mm^2 this results in the current densities of $j = 0.4\,\mathrm{A\,mm^{-2}}$ and $j = 1.2\,\mathrm{A\,mm^{-2}}$. The magnitude of the magnetic flux density is color-coded in fig. 11.3b. The points to highlight in the result are the regions where the central plate and the C-braces are in close vicinity. This leads to an increased magnitude of the $\boldsymbol{B}$-field.

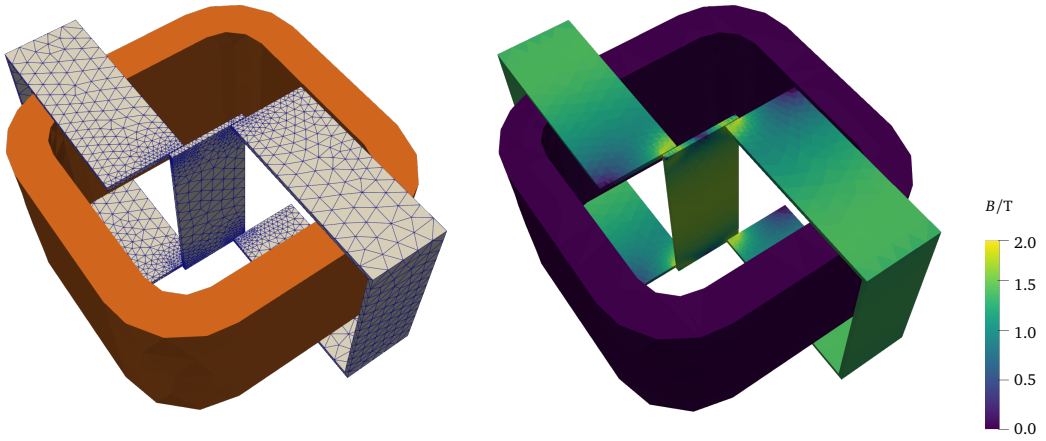

(a) Visualized mesh of the steel parts.

(b) $|\boldsymbol{B}|$-field solution for 3000 AT load.

Figure 11.3: TEAM13 mesh size and static magnetic field plot. The embedding air elements are switched off to see the elements of the structure. The wireframe of the coil's elements is invisible.

Regularization As developed for the EMCP example in section 10.2.2, the regularization term κ is set to $\kappa = 10^{-6}$.

Remark

In NGSolve the steps are represented as the following minimal code. Utilizing the non-linear energy density $w(\boldsymbol{B})$ on the steel material and the curl-curl weak form on the non-steel material:

```
from ngsolve import *

fes = HCurl(mesh, order=3, dirichlet="outer")
u,v = fes.TnT() #Trial and Testfunction

mu0 = 4*pi*1e-7
kappa = 1e-6

hb_curve = BSpline(2,B_datasheet,H_datasheet)
energy_dens = hb_curve.Integrate()

sysE  = BilinearForm(fes)
sysE += SymbolicEnergy(energy_dens(Norm(curl(u)), definedon=mesh.
    Materials("steel"))
sysE += SymbolicBFI(1/mu0*curl(u)*curl(v)+kappa*u*v, definedon=~mesh.
    Materials("steel") )

f  = LinearForm(fes)
f += SymbolicLFI(j*curl(v), definedon=mesh.Materials("coil"))
```

Simulation Results To check the simulated results, the International Compumag Society provides measured magnetic flux densities along various points in the steel plates and the air gap. The measurements and simulation results are combined in fig. 11.4 for both excitation currents. Compared to the computed results by former research teams, which are

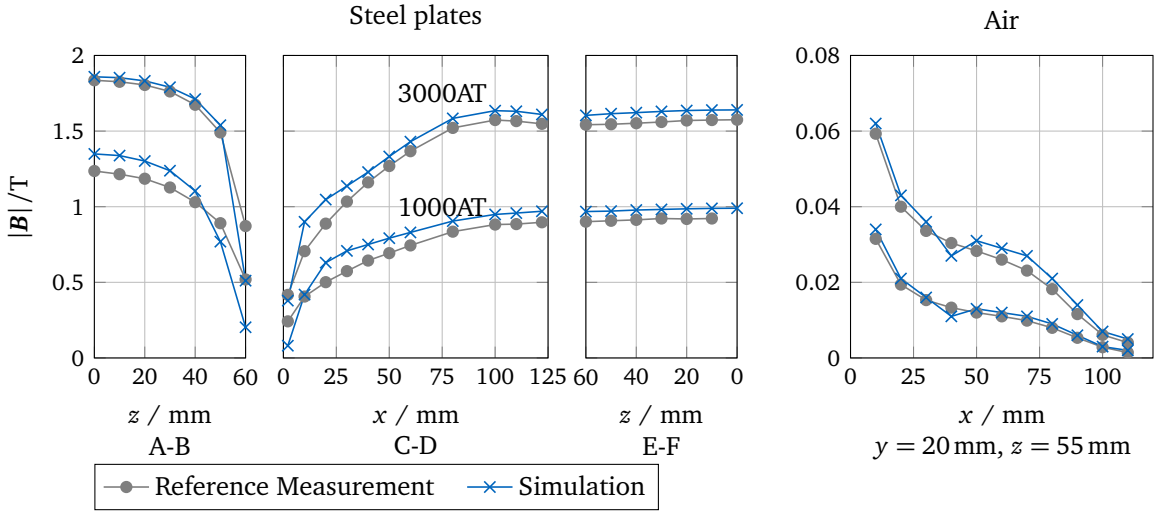

Figure 11.4: Comparison of the benchmark reference measurements and the simulation B-field solution in the steel plates and air, using fe-order=2 and the original material description.

summarized in [47], our results show a very good agreement with the official measurement values. As no convergence issues arose, the conclusion was drawn that the given simulation approach could be used further without modifications.

11.3 TEAM10 - Eddy Currents

The TEAM10 benchmark example is historically the predecessor of TEAM13 but is brought here in second place as it needs a more sophisticated simulation. The benchmark problem is a non-linear transient eddy current problem where the magnetic flux- and eddy current densities are analyzed and compared with experimental results obtained by [48].

The geometry is similar to the TEAM13 problem except that the two steel braces are arranged symmetrically, refer to fig. 11.5.

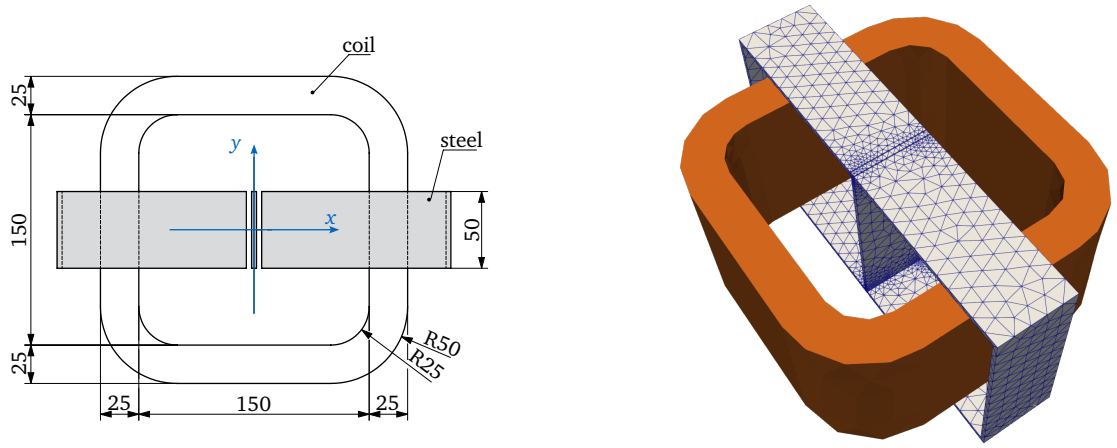

(a) Geometry of TEAM10.

(b) Visualized mesh size for TEAM10.

Figure 11.5: TEAM10 geometry and mesh density.

Excitation The excitation function, i.e., the time trajectory of the current, forms a smooth step using the exponential function.

$$I = \begin{cases} 0 & (t < 0) \\ I_m(1 - e^{-\frac{t}{\tau}}) & (t \geq 0) \end{cases} \qquad (11.1)$$

$$I_m = 5.64\,\mathrm{A}$$
$$\tau = 0.05\,\mathrm{s}$$

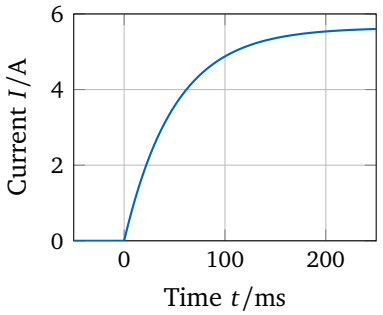

The parameters are chosen such that "the steel parts can be sufficiently saturated" and "the eddy current density is not small, and yet the eddy current in the coil can be neglected", [48].

Regularization Following the theory of modified vector potential, the non-conductive domains lead to a non-unique governing set of equations. This singularity is overcome by a small regularization term that is added to the equation like a very small mass matrix, i.e., a very small conductivity in the order of $1\,\mathrm{S\,m^{-1}}$.

Evaluation Points The evaluation of the magnetic flux density follows the experimental possibilities of the test setup. The average flux densities were measured by a so-called search coil, i.e., one turn of wire precisely around the surface of the steel plates. The magnetic flux density is therefore an average value. In the simulation, an average was computed for 20

virtual measurement points distributed evenly in the cross-section as given from [48]. Three cross sections S1, S2, S3 are defined. A plane, defined by $z = 0$, results in S1 by intersection with the center plate. S3 by intersection with the C-brace. S2 is defined by the intersection of the C-brace with a plane $x = 41.8\,\mathrm{mm}$. The same averaging cross sections are used for the eddy current evaluation.

Simulation Results The time integration results for the given excitation are shown in fig. 11.6. The official benchmark measurements of their physical test setup are given for the three measurement points S1, S2, S3. The simulation was conducted with a finite element order of two, and two different time step widths $t = \{0.002\,\mathrm{s}, 0.005\,\mathrm{s}\}$. The magnetic

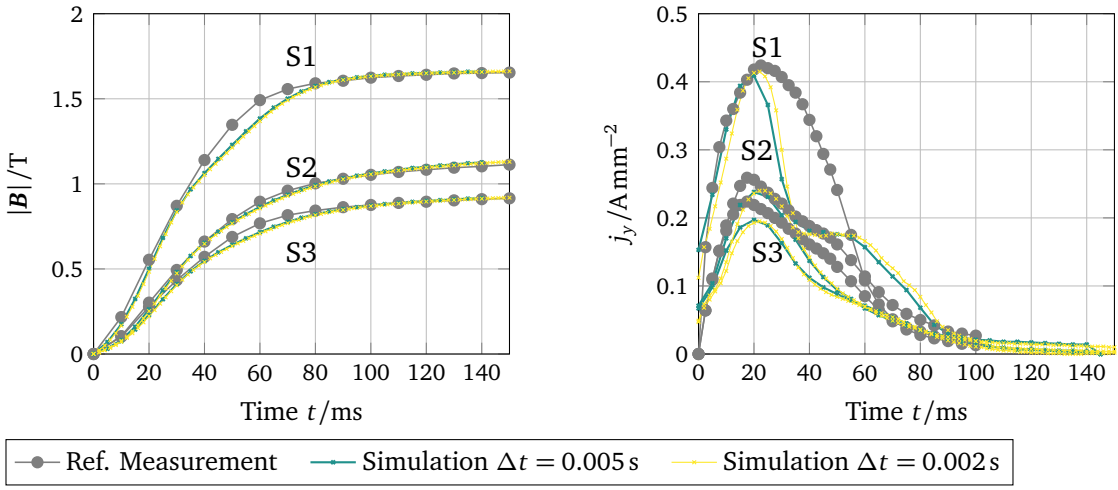

Figure 11.6: TEAM10 time solution for the B-field and the eddy currents compared to the official measurements.

flux density shows a good coincidence with the reference. No difference is seen for the two-time step sizes. Although the result for the eddy currents matches the reference well in the first time steps, deviations around $t = 50\,\mathrm{ms}$ are obvious. Further investigation showed that a finer mesh would be necessary to fully represent the eddy current distribution. As this would increase the model size and computational times significantly, it was not considered here, and a timestep of $t = 0.005\,\mathrm{ms}$ was selected.

In fig. 11.7, the current densities at three consequent time steps are shown. The current density in the exciting coil increases following the load trajectory. On the other hand, the induced eddy current in the middle steel plates decreases as the rate of change of the load decreases with time.

In conclusion, the shown formulation, in combination with the implementation, can prove their validity and therefore form a sufficient basis to work with.

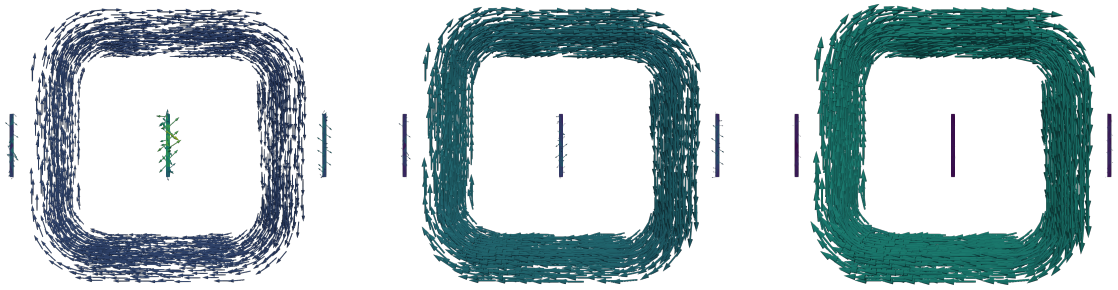

(a) $t = 25\,\mathrm{ms}$ **(b)** $t = 50\,\mathrm{ms}$ **(c)** $t = 75\,\mathrm{ms}$

Figure 11.7: TEAM10 eddy current snapshots at three consecutive time steps. The applied current in the coil increases with a steep slope in the beginning and is then flattened. As a consequence, the eddy currents in the steel sheet cross-sections decay over time.

11.4 TEAM20 - Static Force

The 3D geometry for the TEAM20 example is clearly more different from the previous examples, although it still shares the common structure. The geometry is defined as seen in fig. 11.8. It consists of three parts. A ferromagnetic yoke structure embraces a copper coil. Inside the coil, a cuboid of the same ferromagnetic material as the yoke is mounted to be freely movable in the vertical direction. For a current, reluctance forces emerge that tend to draw the free body in. The solids and the surrounding air are meshed with in total 65 740

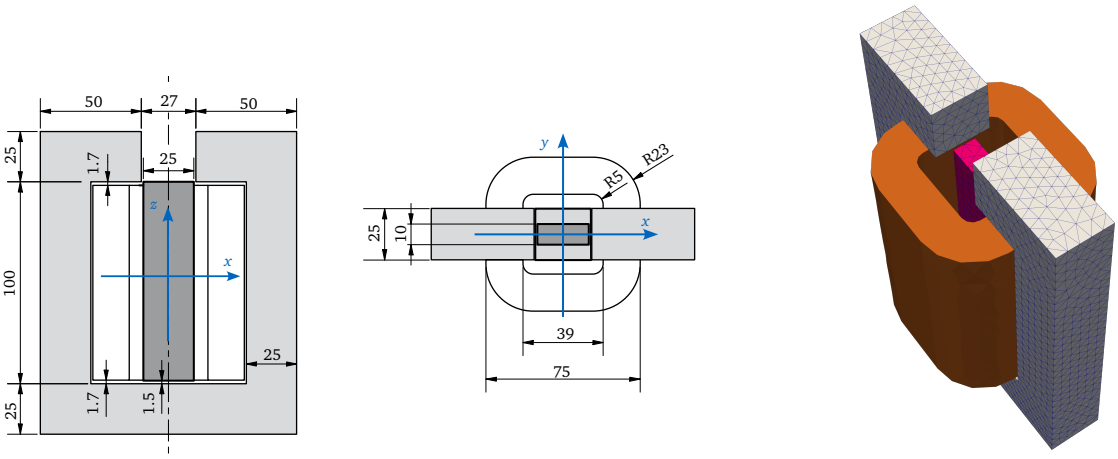

(a) Sideview **(b)** Planview **(c)** Mesh

Figure 11.8: TEAM20 geometry and mesh.

tetrahedral elements, cf fig. 11.8c. A finite element order (fe-order) 1 leads to 76 564 dofs, fe-order 2 results in 338 984 dofs.

Evaluation Points The simulation values are evaluated using two local points and two cross-section areas. The benchmark is also evaluated both in simulation and experiment at point P_1, as well as the lines α-β and γ-δ [47], see fig. 11.9. Point P_j is introduced to measure the eddy current values that counteract the coil's driving current.

Simulation Results For the static reference, the coil is excited by DC-currents with a resulting applied magnetomotive force between 1000 AT and 5000 AT. With a cross section of

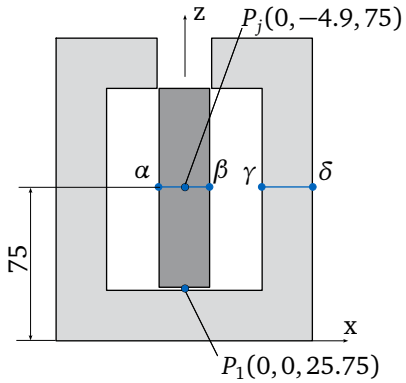

Figure 11.9: Evaluation points. P_1 and P_j evaluate the field quantity $\boldsymbol{B}$ and $\boldsymbol{j}_{\text{eddy}}$. An average is built over the cross-section area defined by the lines α-β and γ-δ.

$1738.8\times10^{-6}\,\text{m}^2$ this results in the current densities of $j = 0.575\,\text{A}\,\text{mm}^{-2}$ and $j = 2.876\,\text{A}\,\text{mm}^{-2}$ respectively.

The magnetic field at the point P_1 and the averaged magnetic field along two lines $\alpha-\beta$ and $\gamma-\delta$ as well as the force of the plunger in z-direction (cf. fig. 11.10) coincide well with the measurement from the official results, summarized in [67]. Also, the force calculation using the local Jacobian method is very close to the measured values. In conclusion, the

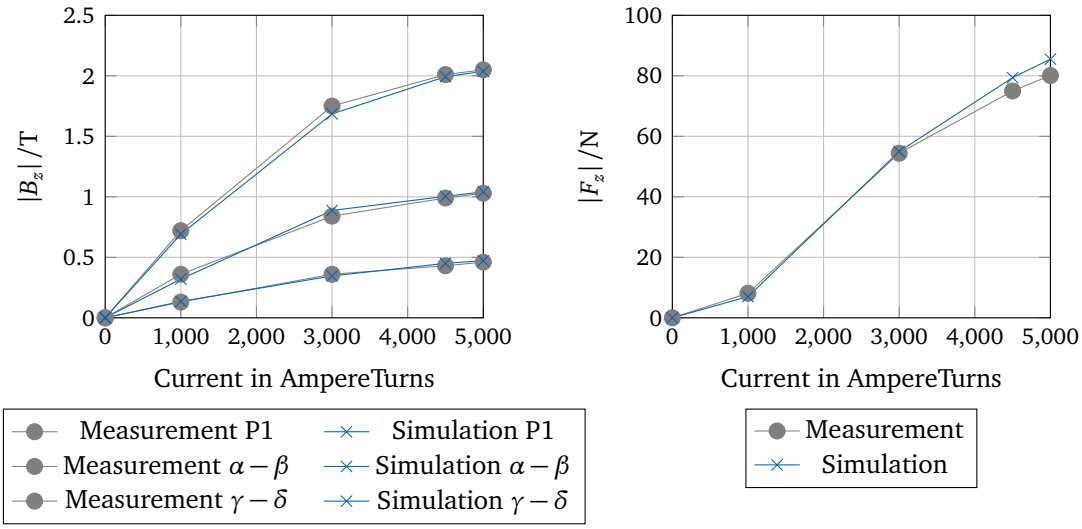

Figure 11.10: TEAM20 solution for the B-field and forces compared to the official measurements.

established setup of the code framework not only efficiently serves the current state-of-the-art needs but also presents a robust foundation to proceed with method development in the field of model order reduction.

Chapter 12

Summary of Part I

The first part of the thesis gave an introduction to the physics of electromagnetic fields with a clear focus on the magnetic field. From Maxwell's equations and their interpretation, the assumptions for low-frequency magnetic fields were woven in. Discussing different formulations, the modified vector potential formulation for magnetodynamic systems was derived. Continuing with the basic aspects of the numerical field computation, a general introduction to the application of the finite element method with edge elements that fit the needs for the vector potential formulation was given. Finally, the solution framework is presented for solving static and time-transient problems using the backward Euler and Newton-Raphson schemes.

Different software frameworks are shortly presented, and the open-source software package NGSolve in combination with Python, was chosen to perform all subsequent calculations.

To demonstrate the discussed effects, a minimal academic model was introduced. The system is inspired by solenoid actuators and is mainly considered in 2D cross sections, which allows the visualization of each element conveniently. This allowed us to demonstrate the theoretically discussed effects and some insights into the art of setting up a successful simulation of arbitrary magnetodynamic systems. This includes parameters such as the mesh density, the regularization term, and an appropriate time step size.

The three benchmark examples (TEAM10,13,20) from the International Compumag Society were described and used to prove a correct basic setup, as the official result could be matched. A valid and trustworthy full-order simulation is the basis for proceeding with method development for model order reduction.

References

[1] Achilles, M. “Hans Christian Oersted und der elektromagnetische Grundversuch”. In: *Historische Versuche der Physik*. Springer Berlin Heidelberg, 1989, pp. 52–58. DOI: 10.1007/978-3-642-46683-0_9.

[2] Ahagon, A., Kameari, A., Ebrahimi, H., Fujiwara, K., and Takahashi, Y. “New Type of Second-Order Tetrahedral Edge Elements by Reducing Edge Variables for Quasi-Static Field Analysis”. In: 54.3 (Mar. 2018), pp. 1–4. DOI: 10.1109/tmag.2017.2749444.

[3] Ancelle, B., Coulomb, J., Masse, P., Meunier, G., and Sabonnadiere, J. “Computer methods for electrical and magnetic devices designed by field analysis”. In: *IEEE Transactions on Magnetics* 15.6 (Nov. 1979), pp. 1671–1673. DOI: 10.1109/tmag.1979.1060408.

[4] Barrett, R., Berry, M., Chan, T. F., Demmel, J., Donato, J., Dongarra, J., Eijkhout, V., Pozo, R., Romine, C., and Vorst, H. van der. *Templates for the Solution of Linear Systems: Building Blocks for Iterative Methods*. Society for Industrial and Applied Mathematics, Jan. 1994. DOI: 10.1137/1.9781611971538.

[5] Biro, O. and Preis, K. “On the use of the magnetic vector potential in the finite-element analysis of three-dimensional eddy currents”. In: *IEEE Transactions on Magnetics* 25.4 (July 1989), pp. 3145–3159. ISSN: 1941-0069. DOI: 10.1109/20.34388.

[6] Biro, O., Preis, K., Renhart, W., Vrisk, G., and Richter, K. “Computation of 3-D current driven skin effect problems using a current vector potential”. In: *IEEE Transactions on Magnetics* 29.2 (Mar. 1993), pp. 1325–1328. DOI: 10.1109/20.250642.

[7] Bíró, O., Preis, K., and C., P. *The use of a reduced vector potential A_r formulation for the calculation of iron induced field errors*. en. 1999. DOI: 10.5170/CERN-1999-001.31.

[8] Bró, O. “Edge element formulations of eddy current problems”. In: *Computer methods in applied mechanics and engineering* 169.3-4 (1999), pp. 391–405. DOI: 10.1016/S0045-7825(98)00165-0.

[9] Books, M. H. *A Dictionary of scientists.* Oxford University Press, 1999, p. 586. ISBN: 0585110476.

[10] Bossavit, A. “A rationale for ’edge-elements’ in 3-D fields computations”. In: 24.1 (1988), pp. 74–79. DOI: 10.1109/20.43860.

[11] Bossavit, A. “Two Dual Formulations of the 3-D Eddy-Currents Problem”. In: *COMPEL - The international journal for computation and mathematics in electrical and electronic engineering* 4.2 (Feb. 1985), pp. 103–116. DOI: 10.1108/eb010005.

[12] Bossavit, A. *Computational electromagnetism. variational formulations, complementarity, edge elements*. Academic Press, 1998, p. 352. ISBN: 0121187101.

[13] Bossavit, A. “Virtual power principle and Maxwell’s tensor: which comes first?” In: *COMPEL - The international journal for computation and mathematics in electrical and electronic engineering* 30.6 (Nov. 2011). Ed. by Bró, O., pp. 1804–1814. DOI: 10.1108/03321641111168110.

[14] Buckley, O. E. “A tribute to Oliver Heaviside”. In: *Electrical Engineering* 69.7 (July 1950), pp. 587–587. DOI: 10.1109/ee.1950.6433948.

[15] Calkins, F. T., Flatau, A. B., and Dapino, M. J. “Overview of Magnetostrictive Sensor Technology”. In: *Journal of Intelligent Material Systems and Structures* 18.10 (Oct. 2007), pp. 1057–1066. DOI: 10.1177/1045389x06072358.

[16] Cheney, W. L. “Preparation and properties of pure Iron alloys: II. Magnetic properties of iron-carbon alloys as affected by heat treatment and carbon content”. In: *Scientific Papers of the Bureau of Standards* 18 (July 1922), p. 609. DOI: 10.6028/nbsscipaper.137.

[17] Clough, R. W. “Original formulation of the finite element method”. In: 7.2 (Nov. 1990), pp. 89–101. DOI: 10.1016/0168-874x(90)90001-u.

[18] Clough, R. W. “The finite element method in plane stress analysis”. In: *2nd A.S.C.E. Conf. on Electronic Computation* 2 (Sept. 1960).

[19] Coulomb, J. “A methodology for the determination of global electromechanical quantities from a finite element analysis and its application to the evaluation of magnetic forces, torques and stiffness”. In: *IEEE Transactions on Magnetics* 19.6 (Nov. 1983), pp. 2514–2519. DOI: 10.1109/tmag.1983.1062812.

[20] Coulomb, J. and Meunier, G. “Finite element implementation of virtual work principle for magnetic or electric force and torque computation”. In: 20.5 (Sept. 1984), pp. 1894–1896. DOI: 10.1109/tmag.1984.1063232.

[21] D.C. Meeker. *Finite Element Method Magnetics*. Version 4.2. Jan. 16, 2016. URL: https://femm.info.

[22] Dapino, M. J. *Magnetostrictive Materials*. July 2002. DOI: 10.1002/0471216275.esm051.

[23] Davis, T. A. *Direct Methods for Sparse Linear Systems*. Society for Industrial and Applied Mathematics, Jan. 2006. DOI: 10.1137/1.9780898718881.

[24] Davis, T. A., Rajamanickam, S., and Sid-Lakhdar, W. M. “A survey of direct methods for sparse linear systems”. In: *Acta Numerica* 25 (May 2016), pp. 383–566. DOI: 10.1017/s0962492916000076.

[25] Dular, P., Sabariego, R. V., Gyselinck, J., and Krähenbühl, L. “Sub-domain finite element method for efficiently considering strong skin and proximity effects”. In: *COMPEL-The international journal for computation and mathematics in electrical and electronic engineering* 26.4 (2007), pp. 974–985. DOI: 10.1108/03321640710756311.

[26] Goldhaber, A. S. and Trower, W. P. “Resource Letter MM-1: Magnetic monopoles”. In: *American Journal of Physics* 58.5 (May 1990), pp. 429–439. ISSN: 1943-2909. DOI: 10.1119/1.16474.

[27] Golub, G. H. *Matrix computations*. John Hopkins, 2013. ISBN: 9781421407944.

[28] Griffiths, D. J. *Introduction to Electrodynamics*. Cambridge University Press, June 2017. ISBN: 9781108420419. DOI: 10.1017/9781108333511.

[29] Hameyer, K. and Belmans, R. *Numerical modelling and design of electrical machines and devices*. Advances in electrical and electronic engineering. Literaturverz. S. [295] - 305. Southampton [u.a.]: WIT Press [u.a.], 1999. 305 pp. ISBN: 1853126268.

[30] Henneron, T., Menach, Y. L., Piriou, F., Moreau, O., Clnet, S., Ducreux, J.-P., and Vrit, J.-C. “Source Field Computation in NDT Applications”. In: *IEEE Transactions on Magnetics* 43.4 (Apr. 2007), pp. 1785–1788. DOI: 10.1109/tmag.2007.892522.

[31] Henrotte, F. and Hameyer, K. “Computation of electromagnetic force densities: Maxwell stress tensor vs. virtual work principle”. In: *Journal of Computational and Applied Mathematics* 168.1-2 (2004), pp. 235–243. DOI: 10.1016/j.cam.2003.06.012.

[32] Ida, N. *Engineering Electromagnetics*. Springer International Publishing, 2015. DOI: 10.1007/978-3-319-07806-9.

[33] Jung, M. and Langer, U. *Methode der finiten Elemente für Ingenieure*. Springer Fachmedien Wiesbaden, 2013. DOI: 10.1007/978-3-658-01101-7.

[34] Kaltenbacher, M. *Numerical Simulation of Mechatronic Sensors and Actuators*. Springer-Verlag GmbH, Feb. 2015. 587 pp. ISBN: 9783642401701. URL: https://www.ebook.de/de/product/23673882/manfred_kaltenbacher_numerical_simulation_of_mechatronic_sensors_and_actuators.html.

[35] Kameari, A. “Three-dimensional eddy current calculation using finite element method with A-V in conductor and Omega in vacuum”. In: *IEEE Transactions on Magnetics* 24.1 (1988), pp. 118–121. DOI: 10.1109/20.43870.

[36] Kost, A. *Numerische Methoden in der Berechnung elektromagnetischer Felder*. Springer, 1994. DOI: 10.1007/978-3-642-57910-3.

[37] Küchler, A. *Hochspannungstechnik*. Springer-Verlag, 2005. DOI: 10.1007/b138561.

[38] Lehner, G. *Elektromagnetische Feldtheorie*. Springer Berlin Heidelberg, 2008. DOI: 10.1007/978-3-642-13042-7.

[39] Leisi, H. J. *Klassische Physik*. Birkhäuser Basel, 1998. DOI: 10.1007/978-3-0348-8807-3.

[40] Li, Y.-L., Sun, S., Dai, Q. I., and Chew, W. C. “Vectorial Solution to Double Curl Equation With Generalized Coulomb Gauge for Magnetostatic Problems”. In: *IEEE Transactions on Magnetics* 51.8 (Aug. 2015), pp. 1–6. DOI: 10.1109/tmag.2015.2417492.

[41] Liu, W. K., Li, S., and Park, H. S. “Eighty Years of the Finite Element Method: Birth, Evolution, and Future”. In: *Archives of Computational Methods in Engineering* 29.6 (June 2022), pp. 4431–4453. DOI: 10.1007/s11831-022-09740-9.

[42] Manges, J. and Cendes, Z. “A generalized tree-cotree gauge for magnetic field computation”. In: *IEEE Transactions on Magnetics* 31.3 (May 1995), pp. 1342–1347. DOI: 10.1109/20.376275.

[43] Matsuo, T., Kameari, A., Sugahara, K., and Shindo, Y. “Matrix Formulation of the Cauer Ladder Network Method for Efficient Eddy-Current Analysis”. In: 54.11 (Nov. 2018), pp. 1–5. DOI: 10.1109/tmag.2018.2839768.

[44] Maxwell, J. C. *A Treatise on Electricity and Magnetism*. Vol. 1. Cambridge University Press, 1873. DOI: 10.1017/cbo9780511709333.

[45] Maxwell, J. C. *A Treatise on Electricity and Magnetism*. Vol. 2. Cambridge University Press, 1873. DOI: 10.1017/CBO9780511709340.

[46] Meunier, G. *The finite element method for electromagnetic modeling*. Vol. 33. John Wiley & Sons, 2010. DOI: 10.1002/9780470611173.

[47] Nakata, T. and Fujiwara, K. “Summary of results for benchmark problem 13 (3-D nonlinear Magnetostatic Model)”. In: *COMPEL - The international journal for computation and mathematics in electrical and electronic engineering* 11.3 (Mar. 1992), pp. 345–369. DOI: 10.1108/eb010097.

[48] Nakata, T., Takahshi, N., and Fujiwara, K. “Summary of results for Benchmark Problem 10 (Steel Plates around a Coil)”. In: *COMPEL - The international journal for computation and mathematics in electrical and electronic engineering* 11.3 (Mar. 1992), pp. 335–344. DOI: 10.1108/eb010096.

[49] Nédélec, J.-C. “Mixed finite elements in $\mathbb{R}^3$”. In: *Numerische Mathematik* 35.3 (1980), pp. 315–341. DOI: 10.1007/BF01396415.

[50] O’Raifeartaigh, L. and Straumann, N. “Gauge theory: Historical origins and some modern developments”. In: *Reviews of Modern Physics* 72.1 (Jan. 2000), pp. 1–23. DOI: 10.1103/revmodphys.72.1.

[51] Poppe, M. *Die Maxwell’sche Theorie*. Springer Berlin Heidelberg, 2015. DOI: 10.1007/978-3-662-45593-7.

[52] Pupin, M. I. “Oersted’s and Ampère’s discoveries”. In: *Journal of the American Institute of Electrical Engineers* 39.12 (Dec. 1920), pp. 1028–1031. DOI: 10.1109/joaiee.1920.6594642.

[53] Reichert, K., Freundl, H., and Vogt, W. “The calculation of forces and torques within numerical magnetic field calculation methods”. In: *Proc. Compumag*. Vol. 76. 1976, pp. 64–74.

[54] Ren, Z., Bouillault, F., Razek, A., Bossavit, A., and Verite, J. “A new hybrid model using electric field formulation for 3-D eddy current problems”. In: *IEEE Transactions on Magnetics* 26.2 (Mar. 1990), pp. 470–473. DOI: 10.1109/20.106355.

[55] Ren, Z. “Influence of the RHS on the convergence behaviour of the curl-curl equation”. In: *IEEE Transactions on Magnetics* 32.3 (May 1996), pp. 655–658. DOI: 10.1109/20.497323.

[56] Ritz, W. “Über eine neue Methode zur Lösung gewisser Variationsprobleme der mathematischen Physik.” In: *crll* 1909.135 (1909), pp. 1–61. DOI: 10.1515/crll.1909.135.1.

[57] Rochus, V., Rixen, D. J., and Golinval, J.-C. “Monolithic modelling of electro-mechanical coupling in micro-structures”. In: *International Journal for Numerical Methods in Engineering* 65.4 (2005), pp. 461–493. DOI: 10.1002/nme.1450.

[58] Rudolph, M. and Schaefer, H. *Elektrothermische Verfahren: Grundlagen, Technologien, Anwendungen*. Springer Berlin Heidelberg, 1989. ISBN: 9783540510642.

[59] Saad, Y. *Iterative Methods for Sparse Linear Systems*. Society for Industrial and Applied Mathematics, Jan. 2003. DOI: 10.1137/1.9780898718003.

[60] Schöberl, J. *C++11 Implementation of Finite Elements in NGSolve*. Sept. 2014.

[61] Schöberl, J. *NETGEN - 4.x*. Jan. 24, 2009. URL: https://netgen-mesher.sourceforge.net/docs/ng4.pdf (visited on 06/01/2023).

[62] Schöberl, J. “NETGEN An advancing front 2D/3D-mesh generator based on abstract rules”. In: *Computing and Visualization in Science* 1.1 (July 1997), pp. 41–52. DOI: 10.1007/s007910050004.

[63] Schöberl, J. “Numerical methods for Maxwell equations”. In: (2009).

[64] Schönherr, M. and Schuricht, F. *A theory of traces and the divergence theorem*. 2022. DOI: 10.48550/ARXIV.2206.07941.

[65] Silvester, P. and Chari, M. K. “Finite Element Solution of Saturable Magnetic Field Problems”. In: PAS-89.7 (Sept. 1970), pp. 1642–1651. DOI: 10.1109/tpas.1970.292812.

[66] Steel Europe AG, thyssenkrupp. *Produktinformation powercore M270-35A*. 2017.

[67] Takahshi, N., Nakata, T., and Morishige, H. “Summary of Results for Problem 20 (3-D Static Force Problem)”. In: *COMPEL - The international journal for computation and mathematics in electrical and electronic engineering* 14.2/3 (Feb. 1995), pp. 57–75. DOI: 10.1108/eb010138.

[68] Trowbridge, C. W. “Electromagnetic computing: the way ahead?” In: *IEEE Transactions on Magnetics* 24.1 (1988), pp. 13–18. DOI: 10.1109/20.43845.

[69] Trowbridge, C. W. “Compumag Conference - The First 25 Years”. In: International Compumag Society (2001). URL: https://www.compumag.org/wp/wp-content/uploads/2018/07/TwentyFiveYearsOfCompumag.pdf (visited on 02/08/2023).

[70] Trowbridge, C. W. “Computing electromagnetic fields for research and industry: major achievements and future trends”. In: 32.3 (May 1996), pp. 627–630. DOI: 10.1109/20.497316.

[71] Trowbridge, C. W. “Progress in Magnet Design by Computer”. In: *eConf* C720919 (1972). Ed. by Winterbottom, Y., p. 555.

[72] Turner, L. R. *The TEAM Workshops: A Short History*. 1990.

[73] Turner, M. J., Clough, R. W., Martin, H. C., and Topp, L. J. “Stiffness and Deflection Analysis of Complex Structures”. In: 23.9 (Sept. 1956), pp. 805–823. DOI: 10.2514/8.3664.

[74] Unz, H. “Oliver Heaviside (185O-1925)”. In: *IEEE Transactions on Education* 6.1 (1963), pp. 30–33. DOI: 10.1109/te.1963.4321796.

[75] Willner, K. *Kontinuums- und Kontaktmechanik*. Springer Berlin Heidelberg, 2003. DOI: 10.1007/978-3-642-55814-6.

[76] Yang, C. N. “The conceptual origins of Maxwell’s equations and gauge theory”. In: *Physics Today* 67.11 (Nov. 2014), pp. 45–51. DOI: 10.1063/pt.3.2585.

[77] Zollner, M. *Physik der Elektrogitarre*. Regensburg: Eigenverlag, 2014.

Part II

Model Order Reduction

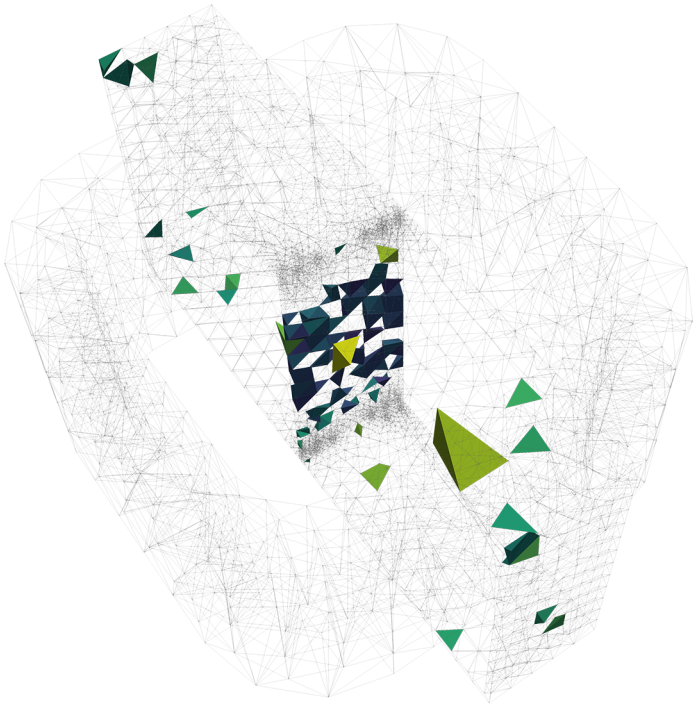

Chapter 13

Introduction

Model Order Reduction (MOR) strives to reduce computational costs associated with numerical simulations. Right at the beginning, a strict distinction must be made between simplification through the intelligent saving of unnecessary calculation steps and simplification through approximation. MOR happens at very different levels during the development of a simulation of a real-world problem. First, very conscious approximations are made during the selection of the considered physics. Approximations in the idealization of the systems regarding the precision of the geometry and the material parameters follow. The row is continued by discretizing the problem with, e.g., the finite element method. Transforming the equations to another space and truncating less important directions from that space is one of many further deliberate reduction options. A last, inevitable approximation is the accuracy of the used solvers.

The question that guides every MOR is the desired range of prediction made with the resulting simulation. A key feature of a model is the ability to predict the specific behavior of a system. This prediction is only valid in a certain range of parameters and conditions. By reducing the complexity of the model, the desired range of validity must not be limited to more than the application demands.

The second key question aims at the objective of MOR. In the framework of monitoring, edge-computing devices with limited hardware (storage and computational power) are becoming more and more important. A reduced model running on such devices must provide a small footprint and low computing power requirements simultaneously. In the framework of a real-time controller, the reduced model needs to serve a minimum computation time with a guaranteed convergence behavior. This second objective is not the topic of this thesis.

Throughout this thesis, the focus is set on investigating mathematical methods that can reduce the numerical size of finite element models by approximation, especially for nonlinear systems.

13.1 Selection of MOR Strategy

As the field of MOR is a sea of options, one needs to narrow down the map of possibilities. In [11], the authors give categories of comparison of (in their case linear) MOR methods. A short summary with our own extensions is given here to select the branch of interest for this work.

- Linear vs. non-linear systems: Although the core idea of MOR is similar for linear and non-linear problems, it is perhaps the strictest subdivision regarding the mathematical tools and methods that are applicable.

- Local vs. global approximation in a spatial sense: The objective is to either determine an approximation of the solution at specific local points or to obtain the complete solution field.
- Automatic vs. user-dependent: The degree of knowledge and empirical effort required of the user to achieve a successful MOR.
- Single-use vs. multi-use: Depending on the planned number of use cases of the reduced model, the proportion of offline and online costs must be carefully considered.

The objective of this thesis is to achieve a MOR strategy for underlying non-linear systems of first-order and a global approximation with a medium user experience and high model re-usability. The global approximation of the magnetic field allows the use of the full field for further post-processing as an in-place substitute for the full-order model. The requirement for a medium user experience means that the user can influence the reduction process via its crucial parameters but only needs an understanding of the abstract concept. The final reduced-order model must be capable of being used for arbitrarily different right-hand sides, i.e. excitation.

13.2 Short History of Model Order Reduction

Going through the history of MOR, no fundamental beginning of this research area can be fixed. Although the topic is driven by mathematics, it is only useful in combination with any model. Therefore, methods were developed in different physical domains, and some were then adapted to other domains and further developed from there. Important fields of MOR development are *Statistics*, *System & Control Theory*, *Structural Dynamics*, and *Electrodynamics*.

General MOR With B.G. GALERKIN (*1871-†1945), the history of MOR can (as the author's interpretation) be dated back to around 1915. His approach yields the same origin for FEM as well as MOR. Approximating a PDE by a finite number of parameters is already an early kind of MOR. The same idea is still used in the form of projection into different subspaces where a FEM solution can be represented with fewer degrees of freedom. The key point to successfully apply the Galerkin projection is to define meaningful test-functions, alias a good fitting subspace. The following paragraphs sketch the traces of the methods' origins that are used to find appropriate subspaces.

A few years back from GALERKIN, in 1901, K. PEARSON (*1857-†1936) laid the fundament for the *Principal Component Analysis (PCA)* in [44]. PEARSON invented the idea of fitting a p-dimensional ellipsoid to a set of data. The axes of the ellipsoid are the principal components.

The statisticians KARHUNEN (*1912-†1992) and LOÈVE (*1907-†1979) introduced 1947 /1948 a transformation which decomposes every stochastic process (even non-stationary) into an (infinite) series of orthogonal functions weighted by independent random variables [27, 31]. The transformation is optimal in a total mean squared error sense. For discrete events, the *Karhunen-Loève-Transformation (KLT)* becomes the PCA. The technique has a broad band of applications. It is used to extract signals from noisy measurements or to reduce the data of an electrocardiogram in medicine. Today, the computation of the PCA or KLT is performed under the use of the algorithm for the *Singular Value Decomposition*.

The *Singular Value Decomposition (SVD)* as a linear algebra method was found by several mathematicians since the 1870s, including J.J. SYLVESTER (*1814-†1897). Without the com-

putational power of today, the use of the SVD was more for theoretical investigations. 1970 G.H. GOLUB developed one of the until today most used implementations of the SVD in [20]. Today, calculating PCA is performed by using efficient SVD implementation and writing the principal components as the left singular vectors multiplied by the corresponding singular values. The SVD became one of the most used algorithms in the 2010s for the topics of Artificial Intelligence, Machine Learning, and Data Mining. As the computational effort for big data sets is still challenging, new algorithms were developed to perform the SVD [36] much more efficiently.

The *Proper Orthogonal Decomposition (POD)* arose in the field of mechanical engineering, especially fluid dynamics. It was first mentioned in 1967 and reviewed in very detail in 1993 in [10]. The POD aims to decompose time-varying vector fields into a set of spatial functions modulated by time coefficients. As a mathematical tool, the previously mentioned SVD is used [28]. The term POD-Galerkin projection is already known in [10] and tested for the Navier-Stokes equations to find finite-dimensional dynamical systems in the truncated space of the spatial functions, i.e., the left singular vectors. With that, the bracket to GALERKIN closes.

For non-linear systems, the POD approach does not always yield the smallest subspace. This circumstance leads to further developments, e.g., *Non-Linear Principal Component Analysis (NLPCA)* and *Vector Quantization Principal Component Analysis (VQPCA)* [28]. Various methods can be grouped as manifold learning techniques that aim at building low-dimensional manifolds, providing non-linear mapping suitable for the underlying non-linear system.

The book [13], released in 2019, introduces the fundamentals of SVD and POD in a data-driven environment. The last chapter handles the interpolation for parametric ROMs with methods such as the *Gappy POD*.

The term *Hyperreduction* was probably introduced first in 2005 by RYCKELYNCK [52] in a finite element context for non-linear problems. It describes a reduction of the integration points in addition to a reduction by the Galerkin projection. Two advanced methods that are based on the idea of hyperreduction are the *Discrete Empirical Interpolation Method (DEIM)* [15] developed under the supervision of D.C. SORENSEN and the *Energy Conserving Sampling and Weighting (ECSW)* [18] of C. FARHAT. Both methods and their development are discussed in detail in their section (section 15.3, section 15.4). In 2017, JAIN and RUTZMOSER were introduced under the supervision of P. TISO and D.J. RIXEN methods for the hyperreduction over non-linear manifolds for large non-linear mechanical systems in [26] and [50]. They extended the ECSW method to allow for hyperreduction using smooth non-linear mappings. By using the tangent space of the manifold, it is possible to preserve the stability properties of the ECSW.

In 2019, the book *Substructuring in Engineering Dynamics* [2], as a collection of lecture notes from the CISM-course, was published. Besides the substructuring of linear structural dynamic systems, the later chapters describe possible MOR techniques for structural mechanics for linear and non-linear systems. Among others, a small excursion is made to the hyperreduction methods DEIM and ECSW. In 2021, a book series of 3 Volumes, *Model Order Reduction*, [6–8] was created as a result of a long-term EU-project (EU-MORNET) which ended in 2018 and a following COST project was funded to manifest the known techniques in the named book series for engineers. The series already contains the methods DEIM and ECSW for structural dynamic applications.

MOR for Magnetodynamic Systems The field of MOR in electrodynamic/magnetodynamic systems is clearly split into two parts. There is quite an amount of literature available for linear input-output reduction, which is completely omitted here as this thesis focuses on a full-field approximation. Research results for full-field non-linear MOR for magnetodynamic systems are rather sparse.

The POD is a common MOR technique [28], successfully applied to quasi-static magnetodynamic systems [54, 55]. An overview of projection-based methods is given in [9]. By the assumption of linearity, [29] used methods based on modal analysis, i.e., eigenvectors of the system matrices, for model reduction. For linear material, POD and Krylov subspace techniques were also investigated in the frequency domain [23, 43].

However, the straightforward projection into reduced space can be insufficient in addressing non-linear problems, where much computational cost arises from evaluating each element's non-linear contribution to the system's energy. This issue has been the focus of many studies [24, 25, 53], with the application of the Discrete Empirical Interpolation Method (DEIM) [15]. In [42], a method is introduced for reducing non-linear magnetodynamic problems by combining POD with manifold interpolation, an approach that has demonstrated superior results compared to classical techniques like direct POD reduction and standard interpolation of pre-computed reduced bases.

In order to improve the accuracy and robustness of reduction for non-linear models, the Energy Conserving Sampling and Weighting (ECSW) method, originating from an idea of computer graphics [4], further developed for structural dynamics [19] has emerged as a promising candidate. The ECSW method might offer significant advantages in electrodynamic systems regarding stability and result quality, even for highly reduced models. Initial steps have been made in recent studies [32–35]. In these works, the ECSW method was successfully utilized to compute the magnetic vector potential, yielding promising results, indicating its ability to significantly reduce computational costs and retain good accuracy. The following chapters go into detail to explain and demonstrate the hyperreduction technique ECSW.

13.3 Definitions and Terms

This section should give an overview of important terms and definitions that form the language of MOR. It is essential for successful communication to build a common sense of terminology.

- The need for simulating the FOM to perform a specific MOR approach can be expressed using the terminologies *a priori* (also known as *simulation-free*) and *a posteriori* reduction approaches.

  The *a priori* approach exploits properties of the systems to construct the system. For linear systems, typically, the eigenproblem is (partially) solved and a subset of modes is used. For non-linear structural mechanics, RUTZMOSER proposed specific static training simulations [49]. The *a posteriori* approach utilizes previously computed results to build the ROM. Adaptive approaches can weaken the border between the two pure definitions. The ROM is updated during the reduced simulation if an appropriate measure indicates that the most recent state evolution is not represented accurately. Different adaptation strategies are possible. One approach is shown in [52].

- *Model-based* and *System-based* are used equally in the following context, even though a difference could be made in the author's opinion by the question if the physical model

in the form of a PDE is meant or a system-theoretic description in discrete state-space form. However, after applying the finite element method to the PDE, both system descriptions are equivalent. The terms *data-driven* and *snapshot-based* are not separated clearly in the literature. In the author's opinion, the *snapshot-based* methods are a subset of *data-driven* methods. For the more general *data-driven* method, the data can arise from measurements (mostly only input-output relations) or from simulations of the high-fidelity model. The snapshots are specifically the resulting states and their evolution in time (or parameter) of simulations. The snapshots serve the result at all dofs, whereas measurement data is only point-wise usually.

- A further classification is done by distinguishing between *intrusive* and *non-intrusive* methods. While the *intrusive* methods need access to the element formulation, the *non-intrusive* does not and is therefore interesting in combination with proprietary FEM-software [2].

Hyperreduction The main drawback of projective reduction methods for non-linear systems is the evaluation of the non-linear term. For that, the reduced dofs have to be transformed back into full field space, where the non-linear force is computed. The result is then projected again into the reduced space. In a Newton Raphson algorithm, the mentioned non-linear force evaluation and the generation of a tangential stiffness matrix, including their projection, have to be computed for every iteration.

From Ancient Greek, the prefix *hyper* ($\upsilon\pi\varepsilon\rho$) means *over, above*. For the term *hyperreduction*, this can be interpreted as a reduction on top of another reduction. The core idea of *hyperreduction* methods is the approximation of the non-linear term on top of a projective reduction. This does not imply any order of the two reduction steps. As seen later, both orders are possible but unveil different properties. In particular, the hyperreduction methods reveal two strategies that will be further explained at this point in a general way. C. FARHAT introduced the terminology of *approximate-then-project* and vice versa.

- *Approximate-then-project* describes the process of first evaluating the non-linear function at only a few spatial locations. Using (empirical) basis functions, the full spatial field is interpolated. After that, the Galerkin projection into the desired subspace is performed. The investigated DEIM in section 15.3 is of that type.

- *Project-then-approximate* switches the order, and the approximation of the non-linear function is already performed in the reduced space after the projection. The ECSW method (more in section 15.4) exploits this strategy and therefore leads to unique structure-preserving stability properties [7, 18].

Chapter 14

Subspace Projection

One class of MOR techniques aims to represent the resulting field in a reduced subspace. This subspace has to span the possible solutions field as well as possible and hereby also use a minimum of base vectors. Considering a smaller subspace allows us to project the system in that subspace and solve the problem there with the advantage of the reduced degrees of freedom. This approach is well-known in the field of linear structural dynamics. There, the equations are transformed in a subspace spanned by a truncated set of the system's modes (i.e. eigenvectors). Truncating the modes with respect to the applied load distribution and spectrum can significantly reduce the degrees of freedom [8, 46, 49].

Assume a linear equation $\boldsymbol{A}\boldsymbol{x} = \boldsymbol{f}$, which could, for instance, represent a discretized PDE. The assembled bilinear form $\boldsymbol{A}$ is of dimension $(n \times n)$ and a truncated basis $\boldsymbol{V}$ could be found by various methods, which is then of size $(n \times m)$ where $m < n$. The projection of the equation onto the subspace, spanned by $\boldsymbol{V}$ is written as:

$$\underset{(n\times n)}{\mathbf{A}} \cdot \underset{(n\times 1)}{\mathbf{x}} = \underset{(n\times 1)}{\mathbf{f}}$$

$$\underset{(m\times n)}{\mathbf{V^T}} \cdot \underset{(n\times n)}{\mathbf{A}} \cdot \underset{(n\times m)}{\mathbf{V}} \cdot \underset{(m\times 1)}{\mathbf{q}} = \underset{(m\times n)}{\mathbf{V^T}} \cdot \underset{(n\times 1)}{\mathbf{f}}$$

$$\underset{(m\times m)}{\mathbf{A_r}} \cdot \underset{(m\times 1)}{\mathbf{q}} = \underset{(m\times 1)}{\mathbf{f_r}}$$

The reduced equation (index r) is then of dimensions m. Note that original sparse systems $\boldsymbol{A}$ generally become dense systems $\boldsymbol{A}_r$.

Assume the same system's structure but a non-linear mapping function $\boldsymbol{g}(\boldsymbol{x})$. The combination of the projection and the non-linear function $\boldsymbol{g}(\boldsymbol{x})$ into a new linear function is not directly possible by its nature, but the outcome of the function can be projected to live in the

subspace. The drawback is that the input for the function needs to be expanded back to be evaluated.

$$\underset{(n\times 1)}{\mathbf{g}}\left(\underset{(n\times 1)}{\mathbf{x}}\right) = \underset{(n\times 1)}{\mathbf{f}}$$

$$\underset{(m\times n)}{\mathbf{V}^{\mathrm{T}}} \cdot \underset{(n\times 1)}{\mathbf{g}}\left(\underset{(n\times m)}{\mathbf{V}}\,\underset{(m\times 1)}{\mathbf{q}}\right) = \underset{(m\times 1)}{\mathbf{f}_{\mathbf{r}}}$$

For non-linear systems, it is much harder to find a subspace that covers the information of the system in an appropriate way. There are two strategies to find such a subspace. The first approach is a system analysis-based approach. It is the analogon of computing modes for a linear system via the system's matrices. For the non-linear structural dynamics, it is possible to linearize the system, evaluate the generalized eigenvalue problem, and expand the basis with so-called *Modal derivatives*. Further developments suggest so-called *Krylov-modes*, which take load cases into account. As a starting point for further information, the reader is refered to [49]. For this thesis, the system analysis-based approach is not further investigated. The second strategy to find a suitable subspace is a simulation-based approach. It uses a set of simulation results and extracts, via a singular value decomposition, the relevant directions of which the results are composed. This approach is very straightforward and easy to implement. However, it needs long offline computations to generate all the training snapshot simulations. The full solution vectors of these reference simulations must span the space of all future expected solutions. The parameter and load settings can be chosen in a regular grid or better with an advanced algorithm to reduce the number of training simulations to a minimum by maintaining an equally meaningful basis.

14.1 Data-Driven Basis

The strategy shown here is simulation-based (= data-driven), which means that a full-order time-integration simulation is performed for a certain training trajectory of the load (i.e. the current in the coil). The full-order solution vectors of each time step are called the training snapshots. Truncating the left-sided vectors of a singular value decomposition on a set of training snapshots results in a smaller solution space for the projection.

14.1.1 Generation of Training Snapshots

From the previously shown use of the training snapshots, different strategies for generating and selecting the training snapshots arise. Due to the expenses in the generation of the training snapshots by full-order time integration, a few rules of best practice can be stated:

- Make use of every snapshot generated.
- Choose a trajectory that captures the system's behavior with a minimum of time steps.

14.1.2 Proper Orthogonal Decomposition

POD is a technique used to extract the dominant spatial and temporal patterns from a set of data. The spatial patterns are often referred to as the Proper Orthogonal Modes (POM) and are closely related to the modes known of linear systems. But as the eigenmodes are K and M orthogonal, the POMs are directly orthogonal to each other. This comparison to modes gets even weaker for non-linear systems, [28]. By construction, the basis built from POMs is orthogonal. The energy captured by the POMs arising from a time series of snapshots is a good measure of the needed dimensionality of the reduced model. The computation of the POD is achieved using the mathematical operations of the singular value decomposition.

Singular Value Decomposition Primarily, the SVD is used for factorizing a matrix into three simpler matrices, providing valuable insights into its structure and information content. In the context of extracting patterns of time series data, the left-sided vectors represent the spatial modes, the singular values the significance of each spatial mode and the right-sided vectors the time coefficients associated with each spatial mode.

A point of discussion is the typically recommended centering of data, meaning the subtraction of the mean of each column from the corresponding column's values. For this thesis, no centering is performed on the datasets. This may lead to a first mode representing the mean of the data. As we are not interested in the variance of the data but in generating a reduced order model, this is not an issue but rather helpful to capture the model's behavior.

To find a basis that spans the subspace that is consumed by the solution of the training simulation, a POD of the training snapshots is performed using the singular value decomposition (SVD). The decay of the singular values gives a hint of how much of the solution lives within the most important directions. A strong decay indicates strong first modes. Note however, that truncating the PODs of the same system but gained via different training sets to the same level of singular value leads to reduced models of different quality. The reason is that the singular values are not independent of the configuration space. That means the singular values are not comparable between different training sets in an absolute manner [13].

14.2 Tools for ROM Quality Assessment

This section introduces a few tools to enable the quantitative quality assessment of ROMs generated by different methods or parameters. The developed metrics give insight into the achievable solutions during the MOR process. Also, the quality of the final result can be measured relative to the full-order model.

14.2.1 Energy Fraction of Singular Values

In the context of analyzing the time series of degrees of freedom for a dynamic system, the energy fraction of the singular values obtained through SVD can provide valuable insights into the dominant modes of motion and the significance of these modes. The energy fraction Q of the singular values σ, often calculated as the ratio of the sum of squares of selected singular values $1 \dots m$ to the total sum $1 \dots n$ of squares of all singular values, represents the proportion of the total energy or variance in the dynamic behavior of the structure that is captured by a subset of the modes.

$$Q = \frac{\sum_{i=1}^{m} \sigma_i^2}{\sum_{i=1}^{n} \sigma_i^2} \tag{14.1}$$

The energy fraction helps in deciding how many modes to retain when creating reduced-order models. However, no clear rule of thumb for Q can be given.

14.2.2 Subspace Angles

As the generation of the subspace which the system is projected into is a data-driven approach by performing an SVD on the training snapshots, different training simulations will lead to (slightly) different subspaces. Depending on the unknown trajectory that will be simulated with the reduced-order model, the subspace could be more or less sufficient to represent the true solution. To compare two subspaces without the dependence on their representing vectors, the concept of *subspace angles* is introduced [21, 51].

The subspace angles between two subspaces $\mathcal{S}_1$ and $\mathcal{S}_2$ are defined recursively in eq. (14.2), where the minimum angle θ_i between a pair of principal vectors $\boldsymbol{v}_i \in \mathcal{S}_1$ and $\boldsymbol{w}_i \in \mathcal{S}_2$ is found under the condition that the principal vectors are orthogonal to all previous principal vectors. The algorithm finds as many subspace angles (equivalent to the term principal angles) as the dimension of the smaller subspace, $i = 1 \ldots \min(\dim(\mathcal{S}_1), \dim(\mathcal{S}_2))$.

$$\cos\theta_i = \max(\boldsymbol{v}_i^T \boldsymbol{w}_i), \qquad \boldsymbol{v}_i^T[\boldsymbol{v}_1, ..., \boldsymbol{v}_{i-1}] = 0, \quad \boldsymbol{w}_i^T[\boldsymbol{w}_1, ..., \boldsymbol{w}_{i-1}] = 0 \tag{14.2}$$

An illustration of two planes (i.e. two-dimensional subspaces) with one coincident direction $\boldsymbol{v}_1 = \boldsymbol{w}_1$ is given in fig. 14.1. The intersection line is the common direction in both subspaces leading to a subspace angle $\theta_1 = 0$. The second principal vectors span the angle θ_2 with a possible range of $\theta_2 = 0°$ to $90°$. To give the two extreme situations as an illustration: Any

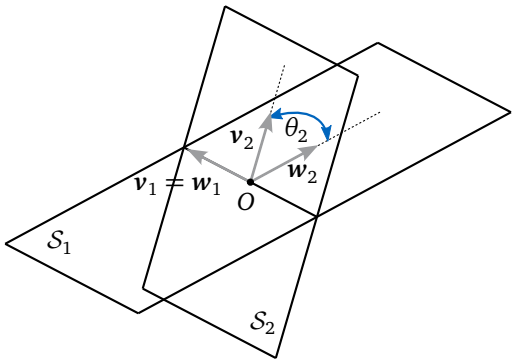

Figure 14.1: Visualization of two subspaces with subspace angle $\theta_1 = 0$ and $\theta_2 > 0$, [51].

vector $\boldsymbol{v}_i \in \mathcal{S}_1$ is orthogonal to any other vector $\boldsymbol{w}_i \in \mathcal{S}_2$, resulting in $\theta = 90°$. Two subspaces are identical if all subspace angles are $\theta = 0$.

Also, for subspaces of different sizes, the concept of subspace angles still gives valuable results. The subspace angles show how well the smaller subspace is included in the wider one. The number of directions of the smaller subspace limits the number of subspace angles. No angles can be computed beyond the size of the smaller subspace.

To find the principal vectors of subspaces that are defined as matrix ranges (as is the case for this work), a QR factorization and an SVD need to be applied to the columns of the matrices. For the exact algorithm, the interested reader is hinted to [21].

14.2.3 Relative Error

The relative error compares resulting values with reference values (i.e. the full-order model results) over all time steps. The relative error is applicable to local or global measures. An example of a local measure is the relative error of the $\boldsymbol{B}$-field at one specific point. An example of a global measure is the total magnetic energy in the system.

The most general definition of the relative error (RE) evaluation for any arbitrary field quantity $\boldsymbol{u}(\boldsymbol{x})$, for each discretization point k, summed over all time steps t_i, is as follows [18]:

$$RE = \sum_k \frac{\sqrt{\sum_i (\boldsymbol{u}_{\mathrm{ref}}(t_i) - \boldsymbol{u}(t_i))^T (\boldsymbol{u}_{\mathrm{ref}}(t_i) - \boldsymbol{u}(t_i))}}{\sqrt{\sum_i \boldsymbol{u}_{\mathrm{ref}}(t_i)^T \boldsymbol{u}_{\mathrm{ref}}(t_i)}} \times 100\,\% \tag{14.3}$$

The reference values must represent the same quantity in the same time scale. To compare time series with different sample rates, a linear interpolation of the coarser signal is performed to match the fine sampled signal.

For point quantities (local point of field or global quantities, i.e., force), the definition becomes:

$$RE = \frac{\sqrt{\sum_i (\boldsymbol{F}_{\mathrm{ref}}(t_i) - \boldsymbol{F}(t_i))^T (\boldsymbol{F}_{\mathrm{ref}}(t_i) - \boldsymbol{F}(t_i))}}{\sqrt{\sum_i \boldsymbol{F}_{\mathrm{ref}}(t_i)^T \boldsymbol{F}_{\mathrm{ref}}(t_i)}} \times 100\,\% \tag{14.4}$$

In most cases, it is beneficial to compute the relative error only for one direction to avoid diffusion of the relative error in small-valued quantities by errors in large-valued quantities.

For scalar quantities (e.g. global energy), the definition of the relative error simplifies to:

$$RE = \frac{\sqrt{\sum_i (W_{\mathrm{ref}}(t_i) - W(t_i))^2}}{\sqrt{\sum_i W_{\mathrm{ref}}(t_i)^2}} \times 100\,\% \tag{14.5}$$

In conclusion, the relative error is a measure to quantify the quality of the reduced-order model. In contrast, the subspace angles and the singular values give insights into the similarity of the subspaces, but the quality of the ROM can't be directly drawn.

Chapter 15

Hyperreduction Methods (DEIM, ECSW) for Magnetodynamic Problems

This chapter introduces two hyperreduction methods, namely the *Discrete Empirical Interpolation method (DEIM)* and the *Energy Conserving Sampling and Weighting Method (ECSW)* for magnetodynamic systems.

Remark

This chapter is mainly taken from the author's publication *Model Order Reduction using Hyperreduction Methods (DEIM, ECSW) for Magnetodynamic FEM Problems*, [33].

A detailed derivation of the magnetodynamic equations is found in part I of the thesis. Nevertheless, a short description is presented here to keep the chapter self-contained and all relevant information close together.

15.1 Magnetodynamic System Description

For magnetodynamic problems, i.e., systems with low-frequency content, the influence of the changing electrical field ($\frac{\partial \boldsymbol{E}}{\partial t}$) on the magnetic field is neglected in the following. Additionally, it is assumed that in the whole domain Ω, no free charges are present ($\rho = 0$). Assuming that the material does not exhibit any hysteresis, the so-called quasi-stationary Maxwell equations are obtained, which include the effect of eddy currents.

$$\nabla \times \boldsymbol{E} = -\frac{\partial \boldsymbol{B}}{\partial t} \tag{15.1}$$

$$\nabla \times \boldsymbol{H} = \boldsymbol{j} \tag{15.2}$$

Eddy currents can only occur in the electrical conductive domain $\Omega_c \subset \Omega$, and the conductivity is given by

$$\sigma(\boldsymbol{x}) = \begin{cases} \sigma_c & \forall \boldsymbol{x} \in \Omega_c \\ 0 & \forall \boldsymbol{x} \in \Omega \setminus \Omega_c \end{cases} \tag{15.3}$$

Because of eq. (15.3) and Ohm's law, the eddy currents vanish in the domains around Ω_c and eq. (15.4) must be satisfied [30]:

$$\boldsymbol{n}_c \cdot \boldsymbol{j}_c = 0 \quad \text{on } \Gamma_c \tag{15.4}$$

where $\boldsymbol{n}_c$ is the normal to the interface Γ_c and $\boldsymbol{j}_c$ denotes the eddy currents in Ω_c. The excitation current $\boldsymbol{j}_0$ is located in domain Ω_0, where we assume that no eddy currents are

present. Therefore, the conductive domains are not overlapping: $\Omega_0 \cap \Omega_c = \emptyset$. The full current is $\boldsymbol{j} = \boldsymbol{j}_0 + \boldsymbol{j}_c$ while only one term of the sum can be nonzero in a given domain.

The vector potential $\boldsymbol{A}$ is defined as

$$\boldsymbol{B} = \boldsymbol{\nabla} \times \boldsymbol{A} \tag{15.5}$$

Substituting eq. (15.5) in Faraday's eq. (15.1) and Ampere's law eq. (15.2) leads to the curl-curl formulation for $\boldsymbol{A}$ (see eq. (15.7)).

$$\boldsymbol{\nabla} \times \boldsymbol{E} = -\boldsymbol{\nabla} \times \frac{\partial \boldsymbol{A}}{\partial t} \tag{15.6}$$

$$\boldsymbol{\nabla} \times \frac{1}{\mu(B)} \boldsymbol{\nabla} \times \boldsymbol{A} = \boldsymbol{j} \tag{15.7}$$

Due to the properties of the curl operation, the gradient of any arbitrary scalar field V can be added to the vector potential $\boldsymbol{A}$ without changing the magnetic field density $\boldsymbol{B}$. Also, a gradient field $\boldsymbol{\nabla} V$ can be added to the $\boldsymbol{E}$-field. Therefore, also considering Ohm's law, eq. (15.6) can be used to write the equation expressing the eddy current in terms of $\boldsymbol{A}$ and V:

$$\boldsymbol{j}_c = \sigma \boldsymbol{E} = -\sigma \frac{\partial \boldsymbol{A}}{\partial t} + \sigma \boldsymbol{\nabla} V \tag{15.8}$$

and eq. (15.7) can now be written as the governing equation for $\boldsymbol{A}$:

$$\boldsymbol{\nabla} \times \frac{1}{\mu} \boldsymbol{\nabla} \times \boldsymbol{A} = \boldsymbol{j}_0 - \sigma \frac{\partial \boldsymbol{A}}{\partial t} + \sigma \boldsymbol{\nabla} V \tag{15.9}$$

To find a valid scalar field V, an additional (naturally given) condition for eq. (15.9) is evaluated: The divergence of the rhs of eq. (15.9) has to be zero as $\boldsymbol{H}$ in eq. (15.2) can only generate a solenoidal vector field. Additionally, the Coulomb gauging $\mathrm{div}(\boldsymbol{A}) = 0$ is applied. With that, the divergence of the first two terms of the rhs of eq. (15.9) are zero by default, and for the special case of spatially constant conductivity σ, the third term has to satisfy $\sigma \boldsymbol{\nabla} \cdot (\boldsymbol{\nabla} V) = 0$. One valid solution for that is $V = 0$, which comes in handy, as the degrees of freedom for V vanish completely [12].

After discretization, eq. (15.10) can be written as

$$\boldsymbol{M}_A \dot{\boldsymbol{u}}_A + \boldsymbol{g}_A(\boldsymbol{u}_A) = \boldsymbol{f}_A \tag{15.10}$$

Hereby $\boldsymbol{M}_A$ is the so-called magnetic mass matrix, $\boldsymbol{u}_A$ the unknown values of the vector potential, $\boldsymbol{f}_A$ the load vector, and $\boldsymbol{g}_A$ the discretized internal current. The internal currents are the analogon to the internal forces known from structural dynamics. The index A, denoting the vector potential, will be omitted in the following to keep the notations clean.

The non-linear problem is simulated using a time integration with the Backward-Euler scheme with integrated Newton-Raphson-Iteration as shown in section 8.3 of part I.

15.2 Outline of Investigated MOR Methods

The need for model order reduction becomes clear by considering the mesh size needed to correctly represent the eddy current distribution due to the skin effect. Reduction methods based on the projection of the problem in a subspace perform well only for linear problems where the function $\boldsymbol{g}(\boldsymbol{u})$ can be expressed as a matrix-vector product that can be projected cost-effectively in a subspace. The focus here is on methods that use a second reduction, the so-called *hyperreduction*, of the non-linear internal forces to speed the calculation up. Two methods used in structural mechanics are discussed here. The first approach is called the **Discrete Empirical Interpolation method (DEIM)** and tries to approximate the full non-linear internal forces by expanding the force of selected dofs via a dedicated basis, [15, 60]. The second method is the **Energy Conserving Sampling and Weighting Method (ECSW)** that weights selected elements such that the internal forces produce the same virtual work as the non-reduced system, [19]. Both methods gain their time reduction from the idea of reducing the number of elements called for the computation of the non-linear internal force term. A short summary of the methods in the context of structural dynamic systems is given in [3].

The magnetodynamic systems examined in the course of this work have a few properties that are very specific to magnetodynamic FEM problems, and it is not clear how they interfere with hyperreduction methods.

- The problem is strongly in-homogeneous: The solution domain consists of at least two material domains, namely air and a ferromagnetic material. Their constitutive properties differ by up to 3 orders of magnitudes. With that also, the field energy distribution is highly inhomogeneous.
- The finite element model is built using so-called edge elements instead of nodal elements as known from classical structural dynamics.
- Only parts of the system behave dynamically, as eddy currents cannot occur in non-conducting domains such as air.

Notations used for the Galerkin Projection The DEIM, as well as the ECSW method, combines a Galerkin projection to a subspace of the solution to reduce the degrees of freedom and a hyperreduction to reduce the non-linear force term to a small evaluation set. Here, in a pre-processing step, a solution of a full representative problem is computed while applying an excitation similar to the one applied in further simulations, and an SVD of the solution snapshots $\boldsymbol{U} = [\boldsymbol{u}_1, \ldots, \boldsymbol{u}_m]$ is performed. The reduction basis $\boldsymbol{V}$ contains the most important left singular vectors of that decomposition, and the solution is then approximated by

$$\boldsymbol{u} \approx \boldsymbol{V}\boldsymbol{q} \tag{15.11}$$

where $\boldsymbol{q}$ are the generalized degrees of freedom in the reduced space. The reduced problem is then obtained by projection of eq. (15.10) on $\boldsymbol{V}$:

$$\boldsymbol{V}^T\boldsymbol{M}\boldsymbol{V}\dot{\boldsymbol{q}} + \boldsymbol{V}^T\boldsymbol{g}(\boldsymbol{V}\boldsymbol{q}) = \boldsymbol{V}^T\boldsymbol{f} \tag{15.12}$$

15.3 DEIM - Discrete Empirical Interpolation Method

The idea of Empirical Interpolation was first proposed in [5] and further developed for discrete problems (DEI-Method) in [15] and [60]. Its application to structural dynamics problems was investigated in [59] and [47]. It was applied in combination with a POD to magnetostatic problems in [1, 24, 40, 53].

15.3.1 Method Description

The key idea of DEIM is to find a subspace $\boldsymbol{G}$ for the internal currents and approximate the full internal current vector $\boldsymbol{g}(\boldsymbol{u})$ as a linear combination of fewer amplitudes gathered in the vector $\boldsymbol{c}$. The basis $\boldsymbol{G}$ is a subspace of the full internal current space and can thus be used to write the currents as

$$\boldsymbol{g}(\boldsymbol{u}) = \boldsymbol{G}\boldsymbol{c}(\boldsymbol{u}) + \boldsymbol{r} \tag{15.13}$$

where $\boldsymbol{r}$ is a residuum resulting from the approximation in the subspace.

Internal Current Subspace To build the subspace $\boldsymbol{G}$ for the internal currents, the internal currents obtained during the pre-processing (representative full simulation) are stored as internal current snapshots[1] $[\boldsymbol{g}(\boldsymbol{u}_1), \ldots, \boldsymbol{g}(\boldsymbol{u}_m)]$. A representation subspace $\boldsymbol{G}$ for the internal currents is then generated by performing and truncating a POD on those internal current snapshots.

Collocation Points With a truncated $\boldsymbol{G}$, equation eq. (15.13) is overdetermined. The minimization of $\boldsymbol{r}$ can be achieved by selecting dofs where eq. (15.13) has to be fulfilled:

$$\boldsymbol{P}^T\boldsymbol{g} = \boldsymbol{P}^T\boldsymbol{G}\boldsymbol{c} \tag{15.14}$$

The Boolean matrix $\boldsymbol{P}$ selects the so-called collocation points chosen using an empirical greedy algorithm that recursively picks the dof with the biggest residuum of eq. (15.13). The internal current can then be approximated as follows, while the superscript "+" indicates the pseudo inverse:

$$\boldsymbol{g} \approx \boldsymbol{G}(\boldsymbol{P}^T\boldsymbol{G})^+\boldsymbol{P}^T\boldsymbol{g} \tag{15.15}$$

In [47], it is shown that only a few DEIM collocation points are needed to represent the non-linear current vector. Too many collocation dofs could lead to overfitting of the internal current vector and, therefore, to instabilities in mechanical systems. This effect is not further investigated in this contribution. Further information can be found in [23].

Evaluated Elements For this contribution, the number of collocated dofs is chosen to be n_s. The internal current values at the n_s chosen collocation dofs needed for the approximation of the full $\boldsymbol{g}$ have to be evaluated during the solution process. As $\boldsymbol{g}$ results from a FEM discretization, all neighboring elements have to be assessed to find the assembled current value at the collocation point. In fig. 15.1, the selected dofs in terms of the edge elements are marked in red. To find the assembled dof value of the internal current, the neighboring elements have to be evaluated.

[1] As the internal current snapshots are used to generate a basis for the internal currents, it is also possible to use different solution vectors as those used for the generation of the Galerkin basis $\boldsymbol{V}$ of the field solution.

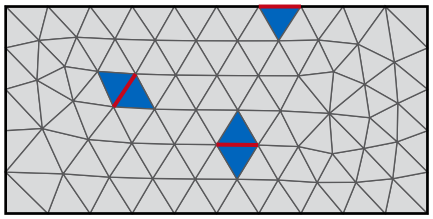

Figure 15.1: Generic example of selected DEIM edges and the neighboring elements.

15.3.2 Hyperreduction

The whole procedure results in an evaluation of only a subset $\tilde{\mathcal{E}}$ of elements $\mathcal{E}$. This is where the time advantage is achieved. The combination of projections can be pre-calculated to an auxiliary matrix $\boldsymbol{H}$:

$$\boldsymbol{H} = \boldsymbol{V}^T \boldsymbol{G} (\boldsymbol{P}^T \boldsymbol{G})^+ \tag{15.16}$$

The hyperreduced internal current vector and tangential stiffness matrix are then given as:

$$\boldsymbol{g}_{r,\mathrm{DEIM}}(\boldsymbol{q}) = \sum_{e \in \tilde{\mathcal{E}}} \boldsymbol{H} \boldsymbol{P}^T \boldsymbol{L}_e^T \boldsymbol{g}_e(\boldsymbol{L}_e \boldsymbol{V} \boldsymbol{q}) \tag{15.17}$$

$$\boldsymbol{K}_{r,\mathrm{DEIM}}(\boldsymbol{q}) = \sum_{e \in \tilde{\mathcal{E}}} \boldsymbol{H} \boldsymbol{P}^T \boldsymbol{L}_e^T \boldsymbol{K}_e(\boldsymbol{L}_e \boldsymbol{V} \boldsymbol{q}) \boldsymbol{L}_e \boldsymbol{V} \tag{15.18}$$

where $\boldsymbol{L}_e$ is the element localization matrix. Note that due to the very formulation of DEIM, the reduced tangent matrices are non-symmetric (see eq. (15.18)). This can be easily understood if we remember that different bases are chosen for the magnetic potential and the internal currents.

15.3.3 Different Flavors of DEIM

TISO et al. [59] proposed different variants of DEIM. One important extension is the *unassembled DEIM* (uDEIM). There, the unassembled force vector is calculated and approximated by the projection procedure. The main advantage is the further reduction of evaluated elements. Only one element per DEIM point needs to be processed. For edge elements, this advantage is less significant since fewer elements are connected over an edge than over a node of an element. Another DEIM extension [45] proposes to generate different local subspaces depending on the current state of the system. The concept is called localized DEIM (LDEIM). Using machine-learning techniques, the different subspaces are applied dynamically during the simulation, which holds the computational effort low by maintaining a high-quality result through a wide range of parameters.

15.4 ECSW - Energy Conserving Sampling and Weighting Method

The concept underlying the ECSW method was developed for non-linear finite element dynamic models in mechanical engineering in [18, 19] around 2014. It turns out that the method is closely related to the method developed in [4] to accelerate computer graphics. The core principle is to evaluate only a subset $\tilde{\mathcal{E}}$ of elements $\mathcal{E}$ and weigh them with a factor $\zeta_e > 0$.

At the Chair of Applied Mechanics, TUM, RUTZMOSER applied the ECSW method to geometrically non-linear U-shaped beam structures [49]. The latest publication on the topic is from the group of FARHAT [22]. They extend the use of ECSW to Petrov-Galerkin methods. In Petrov-Galerkin methods, the set of test functions is chosen independently from the set of basis functions. This allows for additional flexibility and potential advantages in the solution process. These methods typically require more computational effort than using a standard Galerkin method since the test and basis functions are handled separately. The use of ECSW showed a drastic reduction in computational effort by delivering high accuracy.

15.4.1 The Method's Philosophy

Seen from an abstract perspective, the computational effort to reduce arises from an integration problem. Before discretization, a continuous vector function, written for any position point $\boldsymbol{x}$, needs to be integrated to find the solution. Integration problems have been a well-known topic in mathematics ever since, and so different approaches to the approximation of integrals have also been known for a long time.

First, we define two different terms that are repeatedly used in the context of integration.

Quadrature comes probably from the Latin word *quadratura*, meaning *squaring*. Quadrature is the numerical approximation of integrals.

Cubature origins probably in the Latin word *cubus*, meaning *cube*. Cubature is the numerical approximation of integrals in higher dimensions.

Integrations, and with that also quadratures and cubatures, can be approximated using two strategies: A sampling-based strategy and a segment-based strategy. The segment-based strategy involves dividing the integration domain into smaller, manageable segments or subintervals and approximating the integral over each segment separately. These methods are well-suited for integrating functions over regular or well-defined domains, where the integration domain can be easily divided into segments. The applicability of segment-based methods to high-dimensional integrals is limited, as the number of segments required grows exponentially with dimensionality.

The sampling-based strategy involves randomly selecting or systematically choosing a finite number of sample points within the integration domain and then using these samples to estimate the integral. The sampling-based strategy is very flexible and can be applied to integrals with complex and irregular domains, making it suitable for a wide range of integration problems. Additionally, the approach is relatively easy to understand and implement. A common sampling-based integration scheme is the *Monte Carlo Integration*. There, the sampling points are chosen randomly, which leads to a relatively simple algorithm, but many sampling points are needed to provide accurate results [37].

For the development of the ECSW method, we follow the path of sampling-based approaches.

Inspiration by Gauss Integration C.F. GAUSS (*1777-†1855) published in 1814, the probably most famous quadrature algorithm to numerically integrate functions. The often as *Gauss Integration* referred method makes use of optimally chosen sampling points to achieve a stable integration for one-dimensional functions. There is no similarly efficient method known for multi-dimensional functionals. The ECSW method is inspired by the thought that integration by sampling becomes more valuable if the sampling points are chosen in an optimal way.

An additional constraint can be brought into the algorithm when the function to be integrated is **non-negative**. For the Gauss integration, it can be shown that, under special conditions, the weights of each sample must be positive for functions that are non-negative [39].

The research group of D.L. JAMES exploited the idea of searching optimal sampling points and, with them, do a sampling-based cubature in their work *Optimizing cubature for efficient integration of subspace deformations* [4]. Their contribution is applicable to multi-modal (graphics, haptics, sound, vision, physics) applications. For their method, the idea of Gauss was adopted, stating that the cubature of a non-negative function (here an energy functional) is achieved by only positive weights at specific sampled elements. They showed dramatically better efficiency than traditional Monte Carlo integration methods.

The internal currents for magnetodynamic equations can be derived from an internal energy functional Ψ as a function of any position $\boldsymbol{x}$ and the vector potential $\boldsymbol{q}$ in arbitrary basis which leads to (cf. part I, chapter 7):

$$\boldsymbol{g}(\boldsymbol{x},\boldsymbol{q}) = \boldsymbol{\nabla}_{\boldsymbol{q}} \int_{\Omega} \Psi(\boldsymbol{x},\boldsymbol{q})\,\mathrm{d}\Omega \qquad \Psi > 0 \tag{15.19}$$

A sampling-based integration can now be thought of, which transforms the integral into a finite sum over $i = 1 \ldots n$ points. The weights w_i compensate for the reduction from infinite sampling points to a finite number. The internal current density $\boldsymbol{\nabla}\Psi$ is denoted as $\bar{\boldsymbol{g}}$.

$$\boldsymbol{\nabla}_{\boldsymbol{q}} \int_{\Omega} \Psi(\boldsymbol{x},\boldsymbol{q})\,\mathrm{d}\Omega \approx \boldsymbol{\nabla}_{\boldsymbol{q}} \sum_{i}^{n} w_i \Psi(\boldsymbol{x}_i,\boldsymbol{q}) \qquad w_i > 0 \tag{15.20}$$

$$\int_{\Omega} \bar{\boldsymbol{g}}(\boldsymbol{x},\boldsymbol{q})\,\mathrm{d}\Omega \approx \sum_{i}^{n} w_i \boldsymbol{g}(\boldsymbol{x}_i,\boldsymbol{q}) \tag{15.21}$$

The remaining task is to find the sampling points $\boldsymbol{x}_i$ and the weights w_i such that the approximation error is minimal. In order to find the positions and weights, m pairs of true solutions, so-called training sets, are produced (for instance during a pre-simulation)

$$\left\{(\boldsymbol{g}^k,\boldsymbol{q}^k)\right\}_{k=1\ldots m} \tag{15.22}$$

and an optimization is set up. The notation is compressed $\bar{\boldsymbol{g}}(\boldsymbol{x}_i,\boldsymbol{q}_k) = \bar{\boldsymbol{g}}_i^{(k)}$.

$$\begin{bmatrix} \bar{\boldsymbol{g}}_1^{(1)} & \cdots & \bar{\boldsymbol{g}}_n^{(1)} \\ & \vdots & \\ \bar{\boldsymbol{g}}_1^{(m)} & \cdots & \bar{\boldsymbol{g}}_n^{(m)} \end{bmatrix} \begin{bmatrix} w_1 \\ \vdots \\ w_n \end{bmatrix} = \begin{bmatrix} \boldsymbol{g}^{(1)} \\ \vdots \\ \boldsymbol{g}^{(m)} \end{bmatrix} \tag{15.23}$$

Since the quadrature aims at computing a positive energy (see eq. (15.20), all weights w_i are requested to be positive. Further, the collocation condition in eq. (15.23) can be written for more time snapshots m than the number of collocation points n, leading typically to a highly overdetermined problem which is solved by a ***N**on-**N**egative **L**east **S**quare* algorithm.

$$\min ||\boldsymbol{Y}\boldsymbol{w} - \boldsymbol{b}||^2 \quad \forall w_i > 0 \tag{15.24}$$

The set of sampling points is expanded iteratively. Every iteration adds a set of sampling points such that its contribution is the most positively parallel to the current NNLS residual. The residual is then updated, and the iteration is repeated until the residuum undergoes a set tolerance. More details about the algorithm are presented in algorithm 1.

By the nature of the finite element method, the continuous integral is broken up into a sum of N elements, and the position vector and the solution state combine into the vector $\boldsymbol{u}$ with the length of the number of dofs. Sampling now means selecting individual elements and doing the integration only on those.

$$\boldsymbol{g}(\boldsymbol{u}) = \boldsymbol{\nabla}_u \sum_{e=1}^{N} \int_{\Omega_e} \Psi(\boldsymbol{u}) \, \mathrm{d}\Omega_e \tag{15.25}$$

$$\simeq \boldsymbol{\nabla}_u \sum_{e=1}^{n<N} w_e \Psi_e(\boldsymbol{u}) \tag{15.26}$$

$$= \sum_{e=1}^{n<N} w_e \boldsymbol{\nabla}_u \Psi_e(\boldsymbol{u}) \tag{15.27}$$

$$= \sum_{e=1}^{n<N} w_e \boldsymbol{g}_e(\boldsymbol{u}) \tag{15.28}$$

The term ***E**nergy **C**onserving **S**ampling and **W**eighting* was introduced by C. FARHAT in [18] who developed the method in a structural mechanics context and laid a theoretical foundation using the virtual work principle. Additionally, he could present a proof that the ECSW method preserves stability [19].

15.4.2 Method Description

The here given description of the ECSW method follows the thoughts of Farhat and translates the quantities of structural dynamics to the domain of magnetodynamic systems. The method's description is seen as a complementary explanation to the before-seen explanation via continuous integration.

The sum of all virtual work contributions, produced in an element by the internal currents, should be approximated as accurately as possible. Therefore, considering the contribution of each element to the reduced current, one can write

$$\begin{aligned} \boldsymbol{V}^T \boldsymbol{g}(\boldsymbol{V}\boldsymbol{q}) &= \sum_{e \in \mathcal{E}} \boldsymbol{V}^T \boldsymbol{L}_e^T \boldsymbol{g}_e(\boldsymbol{L}_e \boldsymbol{V}\boldsymbol{q}) \\ &\approx \sum_{e \in \tilde{\mathcal{E}}} \zeta_e \boldsymbol{V}^T \boldsymbol{L}_e^T \boldsymbol{g}_e(\boldsymbol{L}_e \boldsymbol{V}\boldsymbol{q}) = \boldsymbol{Y}\boldsymbol{\zeta} \end{aligned} \tag{15.29}$$

where

$$\boldsymbol{Y} = \left[\boldsymbol{V}^T \boldsymbol{L}_1^T \boldsymbol{g}_1(\boldsymbol{L}_1 \boldsymbol{V}\boldsymbol{q}) \; \ldots \; \boldsymbol{V}^T \boldsymbol{L}_{\mathcal{E}}^T \boldsymbol{g}_{\mathcal{E}}(\boldsymbol{L}_{\mathcal{E}} \boldsymbol{V}\boldsymbol{q}) \right]$$

and where $\boldsymbol{\zeta}$ is only non-zero for the selected set $\tilde{\mathcal{E}}$, a subset of the full element set $\mathcal{E}$. This expression is no longer an approximation if $\tilde{\mathcal{E}} = \mathcal{E}$ since $\boldsymbol{\zeta}^\star = \begin{pmatrix} 1 & \ldots & 1 \end{pmatrix}$. To find a $\boldsymbol{\zeta}$ with as many zero entries as possible, which approximates the sum of the virtual work to a defined tolerance, a set of m training sets $\boldsymbol{q}_s$ and their internal currents are needed.

Training Sets The training set generally describes a group of full solution vectors ($\boldsymbol{u}_s$) for arbitrary load situations. Here, each solution vector at each time step (=snapshots) of a given external load trajectory is gathered into the training sets. To further proceed with the sNNLS, the full solution vectors are filtered with the beforehand chosen basis $\boldsymbol{V}$. For that, the snapshots are projected into the subspace by $\boldsymbol{q}_s = \boldsymbol{V}^T \boldsymbol{u}_s$.

Considering the projected solution vectors pre-computed during pre-processing, one can compute the contribution $\boldsymbol{V}^T \boldsymbol{L}_e^T \boldsymbol{g}_e(\boldsymbol{L}_e \boldsymbol{V} \boldsymbol{q}_s)$ of each element to the reduced current $\boldsymbol{V}^T \boldsymbol{g}(\boldsymbol{V}\boldsymbol{q}_s)$ at each computed time step t_s. Indeed, each internal current contribution needs to be recalculated for each snapshot as the values will differ from the values during the time-stepping solution due to the filtering with the new, reduced subspace. [2]

Remark

NGSolve provides a discontinuous space where all the elements are not connected to each other. A given solution vector can be projected into the discontinuous space. This allows us to get the internal currents at the degrees of freedom of each unassembled element in a vector. By selecting the entries of the basis $\boldsymbol{V}$, the computation of the entries for $\boldsymbol{Y}$ is conducted.

sNNLS This elemental contribution information is then used to find a minimum set of non-zero ζ to approximate the reduced currents $\boldsymbol{V}^T \boldsymbol{g}(\boldsymbol{V}\boldsymbol{q}_s)$ up to a given tolerance τ. Also, to guarantee the positive definiteness of the associated energy, all weightings in ζ_e must be positive. A quasi-optimal set $\boldsymbol{\zeta}$ can be found by a ***s**parse **N**on-**N**egative **L**east **S**quare* (sNNLS) solver. More details on this algorithm can be found in [18].

A short description of the element selection algorithm is given in algorithm 1. The sNNLS serves to find the corresponding weights for the given elements. To find the next element, added to the selection $\mathcal{S}$, the element with the biggest virtual work residuum is selected. With that, new weights are computed, and the new residuum is checked against the tolerance τ. If necessary, the next iteration is made.

Algorithm 1 Greedy Element Selection

Require: $m \geq n$
Ensure: $w_i > 0$
  while $res > \tau$ **do**
    $\mathcal{S} \leftarrow$ Select Candidate Elements
    $\boldsymbol{w} \leftarrow NNLS(\boldsymbol{Y}_\mathcal{S}, \boldsymbol{b})$
    $res \leftarrow \boldsymbol{b} - \boldsymbol{Y}_\mathcal{S} \boldsymbol{w}$
  end while

Evaluated Elements As the unassembled currents are used to calculate the virtual work of each element, the weighting factors $\boldsymbol{\zeta}$ are also at the level of unassembled elements. In fig. 15.2, the active elements are marked in blue and their associated dofs in red.

[2] If one knows the subspace, spanned by the basis $\boldsymbol{V}$ beforehand, one could also compute the training snapshots directly in that space and reuse the internal currents for each element for the sNNLS.

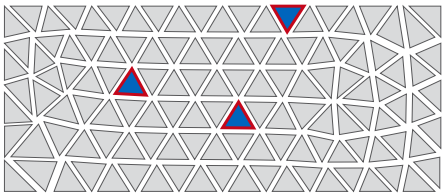

Figure 15.2: Generic example of selected ECSW elements and the associated dofs.

15.4.3 Hyperreduction

After finding the desired weighting vector $\boldsymbol{\zeta}$, the hyperreduced internal currents vector and tangential stiffness matrix are given as:

$$\boldsymbol{g}_{r,\mathrm{ECSW}}(\boldsymbol{q}) = \sum_{e\in\tilde{\mathcal{E}}} \zeta_e \boldsymbol{V}^T \boldsymbol{L}_e^T \boldsymbol{g}_e(\boldsymbol{L}_e \boldsymbol{V}\boldsymbol{q}) \tag{15.30}$$

$$\boldsymbol{K}_{r,\mathrm{ECSW}}(\boldsymbol{q}) = \sum_{e\in\tilde{\mathcal{E}}} \zeta_e \boldsymbol{V}^T \boldsymbol{L}_e^T \boldsymbol{K}_e(\boldsymbol{L}_e \boldsymbol{V}\boldsymbol{q}) \boldsymbol{L}_e \boldsymbol{V} \tag{15.31}$$

Note here that by construction, the reduced tangent matrix is symmetric and positive definite. This not only reduces the cost of solving the linear problem but also guarantees stability [18].

Let us note that the selection of elements and weights for the hyperreduction could also be performed on the full problem. That means one would apply the concept of ECSW in order to approximate the full internal force, which would then subsequently be projected on $\boldsymbol{V}$ during the simulation with the ROM. The selection of elements and weights would still be determined by eqs. (15.30) and (15.31) but where $\boldsymbol{V} = \boldsymbol{I}$. This would have the advantage that the hyperreduction parameters are not determined for a specific reduction space and would be applicable even when $\boldsymbol{V}$ is changed, but it was observed in [19] that the number of chosen elements would be significantly higher. Indeed, FARHAT observes in his numerical experiments a correlation between the number of selected elements and the dimension of $\boldsymbol{V}$. Considering furthermore that the ECSW parameter are then not optimized for the reduced force related to specific subspace $\boldsymbol{V}$, one expects that the hyperreduction would be less effective.

15.4.4 Variations of ECSW

The shown *sNNLS* is not the only algorithm to find the active set. CHAPMAN compares in [14] two further mesh sampling algorithms which account for a positive ζ, namely the polytope faces pursuit (PFP) solver and the non-negative variant of the least absolute shrinkage and selection operator (LASSO) [17] which come from the statistics field. In summary, [14] showed that the sNNLS was the best choice in most cases.

15.5 EMCP 2D Example - Results

To illustrate the methods and investigate their applicability, an example denoted here as *Electro Magnetic Computing Problem (EMCP)* is constructed (fig. 15.3). It can be seen as a model for a generic electromagnetic actuator/sensor problem where a solenoid is present. The model is first considered in 2D and will later be extended to 3D.

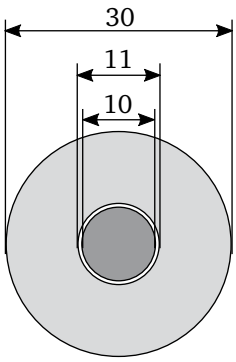

(a) 2D Geometry of the EMPC example.

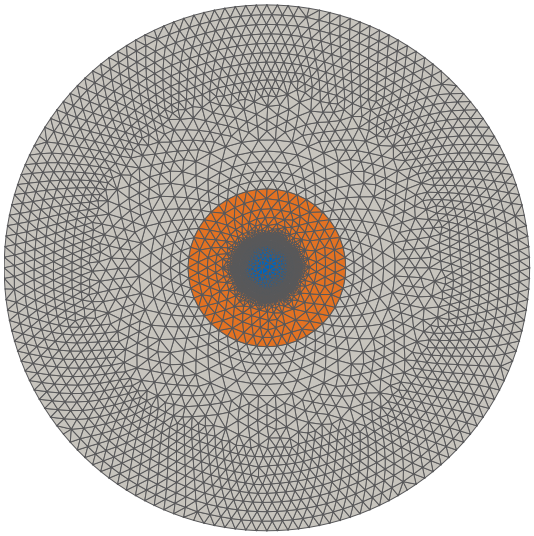

(b) Triangulated Mesh. The core is marked blue, the coil orange. The surrounding air diameter is 10 times the core diameter.

Figure 15.3: 2D example system EMCP1.

The system consists of two parts. A cylindrical core of (non-linear) steel is surrounded by a thin layer of air and a concentrical coil. The system is embedded in a circular area of air with radius 50 mm. The exciting current density vector $\boldsymbol{j}$ is considered to be in the transversal cross-section (plane perpendicular to the solenoid axis). Therefore, the solution field vector $\boldsymbol{A}$ will also be in the plane. To achieve a good FEM approximation, edge elements should be taken. So, the finite element discretization is performed in the $\boldsymbol{H}^{\text{curl}}$-Space, first order with skipping the gradient dofs [58].

Framework All work done for this contribution is performed using the framework *NGSolve* and *Python*. The open source package *NGSolve* is an object-oriented finite element core library, written in C++ with a full Python API [57]. Closely connected to it is the automatic mesh generator *Netgen* [56], which is capable of meshing 2D and 3D geometries provided by a Constructive Solid Geometry (CSG).

15.5.1 Reference and Training Simulation

For the reference simulation, the geometry meshes with 9502 triangular elements, which results in 14 331 dofs (fig. 15.3). The orange part marks the coil area where the external load $\boldsymbol{j}$ is applied in a circular manner. The blue part shows the non-linear ferromagnetic material. The rest is modeled as the vacuum.

The results of this reference simulation are later used as training data to generate the basis for the solution space and to search for the evaluated elements in the hyperreduction process.

Excitation Signal The excitation signal for the reference simulation is a current density (magnitude of $\boldsymbol{j}$) that is applied as a sinus curve with 10 Hz and four different amplitudes in a geometric series $\hat{j} = \{0.5, 1.0, 2.0, 4.0\}\mathrm{A\,mm^{-2}}$, see fig. 15.5. This excitation unveils nicely the non-linear behavior, especially the inertia due to the eddy currents and the saturation of the material.

Material As a non-linear material, a generic steel model is proposed. The constitutive equation is formulated as a polynomial such that it is comparable to real interpolated values from material data sheets (fig. 15.4). The expression for the permeability of the material as a function of the magnetic flux is formulated as

$$\mu_r(B) = \frac{2000}{0.4 + \left(\frac{B}{\mathrm{T}}\right)^8} + 1 \tag{15.32}$$

where the magnetic flux density B is given in Tesla (T).

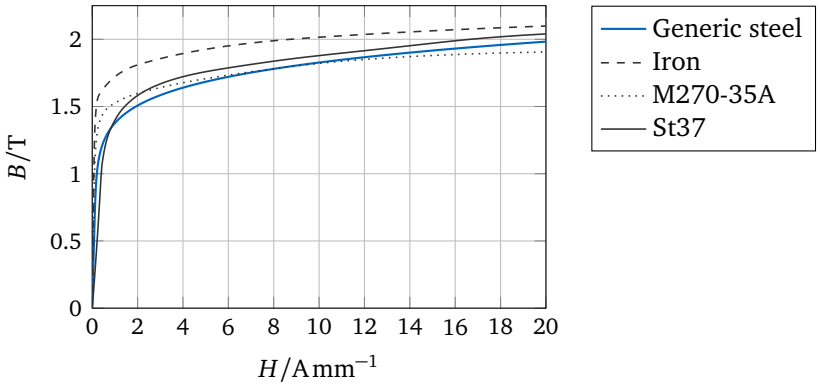

Figure 15.4: Material behavior for different types of steel in comparison to the generic, analytical material law.

The skin depth where eddy currents are dominant is estimated using an averaged $\mu_r = 1000$ and a conductivity of $\sigma = 10 \times 10^6\,\mathrm{A\,V^{-1}\,m^{-1}}$. From eq. (10.6) with an excitation frequency $f = 10\,\mathrm{Hz}$, a depth of eddy currents of around $\delta \approx 5\,\mathrm{mm}$ results. The maximum element size is therefore set to $h = 0.2\,\mathrm{mm}$ in the core mesh.

Evaluation Measures The vector field $\boldsymbol{A}$ is computed for the full problem, and, for the discussion, the magnitude of the $\boldsymbol{B}$-field is evaluated at the center of the ferromagnetic material (see fig. 15.5). In contrast to this local measure, the magnetic energy eq. (15.33) and the power loss eq. (15.34) of the system is computed as a global measure. The magnetic energy W and the power loss P are defined as:

$$W = \int_\Omega \int_0^B H(\tilde{B})\,\mathrm{d}\tilde{B}\,\mathrm{d}\Omega \tag{15.33}$$

$$P = \int_{\Omega_c} \frac{|j_c|^2}{\sigma}\,\mathrm{d}\Omega \tag{15.34}$$

Time step The time integration is performed with the backward Euler with a time step of 0.001 s. Different time step sizes were tested to verify that the solution was well converged.

Table 15.1: Computer configuration with installed environment versions

Processor	Intel®Xeon™E3-1270 v5 @ 3.60 GHz
RAM	32 GB
OS	Win 10
Python	3.8.12
NGSolve	6.2.2105

Discretization Convergence The convergence of this reference simulation was checked with a second computation of the problem with a mesh having 50 % more elements (14 219). The relative error of the evaluation point over all time steps was 0.7 %, and the relative error of the power loss was 0.08 %. With that, the reference simulation was assumed to be accurate enough to investigate the effect of reduction.

Computational Setup The computations were performed on the machine, given in table 15.1. The SuperLU 5.2.1 direct solver (sparse LU factorization, shipped with Scipy 1.7.1 as *spsolve*) was used as a linear solver. In comparison, also the PARDISO 5 solver via the NGSolve API was tested and found to result in slightly less accuracy but better performance.

When specifying the number of dofs, only the free dofs are counted, i.e., the dofs that are not restricted by the Dirichlet boundary. The Dirichlet boundary is applied to the outer boundary of the air volume and set to zero.

Reference Simulation The reference solution (fig. 15.5) exhibits a relatively large phase lag in the local B-field at the center of the core due to the damping characteristics arising from the eddy currents. Also, the saturation of the material can be seen as the amplitude of the B-field is limited and does not follow the sinusoidal variation of the excitation. The power loss is the highest when the rate of change of the load is high, as then most of the eddy currents are induced and converted to heat by the electric resistance. Notice that the system is at rest at the beginning of the simulation. This results in a transient behavior until the system is in a steady state condition. The effect can be seen in the power loss graph.

15.5.2 Reduction Basis

To generate the reduction basis, a set of snapshots is decomposed with the SVD algorithm. For this example, all solution vectors of one sinus cycle of the reference problem are considered. The singular values of the given snapshot matrix are shown in fig. 15.6a for a linear and non-linear material. It is obvious that the non-linear system needs more vectors to be approximated in an accurate way. For better visualization, the rotation of the left singular vectors (dimension of vector potential $\boldsymbol{A}$) of the SVD decomposition is taken to represent modes in a magnetic field-like structure. Also, only the core is shown in fig. 15.6b. All modes exhibit patterns where the magnetic flux density forms concentric circles. In the notation for circular membranes, which are typically numbered with two integers, denoted as (m, n), where m is the number of nodal diameters and n is the number of nodal circles, for this specific case, all modes would have $m = 0$.

To ensure a good quality of the basis, two different relative errors (global and local) are calculated with eq. (14.3) and eq. (14.4) for the training sets filtered ($\boldsymbol{u}_{\text{filtered},n} = \boldsymbol{V}\boldsymbol{V}^T\boldsymbol{u}_{\text{ref},n}$) with the basis V constructed from a rising number of POD vectors, shown in fig. 15.7. The selected evaluation measures are computed from the filtered solution snapshots. While the

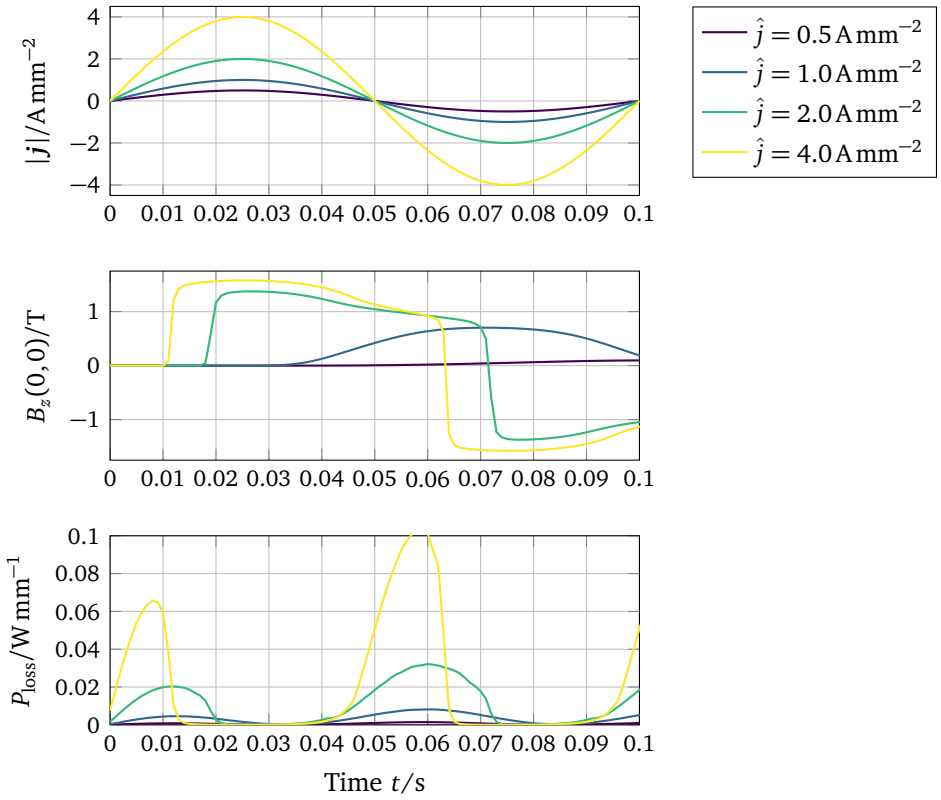

Figure 15.5: The reference results for a sine excitation with increasing amplitude show strong non-linear behavior, measured in the center point of the core. A doubling of the excitation is far away from doubling the magnetic flux density in the center of the core.

error of the power loss in the system is a global measure, the magnitude of the B-field at the center is a very local measure. This local error is much harder to minimize. To show the difference to a linear system, where very few modes are needed to fully describe the system, the comparison is made for a constant, linear ferromagnetic material law.

For the further use of the example, the basis is built using the first 8 left singular vectors. Summing up the squares of the singular values, they represent 99.2 % of the total sum of singular value squares. The squared singular values provide a quantification of the energy associated with different modes in the system's response. Modes with lower energy contribution can potentially be neglected without significantly affecting the system's behavior. In the given example, the relative error of the global power loss drops fast to very low percentages. In contrast, the error of the local B-field point in the middle of the core already needs 10 modes to undergo the 10 % limit. The decrease rate is relatively low. Concluding, it is a question of what the model must be capable of for the final application.

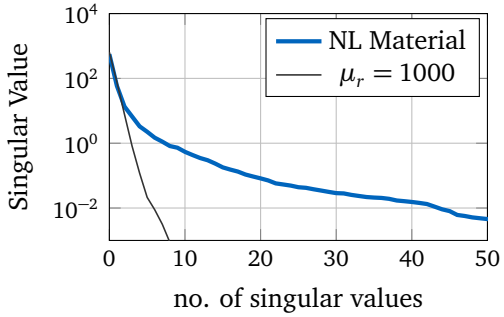

(a) Singular values for the non-linear material decay slower than for the linear material $\mu = \text{const.}$

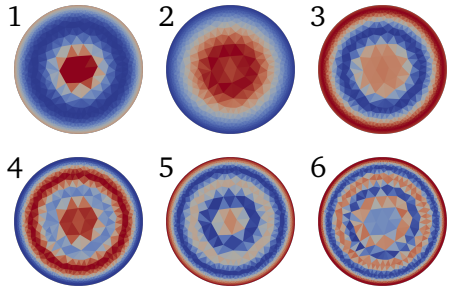

(b) First six modes of the basis from solution vectors.

Figure 15.6: Building the basis from the reference's solution snapshots using the SVD algorithm.

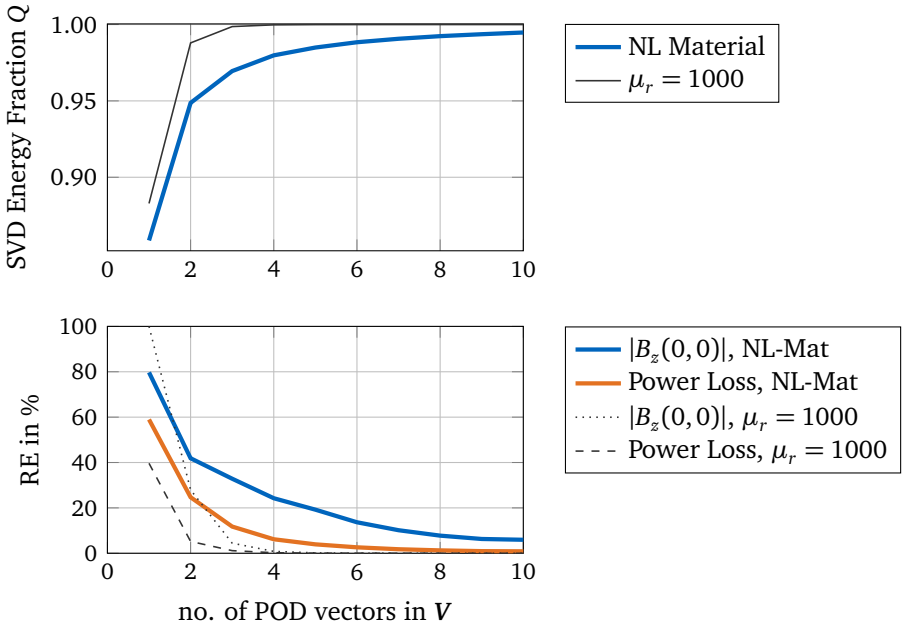

Figure 15.7: Relative singular value energy fraction and relative errors of two field quantities as a function of the numbers of basis vectors (2D problem).

15.5.3 DEIM - Hyperreduction

The subspace for the assembled internal current vector is truncated after the first n_S left singular vectors. This results in the collocation to n_S dofs (for the chosen strategy of equal current-modes and collocation dofs), requiring slightly less than $2n_S$ evaluated elements (boundary dofs don't require two elements).

Variation of Subspace Truncation Changing the truncation limit for the current subspace leads to a change in the active elements. The relative error of the vector potential originating from the hyperreduction then decreases (fig. 15.8). Interestingly, the decrease is not monotonic and not steep. This can be understood by the fact that the collocation points in DEIM are chosen greedy and do not guarantee a global optimum.

The relative error depicted in fig. 15.8 is relative to the projected solution with the chosen basis. This allows us to see the additional error that arises from the hyperreduction. The red-

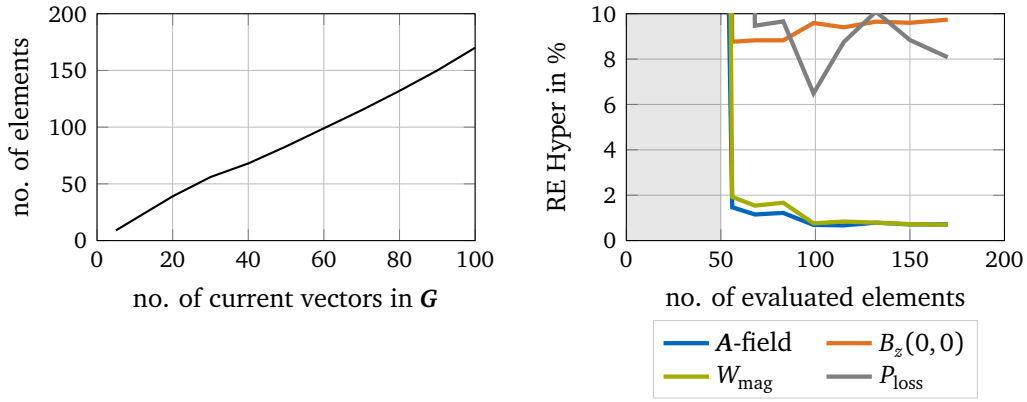

Figure 15.8: Increasing number of current vectors leads to a nearly linear increase of selected elements. The trend of the relative error, comparing the reduced and the hyperreduced solution, is not clear for a higher number of evaluated elements. The gray area indicates that no converging solution could be obtained.

marked area shows configurations of the hyperreduced model where the solution is unstable and does not converge. This is definitely a major drawback of the DEIM.

Solver The tangential stepping matrix for the DEIM-reduced model is not symmetric anymore but is fully populated. Therefore, the solver from LAPACK 3.4 was used via Scipy with the pre-settings for general matrices.

15.5.4 ECSW - Hyperreduction

The 2D problem considered above and hyperreduced with the DEIM is now considered for hyperreduction with ECSW, using the same reduction basis determined in section 15.5.2.

Variation of τ In order to increase the precision of the hyperreduction, the τ-criterion of the sNNLS is set to a range from 10^{-1} to 10^{-5} and plotted in fig. 15.9. With decreasing τ, the number of active elements rises steadily. However, all the relative error measures of the hyperreduction first increase with decreasing τ (which is counter-intuitive), then start falling, reaching a plateau. All this is in a very small bandwidth of the error. At this place, it could not be clarified why the error of the $\boldsymbol{B}$-field stays at that plateau and doesn't improve anymore. Obviously, the ECSW Method is always stable, and the results are meaningful even for a very low number of evaluated and weighted elements.

The sNNLS with a tolerance of $\tau = 10^{-3}$ selected 49 elements (fig. 15.10) with weights in the range from 1.462 to 1991.

Solver The reduced linear problem for the ECSW method is symmetric and positive definite by nature. Therefore, this property can be exploited by the solver. In this case, the non-sparse (the matrix is fully populated) direct Cholesky solver from LAPACK is used via Scipy due to the additional information that the matrix is positive definite. Note that the SuperLU factorization via Scipy was also tested, but it was always significantly slower. But as seen later, the time for solving the linear problem is only a small portion of the complete computational wall time.

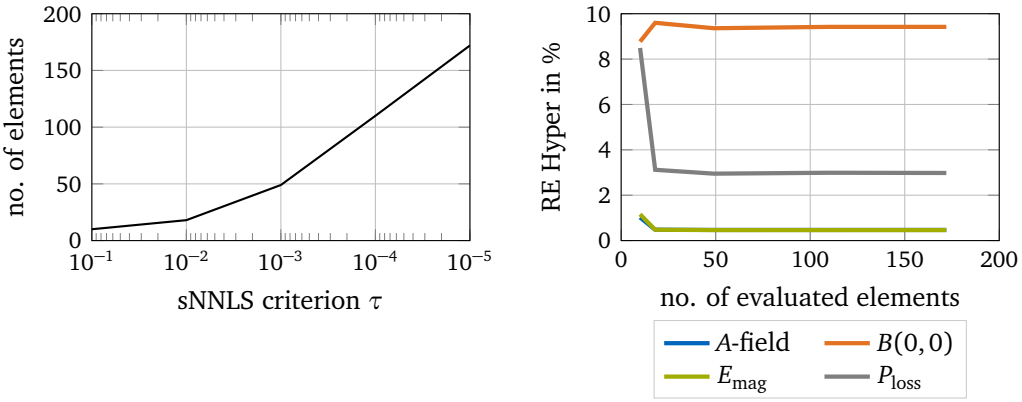

Figure 15.9: A decrease of the tolerance τ leads to an increase of selected elements with progressive tendency. The number of evaluated elements leads to a slight decrease in the relative hyperreduction error. A solution is always obtainable. The error is large for very few elements.

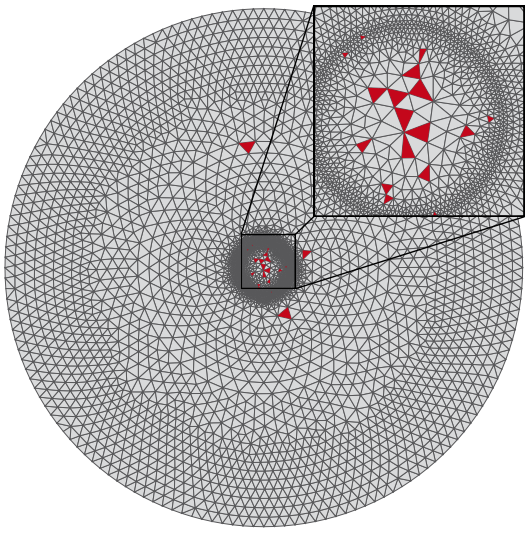

Figure 15.10: Selected ECSW elements are marked red. Most elements are in the core, and only very few are in the coil and the air.

15.5.5 Evaluation of Computational Effort

To investigate the computational effort and, therefore, the achieved speedups for both hyper-reduced models, the solution process is split into three main components. The first step is to apply the latest solution to the non-linear current function to *evaluate the residual* eq. (8.15). Second, the *tangential stiffness* matrix is built. These two steps correlate with the number of elements. The third step, *solving* of the linear problem, scales with the number of dofs the projected system results in. Table 15.2 shows the results, separated by a horizontal line for the element number dependent sizes and the dof number dependent ones. All steps are iterated until convergence is reached. All computational times are given for one simulation time step, meaning that the computational times for every iteration are summed up during the convergence of one time step. As the number of iterations will vary due to the actual load- and system state, all times are averaged over the whole trajectory (i.e. all time steps) of the simulation. It should be noted here that no outliers regarding the times could be identified.

There is a limit to the achievable time reduction due to some overhead time for data-handling operations, which becomes obvious in the step of the residual evaluation. A slight

Table 15.2: Computational effort values for full- and reduced-order model (average values for one time step).

	Full	MOR		
		DEIM	ECSW	rel
Elements	9502	115	110	≈1 %
Residual Evaluation	0.025 s	0.003 s	0.003 s	≈10 %
Tangent Matrix	0.056 s	0.001 s	0.001 s	≈2 %
Dofs	14175	8	≈0.1 %	
LinSolve	46 ms			
"		0.45 ms		≈1 %
"			0.08 ms	≈0.2 %
Iterations	7	5	5	

drawback of the DEIM hyperreduction can be seen in the fact that the reduced matrix is not symmetric and therefore needs a more advanced solver which takes a bit more time. In the further course of the study, computational time data are omitted since they correlate mainly with the element number, as shown here, whatever hyperreduction method is used.

For the next test, the number of current vectors in DEIM and the tolerance τ for approximating (eq. (15.29)) are tuned to keep roughly the same number of elements. So, we will compare the results in terms of accuracy, with the number of elements evaluated in the hyperreduction (and thus the computational time) being similar.

15.5.6 Methods Comparison - Test Trajectory

The obtained hyperreduction parameters (Basis $\boldsymbol{V}$, DEIM: active elements and current-basis $\boldsymbol{G}$, ECSW: active elements and weighting vector ζ) are now frozen and stored for the next reduced computation. Both reduction methods are constructed such that they evaluate approximately the same amount of elements (table 15.3). With that, the time savings are roughly the same, but the quality of the results is examined. First, the stored reduced models are excited with a different frequency applied. As far as the mesh density is high enough to represent the correct eddy currents (see eq. (10.7)), the reduced models should be quite independent of the frequency thus, the reduced results are close to the reference. The results in fig. 15.11 are plotted over one period of four different frequencies, where 10 Hz was the training excitation. The ripples arise from the low number of used modes in the Galerkin projection. Both methods show very similar behavior, except for one point where the DEIM has an unstable point in the power loss while the ECSW always produces smooth results.

Second, the frequency is kept at the training frequency (10 Hz), and the amplitude of the excitation is varied. For a training amplitude of $2.0\,\mathrm{A\,mm^{-2}}$, fig. 15.12 unveils the weak representation of low amplitude behavior for the local probe point. For the global measures, the ECSW method outperforms the DEIM clearly as the results are much smoother and very close to the reference solution.

As seen in fig. 15.12, the reduced models only behave well in the near of the trained amplitudes. Performing the same experiment but with a training amplitude of $1.0\,\mathrm{A\,mm^{-2}}$ leads to fig. 15.13. This leads to a better representation of the local measures and does not affect the high-load performance too much. The advantage of the ECSW method for global measures becomes even more evident.

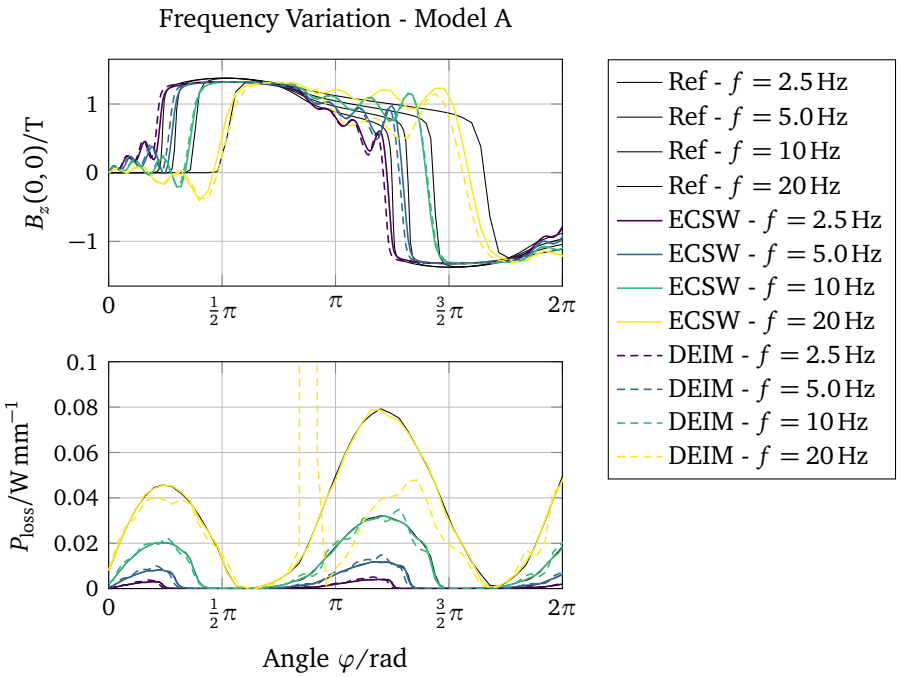

Figure 15.11: Comparison of DEIM- and ECSW-model for the variation of excitation frequency with constant amplitude ($2.0\,\mathrm{A\,mm^{-2}}$).

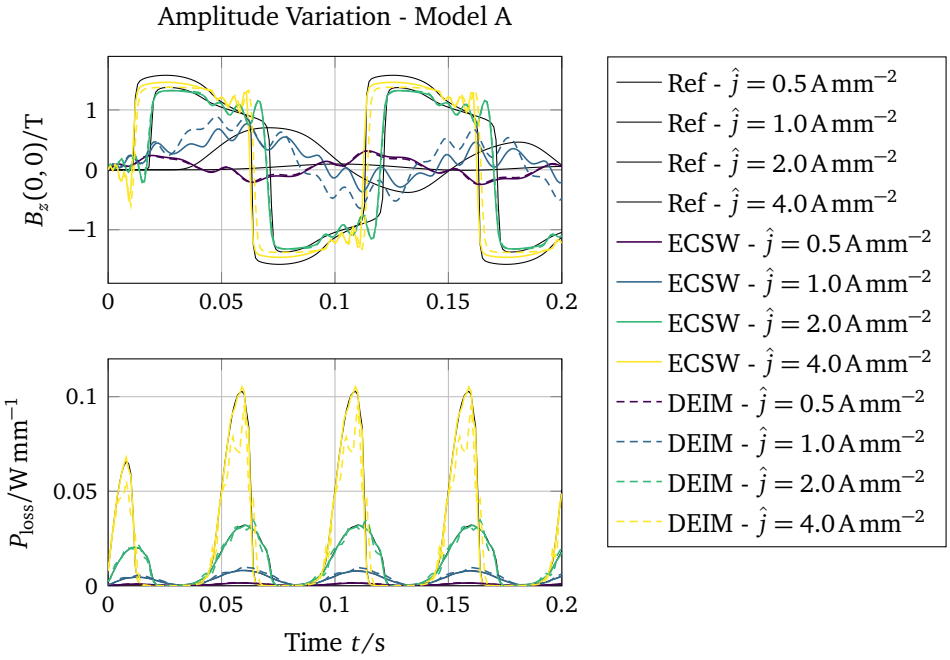

Figure 15.12: Comparison of DEIM- and ECSW-model for the variation of excitation amplitude with constant frequency (10 Hz).

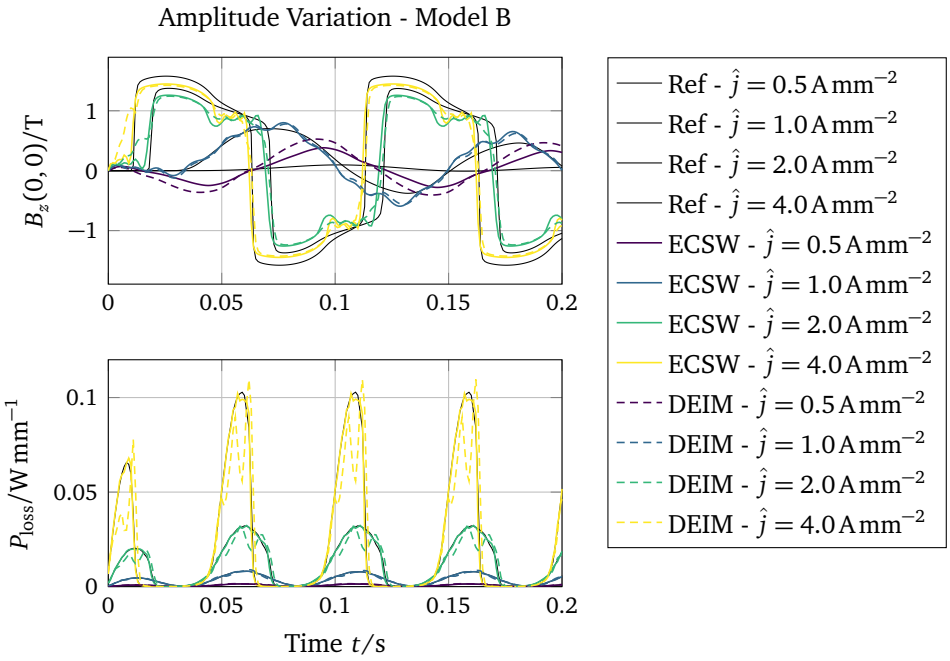

Figure 15.13: Comparison of DEIM- and ECSW-model for a training amplitude of $1.0\,\mathrm{A\,mm^{-2}}$ for the variation of excitation amplitude with constant frequency (10 Hz).

To further test and compare these stored reduced models, a new current excitation consisting of two superimposed sinuses eq. (15.35) is applied to the system.

$$j(t) = 2.0\,\mathrm{A\,mm^{-2}} \cdot \sin(2\pi\,6\,\mathrm{Hz} \cdot t) + 1.0\,\mathrm{A\,mm^{-2}} \cdot \sin(2\pi\,15\,\mathrm{Hz} \cdot t) \tag{15.35}$$

Simulations are then run for the full system, pure Galerkin projection (reduction without hyperreduction), and DEIM and ECSW hyperreduction (training: 10 Hz, $2.0\,\mathrm{A\,mm^{-2}}$) methods (fig. 15.14) with a time step 0.001 s and 500 steps.

In fig. 15.14, one observes that the hyperreduced solution is qualitatively accurate but adds additional errors of the order of the error inherent to the projection of the reduction basis itself (i.e. the Galerkin projection is made without hyperreduction). Qualitatively, the DEIM shows spurious peaks in the power loss, for example, at $t \approx 0.25\,\mathrm{s}$. This could eventually be reduced by changing the number of collocation points.

The relative errors are computed with the full simulation as a reference and listed in table 15.3. It must be highlighted that the global relative error measures are clearly better using the ECSW method even though fewer elements are evaluated.

Table 15.3: Comparison of DEIM and ECSW results using the relative error of the vector potential field.

Reduction	dofs	elements	$RE_{\text{A-field}}$	$RE_{\text{MagEnergy}}$	$RE_{B_{(0,0)}}$
full	14175	9502	-	-	-
POD	8	9502	0.25 %	0.5 %	8.6 %
POD + DEIM	8	56	3.1 %	5.2 %	14 %
POD + ECSW	8	49	0.84 %	1.85 %	13 %

Outcome Both methods result in similar behavior in the representation of the local field for load cases similar to the training sets, while the result's quality is quite independent of the load's frequency. To improve the overall local accuracy, a better basis would be needed.

From a global point of view, the ECSW result can be considered better: although a few fewer elements than for the DEIM were considered, all the relative error measures are smaller, as seen from table 15.3. Also, qualitatively, the ECSW never introduced spurious peaks and precisely estimated the power loss. The ECSW method seems to rather underestimate the system's magnetic energy and is closer to the full simulation overall. The relative error of the magnetic energy confirms this.

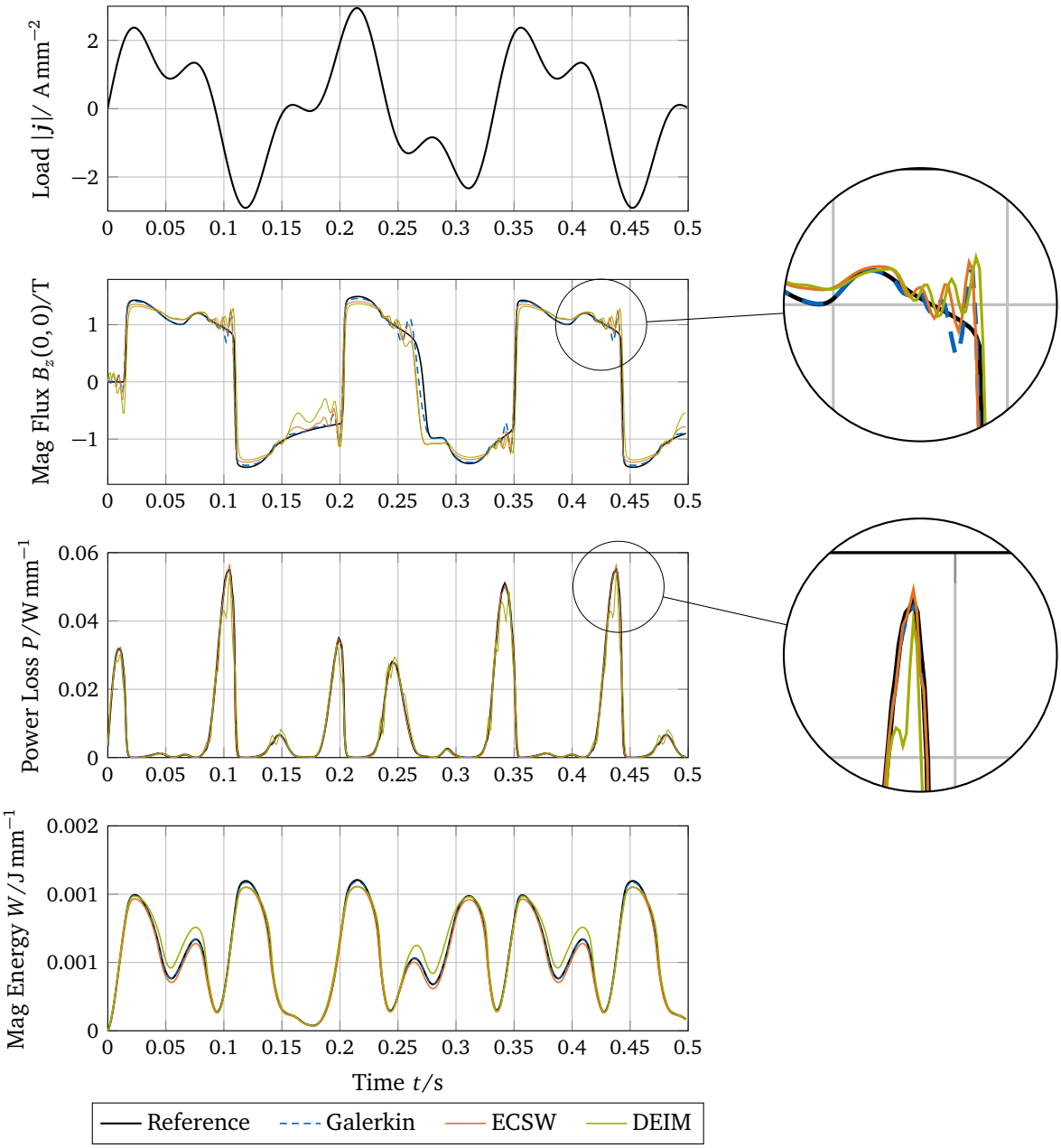

Figure 15.14: Reference result for an arbitrary test trajectory. Galerkin $n = 8$, ECSW $\tau = 10^{-3}$, DEIM $n_f = 30$.

15.6 EMCP 3D Example - Results

To further investigate the performance of the methods, a more complex example is shown here. It is based on the same problem shown before but now is in 3D. Also, a mobile target part is now included and modeled as ferromagnetic material (fig. 15.15a). Again, the number of current modes in DEIM and the criterion τ in ECSW are chosen to roughly evaluate the same amount of elements. The problem parameters are listed in table 15.4.

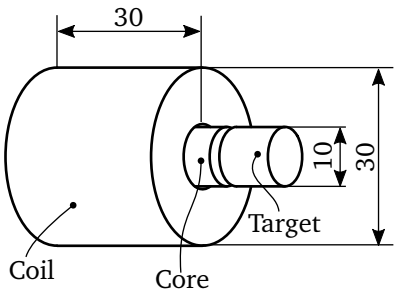

(a) Geometry of the 3D example.

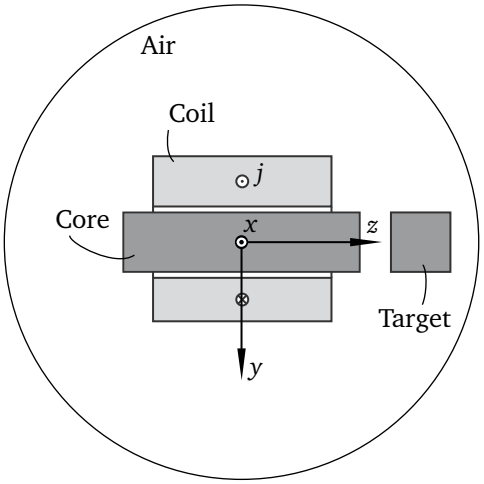

(b) Cross section of the System (not drawn to scale).

Figure 15.15: 3D example system EMCP1.

The geometry is embedded in a sphere of air with 50 mm radius. The meshing process results in a system with 33 910 elements and 40 159 total dofs.

15.6.1 Training Simulation

To find the active elements for the hyperreduction, again, the simple sine trajectory is computed full-order for one period as a training simulation and analyzed as shown before. It needs to be mentioned here that the current density is not directly comparable between the two examples. In the previous example, the cross-section of the coil is in the transverse plane, whereas in this example, the cross-section to calculate the load is in the sagittal plane. With the knowledge of the previous test, the training set should not cause a high saturation result to enable a wide amplitude tolerance in the reduced model.

Table 15.4: Training parameters for the 3D example study.

Parameter	Value
excitation	sine, 10 Hz
amplitude	6 A mm^{-2}
$\triangle t$	0.001 s
time steps	100

Because of the smoother training results with the less pronounced non-linearity, the axis-symmetric system is very well described by 8 modes.

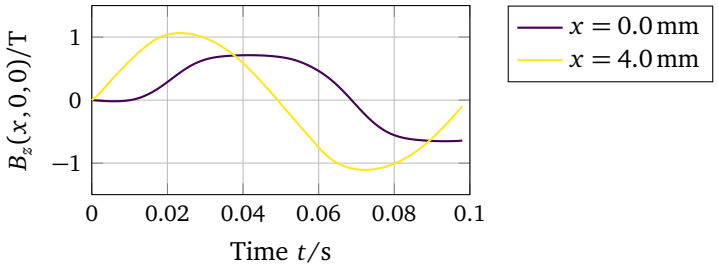

Figure 15.16: Reference result in the core for two different radial positions: Center $x = 0$, near boundary $x = 4.0\,\mathrm{mm}$. The non-linearity is not very pronounced in the training snapshots.

Table 15.5: Number of chosen elements and wall-times for the offline calculations of the DEI- and ECSW methods from the training snapshots for different strengths of hyperreduction.

	Parameter	Duration	Active Elements
DEI	$n_S = 2$	21 s	13
	$n_S = 5$	21 s	28
	$n_S = 10$	21 s	53
sNNLS	$\tau = 10^{-2}$	1.7 s	9
	$\tau = 10^{-3}$	4.9 s	20
	$\tau = 10^{-4}$	19 s	52

Evaluating the offline time that is needed to select the active elements that have to be computed later, two things stand out from table 15.5. First, the selection via DEIM rarely scales with the number of chosen current modes. For small numbers, this is rather malicious, but for a higher number of elements, this becomes a benefit. The sNNLS for the ECSW method scales directly with the tightness of the tolerance τ. For too strong demands, the algorithm will even fail and not converge. From that perspective, the DEIM is more robust.

Onboard Validation - Speedups To discuss the gained speedup of the hyperreduction methods, one exemplary ECSW simulation with the same load trajectory (sine) as the training setup was chosen. The main solution process parts are then evaluated, as shown in the 2D section. The computational time does not only scale directly with the number of evalu-

Table 15.6: Computational wall-times in the solution process of the 3D training simulation.

	Full	MOR	MOR rel
Elements	33910	20	≈0.05 %
Residual Evaluation	0.33 s	0.015 s	≈5 %
Tangent Matrix	0.84 s	0.002 s	≈0.2 %
Dofs	39169	8	≈0.02 %
Iterations	3	3	
LinSolve (SuperLU)	40 s	0.0002 s	$\approx 5 \times 10^{-4}$ %
LinSolve (PARDISO)	2 s	0.0002 s	≈0.01 %

ated elements. That is because of some programming overhead that keeps constant for every Newton iteration. This can be further improved, in which case the advantages of calculating only a fraction of the elements would become even more apparent. The bottleneck of this computation is (see table 15.6) obviously the evaluation of the residuum, which is per-

formed in every Newton-Iteration. The savings in the solution process itself seem very high. By using the PARDISO-Solver, which is much more optimized, this point is somewhat put into perspective.

15.6.2 Result for Test Trajectory

To test the reduced model, again, an unknown test trajectory is applied to the reduced model and validated against a full-order reference simulation. The results are shown in table 15.7. The full-order model already needs wall times of around 20 h with the SuperLU-Solver or 1.25 h using the PARDISO-Solver.

Three different load cases which differ mainly in their amplitude (low $\approx 2\,\mathrm{A\,mm^{-2}}$, medium $\approx 6\,\mathrm{A\,mm^{-2}}$, high $\approx 8\,\mathrm{A\,mm^{-2}}$) are applied to the reduced models. The reduced models differ in their number of elements as seen in table 15.5.

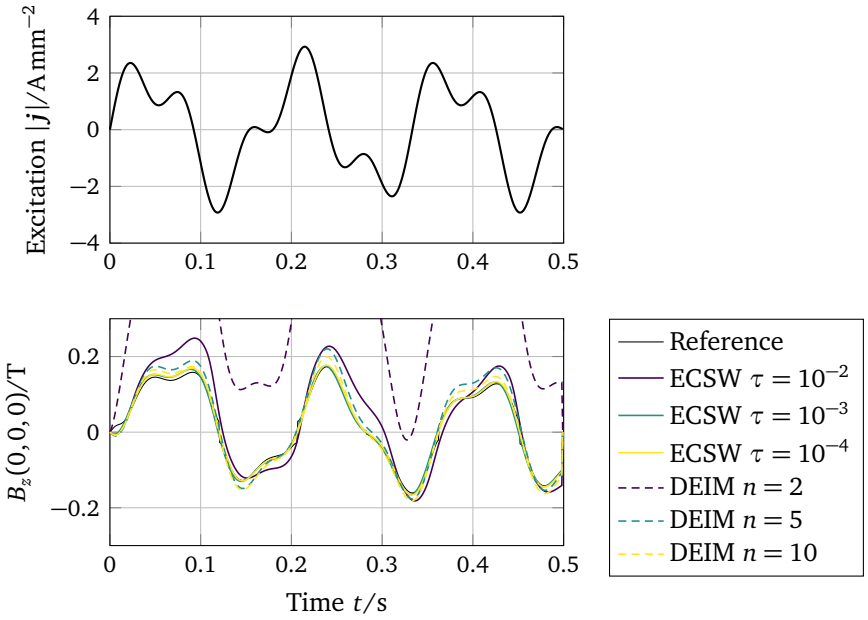

Figure 15.17: Low excitation result. The smallest DEI-model cannot represent the local field.

In figs. 15.17 to 15.19, the reduced model results are plotted for the three sets of reduction parameters. The plots for the power loss and the magnetic field energy aren't shown here, as they do not differ in any method in a visible way. It is noticeable that the approximation with only two current modes is very wrong and cannot represent the dynamics in any way. The result becomes much better when taking into account five current modes. Interestingly, the curve seems to run away for a longer simulation time. This needs to be further evaluated. The ECSW method performs very predictable, even when taking only five elements, the result is close to the reference. By tightening the tolerance τ, the quality of the result increases to a nearly perfect representation of the system's dynamic. Also, here, the ECSW method is more reliable as it keeps the result bounded close to the true reference. The wall-time for the reduced model is around 6 min to 9 min without further code optimization. This represents a significant saving compared to the full solution (1.25 h).

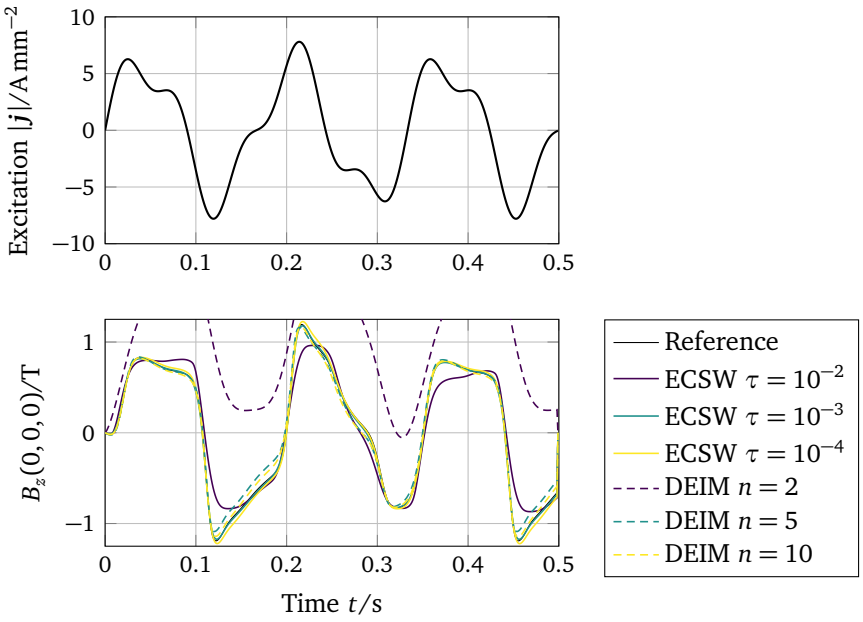

Figure 15.18: Medium excitation result. Again the smallest DEI-model is not capable of reproducing the local B-field values.

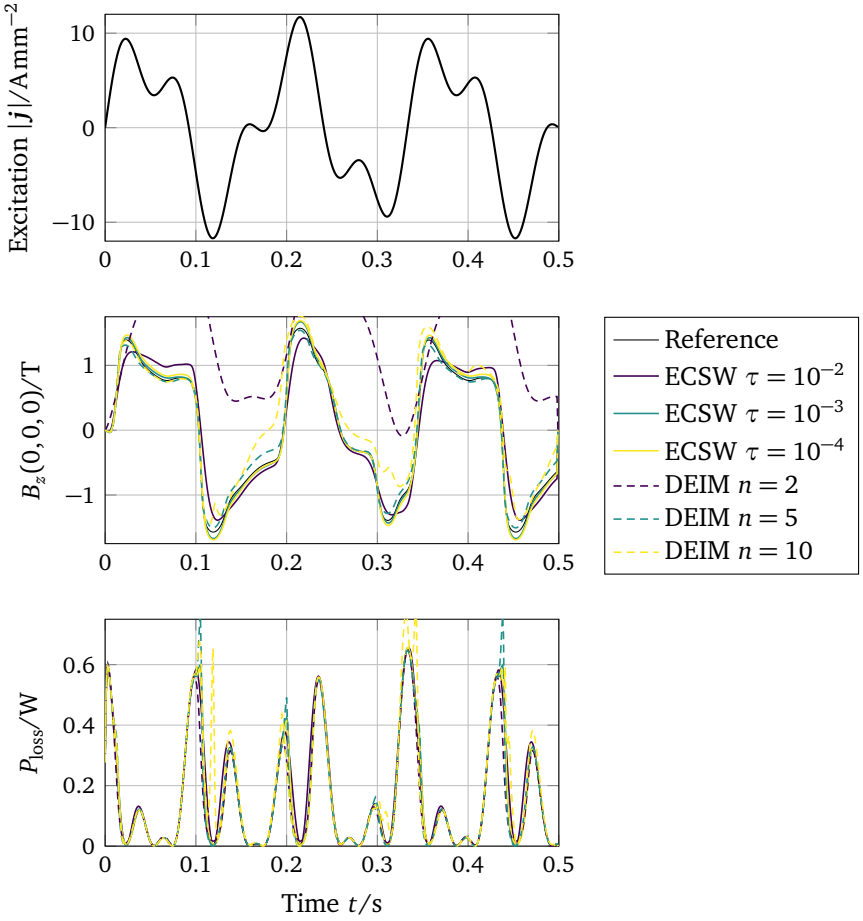

Figure 15.19: High excitation results. Even the higher order DEI-models can not represent the local B-field values well and additionally show spurious peaks in the power loss.

Table 15.7: Relative errors of the global power loss of the 3D example for different parameters and excitations for each of the two hyperreduction methods over all 500 time steps.

Reduction	dofs	elements	low $RE_{P_{\text{loss}}}$	medium $RE_{P_{\text{loss}}}$	high $RE_{P_{\text{loss}}}$
full	39169	33910	-	-	-
POD	8	33910	0.08 %	0.42 %	0.63 %
POD + DEIM	8	13	2.51 %	8.6 %	16.56 %
POD + DEIM	8	28	0.58 %	3.55 %	10.24 %
POD + DEIM	8	53	0.34 %	2.44 %	27.65 %
POD + ECSW	8	9	0.6 %	5.28 %	14.11 %
POD + ECSW	8	20	0.16 %	0.61 %	2.73 %
POD + ECSW	8	52	0.10 %	0.33 %	1.35 %

From table 15.7, one can draw the preliminary conclusion that the ECSW method performs superior DEIM in terms of result quality in relation to the number of evaluated elements. It is clearly noticeable that the ECSW-Method is more predictable as for more elements, the relative error steadily decreases. The DEIM, in contrast, shows weakness for higher amplitudes than trained. Increasing the number of elements can even worsen the result.

15.7 TEAM 10 Example - Results

In the previous section, the hyper-reduction methods have been tested on a simple academic problem. In this section, a more realistic system, namely the benchmark example TEAM 10 (introduced in section 11.3). Here only the ECSW method will be tested.

Remark

This section is partly based on the author's publication *Strategies for Finding Training Snapshots for the Hyperreduction Method ECSW in Magnetodynamic Systems*, [34].

The system fig. 15.20 is dominated by a copper ring (depicted in orange) and three thin sheet metal plates. Two c-shaped plates are arranged symmetrically around the vertical middle plate. The whole structure is surrounded by an air box to allow the magnetic- and electric field to propagate between the solid parts.

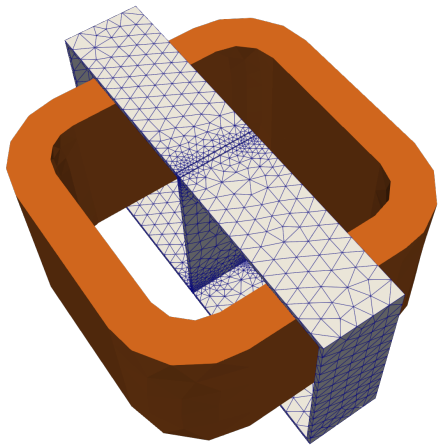

Figure 15.20: TEAM10 benchmark example, showing the mesh for the thin sheet metal plates. The whole system is encapsulated in an air box which is not shown here.

15.7.1 Training Trajectories

Training load trajectories have to fulfill certain constraints. The maximum presentable frequency of the system is determined by the mesh size and the conductivity of the material. The phenomena of skin-effect describes the depth up to which the eddy currents occur in significant amounts due to the change rate in the magnetic field density. The element size has to be at least in the same order of magnitude.

The first excitation function forms a smooth step:

$$I_1(t) = \begin{cases} 0 & (t<0) \\ I_m(1-e^{-\frac{t}{\tau}}) & (t\geq 0) \end{cases} \qquad \begin{matrix} I_m & 5.64\,\mathrm{A} \\ \tau & 0.05\,\mathrm{s} \end{matrix} \tag{15.36}$$

The second excitation function forms an impulse:

$$I_2(t) = I_m e^{-\frac{(t-m)^2}{2a^2}} \qquad I_m = 5.64\,\mathrm{A}, \quad m = 0.05\,\mathrm{s}, \quad a = 0.01\,\mathrm{s} \tag{15.37}$$

The third excitation function forms a sine:

$$I_3(t) = I_m \sin(2\pi f\, t) \qquad I_m = 5.64\,\mathrm{A}, \quad f = 10\,\mathrm{Hz} \tag{15.38}$$

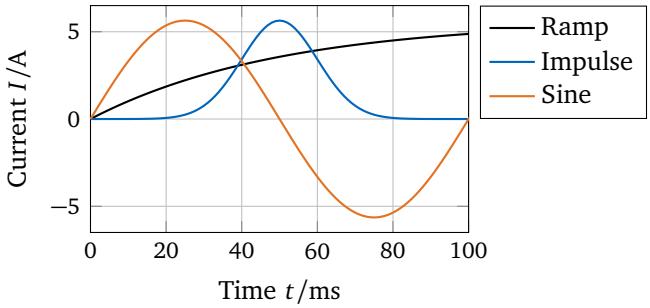

Figure 15.21: The three excitation trajectories used throughout the study.

Three training simulations differing in their excitation function are performed. All simulations are performed using the same settings $\Delta t = 2\,\text{ms}$, $n = 50$ time steps. The excitation functions are ramp, impulse, and sine.

15.7.2 Generation of Solution Subspace

The three resulting snapshot collections are used to compute one POD per experiment. The singular value decay and the subspace angles referenced to the ramp excitation are plotted in fig. 15.22. The ramp excitation leads to the fastest decay of singular values, which indicates

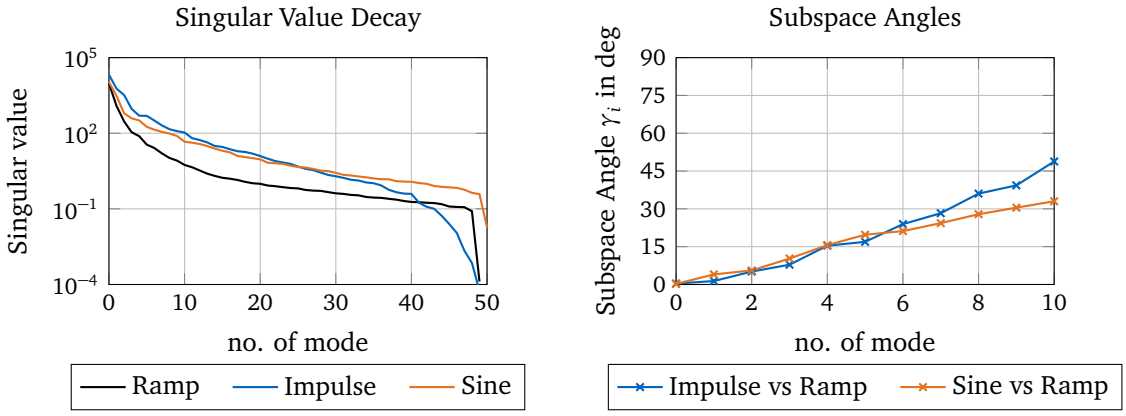

Figure 15.22: Left: Decay of the singular values for each training simulation. Right: Subspace angles of the Impulse and Sine generated subspaces in reference to the Ramp experiment.

that fewer left vectors can represent the major behavior of the solution. The impulse and sine excitation show a very similar pattern. Regarding the subspace angles, the subspaces show quite some deviations even in the first 10 modes. One can not say that one subspace embraces the other fully. The consequences of the final reduced model can't be estimated for now.

15.7.3 Selection of Evaluation Elements

The training snapshots for the element selection process (utilizing sNNLS algorithm) are chosen to be the same as for generating the subspace. The sNNLS algorithm features the tolerance τ, which sets the precision of the weighted result in relation to the evaluation of all elements.

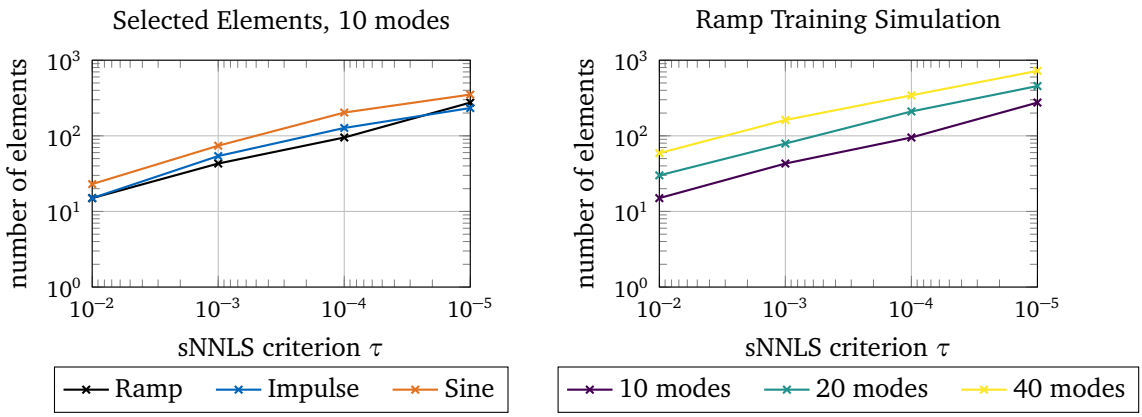

Figure 15.23: Left: Number of elements over the tolerance criterion τ for the three training sets. Right: Influence of subspace size.

The left plot shows the difference in selected numbers of elements due to different training simulations. Again, the ramp training snapshots require fewer elements to meet the tolerance than the comparison partners. A reason could be that the snapshots are simpler in their inner structure. This could indicate that they can not well represent another solution. The right plot indicates that bigger subspaces (i.e. higher number of considered modes) lead to a higher number of selected elements. The shown number of elements arise from the ramp training snapshots.

One exemplary configuration leads to the element distribution shown in fig. 15.24.

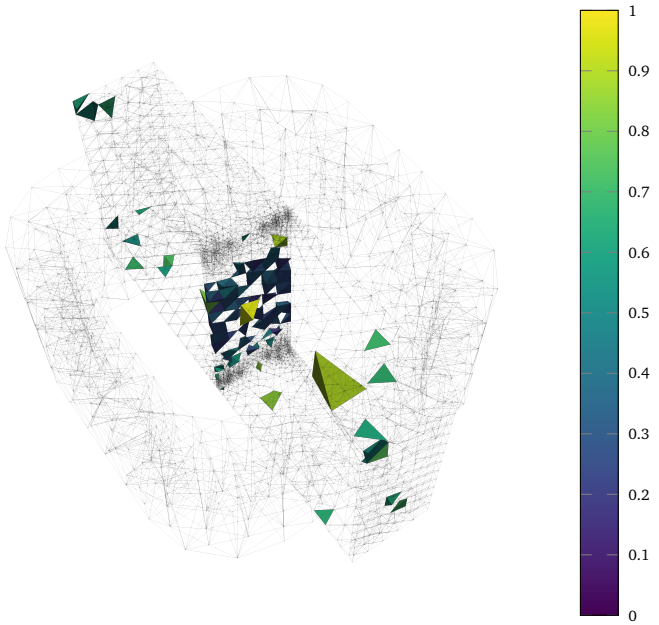

Figure 15.24: Selected elements for the ECSW method. A concentration is seen in the areas of high eddy currents. The color represents the relative weighting factor. The closer the selected elements are, the smaller the weighting factor.

15.7.4 Relative Error

Comparing the results of different hyperreduced models against their full-order reference solution leads to the Kiviat[3] diagram (i.e. a spider chart) in fig. 15.25. Each ray represents a relative error measure, whereas two local (j_{eddy} and B) and two global (W_{mag} and P_{loss}) are chosen. The shorter the circular connecting path, the better.

The time integration of the reduced-order model is computed for all three excitation functions and compared against each other. The results of the three excitations are color-coded as follows: —●— Ramp, —●— Impulse, —●— Sine.
So, the left graph of fig. 15.25 shows the errors obtained when computing the response of the system to the three different excitations using the ROM built with the Ramp training snapshots, and so on. For the middle graph, the errors for the ramp and sine excitation are outside the graph's range and therefore not visible.

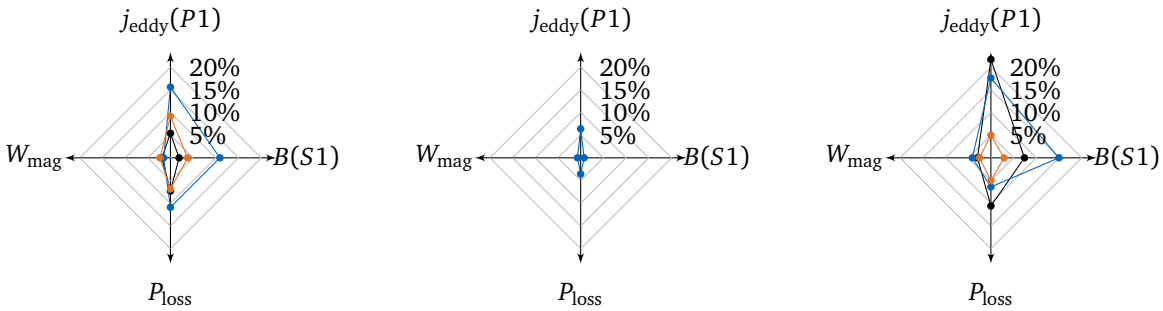

Ramp ROM	Impulse ROM	Sine ROM
10 modes	10 modes	10 modes
$\tau = 10^{-3} \rightarrow 43$ elements	$\tau = 10^{-3} \rightarrow 54$ elements	$\tau = 10^{-3} \rightarrow 74$ elements

Figure 15.25: Relative error, evaluated for different quantities (global energy W_{mag} and power loss P_{loss}, local field quantities B and the eddy current j). The graph contains the three combination groups where the reference is the full simulation respectively.

For the interpretation of the relative error numbers, one has to keep in mind that the reduced-order models are constructed to be as small as possible to give at least reasonable results. This leads to quite big relative errors, which would not be usable in good practice. Two statements can be drawn from fig. 15.25. First, the reduced-order model represents its own training simulation the best. This was expected as this is exactly how the model was trained. This is often called on-board validation. Second, the result of the impulse-trained model in combination with the ramp/sine excitation is not even close to the reference ramp or sine trajectory and is therefore not even plotted in the graph.

[3] Michael J. Kiviat, a former engineer at Lockheed Martin, is credited with inventing Kiviat diagrams, also known as radar charts or spider charts.

Chapter 16

Advanced ECSW Extensions

Calculating the mechanical forces for non-linear magnetodynamic problems in a FEM context leads to a two-stage process. First, the magnetic vector field is computed. Second, the force is derived mostly from an approach that is based on the virtual work principle.

The following chapter proposes a novel strategy to apply the hyperreduction principle for both stages of force calculation. The already established ECSW method is therefore adapted to exploit the structure of mechatronic systems, so the hyperreduction is only applied to the non-linear domain. It is therefore named partial hyperreduction, here the pECSW.

Also, the force calculation is formulated such that ECSW is applied as sampling-based integration. The force computation requires a new element sampling and weighting process, here called cECSW, arising from the configurational updates of the geometry corresponding with the possible motions of the mobile part. The advantage is the possibility of avoiding treating the full-order model for the force calculation. It is sufficient to store the reduced-order model with two element sets for field and force calculation.

The strategy is demonstrated on the TEAM20 problem of the Compumag benchmark systems, which is extended to a dynamic excitation and a conductivity of the ferromagnetic parts to allow eddy currents.

Remark

This chapter is mainly taken from the author's publication *Computing Forces by ECSW-Hyperreduction in nonlinear Magnetodynamic FEM Problems*, [35].

16.1 Introduction

In the classical hyperreduction approach, the magnetic vector potential is computed with the compact, reduced model. The solution needs then to be expanded to the physical coordinates. With that, the force on a mobile target in mechatronic systems is calculated, for example, with the local Jacobian Method, which is itself based on the virtual work principle.

This contribution presents a strategy to also compute the forces using the ECSW method that exploits the special structure of mechatronic systems and is adapted for the force calculation on mobile parts of the system.

16.1.1 Objective

As monitoring mechatronic systems with the use of so-called digital twins in embedded controllers becomes more and more important, demand for small, yet sufficient, models with a small footprint in terms of memory and CPU load rises. The MOR strategy in this investigation is therefore driven by two main objectives:

- Save computational time in the transient, non-linear field computation by investing only the minimal necessary offline effort.
- Generate a fully self-contained minimal model capable of computing dynamic forces for any current trajectory applied.

16.1.2 System Definition

In all generality, the system's structure is shown in fig. 16.1. The air domain Ω (constant μ, no conductivity) encapsulates the excitation domain (copper coils) Ω_0, where the current density $\boldsymbol{j}$ is given. The core Ω_c and the mobile target Ω_t are domains with non-linear material ($\mu(B)$) and constant conductivity σ. Both can therefore induce eddy currents for a changing magnetic field. The mobile target domain Ω_t is moved by the virtual displacement δs to evaluate the mechanical force.

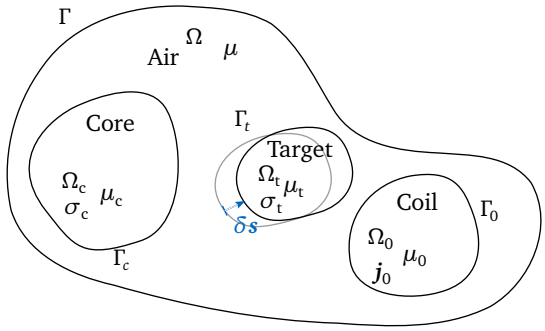

Figure 16.1: Domains of the magneto-dynamic equation.

The magnetodynamic equations, as derived in part I, are solely written in terms of the vector potential $\boldsymbol{A}$:

$$\boldsymbol{\nabla} \times \frac{1}{\mu(\boldsymbol{A})} \boldsymbol{\nabla} \times \boldsymbol{A} = \boldsymbol{j}_0 - \sigma \frac{\partial \boldsymbol{A}}{\partial t}. \tag{16.1}$$

Applying the finite element theory with edge type elements yields the classical discretized 1st time-order differential equation set eq. (16.2), with $\boldsymbol{u}$ being the unknown values of the vector potential, $\boldsymbol{M}$ the magnetic mass matrix, $\boldsymbol{g}$ the internal current vector and $\boldsymbol{f}$ the external load (current) vector.

$$\boldsymbol{M}\dot{\boldsymbol{u}} + \boldsymbol{g}(\boldsymbol{u}) = \boldsymbol{f} \tag{16.2}$$

A more detailed derivation of the here used formulation can be found in chapter 5.

16.2 Partial ECSW

In general, major parts of magnetodynamic systems can be modeled linearly. Only small parts of the domain need a non-linear consideration. To reduce the order of the model, the linear domain can be sufficiently reduced by projection, while in the non-linear domain an additional hyper-reduction step is needed as explained previously. Applying the hyperreduction method ECSW only to a part of the domain will be called *partial ECSW*, short *pECSW* in the following. Applying pECSW saves offline computational effort as the sNNLS only iterates

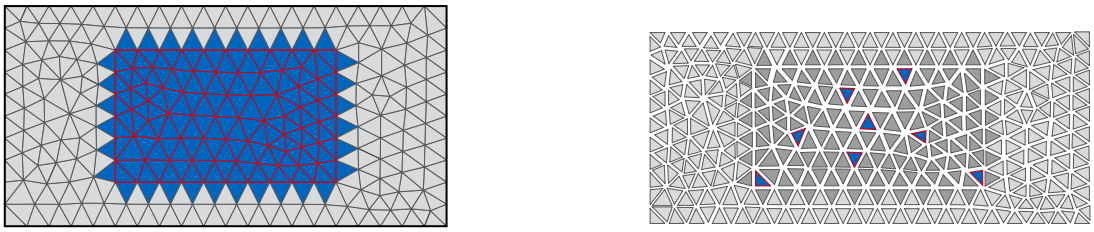

(a) Elements that contribute to edge values of the non-linear material.

(b) ECSW selected elements only in the non-linear material.

Figure 16.2: Generic visualization of the pECSW method. Only elements from the non-linear domain are considered in the hyperreduction algorithm. The linear domain is only reduced by projection.

over a much smaller subset of elements and also avoids a second approximation of the linear domain, fig. 16.2.

Realizing the partial ECSW, two subvariants are imaginable:

A. **Domain decomposition**, i.e., split the domain into a linear and a non-linear subdomain and hyperreduce the non-linear force function of the non-linear subdomain.

B. **Order decomposition** of internal currents, i.e., split non-linear internal currents in the entire domain into linear and higher order terms and hyperreduce only higher order terms.

16.2.1 pECSW - Domain Decomposition

The first approach is inspired by substructuring techniques where structural systems are partitioned into subsystems, cf fig. 16.3. The individual subsystems have different sets of equations that are re-assembled after having reduced the subdomains.

The difference to the classic ECSW formulation is in the assembly process of the $\boldsymbol{Y}$ matrix, where the contribution of each element to the internal current is collected. The full set of elements $\mathcal{E}$ now already is a subset of elements, i.e., the elements in the non-linear domain, noted with a star, $\mathcal{E}^\star$. The selection process for the elements is equal to the classic ECSW except that only the elements from $\mathcal{E}^\star$ contribute.

$$\boldsymbol{g}_e(\boldsymbol{u}) = \begin{cases} \boldsymbol{g}_e(\boldsymbol{u}) & \forall e \in \mathcal{E}^\star \\ \boldsymbol{L}_e^T \boldsymbol{K}_{\text{lin}} \boldsymbol{u} & \forall e \notin \mathcal{E}^\star \end{cases} \tag{16.3}$$

The equations for the Euler-Backward time-stepping are adapted accordingly to consider the linear and the hyperreduced non-linear domain separately. The problem eq. (16.2) can thus be solved at t_{n+1} as:

$$\left[\boldsymbol{V}^T \boldsymbol{M} \boldsymbol{V} + \Delta t \boldsymbol{V}^T \boldsymbol{K}_{\text{lin}} \boldsymbol{V}\right] \boldsymbol{q}_{n+1} + \Delta t \sum_{e \in \tilde{\mathcal{E}}^\star} \zeta_e^\star \boldsymbol{V}^T \boldsymbol{L}_e^T \boldsymbol{g}_e(\boldsymbol{L}_e \boldsymbol{V} \boldsymbol{q}_{n+1}) = \boldsymbol{V}^T \boldsymbol{M} \boldsymbol{V} \boldsymbol{q}_n + \Delta t \boldsymbol{V}^T \boldsymbol{f}_{n+1} \tag{16.4}$$

As for the classic ECSW, the Newton algorithm needs to solve the next solution step in reduced coordinates $\boldsymbol{q}$ with the corresponding stepping matrix $\boldsymbol{K}_{\text{step,red}}(\boldsymbol{q}^i)$ from the time integration scheme. In contrast to the previous stepping matrix algorithm, the reduced stepping matrix now is a combination of the hyperreduced $\boldsymbol{K}_{r,\text{pECSW}}$ and the projected $\boldsymbol{K}_{\text{lin}}$. The linearized problem for a given time step at Newton iteration $i+1$ writes:

$$\boldsymbol{K}_{\text{step,red}}(\boldsymbol{q}^i) \Delta \boldsymbol{q} = \boldsymbol{r}_{\text{red}}(\boldsymbol{q}^i) \tag{16.5}$$

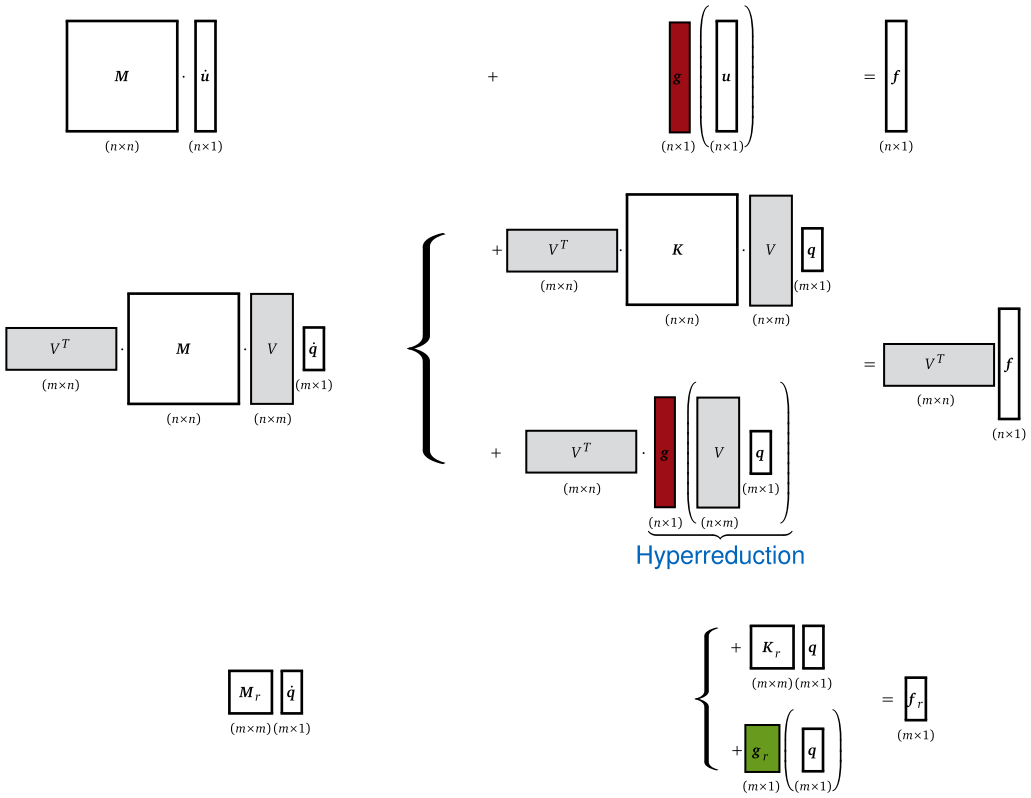

Figure 16.3: pECSW - Domain Decomposition Approach: The basic equation from the first line is split domain-wise to apply the hyperreduction algorithm only on the non-linear domain. Here, the full non-linear internal current $\boldsymbol{g}$ in the non-linear domain considered for the hyperreduciton process.

where

$$\boldsymbol{K}_{\text{step,red}}(\boldsymbol{q}^i) = \boldsymbol{V}^T[\boldsymbol{M} + \Delta t \boldsymbol{K}_{\text{lin}}]\boldsymbol{V} + \boldsymbol{K}_{r,\text{pECSW}}(\boldsymbol{q}^i) \tag{16.6}$$

$$\boldsymbol{r}_{\text{red}}(\boldsymbol{q}^i) = \Delta t \left(\boldsymbol{f}_r - \boldsymbol{g}_{r,\text{pECSW}}(\boldsymbol{q}^i)\right) - \boldsymbol{V}^T[\boldsymbol{M} + \Delta t \boldsymbol{K}_{\text{lin}}]\boldsymbol{V}\boldsymbol{q}^i \tag{16.7}$$

16.2.2 pECSW - Order Decomposition

A second way to separate linear and non-linear behavior is interpreted as a local modification technique. As a baseline, a linear system is assumed with a constant permeability that fits the material curve for small magnetic fluxes. The non-linear domains are then modified with an additional term, which represents the non-linearity. This additional term now contains all the higher-order terms of the magnetic flux density without the linear order. In fig. 16.4, the gap between the assumed linear and the true non-linear material law is visualized.

While the matrix representation of the domain decomposition approach (cf fig. 16.3) shows a splitting of the equations (*vertical splitting*), the order decomposition splits the force contributions (*horizontal splitting*). The finally hyperreduced internal current vector is marked in yellow, as it is a modified function, cf fig. 16.5.

As the method relies on the unassembled internal currents of the finite elements, two weak forms, respectively, for linear (resulting in a matrix $\boldsymbol{K}^1$) and non-linear material (resulting in $\boldsymbol{g}(\boldsymbol{u})$) are formulated and evaluated on the mesh. The difference is consequently

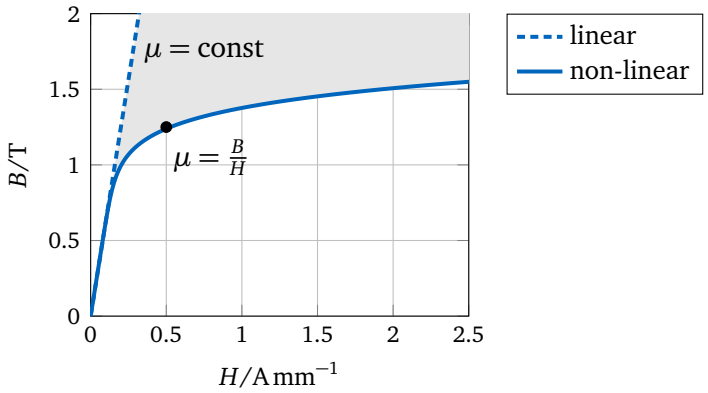

Figure 16.4: Comparison of non-linear and linear material behavior.

then the higher order internal currents $\boldsymbol{g}^\star$ and is used for the training of the hyperreduction algorithm.

$$\boldsymbol{g}^\star(\boldsymbol{u}) = \boldsymbol{g}(\boldsymbol{u}) - \boldsymbol{K}^1\boldsymbol{u} \tag{16.8}$$

Finally, depending on whether an element is in a linear domain or a non-linear domain, its internal current will be computed by

$$\boldsymbol{g}_e(\boldsymbol{u}) = \begin{cases} \boldsymbol{g}_e^\star(\boldsymbol{u}) + \boldsymbol{L}_e^T\boldsymbol{K}^1\boldsymbol{u} & \forall e \in \mathcal{E}^\star \\ \boldsymbol{L}_e^T\boldsymbol{K}_{\text{lin}}\boldsymbol{u} & \forall e \notin \mathcal{E}^\star \end{cases} \tag{16.9}$$

The further procedure is analog to the previously shown pECSW method, i.e., projection of the internal currents in the chosen basis, then solving the next solution vector in generalized coordinates using the modified stepping matrix.

16.2.3 pECSW Conclusion

This extension of the ECSW method is not primarily intended to reduce the computed elements further to gain lower computational effort in the online calculations. Rather the objective is to increase trust in the results as the hyperreduction is only applied where actually needed. A nice benefit in terms of lower effort arises in the sNNLS algorithm that selects the elements. By only allowing a subset of elements, the algorithm becomes faster.

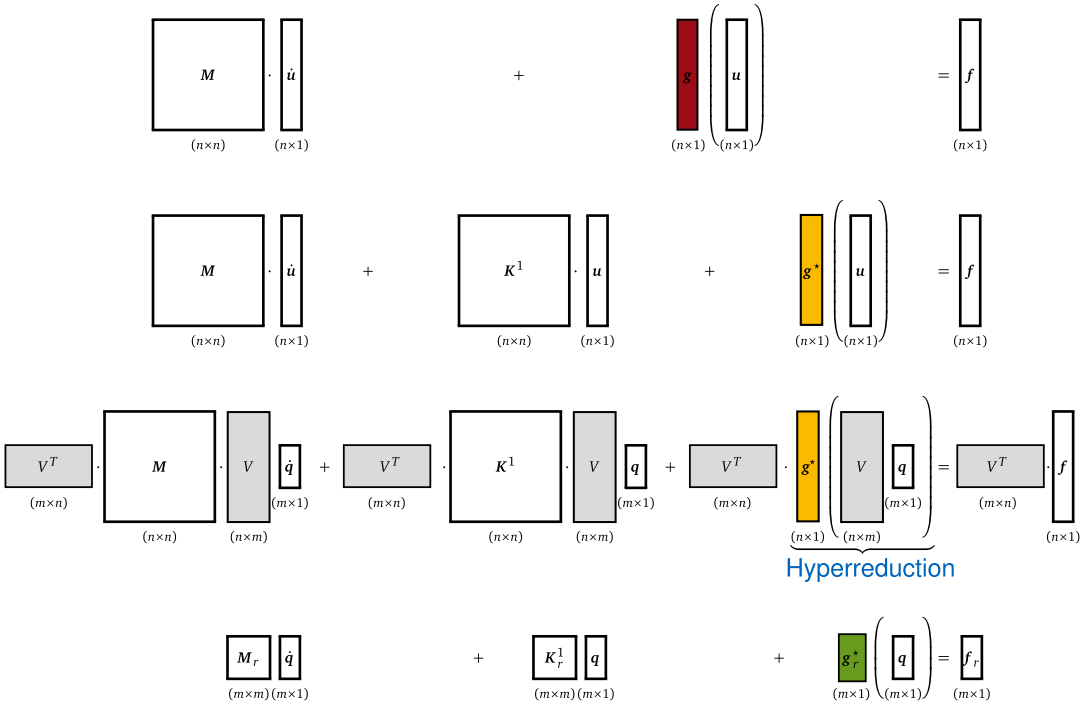

Figure 16.5: pECSW - Order Decomposition Approach: The basic magnetodynamic equation is split horizontally before applying the ECSW method. A linear approximation is drawn out and a new non-linear internal current $g^\star$ is generated. This new internal current function is hyperreduced.

16.3 Configurational ECSW

To correctly represent eddy currents in magnetodynamic systems, a maximum element size in the boundary vicinity is prescribed. The size depends on the frequency of the time-varying fields and their material properties. This element size is an absolute value, which means it does not scale with the overall model's size. The bigger the modeled system, the more elements are needed. However, calculating global forces would not require a high element resolution, which leads to reducing the number of evaluated elements for the post-processing step of calculating mechanical forces of magnetodynamic systems.

The here called *configurational ECSW*, short *cECSW*, is an adaption of the ECSW idea to the post-processing. It is therefore not involved in the actual solution process and so is independent of the method used for the computation of the magnetic field. In the presented case, the method is aimed at computing the magnetic force on a mobile ferromagnetic target. The cECSW is trained by different configurations of the geometry, which represent the virtual displacement needed for the force computation according to the virtual work principle (shortly explained in section 16.3.1). The underlying assumption is that the weights of the selected elements in the computation of the mechanical force are not dependent on the configuration. Two configurations for a horizontal displacement of the target are shown generically as an example for the discussion in fig. 16.6.

Remark A strict distinction must be made between parametric and configurational geometry changes. The parametric geometry changes are real changes in the geometry with no limit to their size, as typically encountered in modification loops during design optimization or when performing the analysis by changing the position of the bolt in a solenoid actuator

or the rotor rotation in an electric machine. These changes are not covered in this contribution, as they would not fulfill the assumption that the weights of the selected elements are independent of the configuration. The here-handled configurational changes are only virtual changes that indicate what kinematically admissible motions the body could undergo. The mesh topology must stay constant. It is common to just deform one layer of elements, as these virtual changes can be very small, even for a finite difference evaluation as seen in section 16.3.1.

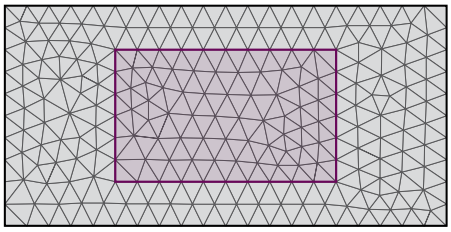

(a) First training configuration. The rigid, moveable body is marked in red.

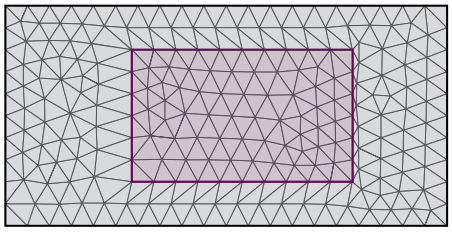

(b) Second training configuration. Virtually displaced body (exaggerated for visualization).

Figure 16.6: Generic example of configurational training.

16.3.1 Force Calculation

The global mechanical force on a mobile target body is derived in general from the total change of energy W due to the change of the system's configuration (i.e. position) with an amplitude denoted by s [38]. For an applied, constant current density $\boldsymbol{j}$, the force energetically conjugated to the considered configurational change (e.g. resulting horizontal force in fig. 16.6) is obtained from the change of magnetic co-energy W'. Considering several possible configurational changes (e.g. vertical and rotational motion) and calling $\boldsymbol{s}$ the set of their amplitudes, the associate conjugate forces are obtained from

$$\boldsymbol{F} = \frac{\mathrm{d}W'}{\mathrm{d}\boldsymbol{s}}. \tag{16.10}$$

For quasi-static systems (as claimed during the derivation), the force can be computed for any timestep purely from the conservative system. Note that the eddy currents are also included in the current density $\boldsymbol{j}$. The following static consideration is therefore only valid for one instant stop in time. For considerations regarding the mechanical forces, only the magnetic (co)-energy density is relevant. The energy stored in the electrical field is not considered. Let us recall that the finite element formulation searches for a vector potential $\boldsymbol{A}$ such that it minimizes the energy functional of the system.

$$\delta\left(\int_\Omega w(\boldsymbol{A})\,\mathrm{d}\Omega - \int_\Omega \boldsymbol{j}^T\boldsymbol{A}\,\mathrm{d}\Omega\right) = 0 \tag{16.11}$$

Using the relation $W_\square = \int_\Omega \boldsymbol{B}^T\boldsymbol{H}\,\mathrm{d}\Omega = \int_\Omega \boldsymbol{j}^T\boldsymbol{A}\,\mathrm{d}\Omega$, which is the sum of the magnetic energy W and co-energy W', the solution of the magnetic problem, written in energy densities, satisfies:

$$\min_A\left(w(\boldsymbol{A}) - \boldsymbol{j}^T\boldsymbol{A}\right)$$
$$\min_A\left(w_\square - w'(\boldsymbol{A}) - \boldsymbol{j}^T\boldsymbol{A}\right)$$
$$\min_A\left(-w'(\boldsymbol{A})\right)$$

Hence, around the solution to the problem we have:

$$\frac{\partial w'(\boldsymbol{A})}{\partial \boldsymbol{A}} = 0 \tag{16.12}$$

Using then the chain rule to evaluate the mechanical force eq. (16.10),

$$\boldsymbol{F} = \frac{\mathrm{d}W'}{\mathrm{d}\boldsymbol{s}} = \frac{\partial W'}{\partial \boldsymbol{s}} + \underbrace{\frac{\partial W'}{\partial \boldsymbol{A}}}_{=0} \frac{\partial \boldsymbol{A}}{\partial \boldsymbol{s}} = \boldsymbol{\nabla}_{\boldsymbol{s}} W' \tag{16.13}$$

The global co-energy is obtained by integrating the co-energy density $w'(\boldsymbol{A})$, which is the integral under the constitutive material law. With the material being assumed as isotropic, $\boldsymbol{B}$ and $\boldsymbol{H}$ are always oriented collinear which allows to write eq. (16.14) in terms of magnitudes:

$$W' = \int_{\Omega} \int_{0}^{H} B(\tilde{H})\, \mathrm{d}\tilde{H}\, \mathrm{d}\Omega \tag{16.14}$$

Conducting the derivation, note that the partial derivative means that the remaining quantities are constant by definition. The expression for the force becomes:

$$\begin{aligned} \boldsymbol{F} &= \boldsymbol{\nabla}_{\boldsymbol{s}} W' \\ &= \int_{\Omega} \boldsymbol{\nabla}_{\boldsymbol{s}} \int_{0}^{H} B(\tilde{H})\, \mathrm{d}\tilde{H}\, \mathrm{d}\Omega + \int_{\Omega} \int_{0}^{H} B(\tilde{H})\, \mathrm{d}\tilde{H} \boldsymbol{\nabla}_{\boldsymbol{s}}\, \mathrm{d}\Omega \end{aligned} \tag{16.15}$$

The change of position of the part leads to a change of the Jacobian, which describes the coordinate transformation between physical coordinates and the isometric coordinates for the FEM elements. The Jacobian of the isogeometric mapping is denoted by $\mathcal{J}$, and its determinant is $|\mathcal{J}| = \det(\mathcal{J})$. A shift of the derivative from the magnetic field to the Jacobian in the first term of eq. (16.15) allows us to write all field quantities within one configuration [48]. In all generality, the force arising from the co-energy is written for all quantities given in the original configuration [16]:

$$\boldsymbol{F} = \int_{\Omega} \Bigg[\underbrace{-\boldsymbol{B}^{T} \frac{\partial \mathcal{J}}{\partial \boldsymbol{s}} \mathcal{J}^{-1} \boldsymbol{H}}_{\text{Change due to change of derivation operator curl}} + \underbrace{\int_{0}^{H} B(\tilde{H})\, \mathrm{d}\tilde{H} |\mathcal{J}|^{-1} \frac{\partial |\mathcal{J}|}{\partial \boldsymbol{s}}}_{\text{Change due to change of geometry}} \Bigg] \mathrm{d}\Omega \tag{16.16}$$

An overview of the different ways to use eq. (16.16) for force calculation on a given mesh is given in fig. 16.7 and will be discussed next. After a successful field calculation per time step, the vector potential is further processed to gain the global mechanical forces. While the classical Jacobian method needs all the virtually deformed elements (marked yellow in fig. 16.7), the cECSW approach proposed in the following paragraphs, samples and weighs those elements in either a non-linear or a linear way which reduces the evaluated sub-subset of elements (marked green in fig. 16.7).

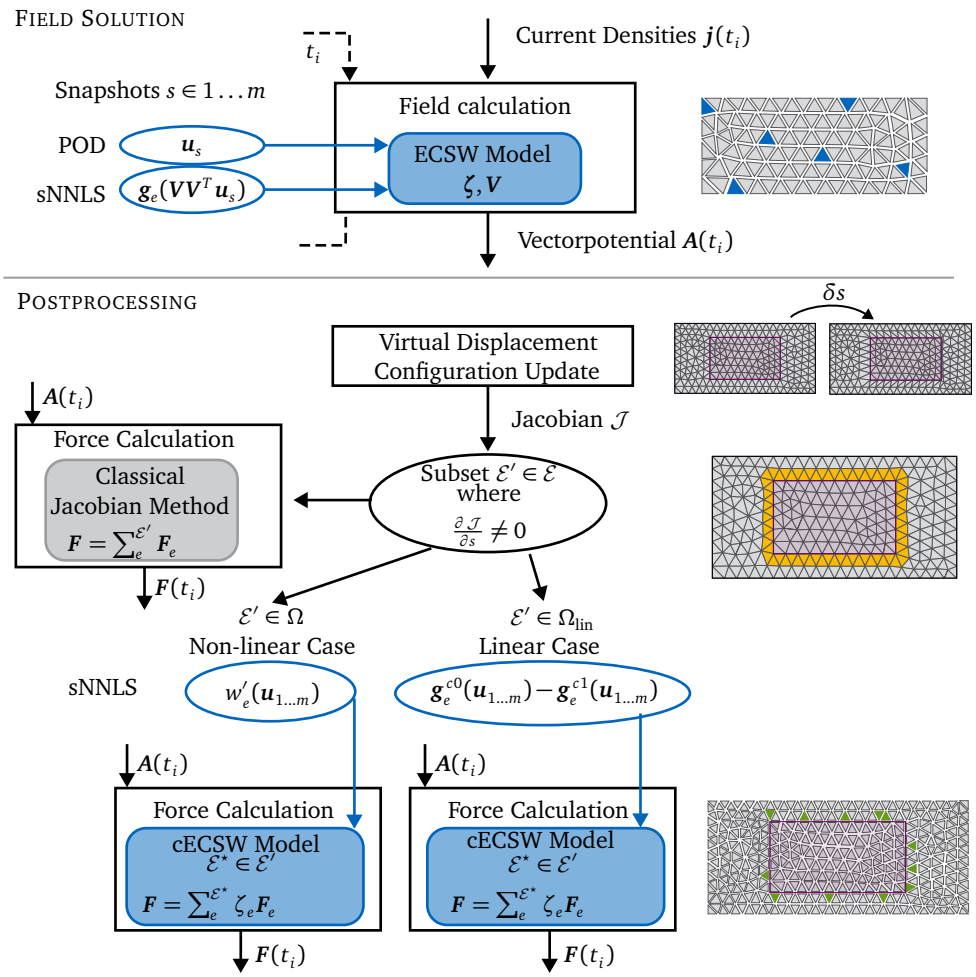

Figure 16.7: cECSW Scheme: After the field solution, which could be computed with the previously seen ECSW method, the post-processing step to calculate the mechanical forces is applied. Three options are possible, First, the classical Jacobian method with no further reduction. Second and third, the application of the cECSW method, depending on the surrounding material linearity.

16.3.2 Force Integration by Classical Jacobian Method

For elements that are not deformed during the virtual displacement of the mobile target, the derivative of the Jacobian with respect to the displacement is zero. That results in a subset of elements that don't contribute to the global force. Therefore, only a subset of elements needs to be evaluated. The integral over the domain changes into integrals over each element Ω_e and a sum over all elements in the subset $\mathcal{E}'$.

$$\boldsymbol{F} = \sum_{e \in \mathcal{E}'} \boldsymbol{F}_e \tag{16.17}$$

16.3.3 Force Integration by ECSW

Applying the ECSW method for the force calculation to reduce the computational effort and shrinking the model size means selecting elements and calculating weights. The sum over the element forces (the set of elements which undergo a deformation is denoted with $\mathcal{E}'$) is approximated by a sum over a subset of elements $\mathcal{E}^\star$ which are then weighted with the factor

$\zeta_e^\star$ to compensate for the neglected elements. The localization operator $\boldsymbol{L}_e$ picks the solution dofs for the corresponding element e, and thus

$$\boldsymbol{F} = \boldsymbol{\nabla}_s \sum_{e \in \mathcal{E}'} \int_{\Omega_e} w'_e(\boldsymbol{L}_e \boldsymbol{u}) \, \mathrm{d}\Omega_e. \tag{16.18}$$

With the energy being positive, the idea of ECSW can be applied, approximating the energy with positive weighted elements. Assuming that the weights are constant with respect to the virtual deformation, the gradient is shifted behind the weight $\zeta_e^\star$. This is a reasonable assumption, considering that the virtual configurational change is infinitesimal.

$$\boldsymbol{F} \approx \boldsymbol{\nabla}_s \sum_{e \in \mathcal{E}^\star} \zeta_e^\star \int_{\Omega_e} w'_e(\boldsymbol{L}_e \boldsymbol{u}) \, \mathrm{d}\Omega_e \tag{16.19}$$

$$\approx \sum_{e \in \mathcal{E}^\star} \zeta_e^\star \boldsymbol{\nabla}_s \int_{\Omega_e} w'_e(\boldsymbol{L}_e \boldsymbol{u}) \, \mathrm{d}\Omega_e \tag{16.20}$$

$$= \sum_{e \in \mathcal{E}^\star} \zeta_e^\star \boldsymbol{F}_e \tag{16.21}$$

To select the elements using the sNNLS algorithm, training snapshots need to be prepared. Considering the m solution snapshots of a pre-simulation, the change of co-energy in each element due to a set of c possible configurational changes is computed. This generates a set of mc training sets from which a minimum set of elements and the corresponding weights can be selected following the ECSW strategy.

In order to avoid the evaluation of the Jacobian derivatives for each training data set for each element, the gradient is approximated with a finite difference.

Non-linear Material Elements In the general case, where the deformed elements contain non-linear material, the training is performed using the co-energy of every element in $\mathcal{E}'$, $W'_e(\boldsymbol{L}_e \boldsymbol{u})$. The finite configuration steps used for the finite difference are denoted with the superscript $c0$ and $c1$. The subscript denotes the element number $1 \dots n$ and the snapshot number $1 \dots mc$. Using the same amplitude s for each direction of configurational change allows us to omit the scaling in the following explanations. The adapted $\boldsymbol{Y}$ matrix for the force approximation to be used for the sNNLS algorithm becomes:

$$\boldsymbol{Y}\boldsymbol{\zeta} = \begin{bmatrix} \left(W'^{c0}_{11} - W'^{c1}_{11}\right) & \dots & \left(W'^{c0}_{n1} - W'^{c1}_{n1}\right) \\ & \vdots & \\ \left(W'^{c0}_{1mc} - W'^{c1}_{1mc}\right) & \dots & \left(W'^{c0}_{nmc} - W'^{c1}_{nmc}\right) \end{bmatrix} \begin{bmatrix} \zeta_1 \\ \dots \\ \zeta_n \end{bmatrix} \tag{16.22}$$

In general, the co-energy for the mc different snapshots need to be integrated as in eq. (16.14). As explained next, this costly computation can be avoided if the elements are linear.

Linear Material Elements If all the virtually deformed elements are of linear material, a simplification during the preparation of the sNNLS can be conducted. This situation occurs for systems where the non-linear material is completely encapsulated in air and only rigid body motions are allowed. For real application systems, this is a very common assumption. A few transformations are carried out to extract the co-energy directly from the internal currents already known from the training simulations.

The linear energy density is written as the product of the internal current density $\boldsymbol{g}(\boldsymbol{u})$ and the solution vector $\boldsymbol{u}$. The solution vector does by definition not change with a change

in configuration, so the derivative is only effective on the internal currents. Written for each element, the force becomes:

$$\boldsymbol{F} = \sum_{e\in\mathcal{E}'} \boldsymbol{\nabla}_s \frac{1}{2}(\boldsymbol{L}_e\boldsymbol{u})^T(\boldsymbol{L}_e\boldsymbol{g}) \tag{16.23}$$

$$= \frac{1}{2}\sum_{e\in\mathcal{E}'} (\boldsymbol{u}_e)^T \boldsymbol{\nabla}_s(\boldsymbol{g}_e) \tag{16.24}$$

$$\approx \sum_{e\in\mathcal{E}^\star} \zeta_e^\star \boldsymbol{F}_e \tag{16.25}$$

With the same justification as for the classic ECSW, the elements can be sampled and weighted with positive values, but now the difference of the internal currents for different configurations is approximated. For each training snapshot ij, $i = 1\dots m, j = 1\dots c$, hence each line in eq. (16.22), an equation for the sNNLS is added:

$$\boldsymbol{Y}_{ij}\boldsymbol{\zeta} = \begin{bmatrix} \boldsymbol{V}^T\boldsymbol{L}_1^T\left(\boldsymbol{g}_1^{c0}(\boldsymbol{L}_1\boldsymbol{V}\boldsymbol{q}_{ij}) - \boldsymbol{g}_1^{c1}(\boldsymbol{L}_1\boldsymbol{V}\boldsymbol{q}_{ij})\right) \\ \dots \\ \boldsymbol{V}^T\boldsymbol{L}_n^T\left(\boldsymbol{g}_n^{c0}(\boldsymbol{L}_n\boldsymbol{V}\boldsymbol{q}_{ij}) - \boldsymbol{g}_n^{c1}(\boldsymbol{L}_n\boldsymbol{V}\boldsymbol{q}_{ij})\right) \end{bmatrix}^T \begin{bmatrix} \zeta_1 \\ \dots \\ \zeta_n \end{bmatrix} \tag{16.26}$$

This shows that in case the elements in $\mathcal{E}'$ are linear, the force can be evaluated by cECSW from eq. (16.25) with a reduced element set and weights obtained from the training with eq. (16.26) where no co-energy needs to be evaluated, but only known internal currents obtained from the configurational steps are needed. The element forces $\boldsymbol{F}_e$ can be evaluated either by finite differences or the local Jacobian method (eq. (6.34)). Note that, when using eq. (6.34), there is only the need to save the weights for the evaluated elements and their Jacobian relations. The weights, once computed, stay constant after the training, while the Jacobi values depend on the actual (virtual) configuration change.

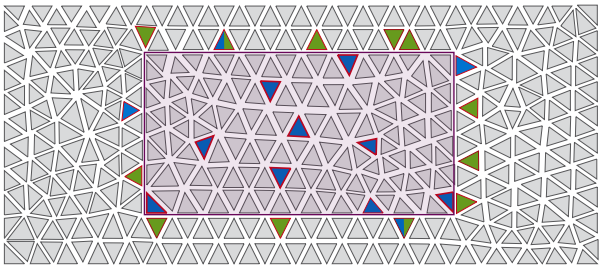

Figure 16.8: Selected elements for both stages marked in blue and green. Blue elements serve for the field calculation and green elements for the post-processing. Some elements are in both subsets.

16.3.4 cECSW Conclusion

The goal of the cECSW is to find an optimized reduced model that serves for the post-processing, i.e., calculating forces. For this, the ECSW method is applied as sampling and weighting the subset of elements which are evaluated in the course of the local Jacobian method to integrate the global mechanical force. As a result, the cECSW model needs to store significantly fewer elements in the hard drive and, as a nice benefit, computational time is reduced during the post-processing.

16.4 TEAM 20 Example

The previously presented strategy of force calculation utilizing the ECSW method in both stages is demonstrated on the TEAM 20 benchmark problem (fig. 16.9) of the Compumag Society. As the original problem definition is only static, it is extended to a magnetodynamic problem. The dynamic parameters are inspired by the TEAM10 problem, which handles eddy currents in non-linear systems of similar structures. All ferromagnetic parts provide a constant and isotropic conductivity.

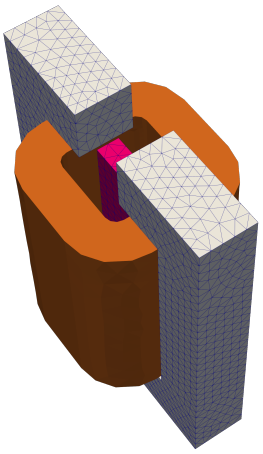

(a) Visualized mesh TEAM20.

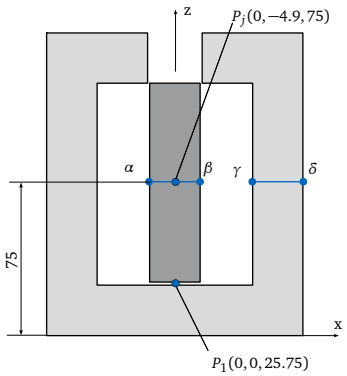

(b) Evaluation points P_1 and P_j evaluate the field quantity B and j_{eddy}. The cross-section area defined by the lines α-β and γ-δ is averaged.

Figure 16.9: TEAM20 with extensions to investigate also the dynamic behavior including eddy currents.

The dynamic simulations are performed with an excitation function that forms a smooth step as it was proposed for the TEAM10 example, see section 11.3.

$$j(t) = \begin{cases} 0 & (t < 0) \\ j_0(1 - e^{-\frac{t}{\tau}}) & (t \geq 0) \end{cases} \tag{16.27}$$

For the following simulation study, two different terminal current densities $j_0 = \{1.725\,\mathrm{A\,mm^{-2}}; 2.876\,\mathrm{A\,mm^{-2}}\}$ are tested. The time constant τ is fixed to 0.05 s. As a time step, two different values ($t = 0.001\,\mathrm{s}$ and $t = 0.005\,\mathrm{s}$) are used to test the convergence of the simulation. Both reveal nearly exact same behavior, so the time step $t = 0.005\,\mathrm{s}$ is chosen. The simulation values are evaluated using two local points and the average results on two cross-section areas. The benchmark is also evaluated both in simulation and experiment at point P_1, as well as the lines α-β and γ-δ, see [41]. Point P_j, see fig. 11.9, is introduced here to measure the eddy current values that counteract the coil's driving current.

16.4.1 Material

The non-linear BH-curve of the steel is given in a tabular form which is plotted in fig. 16.10. A spline interpolation is performed to obtain a continuous function that is integrable in order to find the energy density. For the pECSW-Order-Decomposition, the first section of the curve is fitted with a linear permeability of $\mu_r = 1500$. To compare the performance, two further linear permeabilities are considered which do not fit the actual material well, $\mu_{r,\text{low}} = 750$ and $\mu_{r,\text{high}} = 3000$. The conductivity is given as $\sigma = 7.505 \times 10^6\,\mathrm{S\,m^{-1}}$.

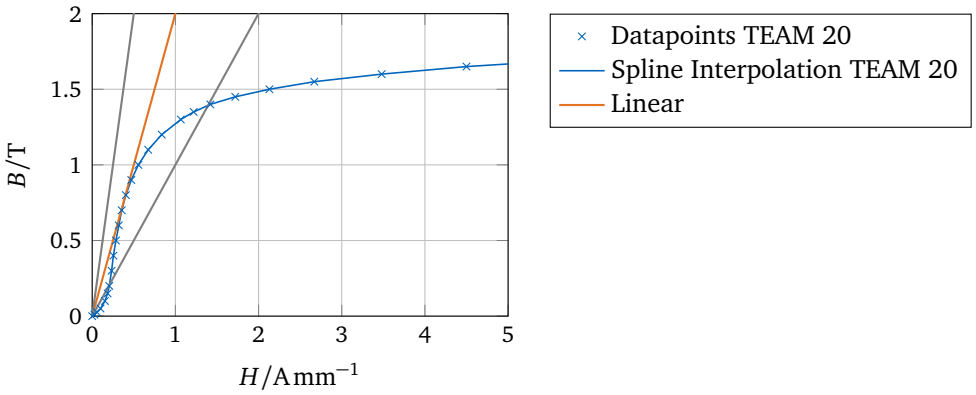

Figure 16.10: Official material parameter points interpolated with a spline function. Three linear permeability tangents demonstrate the approximation for different ranges.

Regularization Following the theory of modified vector potential, the non-conductive domains lead to a non-unique governing set of equations. This singularity is overcome by a small regularization term that is added to the equation like a very small mass matrix, i.e., a very small conductivity. For the sNNLS, the regularization term is neglected, although this is actually a small discrepancy between the computed vector field and the evaluated energy densities. We do this to feed the weighting process only with the physical necessary properties.

Computational Setup The computations were performed on the machine, given in table 16.1.

Table 16.1: Computer configuration with installed environment versions

Processor	Intel®Xeon™E3-1270 v5 @ 3.60 GHz
RAM	32 GB
OS	Win 10
Python	3.11.3
NGSolve	6.2301

Relative Error The relative error (RE) compares reduced problem solutions to their corresponding reference. For more details see section 14.2.3. The comparison for this study is limited to scalar values (field quantities evaluated locally or globally). The error at each time step t_i is summed to produce a single significant value. The RE formula is

$$RE = \frac{\sqrt{\sum_i (u_{\text{ref}}(t_i) - u(t_i))^2}}{\sqrt{\sum_i u_{\text{ref}}(t_i)^2}} \tag{16.28}$$

The RE definition is harsh, and a small offset over multiple time steps results in a high error number. But it is also a useful one-number criterion to see how well two measurement histories match.

Table 16.2: Relative error due to the projection (without any hyperreduction) in the subspace spanned by POD modes.

# snaps	modes	RE B_z	RE j_x	RE F
50	2	5.02 %	17.83 %	0.35 %
50	5	1.59 %	4.41 %	0.10 %
50	10	0.1 %	0.48 %	0.01 %
50	20	0 %	0.03 %	0 %
20	2	6.59 %	13.4 %	2.02 %
20	5	4.22 %	4.11 %	0.65 %
20	10	0.86 %	0.5 %	0.38 %
20	20	1.37 %	0.92 %	0.44 %

16.4.2 Field Computation - pECSW Results

To reduce the system with the proposed two-stage method, first, a good field computation is aimed. Therefore, the full system needs to be computed, and the resulting magnetic vector snapshots are fed into the SVD to find a solution basis. The POD is computed from the first 20 time steps of the high-load training trajectory, i.e. the smooth step trajectory with 5000AT ($j_0 = 2.876\,\mathrm{A\,m^{-2}}$). Projecting the solution on a subspace of {5,10,20} modes and comparing it with the original solution, three different relative errors of local measures are plotted in table 16.2. The results at the evaluated points can be approximated within 1 % by the use of 10 modes. A slight increase in the relative errors for the use of 20 modes could be due to the summation of numerical errors.

Regularization Due to the projection into the subspace, the regularization of the air domain isn't necessary anymore. The standard ECSW method does not violate the well-posed property of the problem. The final stepping matrix unveils condition numbers around 5 to 25, which leads to easy and robust solutions in the linear solver. The pECSW-DD can be upgraded with a regularization term for the linear domain, which lowers the condition numbers but isn't necessary. The pECSW-OD does not lead to a bounded condition number. There were cases where the stepping matrix became singular after a few time steps. This behavior could be hindered but not consequently inhibited with a regularization term in the linear domain.

Hyperreduced Models - Constant Tau Applying the presented variations (classic, DD, OD) of the hyperreduction method ECSW leads to model sizes that are a fraction of the full-size model. All ROMs were generated from the previously used training set (5000AT smooth step) with element selection algorithms parameterized with $\tau = 10^{-3}$. Two variants are generated with finite element orders 1 and 2. As the speedup is directly related to the number of evaluated elements, it is not explicitly discussed here. Of course, some data-handling overhead remains constant throughout all the simulations. The timings given are the wall times of the computation of one single time step, averaged over all time steps. The system's element count decreases from 65740 to a range between 10 and 100. And nearly with the same ratio do the computation times reduce for the evaluation of the elements. The finite element order influences the computational effort, but the rates of reduction itself are quite independent.

Table 16.3: Comparison of ECSW time consumption results. The offline time represents the time spent on the sNNLS to find the selected elements and corresponding weights. The duration to compute the next integration time step is averaged.

Reduction	dofs	elements	offline t	avg t/step
full fe-order=1	76 564	65740	0	22.5s
full fe-order=2	338 984	65740	0	257s
POD + ECSW fe=1	10	52	30s	0.64s
POD + ECSW fe=2	10	47	12s	2.82s
POD + pECSW DD fe=1	10	57	1.5s	0.66s
POD + pECSW DD fe=2	10	69	3.0s	2.90s
POD + pECSW OD fe=1	10	42	1.6s	0.72s
POD + pECSW OD fe=2	10	66	n.a.	n.a.

Hyperreduced Models - Constant No. of Elements In order to reach a fair comparison of the capability of the reduced models, all three ROM models are generated such that they evaluate the same number of elements, so they have the same computational effort. The results of the standard ECSW, pECSW Domain Decomposition (pECSW-DD), and pECSW Order Decomposition (pECSW-OD) are plotted for two reduction levels (11 and 55 elements). These element numbers correspond to the number of elements chosen by the standard ECSW for $\tau = 0.1$ and $\tau = 0.001$. The plot in fig. 16.11 shows the magnetic flux density B_z at P_1 and the eddy current density j_x at P_j for the training excitation.

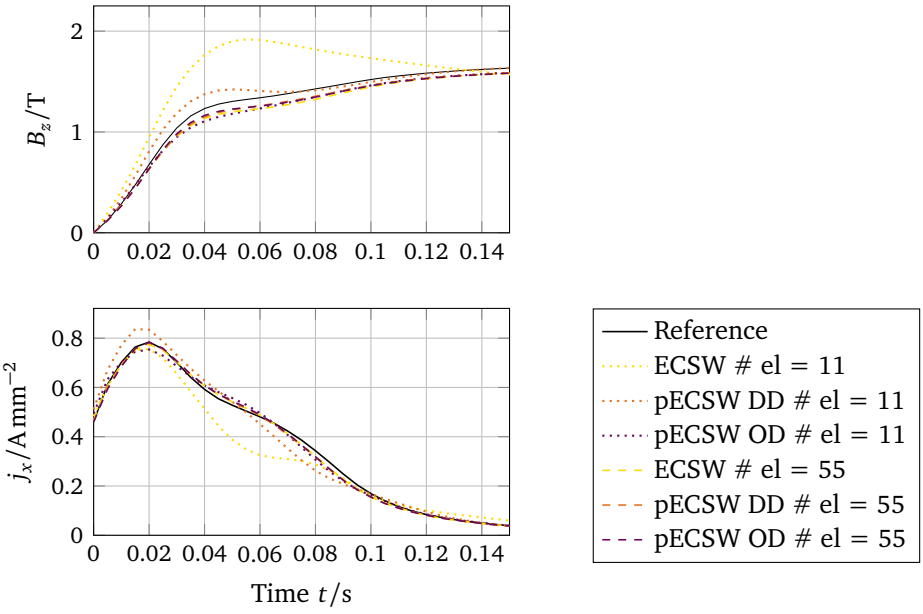

Figure 16.11: Result curves for the three ECSW methods for two numbers of elements considered.

The takeaway message from fig. 16.11 is the indication that both pECSW methods perform better than the standard ECSW. This was expected as for the pECSW all evaluated elements contribute to the approximation of the non-linearity. The Order Decomposition method works the best. For higher element numbers considered in the ECSW hyperreduced model, the differences between the methods vanish, and all the results achieve a good match with the reference. However, the pECSW-OD has the major drawback of becoming potentially unstable due to bad conditions.

Conclusion Both pECSW approaches fulfill the expectations in terms of building a reduced-order model to compute the magnetic vector potential. Discussing whether it is necessary or even worth applying the pECSW approach instead of the standard ECSW, which considers the full domain despite its non-linearity, two points are to be highlighted:

- Implementation effort: If an intrusive implementation is possible, the extra effort for pECSW is very small as all the techniques are already there.
- Offline costs: The offline costs are remarkably smaller (10-20 times smaller) for the pECSW approaches. This leads to the strong recommendation to use a pECSW method.
- Convergence: The convergence of the pECSW-OD is not always guaranteed and therefore the method is not recommended, although it would provide the best results when stable.

In summary, the most promising implementation of the ECSW method to compute the field quantities is the classic ECSW which performs very well and does not need any further implementation complexity but needs some more elements to exhibit similar accuracy. Adding one step of complexity, i.e., the partitioning of the system, the pECSW-DD is the most intuitive and robust hyperreduction approach.

16.4.3 Force Calculation - cECSW Results

After investigating the field calculation, the application of the ECSW approach to post-processing in terms of force calculation is discussed in the example. The following cECSW model is generated with the same training set as the previous ROM and combined with the pECSW-DD approach.

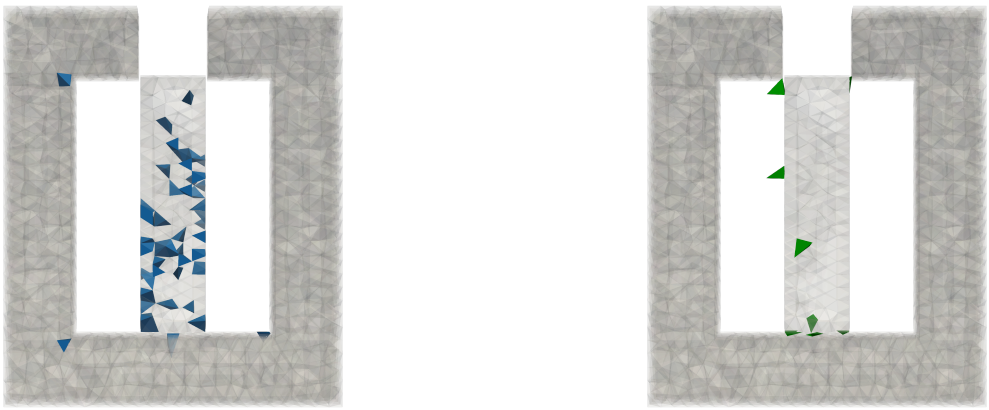

(a) pECSW selected elements are located in the ferromagnetic materials. A higher density of elements is found in the target body, which undergoes a higher magnetic flux density.

(b) cECSW selected elements are all in the air domain as the target body was considered rigid.

Figure 16.12: TEAM20 showing the selected elements for pECSW and cECSW respectively.

Due to the ramp excitation, the final force value converges to the static forces. For a single rigid body mode of the mobile target in the z-direction, 14 elements were selected for

an sNNLS tolerance of $\tau = 10^{-3}$ in the cECSW for the forces. The offline costs were around $t = 1\,\mathrm{s}$. The online costs for a single force integration decrease from $0.7\,\mathrm{s}$ to $0.002\,\mathrm{s}$. The resulting forces in the on-board test are very accurate, refer to fig. 16.13.

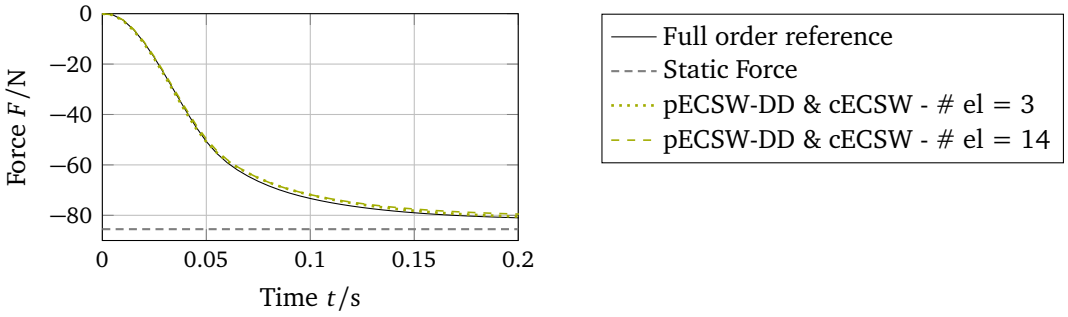

Figure 16.13: Comparison of the global force from standard ECSW and cECSW.

16.4.4 ROM Results for Test-Trajectories

In the following, the beforehand created reduced model (pECSW-DD for the field calculation and cECSW for the force, trained once with the ramp seen above), will be tested for 3 different excitations against their full-order reference solution. The results are visualized in the radar chart in fig. 16.15. Each ray represents a relative error measure (local and global). The shorter the circular path, the better.

The first excitation is the same ramp as for the training, see eq. (16.27). This leads to the so-called onboard validation of the reduced model. The two following trajectories are unknown to the system and are therefore a cross-validation of the reduced-order model. The second excitation function forms a sine:

$$I_2(t) = I_0 \sin(2\pi f\, t) \qquad f = 10\,\mathrm{Hz} \tag{16.29}$$

The third excitation function forms an impulse:

$$I_3(t) = I_0 e^{-\frac{(t-m)^2}{2a^2}} \qquad m = 0.05\,\mathrm{s}, \quad a = 0.01\,\mathrm{s} \tag{16.30}$$

All experiments are conducted with two current density peak amplitudes, namely 3000 AT and 5000 AT.

The results for the impulse validation (excitation eq. (16.30)) are plotted in fig. 16.14. The two amplitudes nicely show the non-linear saturation effect for the magnetic flux density. The reduced model leads to a small deviation in the relaxation phase right after the impulse. Also, the effect of the eddy currents is intuitive and is well represented by the reduced model. In all categories, the pECSW method performs better. The global quantities like the magnetic energy and the force, match nearly perfectly with the reference.

To generate a weighted single error measure over multiple evaluation points, the area and the circumference length in the radar plot of the reduction error fig. 16.15 are computed and displayed in the corresponding legend.

Two statements can be drawn from fig. 16.15. First, the reduced-order model represents its own training simulation the best. This was to be expected. This is often called onboard validation. Second, the estimation of the force is relatively robust. In general, the results of the simulation show a changing accuracy when the amplitude of the excitation is changed, but no clear correlation was found between the excitation level and the accuracy of the reduction strategies.

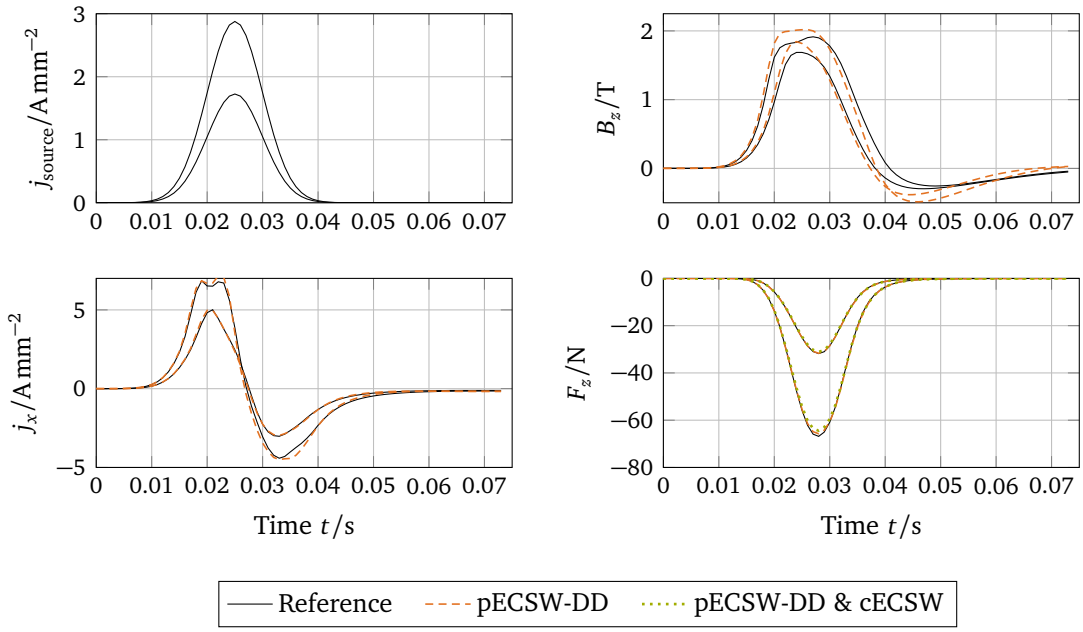

Figure 16.14: Cross Validation of the reduced-order model with an impulse excitation for 2 excitation amplitudes.

Conclusion The cECSW method brings major advantages to the computation of mechanical forces in electromechanical systems. With relatively small offline effort, the model can be reduced significantly. This allows the model to be stored in very limited memory environments and the force to be computed with only very small computational power.

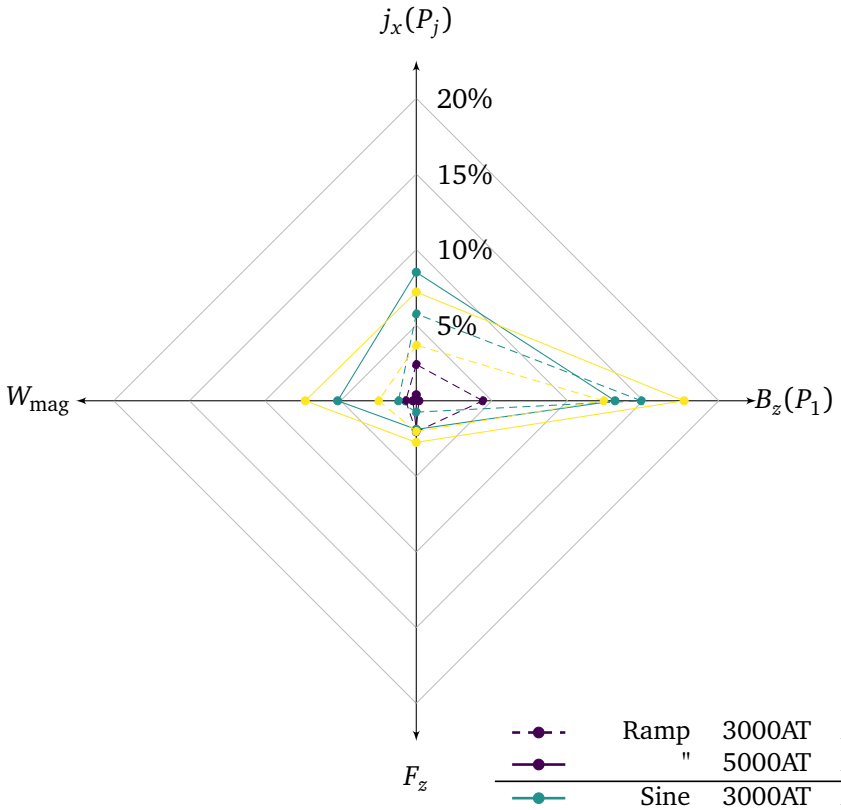

Ramp	3000AT	$A = 11\,\%^2$	$L = 14\,\%$
"	5000AT	$A = 0.5\,\%^2$	$L = 5.0\,\%$
Sine	3000AT	$A = 52\,\%^2$	$L = 38\,\%$
"	5000AT	$A = 95\,\%^2$	$L = 44\,\%$
Impulse	3000AT	$A = 42\,\%^2$	$L = 33\,\%$
"	5000AT	$A = 124\,\%^2$	$L = 55\,\%$

Figure 16.15: Relative error RE eq. (16.28), evaluated for different quantities (global energy W_{mag} and force F_z, local field quantities B and j). The graph contains the three test trajectories, and the reference is the full simulation, respectively. A is the area enclosed by the error points. L is the circumference length.

Chapter 17

Summary of Part II

Summary

Model order reduction was shown to be a sea of options. The thread was taken from projection-based methods to the methods of hyperreduction. The term hyperreduction is meant in the sense that the evaluation of the non-linear elements is reduced on top of the projected equations.

The first explained hyperreduction method was DEIM, which is already known in the field of electromagnetic systems. For the DEIM, a basis is extracted, which is then used for a collocation-based interpolation. Potential instability behavior was demonstrated with examples. The second method investigated was the ECSW method, which had not been applied to magnetodynamic systems before. ECSW uses information on the internal currents for the calibration of weighting factors of a quadrature of the energy. The method showed big potential. The results show some obvious behavior that seems very robust: The more elements, the better the hyperreduction result. With a study, the question of finding efficient training simulations was investigated, proposing three different approaches and comparing using various quantification methods. Also, finding an appropriate subspace was possible using all three training simulations. However, finding a measure to determine bad reduced-order models in advance was impossible.

Subsequent research was done to adapt the ECSW idea specifically to the characteristic properties of mechatronic systems. The proposed pECSW method only applies the element selection process of the non-linear domain (due to saturation), making the reduction process more efficient and robust. Bringing the ECSW approach also to the post-processing, where the system's mechanical force is computed, leads to the novel cECSW method. Here, the reduced system is trained for the energy difference between neighboring configurations, which correlate via the virtual work principle with the mechanical forces.

Two types of simulation examples were conducted, where the first one shows the method's mechanism, especially for the 2D case. The second group of examples are official 3D benchmark examples (some with modifications) of the Compumag society, showing the methods' potential to gain a higher speed-up while still preserving very high accuracy.

Conclusion

All used hyperreduction approaches (DEIM and the ECSW methods) use the information of the internal currents. For the shown generic example of a solenoidal system, computational speed-ups of up to one order of magnitude were achieved. Although care was taken to implement all methods properly in the framework of NGSolve, a further significant reduction of computational time could be achieved by putting additional effort into code optimization. In these examples, the resulting accuracy of the applied ECSW method is better than the DEIM for a similar number of elements kept in the hyperreduction.

Finally, it remains a difficult task to classify the reduction quality for non-linear models beforehand. Although tools like the subspace angles give more insight into the reduction basis, the interpretation remains open until more case studies bring higher confidence.

Closing

Both methods show that hyperreduction has the potential to reduce electro-dynamic systems drastically. Finding a good reduction basis is identified as key to a successful reduction. The hyperreduction part is found to be quite robust and does not degrade the result markedly but is essential to significantly reduce the computational costs of the reduced model. While the DEIM has the major disadvantage that it can lead to unstable models, the ECSW method exhibits high robustness and better results for less evaluated elements.

The next step to raise the full potential of the ECSW method is to introduce a completely different approach to find the reduction parameter sets utilizing the branch of simulation-free approaches. There, the idea is to exploit the system properties through eigenvalue problems or use different quasi-static solutions. This has the advantage that the full-order system never has to be computed.

References

[1] Al Eit, M., Bouillault, F., Marchand, C., and Krebs, G. *Model-order nonlinear subspace reduction of electric machines by means of POD and DEI methods for copper losses calculation*. 2018. DOI: 10.1002/jnm.2274.

[2] Allen, M. S., Rixen, D., Seijs, M. van der, Tiso, P., Abrahamsson, T., and Mayes, R. L. "Introduction and Motivation". In: *Substructuring in Engineering Dynamics*. Springer International Publishing, Aug. 2019, pp. 1–4. DOI: 10.1007/978-3-030-25532-9_1.

[3] Allen, M. S., Rixen, D., Seijs, M. van der, Tiso, P., Abrahamsson, T., and Mayes, R. L. *Substructuring in Engineering Dynamics*. Springer International Publishing, 2020. DOI: 10.1007/978-3-030-25532-9.

[4] An, S. S., Kim, T., and James, D. L. "Optimizing Cubature for Efficient Integration of Subspace Deformations". In: *ACM Transactions on Graphics (SIGGRAPH ASIA Conference Proceedings)* 27.5 (Dec. 2008), 164:1–164:11. DOI: 10.1145/1457515.1409118.

[5] Barrault, M., Maday, Y., Nguyen, N. C., and Patera, A. T. "An 'empirical interpolation' method: application to efficient reduced-basis discretization of partial differential equations". In: *Comptes Rendus Mathematique* 339.9 (Nov. 2004), pp. 667–672. DOI: 10.1016/j.crma.2004.08.006.

[6] Benner, P., Grivet-Talocia, S., Quarteroni, A., Rozza, G., Schilders, W., and Silveira, L. M. *Applications*. De Gruyter, Jan. 2021. DOI: 10.1515/9783110499001.

[7] Benner, P., Grivet-Talocia, S., Quarteroni, A., Rozza, G., Schilders, W., and Silveira, L. M. *Snapshot-Based Methods and Algorithms*. De Gruyter, Jan. 2021. DOI: 10.1515/9783110671490.

[8] Benner, P., Grivet-Talocia, S., Quarteroni, A., Rozza, G., Schilders, W., and Silveira, L. M. *System- and Data-Driven Methods and Algorithms*. De Gruyter, Oct. 2021. DOI: 10.1515/9783110498967.

[9] Benner, P., Gugercin, S., and Willcox, K. "A Survey of Projection-Based Model Reduction Methods for Parametric Dynamical Systems". In: *SIAM Review* 57.4 (Jan. 2015), pp. 483–531. DOI: 10.1137/130932715.

[10] Berkooz, G., Holmes, P., and Lumley, J. L. "The Proper Orthogonal Decomposition in the Analysis of Turbulent Flows". In: *Annual Review of Fluid Mechanics* 25.1 (Jan. 1993), pp. 539–575. DOI: 10.1146/annurev.fl.25.010193.002543.

[11] Besselink, B., Tabak, U., Lutowska, A., Wouw, N. van de, Nijmeijer, H., Rixen, D., Hochstenbach, M., and Schilders, W. "A comparison of model reduction techniques from structural dynamics, numerical mathematics and systems and control". In: *Journal of Sound and Vibration* 332.19 (Sept. 2013), pp. 4403–4422. DOI: 10.1016/j.jsv.2013.03.025.

[12] Biro, O. and Preis, K. "On the use of the magnetic vector potential in the finite-element analysis of three-dimensional eddy currents". In: *IEEE Transactions on Magnetics* 25.4 (July 1989), pp. 3145–3159. ISSN: 1941-0069. DOI: 10.1109/20.34388.

[13] Brunton, S. L. and Kutz, J. N. *Data-Driven Science and Engineering*. Cambridge University Press, Jan. 2019. DOI: 10.1017/9781108380690.

[14] Chapman, T., Avery, P., Collins, P., and Farhat, C. "Accelerated mesh sampling for the hyper reduction of nonlinear computational models". In: *International Journal for Numerical Methods in Engineering* 109.12 (Jan. 2017), pp. 1623–1654. DOI: 10.1002/nme.5332.

[15] Chaturantabut, S. and Sorensen, D. C. "Nonlinear Model Reduction via Discrete Empirical Interpolation". In: *SIAM Journal on Scientific Computing* 32.5 (Jan. 2010), pp. 2737–2764. ISSN: 1064-8275. DOI: 10.1137/090766498.

[16] Coulomb, J. and Meunier, G. "Finite element implementation of virtual work principle for magnetic or electric force and torque computation". In: 20.5 (Sept. 1984), pp. 1894–1896. DOI: 10.1109/tmag.1984.1063232.

[17] Efron, B., Hastie, T., Johnstone, I., and Tibshirani, R. "Least angle regression". In: *The Annals of Statistics* 32.2 (Apr. 2004). DOI: 10.1214/009053604000000067.

[18] Farhat, C., Avery, P., Chapman, T., and Cortial, J. "Dimensional reduction of nonlinear finite element dynamic models with finite rotations and energy-based mesh sampling and weighting for computational efficiency". In: *International Journal for Numerical Methods in Engineering* 98.9 (June 2014), pp. 625–662. ISSN: 0029-5981. DOI: 10.1002/nme.4668.

[19] Farhat, C., Chapman, T., and Avery, P. "Structure-preserving, stability, and accuracy properties of the energy-conserving sampling and weighting method for the hyper reduction of nonlinear finite element dynamic models". In: *International Journal for Numerical Methods in Engineering* 102.5 (May 2015), pp. 1077–1110. ISSN: 0029-5981. DOI: 10.1002/nme.4820.

[20] Golub, G. H. and Reinsch, C. "Singular value decomposition and least squares solutions". In: *Numerische Mathematik* 14.5 (Apr. 1970), pp. 403–420. DOI: 10.1007/bf02163027.

[21] Golub, G. H. *Matrix computations*. John Hopkins, 2013. ISBN: 9781421407944.

[22] Grimberg, S., Farhat, C., Tezaur, R., and Bou-Mosleh, C. "Mesh sampling and weighting for the hyperreduction of nonlinear PetrovGalerkin reduced-order models with local reduced-order bases". In: *International Journal for Numerical Methods in Engineering* 122.7 (Jan. 2021), pp. 1846–1874. DOI: 10.1002/nme.6603.

[23] Hasan, M. R., Montier, L., Henneron, T., and Sabariego, R. V. "Stabilized Reduced-Order Model of a Non-Linear Eddy Current Problem by a Gappy-POD Approach". In: *IEEE Transactions on Magnetics* 54.12 (Dec. 2018), pp. 1–8. DOI: 10.1109/tmag.2018.2866449.

[24] Henneron, T. and Clenet, S. "Model order reduction of non-linear magnetostatic problems based on POD and DEI methods". In: *IEEE Transactions on Magnetics* 50.2 (2014), pp. 1–4. ISSN: 0018-9464. DOI: 10.1109/TMAG.2013.2283141.

[25] Henneron, T. and Clenet, S. "Model-Order Reduction of Multiple-Input Non-Linear Systems Based on POD and DEI Methods". In: *IEEE Transactions on Magnetics* 51.3 (Mar. 2015), pp. 1–4. DOI: 10.1109/tmag.2014.2347416.

[26] Jain, S., Tiso, P., Rutzmoser, J. B., and Rixen, D. J. "A quadratic manifold for model order reduction of nonlinear structural dynamics". In: *Computers & Structures* 188 (Aug. 2017), pp. 80–94. DOI: 10.1016/j.compstruc.2017.04.005.

[27] Karhunen, K. "Über lineare MEthoden in der Wahrscheinlichkeitsrechnung". In: *Annals of Academic Science Fennicae, Series A1 Mathematics and Physics 37* (1946).

[28] Kerschen, G., Golinval, J. C., Vakakis, A. F., and Bergman, L. A. “The method of proper orthogonal decomposition for dynamical characterization and order reduction of mechanical systems: An overview”. In: *Nonlinear Dynamics* 41.1-3 (2005), pp. 147–169. ISSN: 0924-090X. DOI: 10.1007/s11071-005-2803-2.

[29] Kirschneck, M., Rixen, D., and Polinder, H. “Model Reduction Methods for Magnetic Fields Based on Modal Analysis”. In: *IEEE Transactions on Magnetics* 50.11 (Nov. 2014), pp. 1–4. DOI: 10.1109/tmag.2014.2328863.

[30] Kost, A. *Numerische Methoden in der Berechnung elektromagnetischer Felder*. Springer, 1994. DOI: 10.1007/978-3-642-57910-3.

[31] Loève, M. “Fonctions Aléatoires du Second Ordre”. In: *Processus stochastiques et mouvement Brownien* (1948).

[32] Maierhofer, J., Dietz, C., Zobel, O. M., and Rixen, D. J. “Multiphysical Simulation, Model Order Reduction (ECSW) and Experimental Validation of an Active Magnetic Bearing”. In: *Actuators* 11.6 (June 2022), p. 169. DOI: 10.3390/act11060169.

[33] Maierhofer, J. and Rixen, D. J. “Model order reduction using hyperreduction methods (DEIM, ECSW) for magnetodynamic FEM problems”. In: *Finite Elements in Analysis and Design* 209 (Oct. 2022), p. 103793. DOI: 10.1016/j.finel.2022.103793.

[34] Maierhofer, J. and Rixen, D. J. “Strategies for Finding Training Snapshots for the Hyperreduction Method ECSW in Magnetodynamic Systems”. In: *PAMM* 22.1 (Mar. 2023). DOI: 10.1002/pamm.202200106.

[35] Maierhofer, J. and Rixen, D. J. “Computing Forces by ECSW-Hyperreduction in Nonlinear Magnetodynamic FEM Problems”. In: *IEEE Transactions on Magnetics* 60.1 (Jan. 2024), pp. 1–13. ISSN: 1941-0069. DOI: 10.1109/tmag.2023.3332210.

[36] MetaResearch. *Fast Randomized SVD*. online. 2014. URL: https://research.facebook.com/blog/2014/9/fast-randomized-svd/.

[37] Metropolis, N. “The Beginning of the Monte Carlo Method”. In: *Los Alamos Science, Special Issue*. 1987. URL: https://api.semanticscholar.org/CorpusID:18607470.

[38] Meunier, G. *The finite element method for electromagnetic modeling*. Vol. 33. John Wiley & Sons, 2010. DOI: 10.1002/9780470611173.

[39] Monegato, G. “Positivity of the weights of extended Gauss-Legendre quadrature rules”. In: *Mathematics of Computation* 32.141 (1978), pp. 243–245. DOI: 10.1090/s0025-5718-1978-0458809-0.

[40] Muller, F., Siokos, A., Kolb, J., Nell, M., and Hameyer, K. “Efficient Estimation of Electrical Machine Behavior by Model Order Reduction”. In: *IEEE Transactions on Magnetics* 57.6 (June 2021), pp. 1–4. DOI: 10.1109/tmag.2021.3070183.

[41] Nakata, T. and Fujiwara, K. “Summary of results for benchmark problem 13 (3-D nonlinear Magnetostatic Model)”. In: *COMPEL - The international journal for computation and mathematics in electrical and electronic engineering* 11.3 (Mar. 1992), pp. 345–369. DOI: 10.1108/eb010097.

[42] Paquay, Y., Bruls, O., and Geuzaine, C. “Nonlinear Interpolation on Manifold of Reduced-Order Models in Magnetodynamic Problems”. In: *IEEE Transactions on Magnetics* 52.3 (Mar. 2016), pp. 1–4. DOI: 10.1109/tmag.2015.2477169.

[43] Paquay, Y., Geuzaine, C., Hasan, R., and Sabariego, R. V. “Reduced-Order Model Accounting for High-Frequency Effects in Power Electronic Components”. In: *IEEE Transactions on Magnetics* 52.3 (Mar. 2016), pp. 1–4. DOI: 10.1109/tmag.2015.2472559.

[44] Pearson, K. “On lines and planes of closest fit to systems of points in space”. In: *The London, Edinburgh, and Dublin Philosophical Magazine and Journal of Science* 2.11 (Nov. 1901), pp. 559–572. DOI: 10.1080/14786440109462720.

[45] Peherstorfer, B., Butnaru, D., Willcox, K., and Bungartz, H.-J. “Localized Discrete Empirical Interpolation Method”. In: *SIAM Journal on Scientific Computing* 36.1 (Jan. 2014), A168–A192. DOI: 10.1137/130924408.

[46] Qu, Z.-Q. *Model Order Reduction Techniques*. Springer London, 2004. DOI: 10.1007/978-1-4471-3827-3.

[47] Radermacher, A. and Reese, S. “POD-based model reduction with empirical interpolation applied to nonlinear elasticity”. In: *International Journal for Numerical Methods in Engineering* 107.6 (Dec. 2015), pp. 477–495. DOI: 10.1002/nme.5177.

[48] Rochus, V., Rixen, D. J., and Golinval, J.-C. “Monolithic modelling of electro-mechanical coupling in micro-structures”. In: *International Journal for Numerical Methods in Engineering* 65.4 (2005), pp. 461–493. DOI: 10.1002/nme.1450.

[49] Rutzmoser, J. and Rixen, D. “A lean and efficient snapshot generation technique for the Hyper-Reduction of nonlinear structural dynamics”. In: *Computer Methods in Applied Mechanics and Engineering* 325 (Oct. 2017), pp. 330–349. DOI: 10.1016/j.cma.2017.06.009.

[50] Rutzmoser, J., Rixen, D., Tiso, P., and Jain, S. “Generalization of quadratic manifolds for reduced order modeling of nonlinear structural dynamics”. In: *Computers & Structures* 192 (Nov. 2017), pp. 196–209. DOI: 10.1016/j.compstruc.2017.06.003.

[51] Rutzmoser, J., Gruber, F., and Rixen, D. J. “A Comparison on Model Order Reduction Techniques for Geometrically Nonlinear Systems based on a Modal Derivaitve Approach using Subspace Angles”. In: *11th International Conference on Engineering Vibration*. Sept. 2015.

[52] Ryckelynck, D. “A priori hyperreduction method: an adaptive approach”. In: *Journal of Computational Physics* 202.1 (Jan. 2005), pp. 346–366. DOI: 10.1016/j.jcp.2004.07.015.

[53] Sato, Y., Clemens, M., and Igarashi, H. “Adaptive Subdomain Model Order Reduction With Discrete Empirical Interpolation Method for Nonlinear Magneto-Quasi-Static Problems”. In: *IEEE Transactions on Magnetics* 52.3 (Mar. 2016), pp. 1–4. DOI: 10.1109/tmag.2015.2489264.

[54] Sato, Y. and Igarashi, H. “Model Reduction of Three-Dimensional Eddy Current Problems Based on the Method of Snapshots”. In: *IEEE Transactions on Magnetics* 49.5 (May 2013), pp. 1697–1700. DOI: 10.1109/tmag.2013.2241412.

[55] Schmidthausler, D. and Clemens, M. “Low-Order Electroquasistatic Field Simulations Based on Proper Orthogonal Decomposition”. In: *IEEE Transactions on Magnetics* 48.2 (Feb. 2012), pp. 567–570. DOI: 10.1109/tmag.2011.2174042.

[56] Schöberl, J. “NETGEN An advancing front 2D/3D-mesh generator based on abstract rules”. In: *Computing and Visualization in Science* 1.1 (July 1997), pp. 41–52. DOI: 10.1007/s007910050004.

[57] Schöberl, J. *C++11 Implementation of Finite Elements in NGSolve*. Sept. 2014.

[58] Schöberl, J. and Zaglmayr, S. “High order Nédélec elements with local complete sequence properties”. In: *COMPEL-The international journal for computation and mathematics in electrical and electronic engineering* 24.2 (2005), pp. 374–384. DOI: 10.1108/03321640510586015.

[59] Tiso, P., Dedden, R., and Rixen, D. “A Modified Discrete Empirical Interpolation Method for Reducing Non-Linear Structural Finite Element Models”. In: *Volume 7B: 9th International Conference on Multibody Systems, Nonlinear Dynamics, and Control*. American Society of Mechanical Engineers, Aug. 2013. ISBN: 978-0-7918-5597-3. DOI: 10.1115/DETC2013-13280.

[60] Tiso, P. and Rixen, D. J. “Discrete Empirical Interpolation Method for Finite Element Structural Dynamics”. In: *Topics in Nonlinear Dynamics, Volume 1*. Springer New York, 2013, pp. 203–212. DOI: 10.1007/978-1-4614-6570-6_18.

Part III

Application

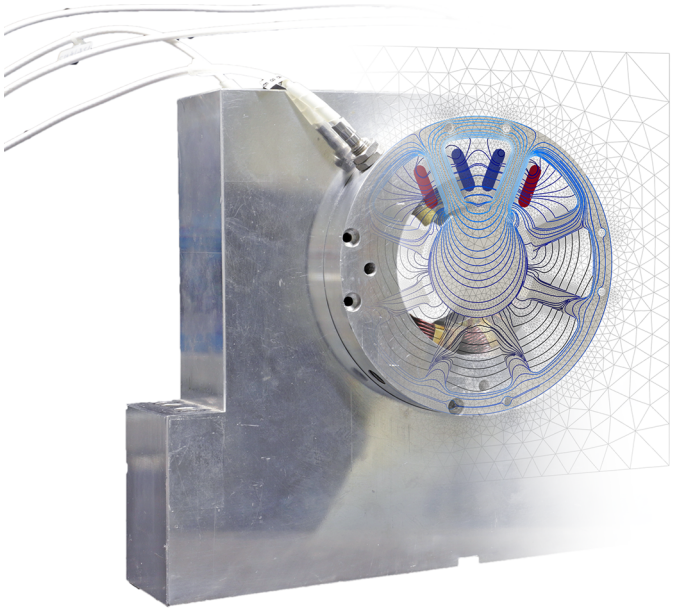

Chapter 18

Introduction

The third part of this thesis presents a case study on an active magnetic bearing at the Chair of Applied Mechanics, TUM. The given active magnetic bearing was numerically modeled with the methods shown in part I, and a test rig was built with instrumentation to measure the electrical currents, the resulting forces, and the temperature at different locations.

To show the potential of MOR techniques, a monitoring scenario is constructed with the active magnetic bearing being the key component. As exemplary high-tech applications with future relevance, so-called Flywheel Energy Storage Systems (FESS) - often also called mechanical batteries - were taken into focus. Their purpose is to store kinetic energy in high-speed rotors.

The part is structured in three chapters. After the introduction, the principle of active magnetic bearings in general and the magnetic bearing used for this study are presented. This is followed by the multiphysical simulation of the used active magnetic bearing. The third chapter shows the experimental setup and results.

Remark

Parts of the following chapters are taken from the author's publication *Multiphysical Simulation, Model Order Reduction (ECSW) and Experimental Validation of an Active Magnetic Bearing*, [14].

18.1 Flywheel Energy Storage Systems

Flywheel Energy Storage Systems (FESS) could potentially be one building block for the answer to the question of a stable and sustainable energy supply of the future in combination with strongly fluctuating renewable energy sources. A generic FESS, as shown in fig. 18.1 consists of a high-speed rotor that is supported by active magnetic bearings in a vacuum containment. Attached to the rotor is a motor/generator unit that allows to speed up the rotor to store electrical energy in kinetic energy and to generate electrical energy by draining the kinetic energy of the rotor. To store a noticeable amount of kinetic energy, the rotor has to rotate with a relatively high rotational speed. As the mechanical battery will have different charging levels, the rotation speed will vary in a broad bandwidth and will undergo multiple dynamic transitions [16].

The key component is obviously the active magnetic bearing (cf. chapter 19) and the controller system. The optimal design is only one application of good simulation techniques in the field of coupled multi-physical systems. Also, during operation, an accurate FESS model offers new opportunities for topics like condition monitoring and maintenance, respectively, predictive maintenance. A major concern is a cost-effective operation that can

only be achieved by performing maintenance before the breakdown while reducing unnecessary pre-emptive actions. Simulations for this topic often have to be very fast and have to evaluate new parameter sets in time spans, like minutes or seconds, to prevent heavy damage in certain cases. To enable stand-alone monitoring systems that are not dependent on the cloud or the network infrastructure, the so-called *edge computing* approach should be favored. The application runs on rather low-end computing devices close to the source of the data [19, 22].

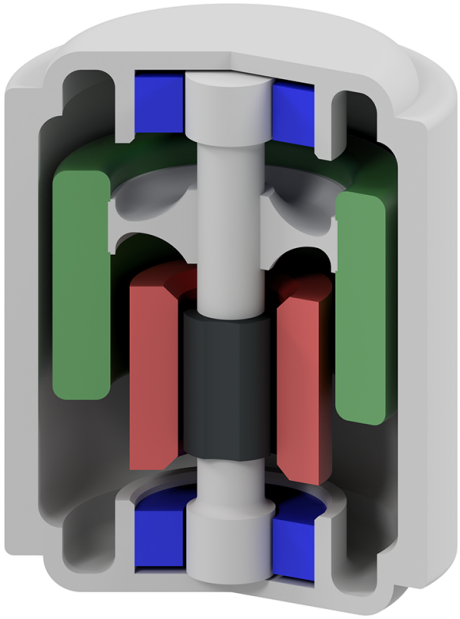

Figure 18.1: Schematic FESS (Flywheel Energy Storage System) with red: Stator, green: Rotor with inertia, blue: Active Magnetic Bearing.

18.2 Monitoring Approach

The idea of the proposed monitoring approach is depicted in fig. 18.2 and reminds us of the concept of model predictive controllers. In the first step, the currents in the coils are recorded during steady-state operation for a few seconds. Together with the initial conditions, the simulation is now performed using the recorded currents as load input. The results predict the future state of the magnetic bearing. In the meantime, the actual quantities, like temperature, also evolve in the bearing. Now, a comparison of the actual temperature with the predicted temperature is made. If the difference is within a given tolerance, we can trust the simulation and read out virtual sensor values, like forces. These forces can then be fed to another monitoring system or simulation, which finally gives the overall health status of the plant system. If the actual temperature is not near the simulated temperature, the simulation cannot be trusted. Various reasons could be at the origin of the deviation. A fault detection system will then apply different fault modes to the simulation until they match again.

Concluding: To build a reliable monitoring system, a precise model of the system is needed that is additionally also capable of running with as little computational effort as possible. This is where the idea of model order reduction is highly suitable.

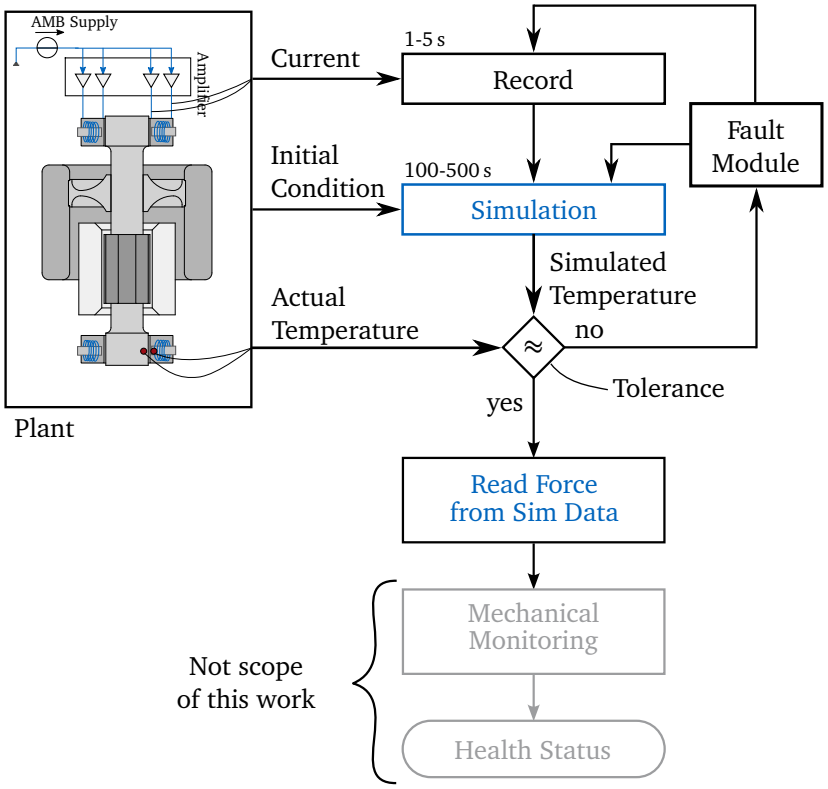

Figure 18.2: Monitoring scheme for the AMB. The simulation is fed with the measured currents and simulates the magnetic bearing. A comparison of the measured temperature with the simulated temperature gives a hint of whether the simulation matches reality and, therefore, can be trusted.

Chapter 19

Active Magnetic Bearings

Active Magnetic Bearings (AMB) are mechatronic machine elements that are used to support rotors by levitating the shaft in a magnetic field [15]. This requires a current amplifier and a position controller. This leads to the much-used term *Active Magnetic Bearing*, short *AMB*. The corresponding norm is found in ISO 14839:1-4[1].

19.1 Short History of Magnetic Bearings

Looking back to the pioneers of magnetic bearings, the name S. EARNSHAW (*1805-†1888) comes to many minds. In 1842 EARNSHAW stated very generally that no stable configuration could be found for a particle that is subjected to inverse-square force laws only [5]. At this time, the electrodynamic equations weren't yet developed in the commonly known way by MAXWELL. The so-called *Earnshaw-Theorem* was later further investigated by W. BRAUNBEK (*1901-†1977) who states: "Ein statisches, stabiles, freies Schweben eines Systems I im elektrischen, magnetischen und Schwerefeld eines anderen Systems II ist unmöglich, solange nicht in mindestens einem der beiden Systeme diamagnetische Materie vorhanden ist.", [3] (A static, stable, free-floating of a system I in the electric, magnetic, and gravitational field of another system II is impossible as long as a diamagnetic matter is not present in at least one of the two systems.) In consequence, active controller components have to be added to use the magnetic forces to levitate objects.

Magnetic bearings, in the broader sense, have played an important role in research for a long time. In 1937 J.W. BEAMS built a machine where steel balls were accelerated in active magnetic bearings until the centrifugal forces exceeded the material strength and the ball burst [1]. In the context of fast-running rotors supported by AMBs, the names SCHWEITZER, TRAXLER, BLEULER, and MASLEN have to be mentioned as they brought active magnetic bearings for rotor systems to a new level. Their knowledge is mainly condensed in their books [17] and [15].

[1] ISO 14839: Mechanical vibration - Vibration of rotating machinery equipped with active magnetic bearings

The important pros and cons of AMBs for rotor systems according to [15] are listed here.

Advantages	Disadvantages
• No mechanical contact • No contamination of fluids by lubricants • Wide range of applications (medical to energy) • Usable for monitoring software	• Highly complex system • Need for external energy • Size requirements are much bigger in relation to conventional bearings

Today's field of use of AMBs is very broad, but still, the individual products are highly specialized and not mass-produced. In research, various test facilities are built to test rotor components, e.g., seals for multiphase flow systems [23]. The bandwidth of commercial high-tech machines spans, on the one side, heavy-duty machines like compressors, pumps, or turbines in the energy sector. Besides the already mentioned flywheel energy storage systems, AMBs are utilized in subsea compressors [4]. On the other side, medical devices benefit from the advantages of AMBS, such as blood pumps. A broad overview of different magnetic levitated blood pumps and their working principle is given in [10]. SCHWEITZER describes his point of view regarding the potential of AMBs in modern machinery in [18].

19.2 General System Description

The general buildup of an AMB is shown in fig. 19.1a. A typical configuration of an AMB is the arrangement of 8 magnetic poles, connected such that they build 4 electromagnets which generate a magnetic force on the shaft. The magnetic forces are per se unstable in the radial direction, as discussed before in Earnshaw's theorem. Therefore, a control system (fig. 19.1b) is needed to stabilize the rotor in the bearing. Using a position sensor and a controller, the current through the coils in the bearing is adjusted such that the rotor is kept centered.

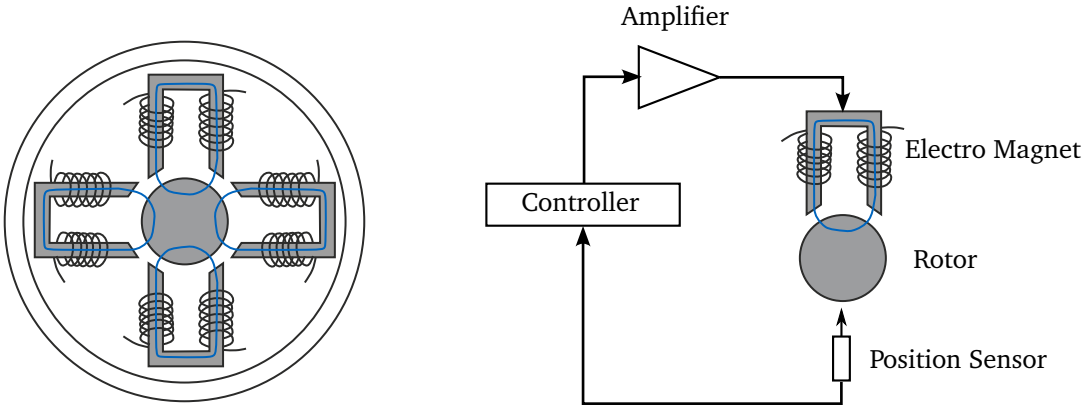

(a) Scheme for an Active Magnetic Bearing.

(b) Scheme for the position controller.

Figure 19.1: AMBs are generally unstable, which makes a position controller necessary.

As the force of an electromagnet is by construction highly non-linear, AMBs are driven in a differential mode fig. 19.2. That means the two opposite magnets are operated - one with the bias current I_0 plus the control current I_c, the other minus the control current. The applied current for two opposite magnets becomes $I = I_0 \pm I_c$. This operation mode linearizes the force-current relation around an operating point [17]. At a greater distance to this point, it is still non-linear.

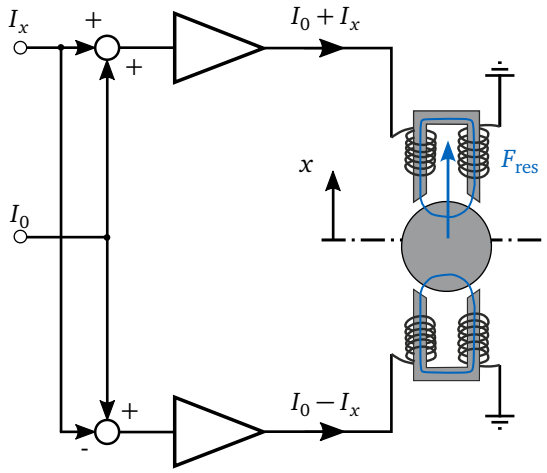

Figure 19.2: Differential mode scheme to linearize the mechanical force - current relation.

19.3 Example Magnetic Bearing

The active magnetic bearing used in the thesis is described in detail in the following section. The shown bearing in fig. 19.3a is built from 3 main parts. The copper coils are wound around the stator ①, made of electrical steel sheet metal. The explosion view in fig. 19.3b shows the AMB assembly. The stator core -blue- is mounted in an aluminum housing ②. Attached to the housing, two sensor carriers are mounted with 2 eddy current displacement sensors -yellow- ③ each to measure the rotor's position. Note that the given coordinate system is along the convention in rotor dynamics which says that the z-axis is along the shaft and the upward direction is denoted as x-axis. The y-axis is now placed to obtain a right-handed coordinate system.

The given magnetic bearing is classified as a radial type with 8 poles. The principal manufacturing process is very similar to an electric motor. A coil is wound around each pole and connected in pairs, as seen in fig. 19.4a. The resulting main field lines are orthogonal to the rotor axis [17]. This causes eddy currents in the rotor, which, therefore, should be laminated to avoid losses. The advantage of 8 pole bearings is the assignment of two opposite magnets to one Cartesian coordinate axis. To load the bearing symmetrically due to the gravity of a horizontal rotor, the poles are rotated to an X arrangement. That means the stator is rotated by 45 deg (see fig. 19.4b). The presented bearing is used in differential driving mode.

To assure good controllability, each pole pair has a collocated position sensor attached to the bearing in the ξ and η direction. As it is hard to place a position sensor in the plane of the bearing, so in the plane of the force actuation, two sensors per direction are placed left and right to the core. In fig. 19.3b, the sensors can be seen as yellow cylinders. Assuming the rotor is a rigid body, the mean value of the two positions represents the collocated translation

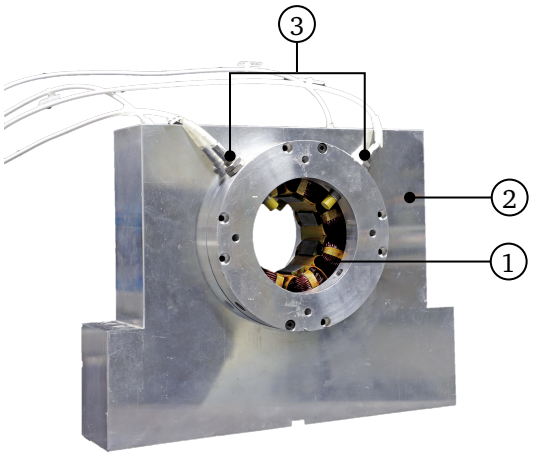

(a) Photo of the used AMB.

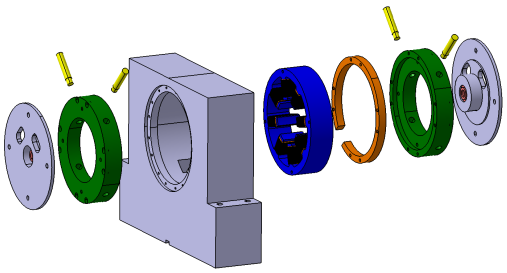

(b) CAD explosion rendering.

Figure 19.3: Example Magnetic Bearing used in this thesis.

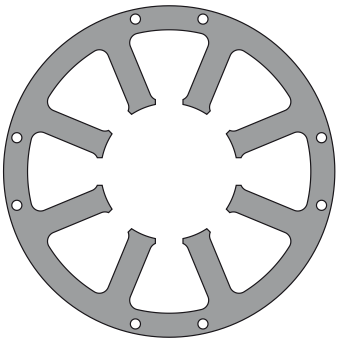

(a) Cross section of the AMB stator.

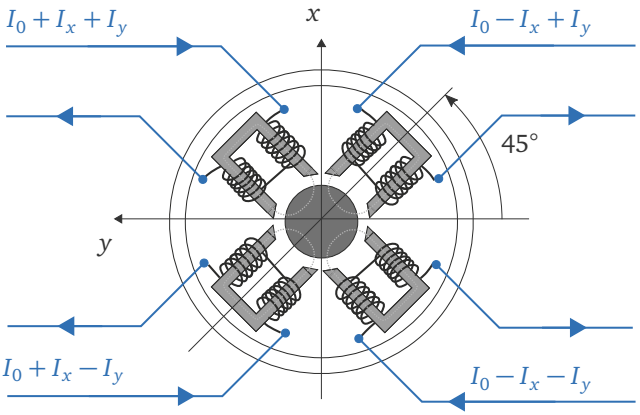

(b) AMB in X-arrangement in differential mode.

Figure 19.4: AMB used for the experimental study.

of the rotor. The additional advantage is the possibility of determining the tilting of the rotor in the bearing. All technical data are arranged in table 19.1.

19.4 AMB Amplifier

To operate the AMB, the power supply for the AMB is realized with digital current controllers. Each pole-pair, i.e., each electromagnet, is driven by one individual controller (cf. fig. 19.5), so there is no limitation in the way one can drive the bearing. This section shows the dimensioning and implementation of the current controller. First, the requirements and limits are defined, thereupon the implementation with control blocks and finally, the experimental validation.

Table 19.1: Technical Data of the used magnetic bearing.

Number of electromagnets (poles)	n	=4(8)
Angular position of the pole	γ	$= \frac{\pi}{8}$
Turns per magnet (2 poles)	N_{ML}	= 2·104
Pole shoe length	l_{ML}	= 26 mm
Cross sectional area of a pole shoe	A_{ML}	= 2.9 cm^2
Nominal stator diameter	D_{ML}	= 57.6 mm
Nominal diameter of the rotor	d_R	= 56 mm
Rest air gap	s_0	= 0.78 mm

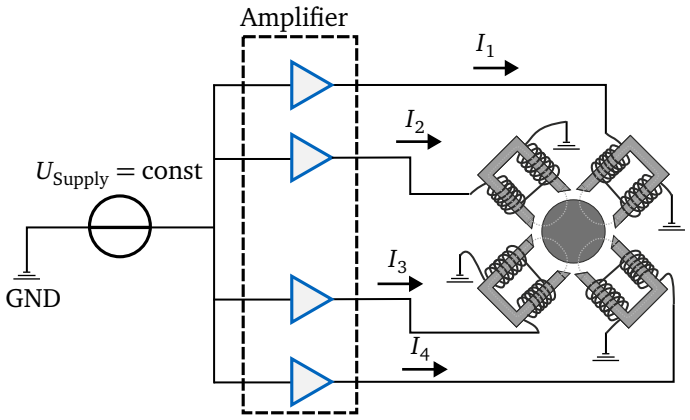

Figure 19.5: Every pole pair is actuated with one individual amplifier.

Electrical Requirements and Limits

The section below gives insights into the requirements for the magnetic bearing amplifier and the limits that cannot be overcome.

Equivalent Circuit Diagram The magnetic bearing of the shown type consists of 4 individual electromagnets that are modeled as a coil with inductivity and resistance. From now on, only one single electromagnet is considered.

Table 19.2: Values of magnetic bearing.

-	Value	method
L_{coil}	10 mH @ 1 kHz	Excort ELC-131D LCR-Meter
R_{coil}	0.35 Ω	Fluke73 series II

The equivalent circuit diagram for an electromagnet attached to a constant voltage is shown in 19.6:

The governing Kirchhoff's loop rule states that the sum of the voltages around a closed loop is zero. For time-variant currents $I(t)$, the basic equation for the inductivity $U = L\dot{I}$ relates the voltage with the change rate of the current. In combination with Ohm's law, the system's equation is written as, whereas the index *coil* is omitted:

$$U = RI + L\dot{I} \tag{19.1}$$

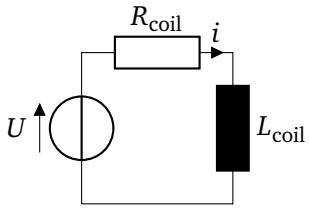

Figure 19.6: Equivalent circuit diagram

Therefore, the necessary voltage to drive a specific time-dependent current is frequency-dependent. In the following, a sinusoidal current is assumed as any time function can be decomposed into a series of sine functions. For a maximum rated current $I = 10\,\text{A}$, a voltage of $U = 3.5\,\text{V}$ is needed to overcome the constant electrical resistance of the coil.

Frequency Limits Neglecting the electrical, internal resistance, fig. 19.7 shows the array of voltage curves for increasing constant peak currents over increasing frequencies. The intersection of the necessary voltage and the maximum available voltage indicates the frequency limit to achieve a sinusoidal current of the given amplitude.

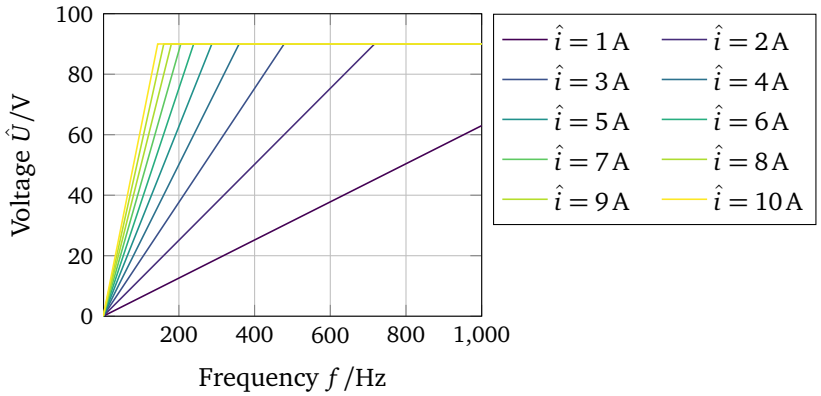

Figure 19.7: Theoretical relation between peak source voltage (90 V) and frequency for an array of peak currents.

The maximum used voltage for the magnetic bearing amplifier in the given laboratory environment is limited by the EN 61140 regulations to the *Extra-low voltage* range which carries a low risk of dangerous electrical shock[2]. The range for DC is $< 120\,\text{V}$, for AC $< 50\,\text{V}$ RMS. The decision was made for 90 V DC source current, which leads to a maximum achievable AC (RMS) Voltage of 64 V, which was tolerated in order to enable a 10 A peak for a 100 Hz frequency. To ensure human safety, all cables to the AMB are double isolated, and each housing is grounded with protective earth.

Power Estimation For sinusoidal currents, the resistance of the electric circuit is extended to the complex electrical impedance, $\underline{Z}$.

$$\underline{Z} = R + \mathrm{j}\omega L \tag{19.2}$$

[2]EN 61140: Protection against electric shock - Common aspects for installation and equipment (IEC 61140:2016); German version EN 61140:2016, chapter 4.2 Table 1

The electrical power computes as

$$\hat{P}_{\max} = \underline{Z}\hat{I}^2 \tag{19.3}$$

$$= R\hat{I}^2 + 2\pi f_{\max} L\hat{I}^2 \tag{19.4}$$

For a constant current of 10 A, a continuous power of 350 W in one electromagnet needs to be provided. For that current and a maximal frequency limited to 100 Hz results in a power of around 650 W.

Current Controller

To apply a desired current to a passive electrical consumer (i.e. the electromagnet), the applied voltage needs to be controlled. Therefore, a control loop has to be implemented. A common choice is a PI-controller. The transfer function in Laplace-space is written as:

$$\underline{G}_{\text{PI-controller}}(s) = \frac{U_{\text{PWM}}(s)}{e(s)} = \frac{K_p s + K_i}{s} \tag{19.5}$$

The magnet system itself results in a PT-1 transfer function from input voltage to output current in the Laplace domain:

$$\underline{G}_{\text{coil}}(s) = \frac{I_{\text{coil}}(s)}{U_{\text{Limit}}(s)} = \frac{1}{Ls + R} \tag{19.6}$$

Due to the digital controller, also a delay has to be considered

$$\underline{G}_{\text{delay}}(s) = e^{\mathrm{j}\omega T_{\text{delay}}} \tag{19.7}$$

As the source voltage is limited, it is not sufficient to consider only the linear transfer function, which is independent of the magnitude of the input. A transient time simulation is performed to show the influence of the source voltage limit in fig. 19.10. A sine chirp signal is taken to excite the system. Transforming both the reference and the resulting signal to the frequency domain allows one to calculate a frequency response function. Depending on the amount of current, the amplitude bends downward at the frequency at which the maximum possible voltage is exhausted.

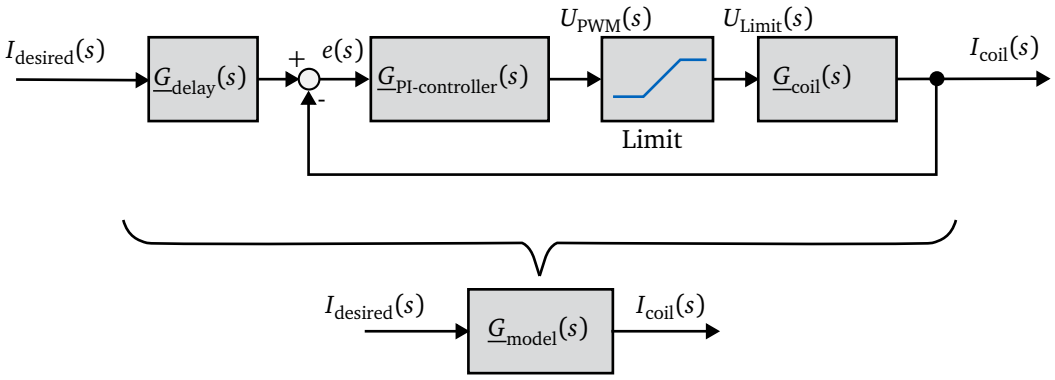

Figure 19.8: Closed current controller loop.

Implementation of the AMB Amplifier

The theoretical considerations shown above are translated into reality using digital control modules from the field of robotics. The drive modules *Whistle* of the *SimplIQ*-series from the manufacturer *ELMO* are suitable for voltages up to 95 V, currents up to 10 A and a continuous power rating of 800 W. The configuration is done via an RS232 interface, while the parametrization and control words can be sent with the implemented CAN protocol. The desired current is delivered as an analog signal, as the CAN bus does not have enough capacity to provide the desired current for 8 modules in one cycle of 4 kHz. After the ELMO modules have been programmed once using the RS232 interface, they can be parametrized by CAN fieldbus communication. To ensure synchronous operation of the individual axis, the desired target current is set on each module by an analog voltage. The actual current can be read using a CAN bus or PWM output signal.

Table 19.3: Features of the motor drivers of the ELMO SimplIQ Whistle series.

Feature	WHI-A10/100
Max. continuous current (DC):	10 A
Peak current:	14 A
Max. continuous power:	800 W
Source voltage:	12 VDC to 95 VDC
Rated voltage:	85 VDC
Controller sample rate:	up to 14 kHz, default 11 kHz
Communication	RS232 and CANopen (DS301, DS305, DS402)

To obtain the required voltage, two AE-800-48 power supplies from COTEK with an output voltage of 48 V each are connected in series, resulting in a voltage level of 96 V. To ensure that the maximum operating voltage of the ELMOs is not exceeded, the output voltage of the power supplies must be trimmed so that a sufficiently low voltage level is achieved. All modules are packed into a housing to provide a robust test rig setup, see fig. 19.9.

Figure 19.9: Top and front view of the built amplifier. Top: Power supply in the top left corner and 2 stacks with each 4 current controller.

Experimental Characterization of the Amplifier

To validate the setup, an experimental current transfer analysis is conducted. The considered AMB is attached to the corresponding controller modules, and a sine chirp trajectory is applied to the controller via the analog input. The true current is measured using external current measuring clamps. The results for one coil for different amplitudes are shown in the Bode plot fig. 19.10. The measurement values are filtered with a moving average and the colored area indicates the standard deviation. The ideal transfer function would show a constant current-to-current factor of 1. Two effects are noticed immediately: First, a constant phase drop which stems from the time delay introduced by the digital controller. Second, the bending towards lower factors for higher frequencies depends on the desired current. This effect was expected and is explained by the limited voltage of the power supply. The sim-

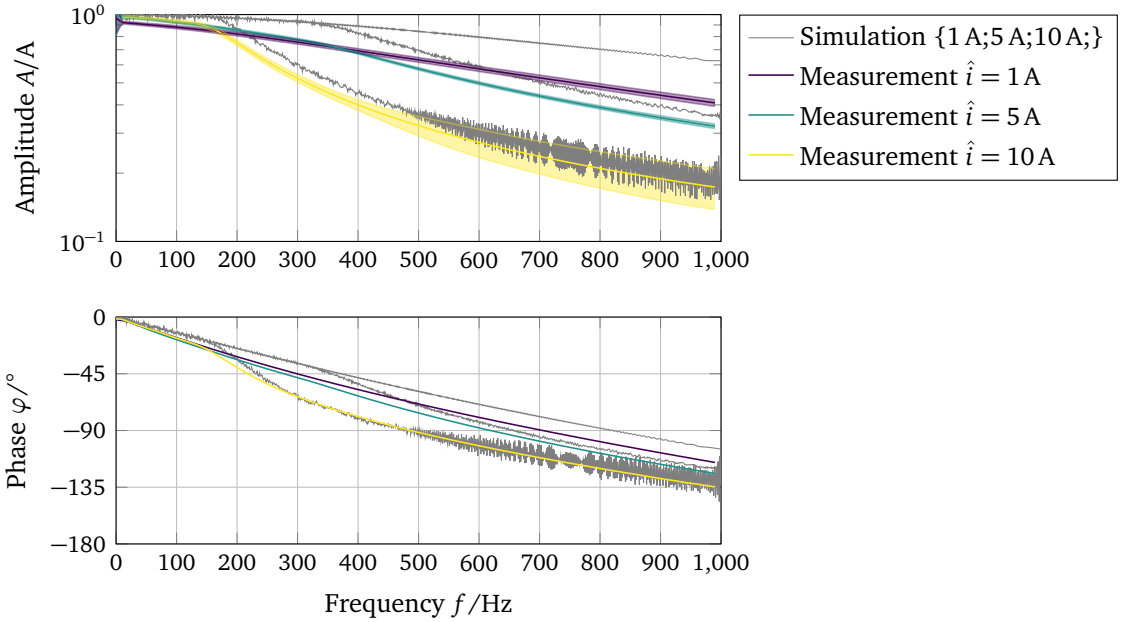

Figure 19.10: Comparison of measurement and simulation for a modeled time delay of 150 μs.

ulation of the amplifier is conducted using an RK45 time integration of the shown transfer functions including the limit of the supply voltage and an empirically identified delay time of 150 μs. With the chosen parameters, the measurements could not be fitted completely, but the overall trend seems acceptable.

Chapter 20

Multiphysical Simulation of the AMB

This chapter presents the simulation setup for the previously described AMB under the consideration of non-linear magnetic permeability as well as temperature-dependent conductivity. After deriving the full-order model, the ECSW method is applied, and a reduced-order model is generated.

20.1 Full-Order Model

First, a full-order model must be set up to capture all relevant physical effects. In the following, the partial differential equations for magnetodynamics and thermodynamics are presented, and a coupled finite element model is derived. Similar approaches are discussed in [11, 24].

20.1.1 Governing Equations

Starting from *Maxwell's equations* for the electrodynamics, a few assumptions are made which simplify the equations for the application of electromagnetism in the low-frequency range. More information on the detailed derivation is given in part I. The first equation to consider is *Ampere's law* eq. (20.1) where the current densities $\boldsymbol{j}$ in the coils lead to a magnetic field $\boldsymbol{H}$, see eq. (20.1), which is related to the magnetic flux density $\boldsymbol{B}$, with the isotropic, non-linear material parameter μ, as shown in eq. (20.3). According to *Faraday's law* eq. (20.2), a change in the magnetic flux density ($\boldsymbol{B}$) results in an electrical field $\boldsymbol{E}$, as shown in eq. (20.2).

$$\nabla \times \boldsymbol{H} = \boldsymbol{j} \tag{20.1}$$

$$\nabla \times \boldsymbol{E} = -\frac{\partial \boldsymbol{B}}{\partial t} \tag{20.2}$$

$$B = \mu(B)H \tag{20.3}$$

A challenging task during the modeling of the existing active magnetic bearing, is the determination of the material parameters for the stator and rotor, as for both no reliable material datapoints were available. Typically, the magnetic permeability μ of the ferromagnetic components decreases significantly for higher flux densities ($\|\boldsymbol{B}\| > 1\,\mathrm{T}$). We choose the approach to generate a generic, isotropic, analytical function for the permeability of each which is tuned later in the process to fit the experimental setup. To guide the initial values, the stator material is assumed to be *M270-35*, according to EN 10106, [21]. The datasheet states different curves for different operation frequencies, where the 50 Hz range is chosen. To get a guess for the rotor material, a piece of material was measured at a partner. The corresponding BH-curves are shown in fig. 20.1 as grey lines. Empirically determined analytical

functions are fitted to represent the characteristics of the measured and datasheet values. The tuned analytical functions are written as follows. Note that the expression assumes SI units.

$$\mu_{\text{Stator}}(B) = \left(\frac{2000}{0.4 + (B/\text{T})^8} + 1\right)\mu_0 \tag{20.4}$$

$$\mu_{\text{Rotor}}(B) = \left(\frac{400}{1 + 0.4(B/\text{T})^8} + 1\right)\mu_0 \tag{20.5}$$

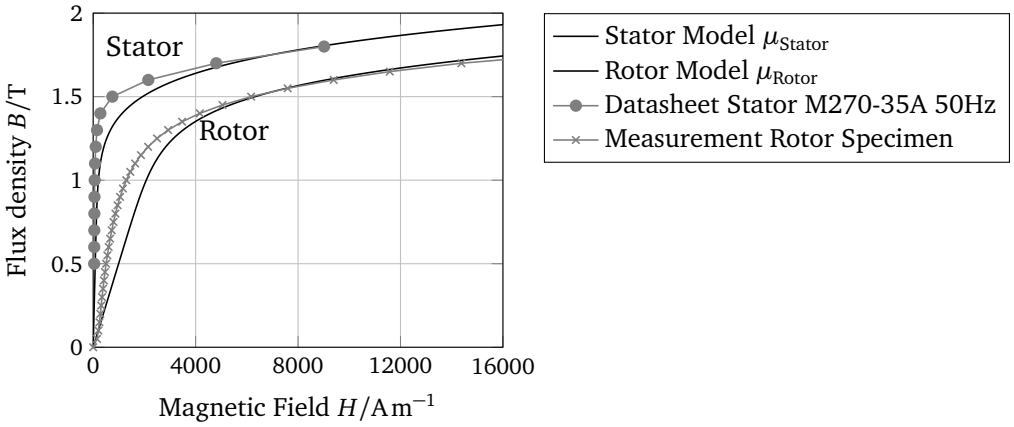

Figure 20.1: Generic material laws for the rotor and stator in comparison to data from the datasheets.

For varying currents, the magnetic field changes in time and induces the rotation of the electrical field $\boldsymbol{E}$, eq. (20.2). The induced electrical field causes the eddy currents, which are described by *Ohm's law* where we consider that the conductivity σ is a function of the temperature T (more information on the physics of conductivity in metals [20]):

$$\boldsymbol{j}_{\text{eddy}} = \sigma(T)\boldsymbol{E} \tag{20.6}$$

The eddy current itself affects the magnetic field $\boldsymbol{B}$ via eq. (20.1). For higher frequencies, the electromagnetic field concentrates in the boundary regions because the local eddy currents prohibit the field from further propagating in the material. This is known as the skin-effect, refer to section 3.3.3. The dissipating eddy currents lead to a temperature rise in the bearing, which has a negative effect on the electrical conductivity σ as shown in fig. 20.2. In the *Handbook of Chemistry and Physics* [8], a vast collection of chemical and physical material properties, values of the temperature dependency of the electrical resistivity, respectively conductivity for pure iron materials are found. Only two parameters are needed to build a simple model, the default conductivity $\sigma_0 = 10\,\text{MS/m}$ and a temperature coefficient $\gamma = 0.0058\,1/\text{K}$.

$$\sigma = \frac{\sigma_0}{1 + \gamma T} \tag{20.7}$$

The specific power loss can now be computed from the eddy currents and the actual conductivity by:

$$q_{\text{heat}} = \frac{\|\boldsymbol{j}_{\text{eddy}}\|^2}{\sigma(T)} \tag{20.8}$$

To model the temperature evolution in the magnetic bearing, q_{heat} is used as the source term in the non-stationary heat equation:

$$\rho c \frac{\partial T}{\partial t} - \nabla \cdot \lambda \nabla T = q_{\text{heat}} \tag{20.9}$$

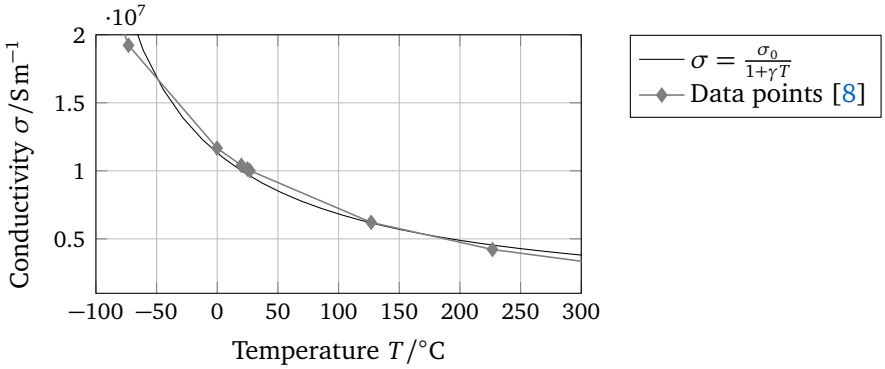

Figure 20.2: Non-linear material law for the electrical conductivity of iron.

Here, $\rho = 7.874 \times 10^3\,\mathrm{kg\,m^{-3}}$ denotes the material density, $c = 449\,\mathrm{J\,kg^{-1}\,K^{-1}}$ the specific heat capacity, and $\lambda = 80\,\mathrm{W\,m^{-1}\,K^{-1}}$ the thermal conductivity. All thermal properties are assumed to remain constant in the scope of this work.

20.1.2 FEM-Discretization

To solve the partial differential equations, the modified vector potential $\boldsymbol{A}$ is introduced such that $\boldsymbol{B} = \boldsymbol{\nabla} \times \boldsymbol{A}$, as explained in detail in chapter 5. In difference to the fundamental assumptions in part I, the electrical conductivity is now assumed to be temperature-dependent but we need to assume it is homogeneous across the stator and rotor. As BIRO points out in [2], in this case, both the magnetic- and the electric field can be derived from the modified vector potential $\boldsymbol{A}$ as shown in eq. (20.10) where $\boldsymbol{j}_0$ is the imposed current density.

$$\boldsymbol{\nabla} \times \left(\frac{1}{\mu(\boldsymbol{A})} \nabla \times \boldsymbol{A} \right) = \boldsymbol{j}_0 - \underbrace{\sigma(T) \frac{\partial \boldsymbol{A}}{\partial t}}_{\text{eddy current}} \tag{20.10}$$

The discretization by finite elements results in a non-linear model with the primary variable $\boldsymbol{u}_E$, denoting the discretized vector potential solution. The model exhibits a non-linear internal current vector (internal forces in analogy to mechanical problems), which stems from the material non-linearity in fig. 20.1. The mass matrix (called as such in reference to mechanical problems and originating from the last term in eq. (5.16)) includes the electrical conductivity and hence depends on the discretized temperature solution $\boldsymbol{u}_T$. After discretization, the equations for the thermo-magneto-electric system have the form:

$$\boldsymbol{M}_E(\boldsymbol{u}_T)\dot{\boldsymbol{u}}_E + \boldsymbol{g}(\boldsymbol{u}_E) = \boldsymbol{f}_E(\boldsymbol{j}_0) \tag{20.11}$$

For the thermal problem, a linear finite element model is used, where the rhs depends on the eddy currents and the temperature solution $\boldsymbol{u}_T$ itself.

$$\boldsymbol{M}_T\dot{\boldsymbol{u}}_T + \boldsymbol{K}_T\boldsymbol{u}_T = \boldsymbol{f}_T(\boldsymbol{j}_{\text{eddy}}, \boldsymbol{u}_T) \tag{20.12}$$

Since the magnetodynamic model in eq. (20.11) and the thermal model in eq. (20.12) are fully coupled, a staggered solution scheme is proposed.

20.1.3 Time Integration

In this application, the temperature changes much slower than the electrodynamics (minutes/hours vs. milliseconds). Therefore, it is reasonable to perform a fully coupled simulation only for a small time frame, e.g., one magnetodynamic period. During this phase, the specific power loss in eq. (20.8) is averaged and fed into the thermal model as a constant heat source afterward. The temperature development can then be computed for a much longer time frame T. Subsequently, the electrodynamics have to be recalculated since the electrical conductivity has changed with the temperature. By using this alternating staggering scheme (fig. 20.3), the long-term force and temperature development can be computed with comparably low computational effort.

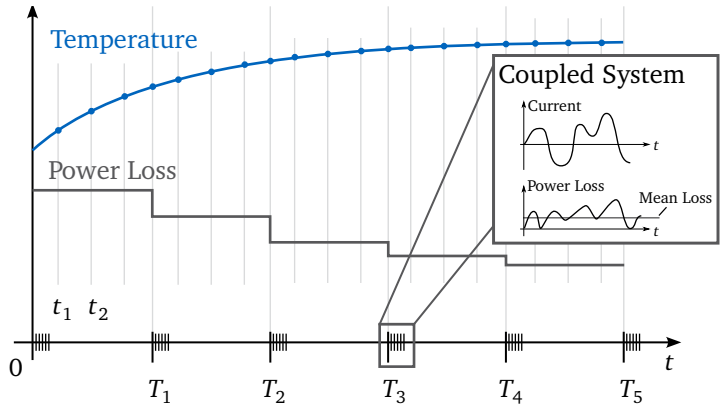

Figure 20.3: Time integration scheme with t_i being the magnetodynamic period and T_j denoting the large time step used for the time integration of the thermodynamic model.

The time integration itself is performed using the backward Euler algorithm with k indicating the time step. For the magnetodynamic domain eq. (20.11), the solution $\boldsymbol{u}_{E,k+1}$ for the next time step t_{k+1} is then found with a Newton-Raphson scheme. For the thermal domain in eq. (20.12), only a linear solution is needed to find $\boldsymbol{u}_{T,k+1}$. Note the difference in the two time steps $\Delta t = t_{k+1} - t_k$ and $\Delta T = T_{k+1} - T_k$, as seen in fig. 20.3.

$$\boldsymbol{M}_E(\boldsymbol{u}_{T,k})\boldsymbol{u}_{E,k+1} + \Delta t \boldsymbol{g}(\boldsymbol{u}_{E,k+1}) = \boldsymbol{M}_E(\boldsymbol{u}_{T,k})\boldsymbol{u}_{E,k} + \Delta t \boldsymbol{f}_E(\boldsymbol{j}_{0,k+1}) \tag{20.13}$$

$$(\boldsymbol{M}_T + \Delta T \boldsymbol{K})\boldsymbol{u}_{T,k+1} = \boldsymbol{M}_T \boldsymbol{u}_{T,k} + \Delta T \boldsymbol{f}_T(\boldsymbol{j}_{\text{eddy},k+1}, \boldsymbol{u}_{T,k+1}) \tag{20.14}$$

20.1.4 Geometry and Mesh

Figure 20.4 shows the 2D finite element model of the magnetic bearing. It consists of the rotor, stator (conductive domain) and the coils. Both are surrounded by air, which is a further simplification compared to the real system (cf. section 19.3). To model the heat loss across the stator boundaries into the housing, a heat transfer coefficient α is introduced and calibrated on the test rig (cf. chapter 21).

The material behavior of the rotor and stator is modeled by the non-linear magnetization curves presented in fig. 20.1 and the temperature-dependent electrical conductivity of iron depicted in fig. 20.2. The magnetization behavior of the coils is equivalent to air ($\mu_{\text{copper}} = \mu_0$).

In order to accurately model the full electrodynamics in the conductive domain, the mesh must fulfill certain requirements. Due to the skin effect, the element size (here defined

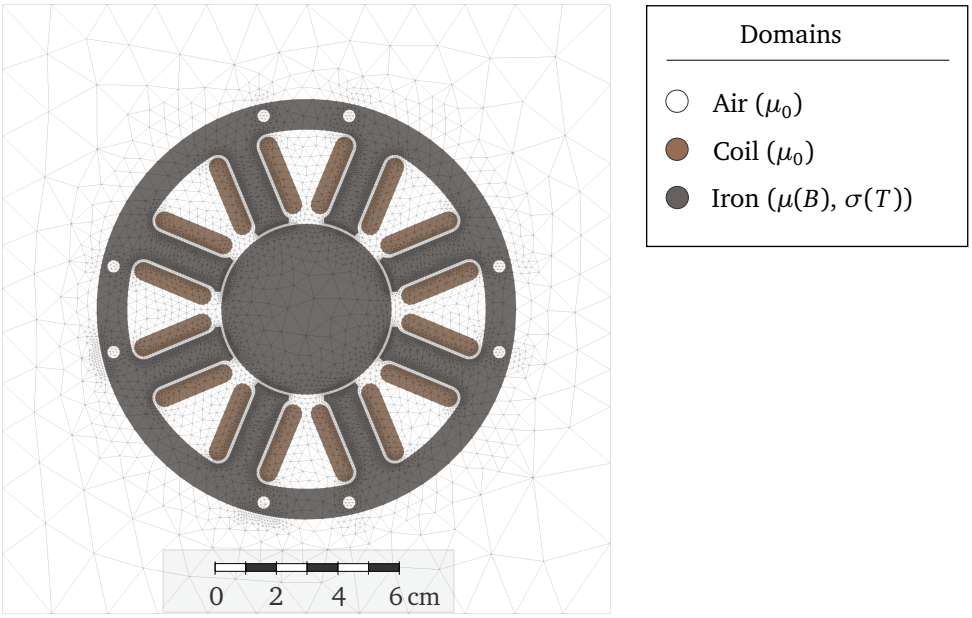

Figure 20.4: 2D-model of an active magnetic bearing with finite element mesh.

as the maximal edge length) in the boundary region should be smaller than half the skin depth δ [6]:

$$h < \frac{1}{2}\delta \qquad \text{with} \quad \delta = \frac{1}{\sqrt{\pi f \mu \sigma}} \tag{20.15}$$

For a frequency f of 100 Hz, $\mu_r = 5000$ and $\sigma = 2 \times 10^6\,\mathrm{S\,m^{-1}}$ the element size on the iron boundary has to be smaller than 0.25 mm. Furthermore, increasing the element size exponentially towards the inner of the iron parts is suggested. The fine spatial discretization leads to a very high-dimensional model with a large number of dofs. The mesh used for this work (fig. 20.4) provides an element size of around 0.25 mm to 25 mm from the iron-air boundary to the outside air volume. Thus, as a rough estimation, the simulation quality will not be appropriate for simulation frequencies above 100 Hz. On the other hand, a more refined mesh makes it impossible to solve fully on simple desktop machines.

20.1.5 Force Computation

The resultant of all magnetic forces on the rotor is computed by applying the principle of virtual work, which is realized as a finite difference. Therefore, the rotor domain and its nodes are displaced by a small displacement. The procedure explained in chapter 6 is then applied to retrieve the mechanical force.

20.2 Applied Model Order Reduction

Since the models for the magnetodynamics and the thermodynamics are uncoupled within the time integration strategy proposed in section 20.1.3, both models can be reduced independently.

20.2.1 Thermal Model

A simple projection to a subset of thermal modes is sufficient for the linear thermal model (scalar temperature field vector $\boldsymbol{u}_T$). The reduction basis is denoted by $\boldsymbol{V}_T$, whereas the generalized temperature coordinates are written as $\boldsymbol{q}_T$.

$$\boldsymbol{u}_T = \boldsymbol{V}_T \boldsymbol{q}_T \tag{20.16}$$

The thermics in the bearing can be mainly covered by the two thermal rigid body modes with equally distributed temperatures in the rotor and the stator respectively. As a positive side effect, a homogeneous temperature solution is enforced in the rotor and stator, which was also an assumption in the derivation of the governing electrodynamic equations (cf. section 20.1.1). The Galerkin projection of eq. (20.12) onto $\boldsymbol{V}_T$ yields a 2×2 system for the thermodynamics:

$$\boldsymbol{M}_{r,T} \dot{\boldsymbol{q}}_T + \boldsymbol{K}_{r,T} \boldsymbol{q}_T = \boldsymbol{V}_T^T \boldsymbol{f}_T(\boldsymbol{j}_{\text{eddy}}, \boldsymbol{q}_T) \tag{20.17}$$

20.2.2 Setup of the Reduced Model

As the ECSW method, in combination with the POD projection, is a data-driven method, the first task is to find an appropriate training set. To generate the snapshots for the PODs and for the internal currents used for training the ECSW (i.e. finding an appropriate reduced set of elements and the corresponding weights), a sinusoidal time history (also called trajectory here) for the imposed currents (load) is chosen and time solutions are computed for the lower and upper extreme load amplitudes and frequencies expected during monitoring. The temperature is held constant at $T = 20\,^{\circ}\text{C}$. For training the ECSW, one period of a mono-harmonic excitation with 10 equidistant snapshots per period was empirically found to be sufficient. The implemented value tuples are listed in table 20.1. As the system is at rest at the beginning of each load trajectory, the snapshots also capture the transient behavior. All generated solution vectors are then gathered into one training set.

Table 20.1: Four simulation setups to find the basis and to train the ECSW element selection at a constant temperature of $T = 20\,^{\circ}\text{C}$.

$j/\text{A/mm}^2$	f/Hz	$\Delta t/\text{ms}$	n_{Steps}
1	10	10	10
1	100	1	10
4	10	10	10
4	100	1	10

The computations are performed on a standard desktop-class computer installed environments as listed in table 20.2.

Table 20.2: Computer configuration with installed environments

Processor	Intel®Core™i7-8850H @ 2.60GHz
RAM	16 GB
OS	macOS 12.4
Python	3.8.10
NGSolve	6.2201

From that training set a POD is computed of which 10 modes are kept. With them, three reduced models are computed using the standard ECSW method as seen in chapter 15. The three ROM differ in their number of included elements. For that, the sNNLS tolerance τ was defined in a logarithmic progression with a base of 10, i.e. $\tau = \{10 \times 10^{-2}; 10 \times 10^{-3}; 10 \times 10^{-4}\}$. In fig. 20.5, the result of one exemplary ECSW training process is shown. The colored elements are chosen with their weight encoded by the color.

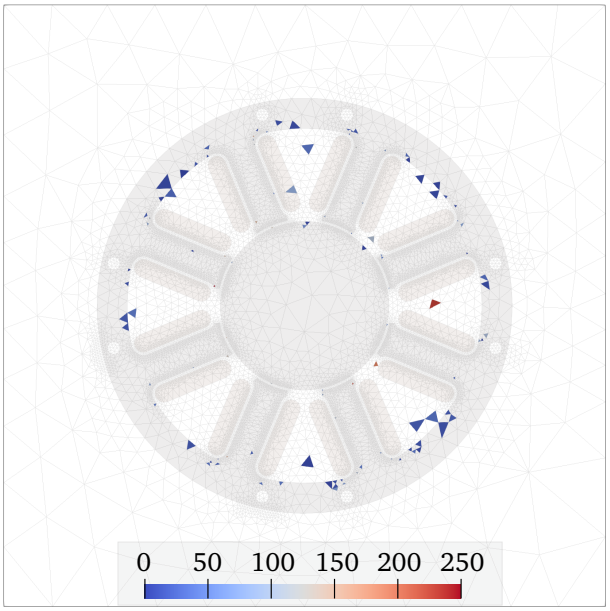

Figure 20.5: Exemplary ECSW-elements and corresponding weights of the reduced mesh.

The three ROMs are characterized in table 20.3. The computational effort is discussed in two stages, namely the offline phase and the online phase. The first row section shows the duration of the offline computation, i.e. the element selection process, for the three different hyper-reduction levels expressed by τ.

A first study to test the ROMs is conducted using the same excitation trajectories (see table 20.1) as for the training simulation. The computational time for key steps of the time integration simulation of this onboard test is condensed in the second section of table 20.3. The computational costs for one time step are compared between the full and reduced-order models (ECSW). Since the computational times vary depending on the actual load step and system state, all times are averaged over the whole trajectory of the training simulation. The step *Residual* lists the costs required to evaluate the non-linearity and to assemble the (reduced) internal current vector. A similar cost reduction can be noticed in the computation of the tangential stiffness matrix (see *Tangent Matrix*). Additionally, the computational time to solve the linear system (see *Linear Solve*) within the Newton-iteration scheme is significantly reduced. It should be noted that some overhead during the solution process cannot be avoided. Thus, the real simulation of the reduced model does not entirely scale with the number of elements. Summing up, the required computational resources can be decreased strongly by the ECSW method while the allowed error on the internal energy allowed during training is small.

Table 20.3: Computational times of different simulation steps for the three reduced-order models compared with the full training simulation.

	Full	ECSW		
		$\tau = 10^{-2}$	$\tau = 10^{-3}$	$\tau = 10^{-4}$
No. of Elements	27466	60	139	273
Element Selection Time	-	11 s	39 s	111 s
Residual Evaluation	45 ms	6 ms	7 ms	7 ms
Tangent Matrix	95 ms	2 ms	3 ms	3 ms
Linear Solve	62 ms	0.1 ms	0.1 ms	0.1 ms
Total Simulation Time	150 s	38 s	39 s	40 s

20.2.3 Validation of the Model

To prove the ability of the reduced models, different load cases are now applied to the reduced models, and the resulting force curve is compared against a full simulation with the same parameters. The quantitative measure for the comparison is a relative error (RE) for the force computed over all the time steps t_i along the test load case as follows:

$$RE = \frac{\sqrt{\sum_i (F_{\text{ref}}(t_i) - F(t_i))^2}}{\sqrt{\sum_i F_{\text{ref}}(t_i)^2}} \times 100\,\% \tag{20.18}$$

Throughout this investigation, the time signal of the load is chosen as a sine. This is, on the one hand, practicable for the test rig as well as for the simulation. On the other hand, it is very close to the load case expected for active magnetic bearings in applications.

The resulting reduced models achieved by the ECSW method offer some very interesting benefits in comparison to purely data-driven black box models. One point is that the same reduced system can also be used for different positions of the rotor in the bearing, as the model still contains the geometric information. Also, different time step sizes do not influence the model. In addition, since the model is still physics-based (the data are only used to train the hyper-reduction of the forces, but the forces in the chosen element are still obtained from a model), one can expect that the reduced model will be able to extrapolate the behavior of the system better than models purely data-driven (e.g. Neural Networks).

To test the ROM capabilities, the mechanical force on the rotor is computed for different parameters of a simple sine load case. The tested load cases are all different from the training cases. The results are given in table 20.4. In the matrix form for each combination of amplitude and frequency, the relative error related to the full simulation is given as a percentage and is also color-coded to give a visual impression. The first conclusion is drawn from the pure POD projection: The relative error is increasing with the frequency. The reason for the bad performance of the cross-validation of the higher frequency (400 Hz) is probably that the skin effect significantly changes and also the delay in the propagation of the fields so that the POD obtained from lower frequencies is no longer appropriate. The second result from table 20.4 shows that the hyperreduction doesn't introduce much new error to the model. In some cases, the error is even reduced, which is explained by the fact that, by coincidence in our example, the errors due to the projection on a reduced space and the ones arising from the hyper-reduction partly compensate.

Table 20.4: Relative errors, always referred to the full simulation reference, of the force for different parameters and excitations for each of the three hyperreduction models built from the training set generated from table 20.1.

	Full	POD	ECSW		
			$\tau = 10^{-2}$	$\tau = 10^{-3}$	$\tau = 10^{-4}$
# dofs	13566	10	10	10	10
# els	27466	27466	60	139	273
		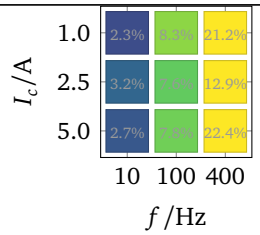	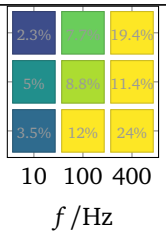	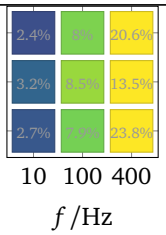	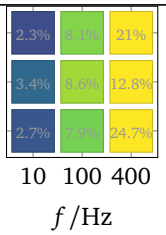

20.2.4 Conclusion

The ECSW method has a big potential noting that only a few elements are necessary to approximate the reduced forces accurately. Further investigation needs to be conducted to find good training snapshots which span a wide field of parameters. Furthermore, the limitation of the mesh size needs to be improved. Optimization of the code would reveal higher time savings which scale better with the number of elements.

Chapter 21

Calibration of the Simulation with the Test Rig

In the previous sections, a (reduced-order) model for the magnetic bearing was derived. In order to predict the force exerted on the rotor correctly, the parameters of the simulation model must be calibrated. For this purpose, a specialized test rig for the AMB was built.

21.1 Test Rig Description

The test rig (fig. 21.1) carries the AMB mounted onto a 6-dof force measurement platform and a rotor that is not rotating and is fixed in the center of the AMB. In this work's scope, only the rotor's center position is considered since it is the idle position in operation mode. In addition to the force sensor, two current sensing clamps and temperature sensors are applied to measure the relevant quantities as proposed in the monitoring scheme, section 18.2.

21.1.1 Mechanical Setup

Two aluminum towers are mounted on each side onto the ground plate. Between the pillars, a platform is attached. On top of this platform, a 6-dof force sensor is fixed. The magnetic bearing is set on the upper part of the sensor. The bearing force is applied to a fixed rotor between two horizontal slides integrated into the tower. The position of the rotor shaft is measured with 4 eddy current sensors arranged in two layers. Therefore, it is possible to set exactly every position in the xy-domain of the bearing and measure all 6 degrees of freedom. The shaft is made from solid iron, as it was not intended to encounter bundle lamination in the simulation. The shaft has a diameter of 15 mm and a free length of around 300 mm. The magnetic relevant part of the shaft in the bearing has a diameter of 40 mm. The full-mounted test rig is shown in fig. 21.1. As the position of the shaft is measured at every moment, it is not problematic if there is little backlash in the test rig. A significant issue that required attention was the so-called pull-in effect of the rotor, which becomes prominent at high forces in the extremal positions. Given that this setup provides no active position controller, the pull-in effect is a potential occurrence. This effect causes the rotor to adhere to one of the poles due to the inverse quadratic force law, which is dependent on the distance between the rotor and the core. Consequently, it was necessary to ensure the shaft was sufficiently rigid to prevent the occurrence of the pull-in effect.

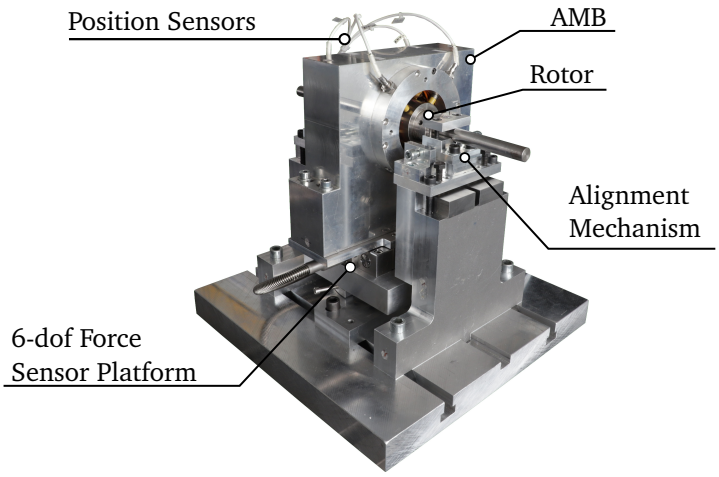

Figure 21.1: Test rig for the AMB with a 6-dof force measurement platform.

21.1.2 Definitions of Directions

For this study, the AMB is considered only in one single direction, the x-direction as visualized in fig. 21.2. The AMB is considered as perfectly symmetric which allows a minimum set of parameters, namely the pre-current I_0 and the control current I_x.

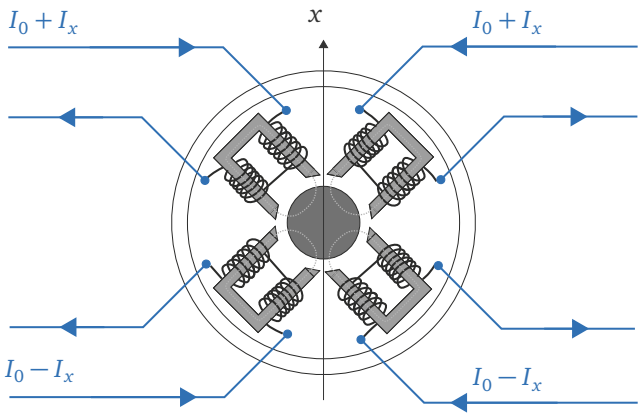

Figure 21.2: Considered direction of the AMB.

21.1.3 Position Sensor

Four eddy current sensors (TQ402-B21) are built into the AMB to measure the shaft's position. Eddy current position sensors use variations in electromagnetic fields generated by eddy currents to detect the position or displacement of a target object without physical contact. During the manual setup process, the sensors are used to position the shaft in the bearing. The measured values have to be transformed from the (ξ, η)-frame of reference, co-linear with the sensors, into the global (x, y)-frame of reference, see fig. 21.3. The attached index i specifies the side of the bearing. Two sensors are on the front side of the bearing, two on the backside. To avoid misalignment, the shaft needs to be adjusted such that the air gap is equal

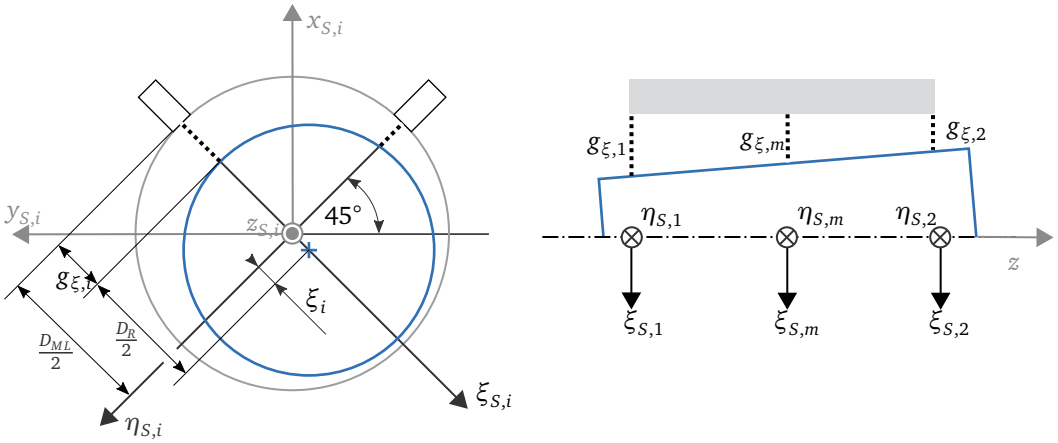

Figure 21.3: Sensor positions in the housing (gray) relative to the rotor shaft (blue). Two sensor planes result in 4 measured air gaps $g_{\xi|\eta,1|2}$.

for both sensor planes, $g_{\xi,1} = g_{\xi,2}$. Due to the X-arrangement of the bearing, the two frames of reference share the same origin and are rotated by 45°, so the coordinate transformation writes:

$$x = -\frac{1}{\sqrt{2}}\xi - \frac{1}{\sqrt{2}}\eta \tag{21.1}$$

$$y = -\frac{1}{\sqrt{2}}\xi + \frac{1}{\sqrt{2}}\eta \tag{21.2}$$

After the assembly process of the test rig, the eddy current sensors need to be calibrated to the actual mounting position, the target shape, and material. For that purpose, aluminum spacer sleeves were manufactured and put around the shaft to mechanically adjust the sensor's position.

21.1.4 Force Sensor

In order to measure the forces exerted by the AMB, it is necessary to use a force sensor that meets several criteria. The primary requirement is a sensor capable of measuring all six degrees of freedom (forces and moments), which enables a comprehensive calibration of the bearing across all potential degrees of freedom in a 3D context. Another critical consideration is that the sensor should provide as much rigidity as possible to prevent any relative displacement of the rotor to the bearing, thereby ensuring accurate sampling of target points. Moreover, the force sensor should be immune to the effects of electromagnetic fields and temperature variations.

The principles underlying piezo-based force measurement are ideally suited to satisfy these conditions. The mechanics of this type of measurement revolve around the quantification of charges that a piezo crystal can absorb to varying degrees based on its level of deformation. The charge is directly proportional to the force applied to the embedded piezo crystal in the sensor.

The company *Kistler* offers a *Multicomponent Dynamomenter (Type 9129AA)*[1], shown in fig. 21.4, which is used for this investigation. The device provides dynamic and quasi-static measurements of 3 orthogonal force components and 3 moments with at the same time high stiffness. It is used with a charge amplifier *Kistler Type 5080A*.

Figure 21.4: Picture of the force sensor *Kistler 9129AA* [12].

Static Response Due to the physical principle, a static measurement using this sensor can be critical. The finite impedance of the input of the charge measuring unit leads to a balancing of the charges over time, and therefore the output signal decreases over time for a constant load of the sensor. In the used charge amplifier, a resistor can be switched on or off to adjust the time constant. For the resistor switched off, the only resistor left is the insulation resistance of the necessary capacitor in the circuit.

Dynamic Response The dynamic response of the force sensor was tested at the Chair of Applied Mechanics. Using an ordinary impact hammer, the z-direction transfer function was investigated in the frequency domain. The results are shown in fig. 21.5.

The lower cut-off frequency can be determined when the resistor is switched off, so only the insulating resistance of the range capacitor is present. As this resistance cannot be measured, the sensor's manual proposes values up to $T_g = 100\,000\,\mathrm{s}$, which results in a frequency $f_u = \frac{1}{2\pi T_g} \approx 0$. The slight mismatch of the amplitude (which should ideally be $0\,\mathrm{dB}$) is attributed to the calibration of the impact hammer.

[1] Kistler AG, Datasheet, 3-Komponenten-Messsystem TYP9129A, 2020

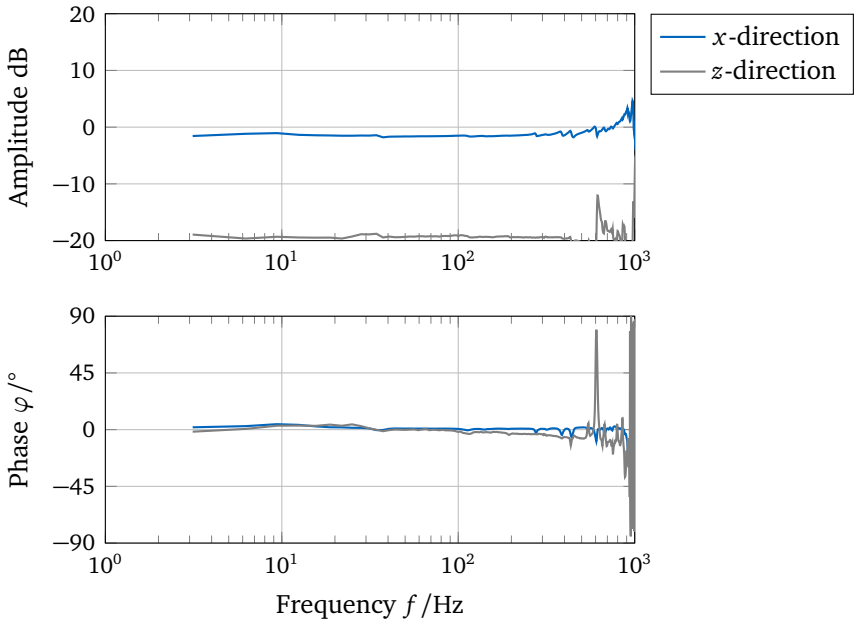

Figure 21.5: Force sensor dynamics: No significant cross-coupling nor change in amplitude or phase was found over the considered frequency range.

21.1.5 Temperature Sensors

To measure the temperature of the core and the coils, K-type thermocouple sensors were utilized. These sensors work based on the principle of thermoelectricity, where a voltage is generated when two different metals are joined at two different temperatures. To read out the sensor's value, a calibrated voltage amplifier is used. One temperature sensor is placed on the rotor's surface in between two teeth of the stator core. The second sensor is placed on the tooth of the core, see fig. 21.6.

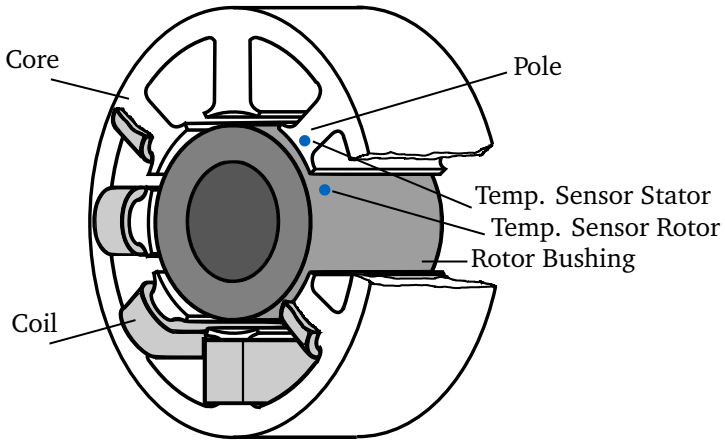

Figure 21.6: AMB schematic with placed temperature sensors.

21.2 Static Force Measurements

Using the presented experimental setup, the magnetic bearing under investigation is evaluated both statically and dynamically. The physical quantity of ultimate interest for this work is the force of the magnetic bearing on the rotor. The static measurements are used to compare the parameters saturation of the material and geometric approximations for the 2D simulation. For the static measurements, the test rig is manually adjusted to the desired position of the rotor in the bearing. A test series is driven for a constant pre-current and the largest range of control currents ($0 < I_x < I_0$) respectively possible. A control current larger than the pre-current is not meaningful, as this would lead to a negative current in the opposite coil. Due to the reluctance principle, a negative current exerts the same force as a positive current would do.

After each measurement point, the current is switched off to unload the force sensor and so avoid drifting of the piezo sensor. A measurement period is 2 s long and is sampled with 1 kHz. The time series (i.e. 2000 measurement points) of the forces and the position sensors are then averaged and stored as one measurement point, leading to very low average standard deviations per point.

Between each measurement point, the components involved in the magnetic circuit (coil, core, shaft) were cooled down by natural convection to room temperature to provide full consistency in the material parameters.

Fixed position The forces at the zero position (rotor is completely symmetrical in the bearing) are shown for different pre-currents in fig. 21.7. The curve is constructed using the mean

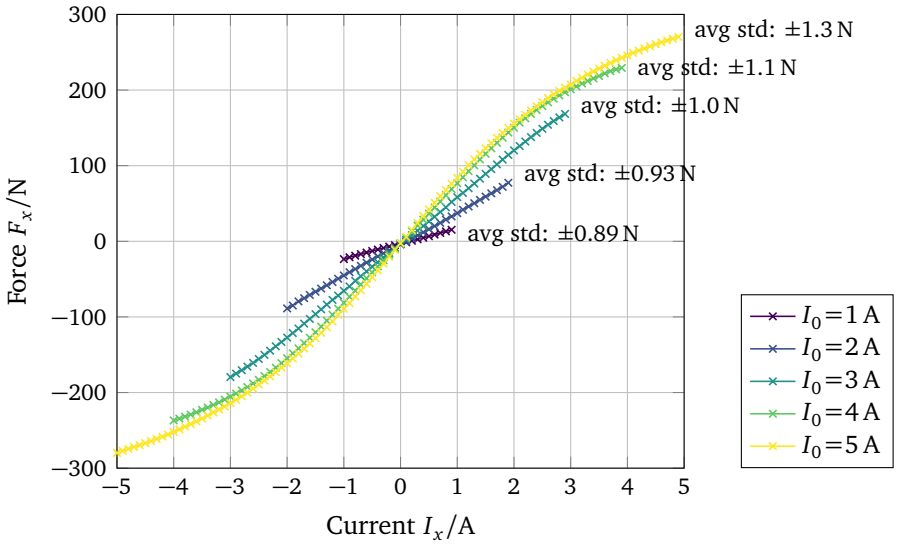

Figure 21.7: Measured forces for different pre-currents I_0 in one fixed position $x = 0$.

value of the measurement time. Each measurement point is visualized by a cross marker. The standard deviation of each series is given as an average over all measurement points. The standard deviation is very small as there is nearly no noise added to the measurement signal. The test rig is adjusted well, which is seen from the zero-crossing of the lines for different pre-currents. If the center of the rotor is not well aligned with the center of the core, the pre-current would also lead to an eccentric force.

The effect of local linearization by the difference current scheme can be seen clearly for each force series around the zero control current. Secondly, the non-linear saturation is obvious for higher currents and, therefore, a higher magnetic field domain.

Fixed Pre-Current To see the full relation between position x and current I_x, a fixed pre-current is chosen, and a map is generated, cf. fig. 21.8.

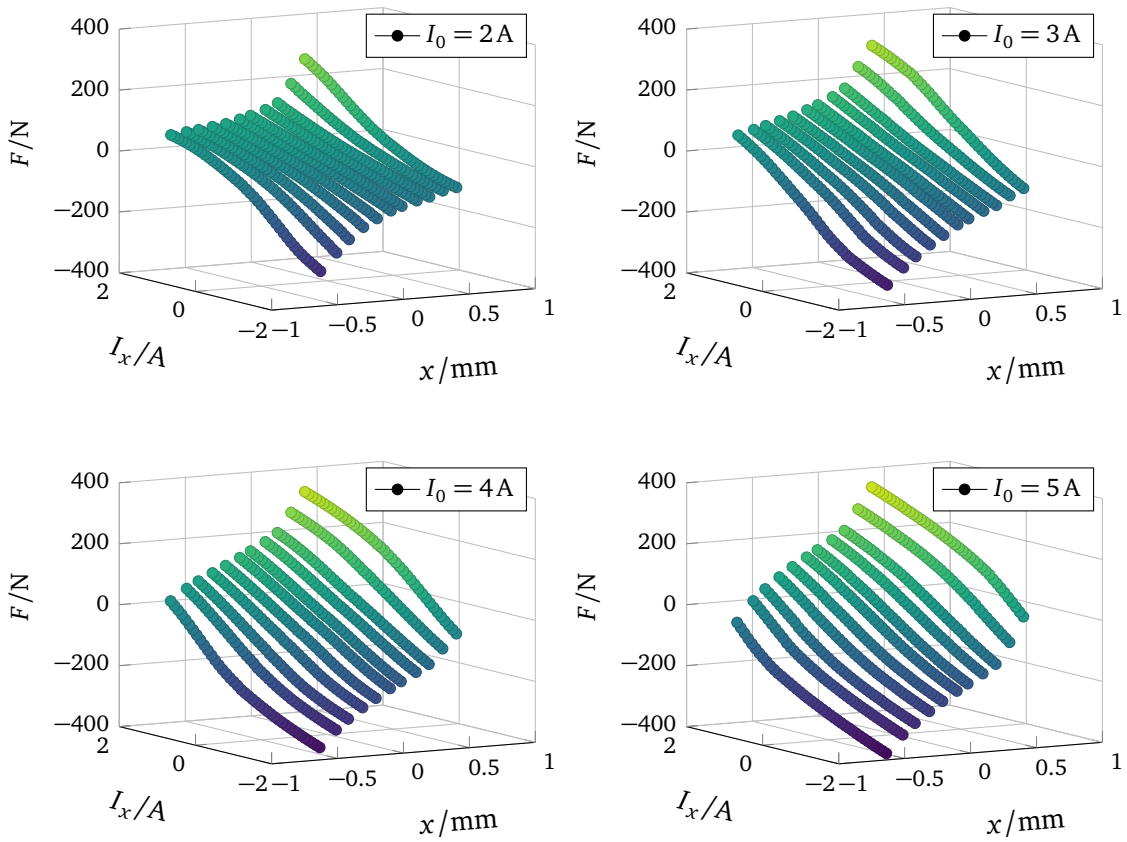

Figure 21.8: Measured forces for four different pre-currents. The higher the currents, the steeper the slope of the map and the more pronounced the saturation effect.

For a pre-current of $I_0 = 1.5\,\mathrm{A}$, the measurements are overlayed with their simulation values and plotted in fig. 21.9. The simulated and the measured characteristic force maps

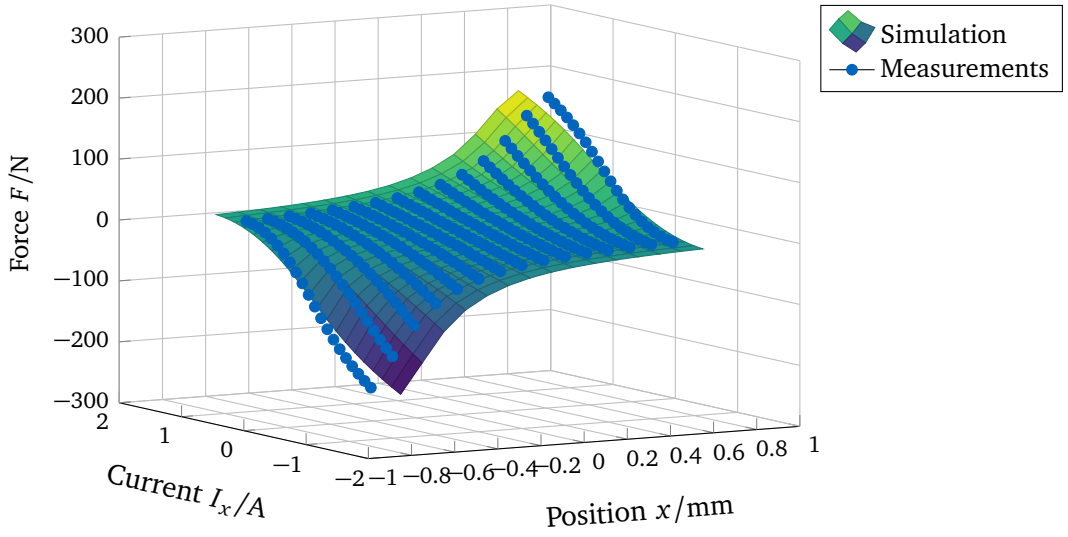

Figure 21.9: Measured forces ($I_0 = 1.5\,\mathrm{A}$) overlayed as points to the simulated characteristic map.

in fig. 21.9 have a similar shape. Around the zero points in the middle, a linear relationship

between force, control current, and rotor position can be expected. In the edge areas, the force increases quite strongly or decreases. At the extremal values of the position, a flattening of the force with the current can be seen. The flattening is caused by the saturation effects but is not very pronounced in this setup, as the currents are in the low range.

21.3 Dynamic Force Measurements

Applying time-varying currents to the magnetic bearing results in dynamic forces. In order to delimit this investigation, the current pattern is always in the explained differential mode (fig. 19.4). Also, the bearing is considered to be fully symmetrical, and with that, only one direction is investigated. Due to inaccuracies in the manufacturing and assembly processes, the properties of the bearing will not be completely equal for the two axes, but this is not the scope of this thesis.

The dynamic measurements are way more complex because now, a lot of effects interact with each other. On the one hand, there are the characteristic physical effects such as eddy currents, and on the other hand, technical conditions. The limited voltage in the magnetic bearing amplifier and the implementation of the current control loop must be mentioned here. The mechanical dynamics of the test bench also become a task.

The frequency range of all dynamic tests is limited to 1 kHz.

21.3.1 Test Rig Dynamics

The dynamics of the shown test rig cannot be neglected. Therefore, an experiment was conducted where the transfer function of an external shaker's force to the force platform's ground reaction force was determined. The most simplified minimal model for the test rig is a 1-dof spring-mass-damper system as shown in fig. 21.10. To validate and parametrize the dynamic model, a shaker with an impedance sensor is hung over the AMB. The force sensor platform is used as the output signal.

(a) Shaker construction to identify test rig dynamics.

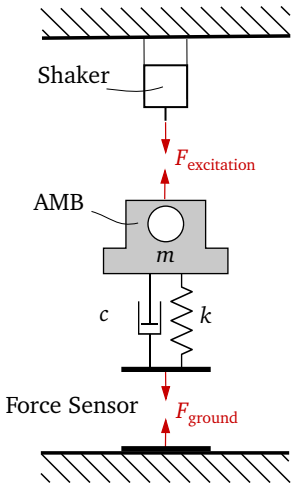

(b) Scheme of the 1-dof test rig.

Figure 21.10: Testing the eigendynamics of the test rig.

The transfer function excitation force $F_{\text{excitation}}$ to ground force F_{ground} is derived with basic dynamics as complex $\underline{G}(\mathrm{j}\Omega)$, where Ω denotes the excitation frequency and m, c, k the classic parameters of a 1-dof spring-mass-damper system.

$$\underline{G}(\mathrm{j}\Omega) = 1 + \frac{m\Omega^2}{-m\Omega^2 + \mathrm{j}c\Omega + k} \tag{21.3}$$

The measured amplitude and phase values are processed with a moving average of 25 Hz and the rolling standard deviation is computed. The upper and lower standard deviation lines are filled gray in fig. 21.11. The 1-dof model is overlayed. A good match is seen for the amplitude. The phase diverges for higher frequencies mainly due to the high damping in the model. The mass of the fully equipped AMB, including the upper adapter mount plate,

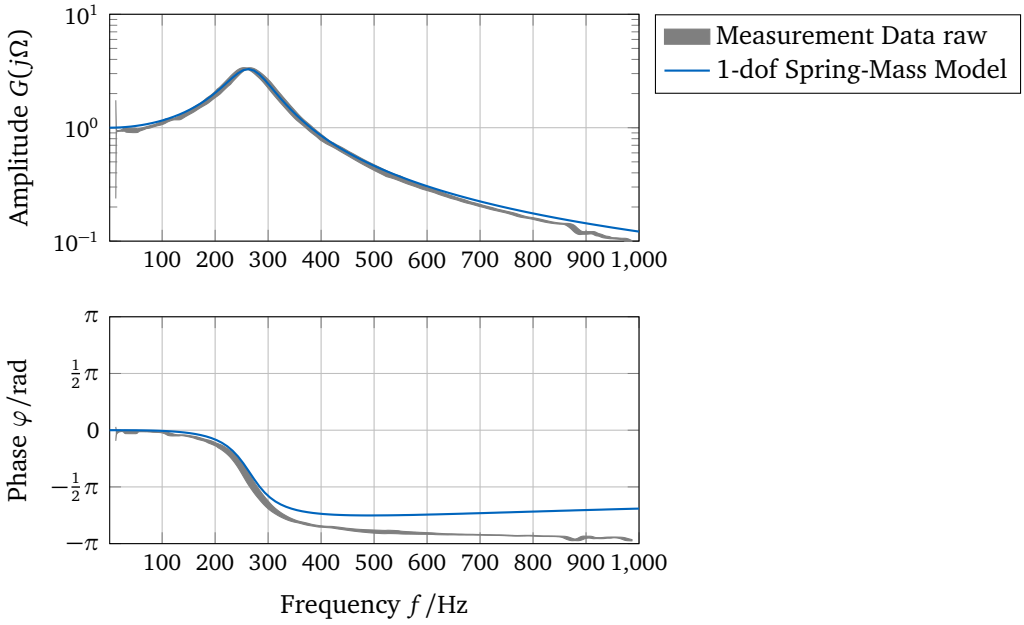

Figure 21.11: Comparison of the transfer function force to force measurement using the shaker and the minimal model.

was measured and therefore fixed. The stiffness and damping parameters are hand-tuned to match the measured FRF data in fig. 21.11. This experiment concludes that the test rig

Table 21.1: Physical quantities for the test rig.

Feature	Quantity
AMB Mass	11.9 kg
1-dof Stiffness	$34 \times 10^6\,\mathrm{N\,m^{-1}}$
1-dof Damping	$6500\,\mathrm{N\,s\,m^{-1}}$

can be assumed to be rigid up to a frequency of 100 Hz. No compensation for the test rig dynamics is needed for the force measured by the platform.

21.3.2 Dynamic AMB Force Measurements

A second dynamic measurement is conducted where the force is generated by the AMB itself. As the excitation force can not be measured directly, a frequency response function is

generated from the applied current to the force measured in the test rig. The pre-current is fixed and the excitation current is applied as a sinus chirp with the full amplitude around the offset of the pre-current. Note that the current for this measurement was taken from external current clamps, directly at the coils of the AMB. This guarantees that the AMB amplifier's amplitude drop does not interact with the here shown effects. The result is plotted in fig. 21.12. Using the temperature sensors, it was ensured that the temperature of the AMB changed only to a small extent, as this also has an effect on the transmission factor, as we will see later. Two points from fig. 21.12 are discussed in the following: The decreasing transmission factor for higher currents, and the frequency shift of the resonance.

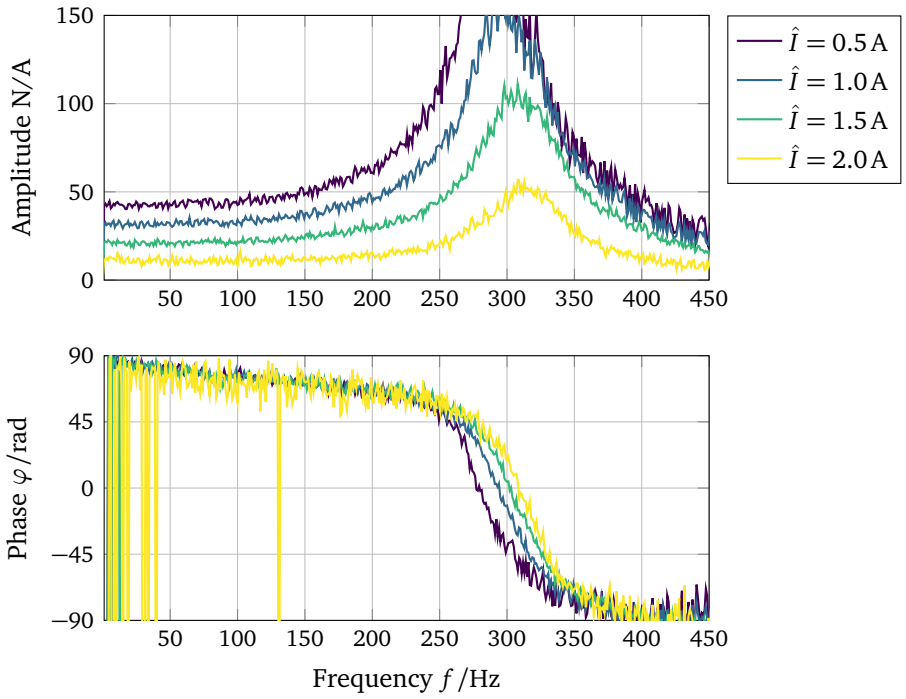

Figure 21.12: Current-to-force FRF measurement of the AMB in the test rig for four different pre-currents and their corresponding max. amplitudes.

For a linear system, one would expect a constant transmission factor from current to force. Due to the saturation of the material, the ratio between current and force becomes amplitude-dependent. As seen in fig. 21.12, the transmission amplitude decreases with increasing load. In addition due to the saturation effect, the force response of the current is not purely sinusoidal anymore. This opens the question, of whether a frequency response function is useful for further discussion. A manual check of the time data of the force response unveils that the deterioration of the signal up to $\hat{I} = 2.0\,\mathrm{A}$ is acceptable. The second point to highlight, is the positive shift in the resonance frequency with increased currents, following higher generated forces. The resonance frequency probably stems from the test rig, as seen before. Whereas the shaker measurements where conducted with relatively low forces, the AMB can generate much higher forces. A positive shift of the resonance indicates a stiffening of the system. The explanation could lie in the clamped-clamped rotor assembly. A clamped-clamped beam shows a stiffening for increasing displacement amplitudes. On the other hand, this is counteracted by the natural negative stiffness of AMBs that increases with increasing pre-currents, see section 19.2.

Intermediate Conclusion The dynamic characterization of AMBs, including the non-linearity effects, is a complex field that would need more in-depth investigations. For the further

course, the simulation model is calibrated to match the measurements in a quasi-static sense, including the effects of eddy currents, temperature-dependent material conductivity and their consequences.

21.4 Model Calibration

Since multiple simplifications are used in the simulation model (2D simulation, no housing, isotropic materials), several parameters need to be calibrated using the real system. One approach could be to use any optimization algorithm to find a set of parameters optimal to an objective function. Unfortunately, this often leads to parameter sets that are not meaningful in a physical sense.

For this work, the identification of the parameters is done stepwise, ordered such that each parameter is as isolated as possible. The investigated parameter is then fixed, and the next is considered. With this procedure, the process of the dependent parameter determination is resolved to some extent, whereby only a suboptimal solution, but an interpretable one, can be found.

21.4.1 Static Model Parameters

Heat Coefficients

In the case of natural convection, a general heat transfer coefficient for iron-air interface values from $5\,\mathrm{W\,m^{-2}\,K^{-1}}$ to $25\,\mathrm{W\,m^{-2}\,K^{-1}}$ can be found in [13]. To perform an experimental calibration of the heat transfer coefficient of both the rotor and the stator, the magnetic bearing is heated up (using a sine trajectory with high current load) and the temperature decay is measured on the test rig. Multiple thermal simulations with varying rotor- and stator coefficients are performed to fit the simulation to the measurement. The chosen pair is given in fig. 21.13, where the solid line indicates simulation and the diamond marks the measurements. The chosen value for the stator is $\alpha_{\mathrm{Stator}} = 10\,\mathrm{W\,m^{-2}\,K^{-1}}$ and for the rotor $\alpha_{\mathrm{Rotor}} = 30\,\mathrm{W\,m^{-2}\,K^{-1}}$.

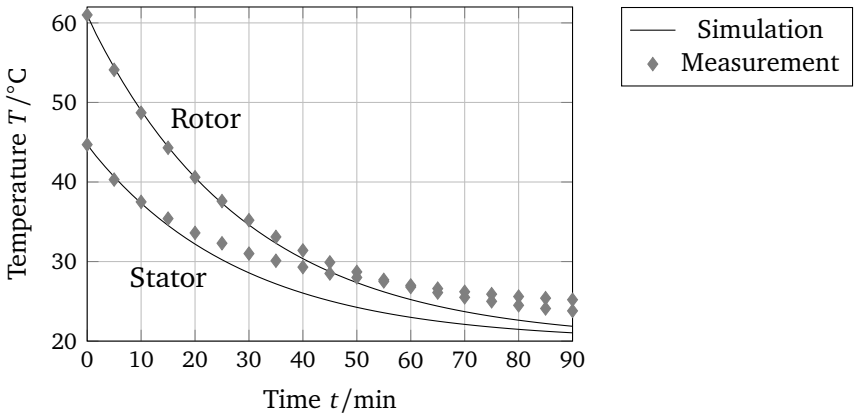

Figure 21.13: Calibration of heat transfer coefficients using the measured temperature decays. The long-term values could not be fitted exactly.

Permeability

The core of the magnetic bearing consists of laminated non-oriented electrical steel sheets (M270-35A, 1.0801, $t = 0.35\,\text{mm}$). The non-linear permeability $\mu(B)$ of the used material is assumed from datasheets [21], approximated by continuous functions (as shown in fig. 20.1) and is fixed without further investigations for this work. The rotor is turned from low-carbon steel (S235JR, 1.0038).

Effective Thickness

To calculate meaningful force values from the 2D model, a thickness (=axial length) parameter is needed. The real geometric thickness is therefore modified using a factor ($t_{\text{eff}} = \kappa \cdot t_{\text{real}}$) that is determined using a static force simulation and corresponding measurements. The effective thickness also incorporates all effects of fringing and the fact that only around 95 % of the volume is filled with steel due to the stacking factor of the sheet lamination. κ is chosen such that static force simulations (no eddy currents occur) fit with the corresponding measurements. For the measured force characteristic in fig. 21.14 it is chosen to be $\kappa = 0.85$, resulting in a maximum force deviation of 7 N.

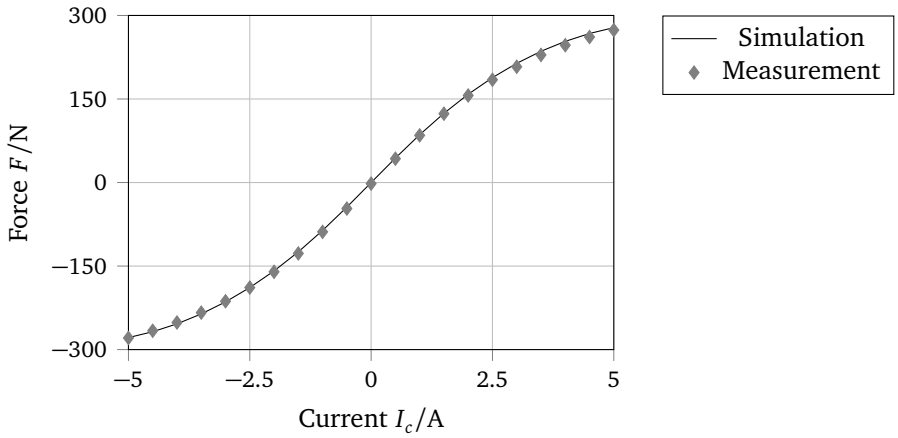

Figure 21.14: Resultant static magneto-static force obtained by simulation with an effective thickness of the bearing to compensate for leakage and fringing effects compared to measured forces.

21.4.2 Dynamic Model Parameters

Fixing the so far parameterized static simulation, the electrical conductivity for the rotor and stator are calibrated in the dynamic regime. To do so, a long-time integration simulation is set up with the shown time integration strategy. The scheme was conducted with two different large time steps ($\Delta T_j = 100\,\text{s}$ and $\Delta T_j = 300\,\text{s}$) resulting in the same graphs of the temperatures.

Heat capacitance

In the used test rig, the rotor is much longer than the axial length of the bearing core. Therefore, a virtual heat capacitance for the 2D simulation was assumed 10 times higher than the datasheet parameter.

Electrical Conductivity

The most difficult parameter to calibrate is the electrical conductivity in the stator of the AMB. The awaited eddy currents are in the out-of-plane direction of the 2D simulation. As the eddy current losses naturally should be avoided, iron cores in alternating field conditions are laminated from sheets (here thickness 0.35 mm) and bonded with non-conductive glue. The conductivity of a single sheet is around $2\,\mathrm{MS\,m^{-1}}$ to $5\,\mathrm{MS\,m^{-1}}$. For the stack of sheets, a substitute model must fulfill the requirement that the power loss and the magnetic field outside the core equal the correct model. Due to the skin effect (cf. section 20.1.1), the relation between sheet thickness and eddy current influence length will vary with the frequency. This leads inevitably to a frequency-dependent parameter [7]. The penetration depth δ eq. (20.15) indicates the length after which the electromagnetic field has decayed by a factor of $\frac{1}{e} \approx 37\,\%$:

Table 21.2: Eddy current penetration depth for $\mu = 5000$, $\sigma = 5\,\mathrm{MS\,m^{-1}}$.

f	$\delta(f)$
10 Hz	1 mm
100 Hz	0.3 mm
1 kHz	0.1 mm

Low frequencies lead to higher depths but have, in principle, less power in the eddy currents. At high frequencies, the eddy currents are at the boundaries, which in the extreme case, would lead to the full conductivity as the skin depth is smaller or equal to the sheet thickness. Introducing the lamination of cores into non-linear 2D simulation is still under research. A solution is shown in [9].

For this work, a bulk lamination model is used which treats the material as a continuum and replaces the laminated core with a reduced conductivity in the direction normal to the sheets [7]. This parametrization needs very strong assumptions that are explainable in principle but can only be quantified using a calibration test rig. The focus was set on choosing meaningful values by hand, so no optimization algorithm was involved.

According to the formula given in [7], the conductivity is assumed to be frequency independent and roughly reduced by a factor of 100 in contrast to the full material for the given geometry. The empirically chosen values for the conductivity of the stator is $\sigma_0 = 5\times10^4\,\mathrm{S\,m^{-1}}$ and for the rotor $\sigma_0 = 5\times10^6\,\mathrm{S\,m^{-1}}$ as the starting value for the temperature dependency found in eq. (20.7). In combination with the coefficient $\gamma = 0.0058\,\mathrm{K^{-1}}$, the results for the temperature development in the stator and rotor for an excitation of 400 Hz and $I_c = 5\,\mathrm{A}$ is plotted in fig. 21.15. Also included in the model are the previously determined parameters for the heat capacity and heat transfer coefficients.

21.4.3 Final Parameter Check

With that last parameter set, a final comparison of measurement and simulation is performed by the investigation of an accidentally discovered effect. Plotting one period (excitation $f = 400\,\mathrm{Hz}$) of the force on the rotor from time to time during a long-term experiment, an interesting effect of temperature-dependent force was observed (fig. 21.16), that could seem unintuitive at first glance. The force increases with increasing temperatures of the stator and the rotor.

Using the above-parameterized simulation, the effect shall be proven to not be a test rig artifact. The peak-to-peak force is plotted against the experiment time fig. 21.17. Note

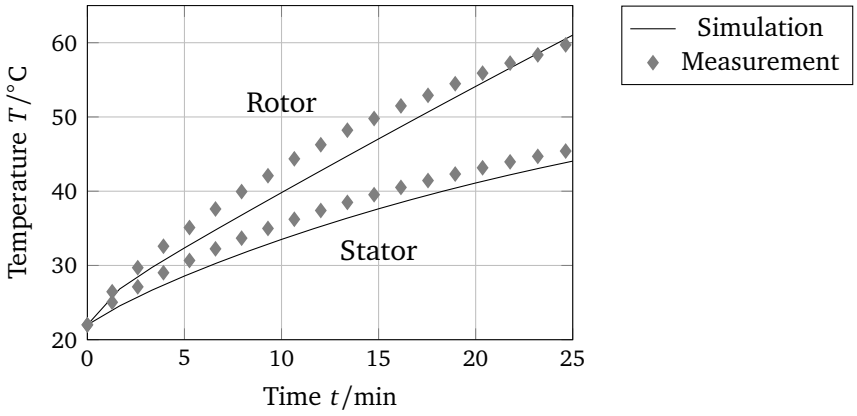

Figure 21.15: Temperature development in the magnetic bearing for a excitation of 400 Hz and $I_c = 5\,\mathrm{A}$.

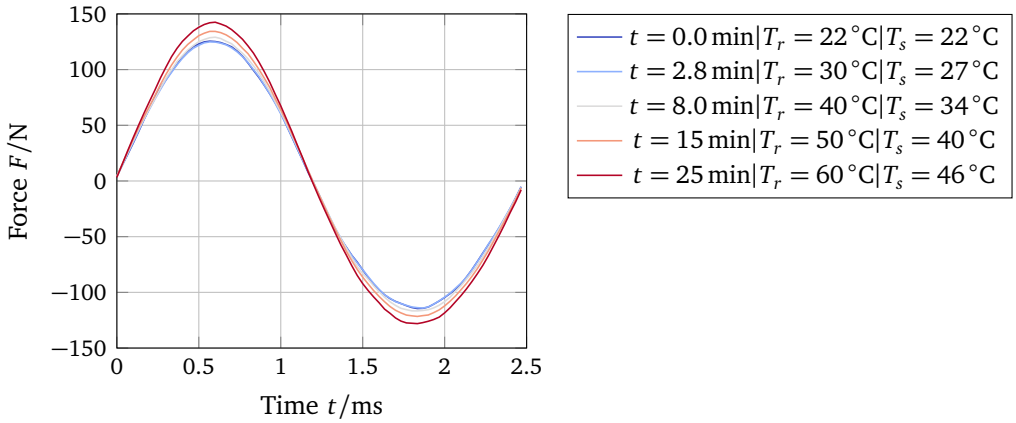

Figure 21.16: Measured force values at $f = 400\,\mathrm{Hz}$ plotted over one period at different time points and temperatures. The peak force increases with increasing temperature.

that the rotor and stator temperatures evolve differently during long experiments (as seen in fig. 21.15). Due to the decreasing conductivity, less power loss is generated by induced eddy currents. That leads to a higher force on the rotor.

Setting up the simulation to fully resemble the experiment, the here-developed model yields the same qualitative behavior, but the effect is significantly less pronounced. To slice out the important relations and visualize them, the simulation is set up in a different way: The temperatures of the components, namely the rotor and the stator, are predefined to fixed values, i.e. $T = \{20\,^\circ\mathrm{C}; 100\,^\circ\mathrm{C}\}$. Each combination is simulated and the peak force is plotted with orange stems in fig. 21.17. The peak forces of the measurements, seen in fig. 21.16, are then entered in the diagram. This shows that the correlation between temperature and force is similar but more pronounced in the measured results. The mismatch between simulation and measurement may have several reasons. The most obvious one is the attempt to represent a complex 3D environment using 2D simulation and appropriate factors. A second factor for this experiment is the mesh grid that is actually too coarse to reliably represent frequencies up to 400 Hz, so the eddy currents in the skin will be underestimated.

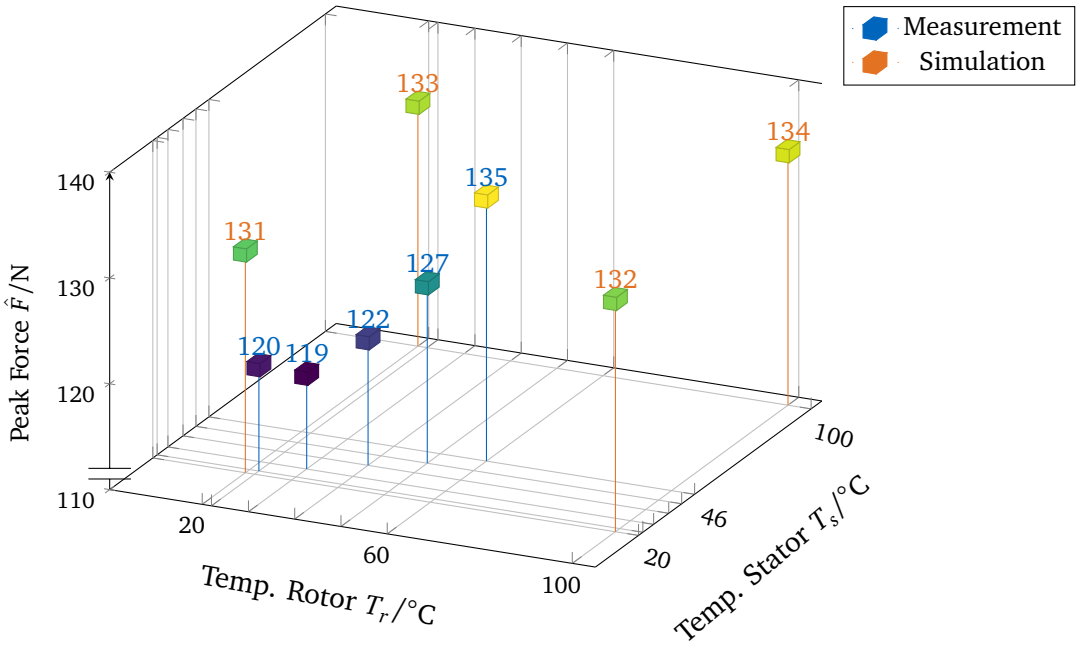

Figure 21.17: Increase of measured and simulated peak force values over different combinations of temperatures in rotor and stator. The simulation can show the qualitative effect compared to the measured values but less pronounced.

Chapter 22

Summary of Part III

Summary

After motivating a small-sized multi-physical model for the aspects of smart monitoring of mechatronic systems, the full-order model was set up. As the focus was on the demonstration of the idea, many simplifications were assumed to keep the full-order system easy to handle. The active magnetic bearing was considered in 2D, only the conductivity was assumed to be temperature dependent, and all mechanical components were assumed to behave rigidly.

Model order reduction in the form of subspace projection via the thermal eigenmodes and a POD was applied to reduce the degrees of freedom of the system. The previously investigated ECSW method was applied to the non-linear internal currents of the magnetodynamic domain. The shown reduced model unveiled a drastically lower computational and memory effort.

Setting up a fully instrumented test rig allowed an experimental parametrization of the model. It was found that this was the most challenging point in this work. The finally conducted experimental study shows basic agreement with the simulation. But there is always the question of the trust level of the different parameters. During the calibration with the experimental setup, the most severe limitation seemed to be the restriction to a 2D model. But globally, all effects of the measured forces could be explained and rebuilt with the simulation. Although a well-trained black-box model could eventually have led to a similar result, the presented white-box approach brings very detailed engineering insights, and the modeling approach can be used to model different geometries accurately without needing a full new calibration.

Reflections

In our opinion, more research is needed to find robust and good theoretical models to describe the relevant physical behavior of magnetodynamic systems in terms of smart monitoring systems. Good parametrizations are essential to use such detailed models in future monitoring systems. This leads to the basic question of how detailed a full-order model has to be to represent all necessary physical effects for the desired purpose. The successive step of model order reduction served well and is therefore useful after determining and parametrizing a full-order model. Finally, this work made a step towards the use of smart monitoring approaches, as the one proposed, enabled by the development of the presented MOR method, ECSW.

Chapter 23

Recommended Future Research

Model Order Reduction of non-linear magnetodynamic systems will become a more and more important topic in various groups where the simulation of mechatronic devices needs to progress. This thesis paves the way for further developments which will finally bring model order reduction into industry-standard workflows. A few suggestions for future research can be made from the experiences gained during the work on this thesis.

First, automatic assessment strategies for the reduced order models should be developed to ensure a good capability of the new model to serve well for the awaited load scenarios. Up to now, it has been the engineer's art to set the number of considered modes and the tolerance of the element selection algorithm. One can then test the model under various scenarios but no well-established measure allows one to assess the model's quality in advance. This is especially important for applications in the field of monitoring, as we showed a concept in part III, where faulty operation conditions can occur.

A second major research direction must be the generation of reduced order models without full solutions of the high-fidelity model. The example of the magnetic bearing already showed that a more advanced high-fidelity model (3D instead of 2D and smaller elements in the boundary regions) would have been necessary to capture the physics better. Generating training sets of large models immediately consumes much more resources. A first approach to implement a simulation-free model creation could be to initially compute the model with randomly selected elements and some generic basis. Then incrementally enrich the basis and improve the selection of the evaluated elements. In this way, the model is constructed from the bottom up rather than being reduced from the top down.

References

[1] Beams, J. W. “High Rotational Speeds”. In: *Journal of Applied Physics* 8.12 (Dec. 1937), pp. 795–806. DOI: 10.1063/1.1710256.

[2] Biro, O. and Preis, K. “On the use of the magnetic vector potential in the finite-element analysis of three-dimensional eddy currents”. In: *IEEE Transactions on Magnetics* 25.4 (July 1989), pp. 3145–3159. ISSN: 1941-0069. DOI: 10.1109/20.34388.

[3] Braunbek, W. “Freischwebende Körper im elektrischen und magnetischen Feld”. In: *Zeitschrift für Physik* 112.11-12 (Nov. 1939), pp. 753–763. DOI: 10.1007/bf01339979.

[4] Büche, D., Aho, T., and Dettwyler, M. “From Design Aspects Through to Testing of the MAN Diesel and Turbo Subsea Motor-Compressor for the Asgard Subsea Project”. In: American Society of Mechanical Engineers, June 2014. DOI: 10.1115/gt2014-26380.

[5] Earnshaw, S. “On the Nature of the Molecular Forces which Regulate the Constitution of the Luminiferous Ether”. In: *Trans. Camb. Phil. Soc.* 7 (1842), pp. 97–114.

[6] Fetzer, J., Haas, M., and Kurz, S. *Numerische Berechnung elektromagnetischer Felder*. 1st ed. Renningen-Malmsheim : expert-Verl., 2002. ISBN: 3816920128.

[7] Hahne, P., Dietz, R., Rieth, B., and Weiland, T. “Determination of anisotropic equivalent conductivity of laminated cores for numerical computation”. In: *IEEE Transactions on Magnetics* 32.3 (May 1996), pp. 1184–1187. DOI: 10.1109/20.497455.

[8] Haynes, W. M. *CRC Handbook of Chemistry and Physics, 95th Edition*. Taylor & Francis Group, 2014, p. 2704. ISBN: 9781482208689.

[9] Hollaus, K., Hannukainen, A., and Schoberl, J. “Two-Scale Homogenization of the Nonlinear Eddy Current Problem With FEM”. In: *IEEE Transactions on Magnetics* 50.2 (Feb. 2014), pp. 413–416. DOI: 10.1109/tmag.2013.2282334.

[10] Hoshi, H., Shinshi, T., and Takatani, S. “Third-generation Blood Pumps With Mechanical Noncontact Magnetic Bearings”. In: *Artificial Organs* 30.5 (May 2006), pp. 324–338. DOI: 10.1111/j.1525-1594.2006.00222.x.

[11] Jiang, Y., Wang, D., Zhang, Q., and Chen, J. “Electromagnetic-Thermal Coupling Simulation by ANSYS Multiphysics of Induction Heater”. In: *Applied Mechanics and Materials* 701-702 (Dec. 2014), pp. 820–825. DOI: 10.4028/www.scientific.net/AMM.701-702.820.

[12] Kistler Instrumente AG. *3-Komponenten-Messsystem Typ 9129A*. Datasheet. 2020. URL: www.kistler.com.

[13] Kosky, P. G., Balmer, R. T., Keat, W., and Wise, G. *Exploring engineering an introduction to engineering and design. an introduction to engineering and design*. 2013, p. 462. ISBN: 9780124158917.

[14] Maierhofer, J., Dietz, C., Zobel, O. M., and Rixen, D. J. “Multiphysical Simulation, Model Order Reduction (ECSW) and Experimental Validation of an Active Magnetic Bearing”. In: *Actuators* 11.6 (June 2022), p. 169. DOI: 10.3390/act11060169.

[15] Maslen, E. H. *Magnetic Bearings Theory, Design, and Application to Rotating Machinery. Theory, Design, and Application to Rotating Machinery*. Springer-Verlag Berlin Heidelberg, 2009. ISBN: 9783642004964.

[16] Mousavi G, S., Faraji, F., Majazi, A., and Al-Haddad, K. "A comprehensive review of Flywheel Energy Storage System technology". In: *Renewable and Sustainable Energy Reviews* 67 (Jan. 2017), pp. 477–490. DOI: 10.1016/j.rser.2016.09.060.

[17] Schweitzer, G., Traxler, A., and Bleuler, H. *Magnetlager: Grundlagen, Eigenschaften und Anwendungen berührungsfreier, elektromagnetischer Lager*. Springer Berlin Heidelberg, 2013. ISBN: 9783662084489.

[18] Schweitzer, G. *Applications and Research Topics for Active Magnetic Bearings*. Ed. by Gupta, K. 2011. DOI: 10.1007/978-94-007-0020-8_23.

[19] Shi, W. and Dustdar, S. "The Promise of Edge Computing". In: *Computer* 49.5 (May 2016), pp. 78–81. DOI: 10.1109/mc.2016.145.

[20] Smallman, R. and Ngan, A. "Physical Properties". In: *Modern Physical Metallurgy*. Elsevier, 2014, pp. 317–356. DOI: 10.1016/b978-0-08-098204-5.00008-0.

[21] Steel Europe AG, thyssenkrupp. *Produktinformation powercore M270-35A*. 2017.

[22] Varghese, B., Wang, N., Barbhuiya, S., Kilpatrick, P., and Nikolopoulos, D. S. "Challenges and Opportunities in Edge Computing". In: *2016 IEEE International Conference on Smart Cloud (SmartCloud)*. IEEE, Nov. 2016. DOI: 10.1109/smartcloud.2016.18.

[23] Voigt, A. J., Mandrup-Poulsen, C., Nielsen, K. K., and Santos, I. F. "Design and Calibration of a Full Scale Active Magnetic Bearing Based Test Facility for Investigating Rotordynamic Properties of Turbomachinery Seals in Multiphase Flow". In: *Journal of Engineering for Gas Turbines and Power* 139.5 (Jan. 2017). DOI: 10.1115/1.4035176.

[24] Vong, P. and Rodger, D. "Coupled electromagnetic-thermal modeling of electrical machines". In: *IEEE Transactions on Magnetics* 39.3 (May 2003), pp. 1614–1617. DOI: 10.1109/tmag.2003.810420.